

ABSTRACT

COLEBANK, MITCHEL JONATHAN. Computational Modeling of Patient Specific Pulmonary Hemodynamics. (Under the direction of Mette S. Olufsen.)

Pulmonary hypertension (PH), defined by an elevated blood pressure in the vasculature within the lungs, is a debilitating disease diagnosed months to years after onset. Under normotensive conditions, the pulmonary vasculature is a system of compliant, deformable blood vessels, transporting blood under a relatively low pressure magnitude. In PH, both the structure and function of the pulmonary vasculature are compromised, causing network-level vascular remodeling. Diagnosis of this disease requires both morphometric imaging and invasive heart catheterization; however, a tool for integrating the two modalities is lacking.

Computational hemodynamics are emerging as a non-invasive tool for determining the progression of cardiovascular disease, but are underutilized in the pulmonary circulation. To address this deficiency, this thesis develops a framework for integrating patient-specific imaging data with a one-dimensional fluid dynamics model of the pulmonary arterial tree. A combination of image segmentation and novel network extraction algorithms convert the vasculature into a labeled, geometric tree fully determined by vessel length and radii and a network connectivity matrix. This is utilized as a pipeline for simulating patient-specific hemodynamics in expansive pulmonary vascular trees.

In order to determine patient-specific physiomarkers, the model is inspected using local and global sensitivity analyses and uncertainty quantification. Hemodynamic data from the clinic are sparse, making it crucial that an identifiable and influential parameter subset is first established. These techniques are applied to normotensive and PH mice, and model parameters that parallel clinical indicators of disease progression are inferred. In PH, parameters describing vascular stiffness increase while those describing pulmonary artery compliance decrease, consistent with physiological intuition.

Lastly, this study innovates on the existing 1D model to simulate hemodynamics in chronic thromboembolic pulmonary hypertension (CTEPH). This PH subgroup is characterized by recurrent pulmonary emboli that impede flow to the alveoli, and constitutes the only curable form of PH. Successful treatment of the disease requires patient-dependent surgical intervention, and provides an avenue for integrating image data with computational treatment planning. This work models two distinctive types of CTEPH lesions, ring- and web-like lesions, to predict hemodynamics with disease worsening. The model predicts wave propagation and wave reflections in the pulmonary arteries, and constructs a new, quantitative index for perfusion heterogeneity in the lung. Finally, improvement in hemodynamic predictions after simulated treatment by balloon pulmonary angioplasty are presented, laying the foundation for a new computational treatment planning framework for CTEPH patients.

© Copyright 2021 by Mitchel Jonathan Colebank

All Rights Reserved

Computational Modeling of Patient Specific Pulmonary
Hemodynamics

by
Mitchel Jonathan Colebank

A dissertation submitted to the Graduate Faculty of
North Carolina State University
in partial fulfillment of the
requirements for the Degree of
Doctor of Philosophy

Biomathematics

Raleigh, North Carolina

2021

APPROVED BY:

Mansoor Haider

Alen Alexanderian

Dirk Husmeier

Mette S. Olufsen
Chair of Advisory Committee

DEDICATION

To my parents, family, and wife. Thank you for never giving up on me.

I did it Dad. I finally did it.

BIOGRAPHY

Mitchel was born in Ft. Lauderdale, FL, and after moving to Illinois and Virginia landed in Greenville, South Carolina. Mitchel struggled with math through grade school, but found a love for the field after taking AP calculus in high school. He attended Clemson University in Clemson, SC, and pursued a B.S. in Mathematical Sciences. During the course of his bachelors degree he was also an active percussionist, performing in the Clemson Drumline, Symphonic Band, and Percussion Ensemble. Through these activities, Mitchel would find his biggest mentor and supporter: his wife, Ansley.

Mitchel struggled with academic coursework during his first two years of college, as well as the loss of his father, George Michael Colebank, due to lung cancer. This latter experience motivated improvements in Mitchel's academic performance and drove him to apply to Ph.D. programs where he could utilize mathematics to improve healthcare and diagnosis of cardiopulmonary diseases. Mitchel began a streak of academic improvement, taking both graduate level mathematics classes and successfully applying to a research experience for undergraduates opportunity at North Carolina State University (NCSU). Here, he worked with Dr. Mette Olufsen, and quickly found a calling in computational hemodynamics and mathematical biology. He graduated from Clemson, and accepted a graduate student offer from the Biomathematics Ph.D. program at NCSU.

Upon arrival, Mitchel quickly began working on projects related to computational hemodynamics in the pulmonary circulation, under the advisement of Mette Olufsen. Existing collaborations with the SofTMeCh program, University of Glasgow, and Olufsen's postdoctoral scholar, Umar Qureshi, provided an environment to start research early. In fall of 2019, Mitchel received an American Heart Association predoctoral fellowship, focusing on image analysis and fluid dynamics in pulmonary hypertension. Upon graduating from NCSU, Mitchel, his wife, and dog (Bowman) will be heading out west to join Naomi Chesler's lab at the University of California, Irvine, as a postdoctoral scholar in the Biomedical Engineering department.

ACKNOWLEDGEMENTS

There are numerous people that have provided the necessary support to complete this dissertation. First, I would like to thank the members of my advisory committee: Profs. Alen Alexanderian, Dirk Husmeier, Mansoor Haider, and Mette Olufsen. I would especially like to my advisor, Mette Olufsen, for her constant support and belief in my abilities as a researcher (even when I doubted myself). I have no doubt that your faith in my work ethic and determination played a large role in where I am today.

I am gracious to the members of SoftMech at the University of Glasgow, especially Profs. Dirk Husmeier and Nick Hill, as well as Mihaela Paun and Jay Mackenzie. I am indebted to the MD's Sudar Rajagopal, Richard Krasuski, and Joe Mammarappallil at Duke University. I wouldn't have thought a simple email about whether you had data would turn into such a fruitful research collaboration.

I'm grateful for the support from students in the NCSU Biomathematics, Applied Mathematics, and Mathematics graduate programs. Many of you have reassured my abilities to carry out the research within this dissertation. In particular, I'm grateful to be a part of the cardiovascular dynamics group (CDG) at NCSU. This close group of colleagues (dare I say, friends?) has provided a backbone of support in all of my research. I'm blessed to have met and worked under Dr. M. Umar Qureshi while he was a postdoc at NCSU in the CDG. Umar, your mentorship and patience helped mold me into the researcher I am today, and I am forever grateful for your willingness to work with me.

I am thankful for research funding from the Biomathematics program's National Science Foundation (NSF) Research Training Grant "Parameter Estimation Methodologies for Mechanistic Biological Models" (#1246991) and Mette Olufsen's grant "Remodeling of Pulmonary Cardiovascular Networks in the Presence of Hypertension" (#1615820). I am gracious for the support from the American Heart Association for my predoctoral fellowship "Quantification of hemodynamic and geometric parameters in pulmonary hypertension" (#19PRE34380459).

I am forever grateful for the love and support from my mother, sister, and extended family. The daily phone calls, constant complaining about how hard school is, and visits to you all played a substantial role in my mental health. To GMC, thanks for watching over me from heaven; you served as my motivation to persevere through all this.

Lastly, and most importantly, I am thankful for the constant support from my wife, Ansley. You have put up with nearly five years of late nights, constant work, and "occasional" moments of forgetfulness when I had work on my mind. You've been my rock through all of this. I can't wait to see what adventures we take on together next.

TABLE OF CONTENTS

LIST OF TABLES	ix
LIST OF FIGURES	x
Chapter 1 Introduction	1
1.1 Summary of the dissertation	2
Chapter 2 Cardiovascular physiology	4
2.1 The vasculature	4
2.2 Pulmonary circulation	7
2.2.1 Pulmonary arteries and arterioles	7
2.2.2 Pulmonary capillaries	10
2.2.3 Pulmonary veins and venules	12
2.3 The pulmonary vascular wall	13
2.4 Pulmonary hypertension (PH)	15
2.4.1 Group I: pulmonary arterial hypertension (PAH)	16
2.4.2 Group II: pulmonary hypertension secondary to left heart disease (PH-LHD)	17
2.4.3 Group III: pulmonary hypertension due to lung disease	17
2.4.4 Group IV: chronic thromboembolic pulmonary hypertension (CTEPH)	18
2.4.5 Group V: pulmonary hypertension due to unknown causes	20
2.5 Disease diagnostics	20
2.5.1 Morphometry	21
2.5.2 Blood pressure	25
2.5.3 Blood flow	26
2.6 Pulmonary hypertension treatments	28
2.6.1 Vasodilators	29
2.6.2 Pulmonary endarterectomy (PEA)	30
2.6.3 Balloon pulmonary angioplasty (BPA)	30
Chapter 3 Image analysis	32
3.1 Medical imaging analysis	32
3.2 Image segmentation	33
3.3 Centerline extraction	35
3.4 Labeled, geometric tree	36
Chapter 4 One-dimensional fluid dynamics	40
4.1 Large vessel hemodynamics	40
4.1.1 Governing equations	41
4.1.2 Velocity Profile	44
4.1.3 Constitutive law	46
4.1.4 Summary	50
4.2 Stenosis models	50
4.3 Small vessel hemodynamics	52
4.3.1 Windkessel model	52
4.3.2 Structured tree	54
4.4 Network model	60

4.4.1	Inflow condition	60
4.4.2	Junction conditions	60
4.4.3	Outflow condition	60
4.5	Numerical Solution	61
4.6	Wave intensity analysis	62
Chapter 5	Parameter inference and uncertainty quantification	67
5.1	Inverse problems	67
5.2	Sensitivity analyses	69
5.2.1	Local sensitivity	69
5.2.2	Global sensitivity	71
5.3	Parameter identifiability	74
5.4	Parameter inference	75
5.4.1	Optimization	76
5.4.2	Marko chain Monte Carlo (MCMC)	77
5.5	Uncertainty quantification	79
5.5.1	Inverse uncertainty quantification	79
5.5.2	Forward uncertainty propagation	81
5.6	Example: unidentifiability for Windkessel boundary conditions	82
Chapter 6	Simulations and investigations	85
Chapter 7	Sensitivity analysis and uncertainty quantification of 1D pulmonary hemo- dynamics in mice under control and hypertensive conditions	88
7.1	Abstract	88
7.2	Introduction	89
7.3	Methods	93
7.3.1	Data	93
7.3.2	Modeling	94
7.3.3	Parameter Reduction	99
7.3.4	Parameter Inference	100
7.4	Model Analysis	100
7.4.1	Sensitivity Analysis	100
7.4.2	Correlation Analysis	103
7.4.3	Optimization	103
7.4.4	Uncertainty Quantification	104
7.5	Results	106
7.5.1	Sensitivity Analysis	106
7.5.2	Correlation Analysis	107
7.5.3	Frequentist analysis	109
7.5.4	Bayesian analysis	111
7.5.5	Network Predictions	113
7.6	Discussion	114
7.7	Conclusion	120
Chapter 8	Influence of image segmentation on 1D pulmonary hemodynamics	121
8.1	Abstract	121
8.2	Introduction	122

8.3	Materials and methods	123
8.3.1	Experimental data	123
8.3.2	Image analysis	124
8.3.3	Mathematical model	127
8.3.4	Inflow and outflow boundary conditions	130
8.3.5	Inverse uncertainty quantification	131
8.3.6	Forward uncertainty quantification	133
8.4	Results	134
8.4.1	Network statistics	135
8.4.2	Inverse uncertainty quantification	136
8.4.3	Forward uncertainty quantification	136
8.5	Discussion	137
8.5.1	Segmentation and construction of network graphs	138
8.5.2	Inverse uncertainty quantification	141
8.5.3	Forward uncertainty quantification	142
8.5.4	Total variation of model simulations	142
8.5.5	Geometric parameter variation	143
8.5.6	Network variation	143
8.5.7	Limitations and future work	144
8.6	Conclusions	145
Chapter 9	A multiscale model of CTEPH pre- and post-surgery	146
9.1	Abstract	146
9.2	Introduction	147
9.3	Materials and Methods	150
9.3.1	Network geometry	150
9.3.2	Fluid dynamics	151
9.3.3	Small vessel hemodynamics	153
9.3.4	Numerical solution	155
9.3.5	Wave intensity analysis	155
9.3.6	Lung perfusion and heterogeneity	156
9.3.7	Chronic thromboembolic pulmonary hypertension (CTEPH)	156
9.4	Results	157
9.4.1	Effects of lesion severity	158
9.4.2	Large vessel hemodynamics	160
9.4.3	Small vessel hemodynamics	161
9.4.4	Wave intensity analysis (WIA)	162
9.4.5	BPA therapy	163
9.5	Discussion	165
9.5.1	Large artery hemodynamics	167
9.5.2	Small vessel hemodynamics	169
9.5.3	Wave intensity analysis	170
9.5.4	Computational treatment planning	170
9.5.5	Limitations and future work	171
9.5.6	Conclusion	172
Chapter 10	Discussion	173
10.1	Future work	176

BIBLIOGRAPHY	177
APPENDICES	195
Appendix A Nondimensional Analysis	196
A.1 Nondimensional analysis of momentum balance	197
A.2 Nondimensional PDE solution	198
Appendix B Root finding and boundary conditions	200
B.1 Inflow	200
B.2 Outflow boundary condition	201
B.3 Junction conditions	204
B.3.1 Bifurcation condition	204
B.3.2 Trifurcation condition	209
B.4 Ring like lesions	212
B.5 Web-like lesions	218
Appendix C DRAM algorithm	222

LIST OF TABLES

Table 2.1	Typical values in the systemic and pulmonary vasculature. Combined from [28] and [157]. Pressure values are listed as maximum/minimum/mean.	7
Table 2.2	Murine and human data collected over the course of this dissertation. ¹ Provided by Dr. Naomi Chesler, previously at the University of Wisconsin, Madison and currently at University of California, Irvine. ² Provided from Dr. Sudar Rajagopal at Duke University Hospital's Center for Pulmonary Vascular Disease. ³ Provided by Dr. Martin Johnson from Golden Jubilee Hospital's Scottish Pulmonary Vascular Unit.	22
Table 4.1	Classification of wave fronts and wave types.	65
Table 7.1	Vessel dimensions and connectivities for SV, SB, and FN networks for the control and hypoxic mice.	95
Table 7.2	List of parameter values and how they are calculated.	99
Table 7.3	Nominal and optimized parameter values and the relative change to the nominal estimates after optimization. The wall parameter β was the same for all three models in each mouse.	111
Table 7.4	Least squares cost for all simulations using both frequentist and Bayesian methods.	113
Table 7.5	Frequentist confidence intervals for the optimized Windkessel parameters $\hat{\theta}_{WK} = \{r_p, r_d, c\}$ and Bayesian posterior variances for the control and hypoxic models.	113
Table 8.1	Summary of pre-segmentation parameters and network features.	126
Table 8.2	Estimated structured tree parameters	135
Table 8.3	Results from simulations. Values are expressed as means \pm s.d. Pressure values are in units of mmHg, flow values are in units of $\text{cm}^3 \text{s}^{-1}$ and volume values are in units of cm^3	141
Table 9.1	Summary of disease scenarios simulated in this study.	158
Table 9.2	Parameter values for simulating the five different disease scenarios described in section 9.3.7. k_3 and Z_{trm} values are listed for vessels both in unobstructed and obstructed paths (in parentheses).	159
Table 9.3	Parameters describing ring- and web-like lesions and their values.	159
Table 9.4	Wave reflection coefficient in the main, left, and right pulmonary arteries (MPA, LPA, and RPA) in each disease case. The coefficient is calculated using equation 9.27.	164

LIST OF FIGURES

Figure 2.1	(a) Diagram of the vascular system including the systemic circulation, the major organs, and the pulmonary circulation. (b) Schematic of the four heart chambers, the four heart valves, and the large arteries and veins directly connected to them. Reproduced and modified from [23] with permission.	5
Figure 2.2	(A) Pressure and volume dynamics in the right heart. The right ventricle contracts after the right atrium, leading to a systolic pressure of ≈ 30 mmHg and the opening of the pulmonary valve. Pulmonary artery pressure rises and then decays to 10 mmHg. (B) Pressure and volume dynamics in the left heart. Left ventricle systole raises pressure to ≈ 125 mmHg before the aortic valve opens. Aortic systolic and diastolic pressures are on the order of 120 mmHg and 80 mmHg. Reproduced from [28].	6
Figure 2.3	Anatomical diagram of the pulmonary arteries. Note that the right lung is subdivided into three main lobes, whereas the left lobe only contains two. Modified from [113] with permission.	8
Figure 2.4	Depiction of the three main ordering schemes for pulmonary vessels. (a) The Weibel ordering scheme [256] begins at the main root vessel and increments vessel generations at each junction. (b) The Horsfield-Strahler scheme [98] labels all terminal vessels as order "1" and increments vessels after each junction up to the root vessel. (c) The diameter defined Strahler ordering scheme from Jiang et al. [110]. All terminal vessels are labeled as order "1," and vessel orders are updated only if the diameter change is significant enough.	10
Figure 2.5	Dynamics in the pulmonary capillaries. (a) Anatomical schematic showing pulmonary arterioles distributing oxygen depleted blood to the pulmonary capillaries at the alveoli and pulmonary venules returning blood to the atrium. Adapted from [28]. (b) A simplistic depiction of blood flowing through the pulmonary alveoli originally proposed by Fung [73]. Note that a single arteriole distributes blood to more than one set of alveoli. The capillaries, located within the rectangular regions, flow by the alveolar posts, shown as circles.	11
Figure 2.6	Blood flow through the physiological zones of the lung. In Zone 1, the pulmonary arterial pressure (p_a) is always smaller than alveolar pressure (p_A) due to hydrostatic forces, causing the capillaries to collapse and reduce flow to negligible values. In zone 2, $p_a > p_A$, causing blood to flow through the capillaries depending on the pulmonary venous pressure (p_v). However, during diastole $p_a < p_A$, again leading to a reduction in flow. Lastly, flow always occurs in zone 3, since $p_v < p_A < p_a$ which leads to a driving pressure gradient.	12
Figure 2.7	Three major ventilation-perfusion (V/Q) scenarios. (a) Normal V/Q . Vascular perfusion matches ventilation by the respiratory system. (b) An extreme case of perfusion limited V/Q , e.g., due to pulmonary emboli. The flow to the alveoli is nearly zero, leading to $V/Q \approx \infty$ even with adequate ventilation. (c) Ventilation limited V/Q , e.g., due to asthma or asphyxiation. A blockage or narrowing of the bronchioles leads to negligible ventilation with normal perfusion, resulting in $V/Q = 0$	13

Figure 2.8	Illustration of the three layers of a healthy, elastic artery. The innermost layer, the intima, is comprised of a thin layer of endothelial cells. Next is the media, which is separated from the intima by a thin elastic lamina. The media contains predominately smooth muscle cells, which contribute the active contraction of the wall in response to changes in shear- and circumferential-stress. The media also contains collagen and elastic fibrils for structural support. The last layer, the adventitia, is composed of helically bound collagen as well as some elastin. The outer layer provides structural support under large deformations. Reproduced with permission from [97].	14
Figure 2.9	Flow chart showing the locations in the vasculature that drive PH in the first four subgroups. Group I, pulmonary arterial hypertension (PAH), initiates in the arterioles via uncontrolled vasoconstriction and remodeling, and propagates to the large arteries. Group II initiates from left-sided heart disease (LHD), affected the pulmonary veins and venules. Isolated post-capillary PH stops at the venules, though combined pre- and post-capillary PH due to PHD eventually affects the capillaries and arterial side. Group III includes PH due to lung-disease, initiating in the capillary beds and progressing the the arterioles and venules. Group IV is chronic thromboembolic pulmonary hypertension (CTEPH), and begins with thromboemboli located in either the large or small arteries. This causes hypoperfusion distal to lesions and hyperperfusion in unobstructed regions, causing subsequent vascular stiffening and remodeling. Figure provided by M. Umar Qureshi.	16
Figure 2.10	Optical coherence tomography (OCT) imaging of lesions in CTEPH. Fractional flow reserve (FFR) measures the pressure drop across the lesions. (A) OCT imaging of a vascular segment before and after percutaneous pulmonary angioplasty (PTPA, synonymous with BPA). FFR is improved, but does not reach a normotensive value near 1. (B) Web like lesion that leads to an FFR of 0.38. Note the non-symmetric, banded appearance of the lesion. (C) OCT imaging and FFR of a lesion after PTPA, with drastically improved FFR values. (D) Web-like lesion that extended throughout a vessel segment. Reproduced with permission from [108].	19
Figure 2.11	Flow and pressure changes in CTEPH. (a) Flow is distributed from a parent vessel to its two daughter vessels based on relative size of the two vessels. Pressure is relatively constant across the junction. (b) The addition of a lesion in CTEPH (in branch d_1) increases the resistance to flow, elevating the parent pressure. Pressure downstream from the lesion drops drastically due to the mechanical obstruction of the lesion. In contrast, the unobstructed vessel (branch d_2) receives a higher flow rate, increasing the pressure in this branch. \hat{P} and \hat{Q} represent the pressure and flow in CTEPH.	20
Figure 2.12	Multiplane view of a CT image from a patient with CTEPH. The red arrow indicates a region of the pulmonary arteries obstructed by a thromboembolism. Data provided by Duke University.	23
Figure 2.13	Ventilation-perfusion scan. (A) Perfusion scan from a typical, healthy individual. (B) Perfusion scan from an individual with a high probability of pulmonary embolism (PE). The patchy regions suggest flow heterogeneity, and provide insight into where lesions may be located. (C) A ventilation scan from a typical, healthy individual. Reproduced from [8] with permission. . . .	24

Figure 2.14	Micro-CT image from a perfused mouse lung. Note that the cannula provides an obvious, rigid shape at the MPA (shown in red) and is used to calibrate the dimensions of the vasculature.	25
Figure 2.15	Progression of catheter placement during RHC and measured blood pressure. (a) Catheter is inserted through the superior vena cava and enters the right atrium (RA). (b) The catheter is advanced through the tricuspid valve into the RV. (c) The catheter is advanced through the pulmonary valve to record MPA pressure. (d) The balloon tip of the catheter is inserted into a smaller artery and inflated, recording the pulmonary artery wedge pressure. Reproduced and modified with permission from https://www.pcipedia.org/images/6/64/RightHeart_Waveforms_Fig1.svg	26
Figure 2.16	Pressure (top) and flow (bottom) data from both normotensive and hypertensive (HPH) mice. There are 7 control animals and 5 HPH.	28
Figure 2.17	A digitized, human flow waveform in the MPA from Simvascular and the OSMSC [261].	28
Figure 2.18	Hypothesized promoter-inhibitor relationship for NO and ET-1 in the progression of pulmonary vascular remodeling. CS: cyclic stretch; WSS: wall shear stress; NO: nitric oxide; ET-1: endothelin-1.	30
Figure 3.1	Workflow for generating connected, labeled vascular networks from imaging data. First, the imaging data must be analyzed and manually labeled as arteries or veins. Then, manual and semi-automated segmentation methods are used to reconstruct the 3D geometry. After segmenting the arteries (and veins), the resulting 3D geometry is passed into a skeletonization or centerline software (e.g., VMTK). Lastly, algorithms presented in Section 3.4 separate the individual vessel components, determine their radius and length, and define the connectivity matrix for the entire vascular network. Note that the greyscale color coding in the constructed network represent different vessels in the network.	33
Figure 3.2	Thresholding functions used in ITK-SNAP. A histogram of image intensities (left y label) are plotting along with the thresholding functions (right y label) with a smoothing parameter value of $\gamma = 0.1, 0.5$, and 8.0 . (a) A lower threshold sigmoidal function with $w_{\text{lower}} = 30$. (b) An upper threshold sigmoidal function with $w_{\text{upper}} = 30$. (c) A combined upper and lower threshold function with $w_{\text{lower}} = 0$ and $w_{\text{upper}} = 30$	35
Figure 3.3	Three segmentations of the same mouse image using ITK-SNAP. Each segmentation utilizes the same number of active-contour evolutions, but has different lower threshold limits and smoothness parameters. Notice the the right pulmonary arteries (left on the page) vary in connectivity and length for differernt segmentation parameters.	35
Figure 3.4	Example of a segmented human image. (a) Segmentation of the pulmonary arteries and veins shown in the axial perspective. (b) 3D rendeding of segmented pulmonary arteries and veins. Images viewed in 3D Slicer.	36
Figure 3.5	Representative segmentation of the mouse vasculature (blue) overlaid with the centerlines produced by VMTK (black). The segmentation was conducted using a deformable snake algorithm in ITK-SNAP.	37

Figure 3.6	(a) Segmentation of human pulmonary arteries along with centerlines generated by VMTK. (b) Zoom in of a vessel in the right upper lobe. (c) Radius values calculated by VMTK (blue circles) along with 25% and 75% cutoffs used to calculate the mean radius (red dashed line) used in the network model.	39
Figure 4.1	Schematic of a cylindrical blood vessel. Notice that the cross sectional area $A(x, t) = \pi R^2(x, t)$ across the vessel length L can change in both space and time.	42
Figure 4.2	The Poiseuille, power-law, and Stokes boundary layer velocity profiles as described in equations (4.20), (4.21), and (4.22).	45
Figure 4.3	Stress exerted on a thin (left) and thick (right) walled pressurized cylinder.	47
Figure 4.4	Constitutive models from Eq. (4.39) (shown in red) and Eq. (4.42) (shown in blue). For large strains (left panel), the two models deviate with Eq. (4.39) blowing up for high strains while 4.42 increases linearly. For small strains (right most panel), Eq. (4.39) and Eq. (4.42) are similar	49
Figure 4.5	Stiffness function as described by Eq. (4.43) and originally derived in [166]. Note that smaller vessels have a greater stiffness. Plot is generated with $k_1 = 10^6$, $k_2 = 22$, and $k_3 = 8 \times 10^4$	49
Figure 4.6	Depiction of how ring- and web-like lesions are modeled. (a) Ring-like lesions are modeled as concentric, short lesions are characterized by their unobstructed area, A_p , obstructed area A_s , and length L_s . (b) Heterogenous strands of fibrous material characterize web-like lesions. The degree of obstruction is determined by the length of the lesion, L_w , and the permeability of the web, K_{perm}	51
Figure 4.7	(a) Physiological depiction of the 3 element Windkessel. Blood ejected out of the heart must overcome some proximal resistance, R_p , and then flows through an artery with total compliance C_T and distal resistance R_d . (b) Electrical circuit analog for the Windkessel model. The circuit consists of a resistor in series with a resistor and capacitor in parallel.	53
Figure 4.8	Schematic of the structured tree. At each bifurcation, daughter vessels are scaled from the parent vessel radius by the radius scaling factors α and β , $0 < \beta \leq \alpha < 1$. The “ α ” pathway (denoted in red) is the longest path in the network, whereas the “ β ” pathway (denoted in blue) is the shortest pathway.	54
Figure 4.9	Nonlinear viscosity function originally proposed in [185] that depends on both vessel diameter and the hematocrit, Hct. Note that viscosity becomes more influential for smaller vessels and that viscosity magnitude is greater for greater Hct.	59
Figure 4.10	Depiction of the Lax-Wendroff method for interior points. The previous time point n (denoted in red) are used with the half-time steps (in blue) to predict the next time point at $n + 1$ (black).	63
Figure 4.11	Schematic of increased wave reflections in disease. (A) A normotensive pressure waveform is composed of a forward traveling wave that propagates before the backward, reflected wave arrives. (B) Stiffer arteries increase the speed of wave propagation and cause a backward wave to occur during forward propagation, augmenting the pressure wave. Reproduced and modified from [243] with permission.	64

Figure 4.12	Wave intensity analysis for a normotensive control mouse. (a) Separation of the pressure (top row) and velocity (bottom row) waveforms into their wavefronts (left column) and the forward and backward running composite signals (right column). (b) Wave intensity results, showing forward compression (FCW) and expansion (FEW) waves as well as backward compression (BCW) and expansion (BEW) waves.	66
Figure 5.1	Kernel density estimation (KDE) with different bandwidths. Realizations from $x \sim \mathcal{N}(-1, 0.50^2)$ and realizations from $x \sim \mathcal{N}(1.5, 0.25^2)$ are shown as crosses, and the true distribution is shown in black. Note that a smaller bandwidth provides a more narrow kernel at each data point, whereas a large bandwidth tends to oversmooth the PDF.	80
Figure 5.2	Posterior density results when estimating the full parameter set and individual Windkessel parameters. Note that some parameters have distinct modes and narrow tails, whereas others have long tails or appear nearly uniform, suggesting unidentifiability.	82
Figure 5.3	Posterior density results when estimating the individual stiffness parameters and the Windkessel scaling parameters r_p , r_d , and c . Windkessel scaling factors have a unimodal shape, as well as k_3 in the stiffness model. In contrast, k_1 and k_2 are relatively uniform, suggesting unidentifiability.	83
Figure 5.4	Posterior density results when estimating a single stiffness parameter and the Windkessel scaling parameters r_p , r_d , and c . Note that the posteriors are unimodal, with finite tails.	84
Figure 7.1	Physiological diagram illustrating (a) the systemic arterial circulation in humans compared to (b) the pulmonary circulation in the lung. The pulmonary circulation begins with the main pulmonary artery (MPA) and bifurcates into the left and right pulmonary arteries, quickly bifurcating afterwards throughout the lung.	92
Figure 7.2	General workflow of the data analysis process. Abbreviations: MCMC: Markov Chain Monte Carlo; SQP: Sequential Quadratic Programming; DRAM: Delayed Rejection Adaptive Metropolis; UQ: Uncertainty Quantification.	92
Figure 7.3	Pulmonary arterial networks constructed from micro-CT images of a control mouse. Three models are analyzed: (a) a single vessel model (SV), (b) a single bifurcation model (SB), and (c) a 21 vessel full network model (FN). The 1D model (d) is constructed by extracting centerlines from an isometric 3D volumetric surface rendered from the segmented images. The networks are represented by a connectivity matrix with nodes, edges, vessel radii, lengths, and orientation. A flow waveform obtained from data is attached at the network inlet, and at the outlets we attach three-element Windkessel models, relating flow and pressure. Pressure data is measured at the midpoint of the MPA and used for parameter inference.	96

Figure 7.4	Normalized local sensitivities in the root of the MPA, pressure during the cardiac cycle for the SV (blue), SB (red), and FN (yellow) models. Light and dark gray lines denote the normalized flow and pressure predictions, respectively. Dashed vertical lines indicate (a) the start of systole, (b) the time of maximum flow, (c) the time of maximum pressure, and (d) the start of diastole. Results show that r_d is the most influential parameter regardless of model or disease type and that vessel stiffness β increases in influence as more vessels are added to the system.	107
Figure 7.5	Normalized Morris' indices μ^* and σ for the (a) SV, (b) SB, and (c) FN models in the control (blue squares) and hypoxic (red circles) mice. For both mice, r_d has the largest value of μ^* and σ . The global sensitivities show that the parameter β increases in influence as more vessels are added to the network.	108
Figure 7.6	Ranking of parameters in the (a) SV, (b) SB, and (c) FN models based on their local and global sensitivity results. All ranking metrics were scaled to the rank value of r_d , which was largest in magnitude. Blue x's indicate control models while red circles indicate hypoxic models.	108
Figure 7.7	(a) Pairwise plots from 10,000 iterations in DRAM for the hypoxic FN model using the full parameter set $\theta = (\beta, r_p, r_d, c)$; (b) Pairwise plots from DRAM when β was fixed at its nominal value. (a) shows that the parameters β and r_p are highly correlated, as was indicated by the structured correlation results. By fixing β (panel (b)), the correlation between parameters, denoted by ν , decreases.	109
Figure 7.8	The MPA pressure data (black, solid curve) and predictions with the SV (dash-dot, blue line), SB (dashed, red line), and FN (dotted, yellow line) models. MPA pressure waveforms for the control (left column) and hypoxic (right column) models are plotted using the nominal parameters ((a) and (b)), the optimized parameter values ((c) and (d)), and the maximum a posteriori parameters ((e) and (f)).	110
Figure 7.9	Posterior densities obtained from 10,000 chain iterations of DRAM from the SV (dash-dot, blue curve), SB (dashed, red curve), and FN (dotted, yellow curve) models for the control and hypoxic mice. Graphs show results after discarding the 2,000 iteration burn-in period. The parameter values obtained from the SQP optimization are plotted with asterisks on the density curves. Values on the abscissa denote the parameter values for the respective scaling factors.	112
Figure 7.10	MPA pressure uncertainty in the proximal and downstream vasculature computed using frequentist and Bayesian techniques. For each vessel blood, pressure predictions in the left column are for the control mouse (denoted by a C) while the right column show pressure predictions in the hypoxic mouse (denoted by an H). Panels (a) and (b) show a zoom in during systole, illustrating that the frequentist analysis agrees with Bayesian estimates and that the data lies within the uncertainty bounds. These panels show that the uncertainty bounds are wider for the control mouse than the hypoxic mouse agreeing with observations that the hypoxic model fits the data better. . . .	114
Figure 7.11	Residuals from the model predictions with the optimized parameters. The residual curves indicate that errors are not independent, violating the simplifying assumptions often made about physical models when performing parameter inference.	119

Figure 8.1	Workflow for uncertainty quantification of hemodynamics. Multiple segmentations were performed to construct the segmented networks (SNs), of which one network was selected as the representative network (RN). Inverse uncertainty quantification (UQ) was performed on the 25 SNs by constructing probability density functions (pdfs) for vessel radius and length measurements. The 25 SNs were used in model simulations to understand the total variation, while the pdfs for the vessel radii and lengths were used to propagate uncertainty in the parameter variation study of a representative network. Lastly, the structure of the representative network was changed to understand the variation induced by network connectivity. Pressure and flow predictions are compared from the three sources of variation.	124
Figure 8.2	<i>ITK-SNAP</i> interface for prescribing pre-segmentation parameters (lower threshold, smoothness). Voxel intensities (x-axis) are converted to probabilities via the threshold function (y-axis). Different pre-segmentation parameters change the form of the red curve, based on which discrimination between the foreground and background is done. Here, a lower threshold on image intensities was assumed, as shown by the constant value of one in the threshold function for all values greater than the lower threshold.	127
Figure 8.3	Qualitative differences in foreground (white) of distal vascular segments when changing the lower threshold for the voxel intensities (θ_1) and the smoothing parameter (θ_2). Top: changes in foreground with θ_1 ; bottom: changes in foreground with θ_2	128
Figure 8.4	Image to network workflow. a) The foreground visible in the image file; b) The 3D rendering of the vascular foreground; c) Centrelines obtained using VMTK; d) A graph representation of the network used in the 1D model with vessels (edges) and bifurcations (nodes) identified using custom MATLAB algorithms, which can be found in https://github.com/mjcolebank/Segmentation_CFD (the different colours are used to distinguish where the vessels begin and end).	128
Figure 8.5	Components of an arterial tree. a) 3D segmentation of network; b) center-line representation of a tree with the 32 vessel-subset (red and blue); c) magnification of the vessel in blue depicting radius estimates; d) radius estimates along the vessel in blue, where the center 80% of points were used to calculate the mean radius.	129
Figure 8.6	Morphometric features from the 25 segmentations marked by different colored lines. The number of vessels (a) is consistent between segmentations until the 5th generation. The average cross-sectional area (b) decreases rapidly after the 1st generation, while the total cross-sectional area (c) varies significantly between segmentations. The segmentation parameters are plotted against each other in (d), with a clear outlier present at (44, 7.6) (in pink) indicating a set of pre-segmentation parameters that have marked effects on the network structure. The outlier has lower number of vessels and total cross-sectional area as depicted in the pink curve in panels (a) and (c).	135

Figure 8.7	Density estimates (a) and (b) and inverse cumulative distribution functions (c) and (d) for the standardised radius and length values, respectively, measured in the 32-vessel subset. The bandwidth parameters used for the length and radius KDEs were determined using Silverman's rule (blue, dash dot) and maximum likelihood cross-validation (MLCV, red, dashed). The Gaussian process (GP) mean and 95% confidence interval are shown as a solid curve with grey bands. Standardised values are denoted by the black tick marks in panels (a) and (b).	137
Figure 8.8	Gaussian Process (GP) regression using non-constant variance for the relationship between length and radius and their coefficient of variation (c_v). The GP means and standard deviations were computed from the c_v data obtained from the 32-vessel subset (asterisks) and plotted against the analytical bound of the image resolution (dash-dot curve), as given in [245]. The mean of the GPs and \pm one and two standard deviations (s.d.) from the mean are shown in (a) and (b) in black, dark grey, and light grey, respectively. The variance of the GPs in (c) and (d) were predicted using an additional GP and provided a mean (black) and variance (dashed curve) for the variance estimate. Both mean curves in (a) and (b) are above the uncertainty bound of the imaging protocol.	138
Figure 8.9	Pressure and flow predictions in the first pulmonary bifurcation when studying total variation, parameter variation, and network variation. Predictions from the total variation (1 st column) include simulations in the 25 segmented networks (SNs), the representative network (RN, in red), and \pm two standard deviations (s.d.) from the mean (blue, dash-dot). The parameter variation plots (2 nd column) show the 10,000 Monte Carlo realisations (grey) along with the mean (black) \pm two s.d. from the mean (blue, dash-dot). Lastly, the network variation predictions (3 rd column) show the predictions when using 219 vessels in the network (bright red) up until the network is reduced to the MPA, LPA, and RPA (black).	139
Figure 8.10	WI analysis in the first pulmonary bifurcation. Forward (positive values) and backward (negative values) waves are calculated for the total variation and parameter variation (grey lines) along with ± 2 s.d. from the mean (forward waves, magenta; backward waves, cyan). Predictions from the network variation study are colour coded according to network size, as described in Figure 8.9.	140
Figure 9.1	Schematic of model development, starting from image analysis and image segmentation and ending in construction of the skeletonized network and computational domain.	151
Figure 9.2	Predictions of mean MPA pressure (top), and fractional flow reserve (FFR, bottom) when increasing lesion severity in ring-like (left) or web-like (right) lesions. FFR predictions correspond to 9 ring-like lesions and 11 web-like lesions. Overall, ring-like lesions have a greater effect on MPA pressure and FFR than web-like lesions.	160

Figure 9.3	Perfusion maps for increasing ring-like stenosis severity. The top left panel (0%) shows the normotensive perfusion map, while the bottom right perfusion map shows 90% severity. The Kullback–Leibler (KL) divergence, constructed from the flow probability density function (PDF), quantifies the flow heterogeneity.	161
Figure 9.4	Pressure, flow, and shear stress in the main, left, and right pulmonary arteries in each disease scenario.	162
Figure 9.5	Pressure predictions in normotension and disease cases (a) and (d) throughout the network at different time points. Yellow segments indicate regions where lesions are present.	163
Figure 9.6	Representative obstructed (red) and unobstructed (blue) pathways in the pulmonary vasculature, along with predictions of pressure and flow for the normotensive and four CTEPH disease scenarios. A zoom in of the flow predictions in the most distal vessels of the tree are shown to the right. Results are consistent with other pathways in the network.	164
Figure 9.7	Hemodynamic predictions in the α and β pathways of the structured tree in the normotensive case and CTEPH cases (a) and (d). (a) Large vessel network with terminal vessels in obstructed (T1-T3, red) and unobstructed (T4-T6, blue) pathways. (b) Schematic of the structured tree (grey branches) and the α and β pathways (red and blue paths, respectively). (c) Mean pressure and flow predictions in the α and β pathways in terminal vessels T1-T3 as a function of radius. (d) Mean pressure and flow predictions in the α and β pathways in terminal vessels T4-T6 as a function of radius.	165
Figure 9.8	Wave intensity analysis (WIA) at the midpoint of the main, left, and right pulmonary arteries (MPA, LPA, and RPA, respectively). Forward and backward running compression waves (FCW, BCW) are distinguished from forward and backward running expansion waves (FEW, BEW).	166
Figure 9.9	Pre and post-BPA metrics used to select the most effective treatment strategies. A total of 1140 interventions are considered. (a) Network of vessels with untreated lesions (cyan) and lesions treated in the best BPA simulation (red) along with pre and post-BPA perfusion maps. The region of the tissue most affected by BPA is identified within the black, dash-dot boxes. (b) Flow probability distribution functions (PDFs) for the normotensive (black), pre-BPA (red), and post-BPA (blue). (c) Pressure in the MPA pre-BPA (red) and post-BPA (black). (d) Wave intensities in the MPA, LPA, and RPA, pre-BPA (solid line) and post-BPA (dotted line).	167
Figure B.1	Schematic of left boundary calculated using the two-step Lax-Wendroff scheme. All red points in the interior domain are known. To determine the ghost point (shown as a blue open circle), the boundary condition is applied at $x = 0$ and $t = n + 1/2$ (shown in black). Once q is determined, A is solved using the Lax-Wendroff method.	201
Figure B.2	Right boundary condition. All variables with a black circle are known. To determine the flow and area at $x = M$ and $t = n + 1$, a ghost point (blue circle) at $x = M + 1/2$ and $t = n + 1/2$ is introduced. The point is determined by averaging from the known values at $x = M - 1/2$ and $x = M$ (red circles).	202

CHAPTER

1

INTRODUCTION

Cardiovascular disease is the leading cause of death in the western world, and is expected to account for approximately 22.2 millions deaths by 2030 [247]. The total financial burden of cardiovascular disease in the United States from 2014-15 is estimated at \$351.2 billion [247]. This disease compromises the structure and function of the cardiovascular system, an intricate network of blood vessels that transport blood and nutrients to all major organs. The interaction between the vascular structure and function makes it critical that both are integrated in clinical diagnosis. Current medical technologies analyze the two separately, leaving an opening for new synergistic approaches including data assimilation and mathematical modeling.

Contributing to cardiovascular mortality is pulmonary hypertension (PH), a serious and progressive disease that affects the circulation within the lungs. The disease is underreported, with increasing incidence rates especially for patients with PH due to heart or lung disease. Approximately 5-10% of individuals age 65 and older are suspected to suffer from PH [96]. High PH mortality rate is linked to late diagnosis, with patients diagnosed around 14 months after disease onset [76]. The disease has five subgroups, only one of which (chronic thromboembolic pulmonary hypertension, CTEPH) is curable, but successful treatment requires patient-specific surgical planning [177]. The common phenotype for all five groups is increased pulmonary vascular stiffness and resistance, and decreased compliance. These metrics are approximated from hemodynamic data but cannot be directly inferred in-vivo, encouraging new clinical measures to assess disease severity. In particular, the inability to link in-vivo biomarkers to hemodynamic observations encourages the use of patient-specific, image-based, computational modeling.

Patient-specific modeling is an evolving technique for understanding cardiovascular disease. One of the first patient-specific modeling approaches was by Taylor [236], who constructed a 3D

finite element cardiovascular model, predicting systemic circulation hemodynamics. Since then, several image-to-hemodynamics softwares have been developed. Taylor’s initial ideas developed into HeartFlow© (Redwood City, CA), an FDA approved treatment planning tool for coronary artery disease [207]. Similar software has been developed by Stanford University’s Alison Marsden (SimVascular, [129]) as well as University of Michigan’s Alberto Figueroa (CRIMSON, [13]), which all integrate patient-specific imaging data to construct hemodynamic predictions. However, only SimVascular has used their platform to understand pulmonary vascular disease and PH [266], and none of these platforms have attempted to model hemodynamic improvement in CTEPH patients post-surgery.

To address these deficiencies, this dissertation is broken into five main aims: (1) to develop an image analysis pipeline that generates a labeled graph representing the pulmonary arterial tree; (2) develop a 1D computational hemodynamics model that predicts large artery fluid dynamics in the imaged geometry coupled to small vessels models that predict dynamics down to the arteriolar level; (3) infer physiological parameter estimators and distributions using hemodynamic data measured under normotensive and PH conditions; (4) determine model sensitivity and quantify uncertainty in model parameters and the model output; and (5) advance the 1D framework to predict lesion-induced energy losses and improvements in lung perfusion after simulated balloon pulmonary angioplasty (BPA). The first two aims are imperative for patient-specific pulmonary hemodynamics modeling, while aims (3) and (4) corroborate model parameters with clinical knowledge, testing the model’s robustness to uncertainty. The final aim utilizes the prior results to construct a computational tool for treatment planning in CTEPH.

Results from this work have been published in eight manuscripts [35, 45, 46, 174, 175, 186, 190, 191], of which Colebank is the first author of two. Three other manuscripts have been submitted, on which Colebank is a first author [47], joint first author manuscript [48], and contributing author [20]. This thesis includes three of the articles [45–47], constituting Chapters 7, 8, and 9. In addition, the author has contributed to seven other published manuscripts, two submitted manuscripts, and has one manuscript in preparation.

1.1 Summary of the dissertation

This dissertation consists of 10 chapters, outlining the relevant physiological, statistical, and mathematical knowledge to address the aforementioned aims. The latter chapters constitute three manuscripts (two published, and one submitted for review) using a 1D fluid dynamics model to understand PH. The proceeding chapters are organized as follows:

- Chapter 2 describes the cardiovascular system, pulmonary circulation, pulmonary hypertension, and the available data.
- Chapter 3 introduces the image analysis techniques for building labeled graphs from vascular images.
- Chapter 4 derives the 1D model fluid dynamic equations. Small vessel hemodynamics models,

including the Windkessel and structured tree models, are described. The boundary conditions for the large vessel network model and the numerical scheme for predicting large vessel hemodynamics are detailed. Finally, a summary of methods for analyzing pulse wave intensity, separating waves into incident and reflected is provided. New contributions include new energy-loss models for vascular lesions and a radius-hematocrit viscosity model.

- Chapter 5 provides an overview of frequentist and Bayesian techniques for model analysis. Sensitivity analyses and parameter identifiability are assessed using both local and global techniques. A description of parameter inference and uncertainty quantification using both frequentist and Bayesian techniques follows. Lastly, I give an example of a non-identifiable 1D model and provide a new, scaling factor approach for parameter inference.
- Chapter 6 overviews the simulations and physiological questions driving the proceeding three chapters.
- Chapter 7 includes the published manuscript "Sensitivity analysis and uncertainty quantification of 1-D models of pulmonary hemodynamics in mice under control and hypertensive conditions" by Colebank, Qureshi, and Olufsen. The study performs local and global sensitivity analyses on the 1D model in three networks of increasing complexity. Networks are constructed from normotensive and PH mice. Identifiable parameters are inferred in all three networks using both normotensive and PH hemodynamic data.
- Chapter 8 includes the published manuscript "Influence of image segmentation on one-dimensional fluid dynamics predictions in the mouse pulmonary arteries" by Colebank, Paun, Qureshi, Chesler, Husmeier, Olufsen, and Ellwein-Fix. The study investigates the uncertainty in image segmentation using a single micro-CT image from a normotensive mouse. The uncertainty in vascular geometry (length and radius) and network connectivity are quantified from 25 segmented geometries. These uncertainties are propagated to 1D hemodynamic predictions.
- Chapter 9 includes the submitted manuscript "A multiscale model of vascular function in chronic thromboembolic pulmonary hypertension," by Colebank, Qureshi, Rajagopal, Krasuski, and Olufsen. The study constructs a multiscale human model and simulates normotension and four CTEPH disease scenarios. Large vessel geometry is derived from a normotensive CT image and small vessel hemodynamics are predicted in the structured tree. Two energy-loss models are introduced in the large vessels and used to predict perfusion defects in the lung tissue. Improvements in hemodynamics and lung perfusion after simulated balloon pulmonary angioplasty are investigated.
- Chapter 10 summarizes the outcomes of the thesis and discusses future work.

CHAPTER

2

CARDIOVASCULAR PHYSIOLOGY

This chapter gives an overview of pulmonary physiology and pathological changes due to pulmonary hypertension. Section 2.1 gives a brief overview of the vasculature. Sections 2.2 and 2.3 give a detailed description of the pulmonary circulation and the pulmonary vascular wall. Section 2.4 defines pulmonary hypertension. Sections 2.5 and 2.6 describe diagnostic tools and treatment strategies for pulmonary hypertension.

2.1 The vasculature

The cardiovascular system, depicted in Figure 2.1a, consists of the heart and the systemic and pulmonary circulations. The systemic circulation transports oxygenated blood from the left heart to the major organs, including the brain, kidneys, stomach, and heart tissue [101]. The systemic veins transport deoxygenated blood from the organs back to the right heart, which ejects deoxygenated blood into the pulmonary arteries. Deoxygenated blood flows to the capillaries at the lung alveoli, exchanges carbon dioxide for oxygen, and flows to the pulmonary veins and left heart.

As shown in Figure 2.1b, both circulations begin at the heart, consisting of four chambers including two atria and two ventricles. There are four heart valves: two atrioventricular (the tricuspid and mitral valves) and two semi-lunar (the pulmonary and aortic valves). The atrioventricular valves provide an interface between the atria and ventricles and the semi-lunar valves provide a boundary between the right (RV) and left (LV) ventricles and the main pulmonary artery (MPA) and the aorta. Flow through the valves is dictated by pressure gradients. Valves open when the proximal pressure exceeds the distal pressure. This ensures that blood flows from the atria to the ventricles and from the ventricles to the systemic and pulmonary arteries.

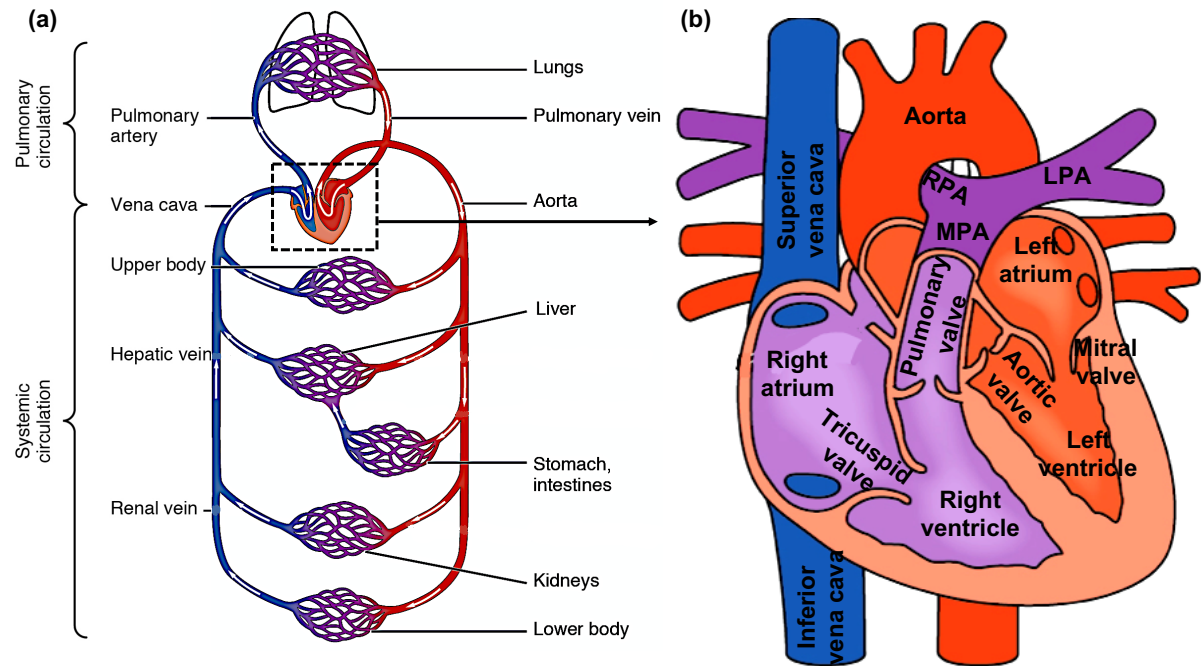


Figure 2.1 (a) Diagram of the vascular system including the systemic circulation, the major organs, and the pulmonary circulation. (b) Schematic of the four heart chambers, the four heart valves, and the large arteries and veins directly connected to them. Reproduced and modified from [23] with permission.

The heart operates as a nearly periodic pump, as shown in Figure 2.2, beginning with atrial contraction that forces blood into the ventricles. Pacemaker cells initiate ventricular *isovolumic contraction*, shutting both sets of valves and elevating ventricular pressure. Once ventricular pressure exceeds aortic and MPA pressure, the semi-lunar valves open and blood is ejected into the vasculature. Systemic and pulmonary arterial pressure increase, eventually exceeding ventricular pressure. Once ventricular pressure and the inertial forces outside the valve are overcome, the semi-lunar valves shut. The brief period when both valves are shut but ventricular pressure decreases is called *isovolumic relaxation*. After ventricular pressure falls below the venous pressure, the atrioventricular valves open, and passive ventricular filling begins. The ventricle continues to fill until the pacemaker cells in the atrioventricular node initiate atrial contraction. The period between subsequent ventricular contractions is called the *cardiac cycle*. The two components of the cycle are *systole*, when the ventricles contract, and *diastole*, when the ventricles relax and fill with blood.

The left ventricle ejects blood through the aortic valve into the *aorta* and *systemic arteries* during systole. The ascending aorta then branches into the subclavian and carotid arteries; the former carries blood to the head, neck, shoulders, and arms while the latter carries blood to the cerebral circulation in the brain. The aortic arch and thoracic aorta continue to the liver, stomach and intestines, and lower extremities. Systemic arterial diameters range from 1-30 mm, and function under a high pressure magnitude, with systolic and diastolic pressures on the order of 130-95 mmHg and 85-75 mmHg, respectively [28].

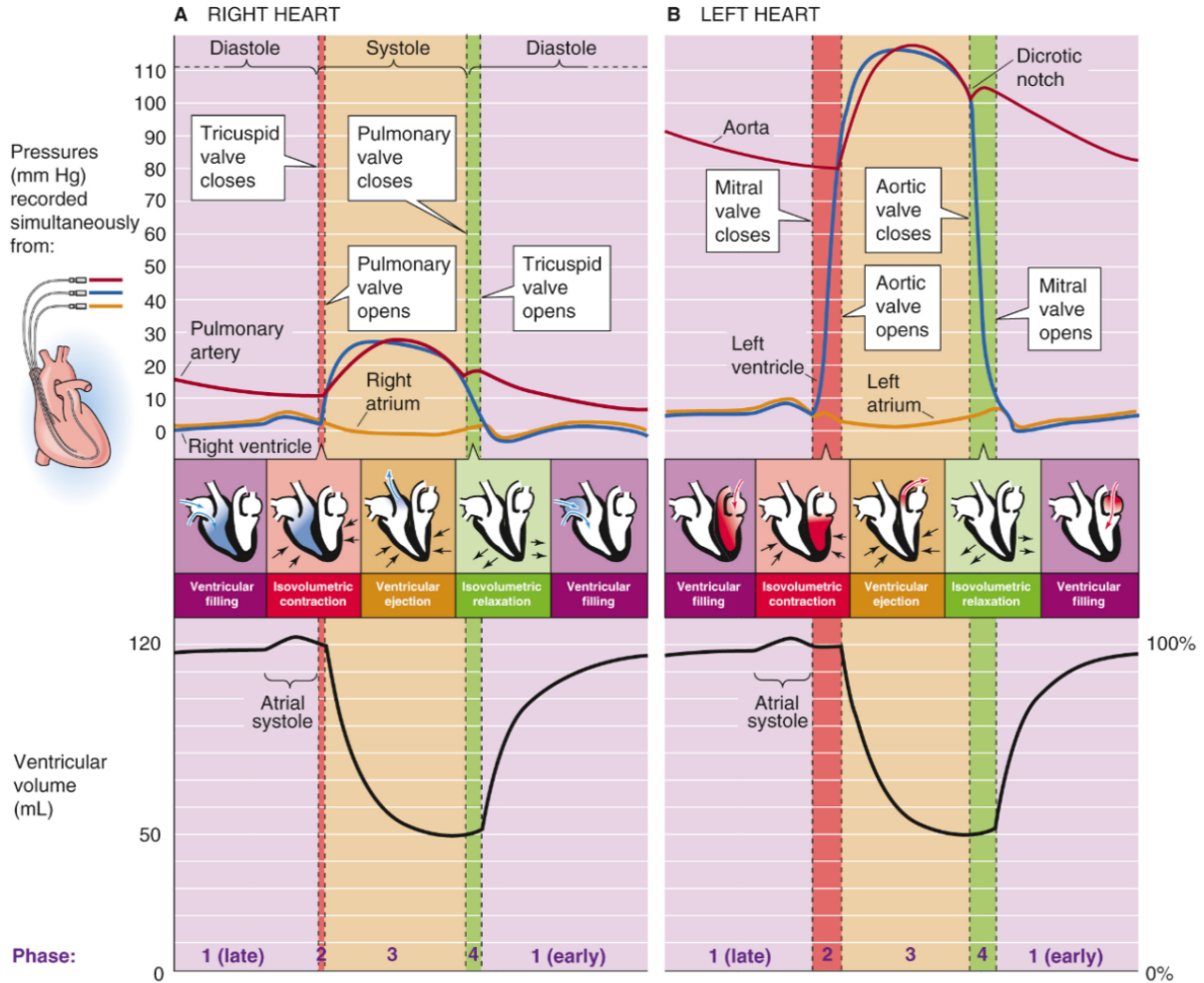


Figure 2.2 (A) Pressure and volume dynamics in the right heart. The right ventricle contracts after the right atrium, leading to a systolic pressure of ≈ 30 mmHg and the opening of the pulmonary valve. Pulmonary artery pressure rises and then decays to 10 mmHg. (B) Pressure and volume dynamics in the left heart. Left ventricle systole raises pressure to ≈ 125 mmHg before the aortic valve opens. Aortic systolic and diastolic pressures are on the order of 120 mmHg and 80 mmHg. Reproduced from [28].

At each arterial junction, individual vessel radii decrease but total cross-sectional area (the sum of the daughter branches) increases. The aorta has the largest diameter (24 mm) while small arteries and arterioles have diameters on the order 1 mm and $30\mu\text{m}$. In contrast, the aggregated cross-sectional area of the aorta is 4 cm^2 , while for the small arteries and arterioles it is 63 cm^2 and 141 cm^2 [28]. Arterioles are resistance vessels, providing the largest drop in mean systemic arterial pressure from approximately 95 mmHg in the large arteries to 60 mmHg in the arterioles [28]. The arterioles link systemic capillary beds within organs and tissues. In contrast to the tree-like branching of the arteries and arterioles, the systemic capillaries form a mesh and provide an expansive interface for gas and nutrient exchange in the tissues and organs. Capillaries empty into the systemic veins, similar in morphometry to the arteries. Veins converge until reaching the superior and inferior vena cava, which drain into the right atrium.

Table 2.1 Typical values in the systemic and pulmonary vasculature. Combined from [28] and [157]. Pressure values are listed as maximum/minimum/mean.

Vessel	Pressure (mmHg)	Volume (mL)
Systemic		
Arteries	120/80/95	300
Arterioles	—/—/65	400
Capillaries	35/15/25	300
Venules	—/—/15	2300
Veins	15/3/7	900
Pulmonary		
Arteries	25/8/15	130
Arterioles	18/8/11	
Capillaries	—/—/7	110
Venules	—/—/5	
Veins	—/—/3	200

2.2 Pulmonary circulation

The pulmonary circulation is a rapidly branching system of vessels that function under a lower pressure than the systemic arteries. The system emanates from the RV, which pumps blood into the MPA and the left and right lung via the left and right pulmonary arteries (LPA and RPA). The branching structure of the system promotes a match between alveolar blood flow and oxygen ventilation [237]. De-oxygenated blood is delivered to the alveoli to be replenished with oxygen before returning to the LA and the systemic circulation [177]. The pulmonary circulation provides an expansive area where blood can pass by the alveoli. The high pulmonary artery compliance keeps pulmonary vascular resistance (PVR) low, even with exercise. A comparison of the pressure and volume values between the systemic and pulmonary circulations are given in Table 2.1.

2.2.1 Pulmonary arteries and arterioles

Morphometry. As noted above, the pulmonary circulation, depicted in Figure 2.3, begins at the MPA (or “pulmonary trunk”) immediately distal to the RV pulmonary valve. The MPA is relatively short, and bifurcates into the LPA and RPA. Both branch into two lobar branches, followed by segmental and subsegmental vessels which parallel the bronchi of the lung (see Figure 2.3) [113]. The lung has a left and right lobe, which are further divided into ten and eight unique segments within the lobes [113]. In humans, the right lung has three lobes (upper, middle, and lower) while the left lung has two (upper and lower). Mice have a single lobe in the left lung and four lobes in the right lung, due to their quadruped anatomy [209]. The pulmonary arteries travel from the heart to the distal segments of the lung tissue, and branch along this principal pathway. The pulmonary arteries also have supernumerary branches, which branch at 90deg angles off of the main arteries and do not run parallel to the bronchial tree [33, 237]. The subsegmental arteries branch to the arterioles, which

eventually terminate at the capillary beds. Capillary bed location is dictated by the lung shape, hence arterioles can reach a pulmonary capillary bed immediately distal to a subsegmental artery or can numerously branch before terminating at the capillary beds [73]. Note that a single pulmonary arteriole can supply multiple alveoli; the pulmonary arterioles in cat lungs can supply an 24.5 alveoli on average [73] (see Figure 2.5).

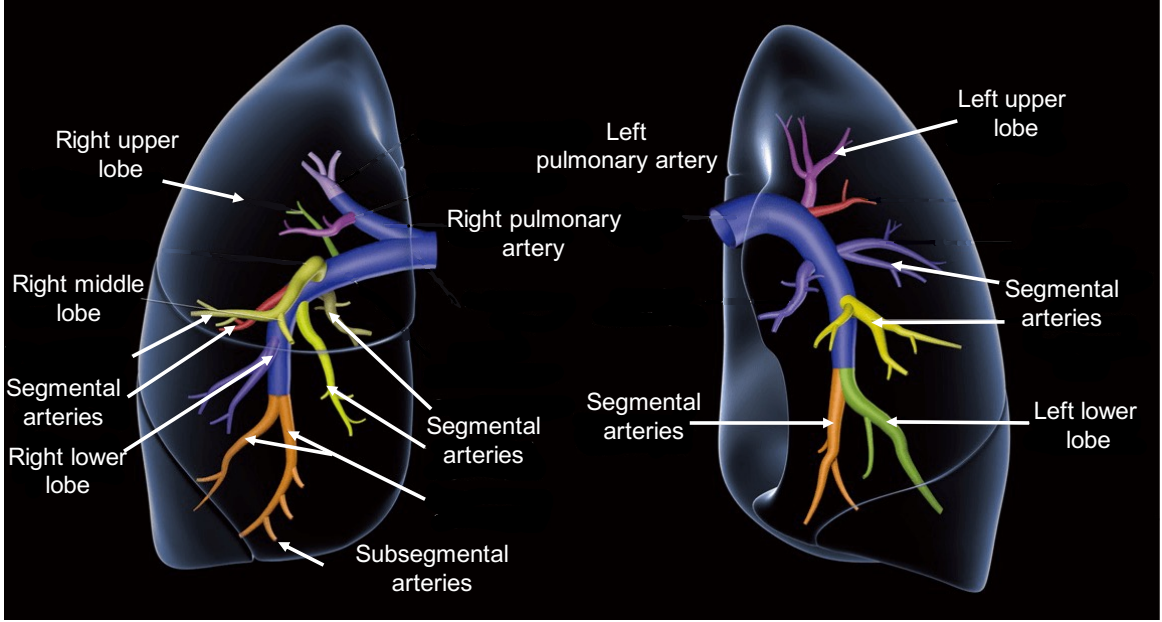


Figure 2.3 Anatomical diagram of the pulmonary arteries. Note that the right lung is subdivided into three main lobes, whereas the left lobe only contains two. Modified from [113] with permission.

A mathematical analysis of vascular branching was first done by Murray [155] in 1926. Assuming a laminar (i.e., fluid particles have a smooth path), Poiseuille flow and minimizing the work of the fluid, Murray determined that the optimal radii at a junction satisfy

$$r_p^3 = \sum_{i=1}^{N_D} r_{d_i}^3, \quad (2.1)$$

where r_p and r_{d_i} are the parent and daughter vessel radii, and N_D is the number of daughter vessels at a junction. Weibel [255] applied Murray's principal to airways and the pulmonary arteries, determining a similar radius scaling. Weibel introduced a "generation" labeling scheme describing a branch's location in the pulmonary tree [256]. Weibel labeled the generation G_i of a blood vessel by incrementing the generation, i.e. $G_i = G_{i-1} + 1$, at each new junction in a tree, depicted in Figure 2.4a. This approach works well for symmetric trees, but doesn't account for vessels of different radii branching off of the principal pathway. To remedy this limitation, the Horsfield et al. [98] proposed a Strahler ordering scheme [227] to account for asymmetric branching. This method first assigns

the terminal vessels an order of 1, and increments the order for each preceding junction by one until reaching the parent vessel (see Figure 2.4b). However, this method ignores the caliber (e.g., diameter) of the daughter branches in a tree. Jiang et al. [110] address this by defining a *diameter-dependent* Strahler ordering scheme, where the order of vessels depends on the change in diameter ΔD , as shown in Figure 2.4c. This gives a more data driven approach to Strahler ordering. In Jiang's approach, the smallest branches in the tree are order 1 branches, and subsequent branches are labeled using

$$G_i = \begin{cases} G_{i-1} + 1, & D_i > D_{i+1} + \Delta D \\ G_{i-1}, & \text{else} \end{cases} . \quad (2.2)$$

where D_i is the diameter of the current branch, D_{i-1} is the diameter values distal to the junction, and ΔD is a specified diameter increment. The ordering moves backwards progressively until reaching the largest branch (order N).

The study by Singhal et al. [219] used Strahler ordering to analyze resin casts of pulmonary arteries from humans. This study concluded that there are 17 orders in pulmonary arterial system, with one order 17 vessel (the MPA) and approximately 3×10^8 order 1 vessels (the pulmonary capillaries). The investigation by Jiang et al. [110] used casts from Sprague-Dawley rats to determine pulmonary artery branching, devising a novel connectivity matrix for Strahler branching structures. Huang et al. [102] used the diameter-defined Strahler ordering on two human lungs. In contrast to Singhal, their results concluded that pulmonary arteries and veins have 15 generations. The results of these studies have ultimately laid the foundation for constructing morphometric trees of the pulmonary arteries and arterioles.

In addition to network structure, other works have focused on quantifying changes in radii and length in the pulmonary vasculature. A survey of the pulmonary vasculature by Townsley [237] concludes that human pulmonary arterial length and radius increase by 46% and 60% for each order. A recent investigation by Chambers et al. [35] (including the author) deduced pulmonary arterial length and radii scaling factors in normotensive and PH mice. Results showed that parent-to-daughter radii scaling at junctions were unchanged between groups, but that the length-to-radius ratio increased in PH, suggesting a decrease in radii due to PH.

Hemodynamics. Typical pulmonary artery pressures are detailed in Table 2.1. In general, pulmonary artery pressure is much lower than systemic artery pressures. However, the pulmonary arteries receive an equivalent CO as the system circulation, approximately 5 L/min [90]. The pressure gradient from the MPA to the pulmonary arterioles is smaller than the systemic circulation. Mean MPA pressure is approximately 15 mmHg, and drops to 12 mmHg at the beginning of the pulmonary capillaries. It is hypothesized that the small pressure gradient is due to the smaller distance needed to travel from the MPA to the alveoli compared to the left heart and major organs [28].

In humans, pulmonary arterial blood pressure is also subject to hydrostatic forces such as gravity. In the upright human, pulmonary arterial pressure can vary by nearly 25 mmHg [90]; pulmonary arterial pressure in the uppermost portion of the lung (the apex) is roughly 15 mmHg less than

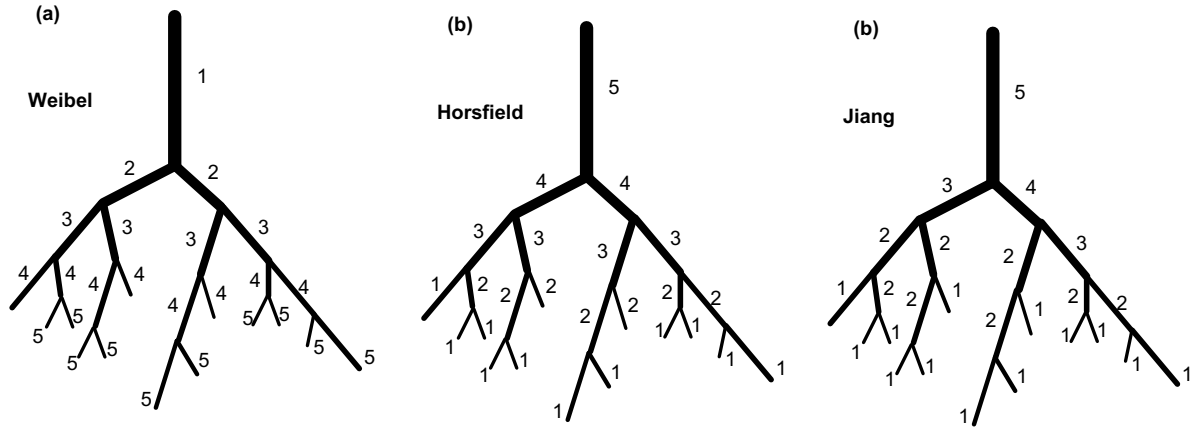


Figure 2.4 Depiction of the three main ordering schemes for pulmonary vessels. (a) The Weibel ordering scheme [256] begins at the main root vessel and increments vessel generations at each junction. (b) The Horsfield-Strahler scheme [98] labels all terminal vessels as order “1” and increments vessels after each junction up to the root vessel. (c) The diameter defined Strahler ordering scheme from Jiang et al. [110]. All terminal vessels are labeled as order “1,” and vessel orders are updated only if the diameter change is significant enough.

the blood pressure at the level of the heart. The pulmonary arterial system is designed to adapt to stress conditions, such as exercise. During upright exercise, cardiac output (CO) increases and RV systolic pressures elevate to 50-70 mmHg [263]. In addition, the pulmonary vasculature increases the number of pulmonary capillaries open for oxygen exchange, called *vessel recruitment* [28, 263].

2.2.2 Pulmonary capillaries

Morphometry. In contrast to systemic capillaries, which originate at the end of arterioles, the pulmonary capillaries emanate from vessels of different caliber. Horsfield [99] showed that pulmonary capillaries can originate both at the distal end of the arteriolar tree and at arterioles immediately after a subsegmental artery. For instance, a small artery can abruptly end in a capillary network [237]. The pulmonary capillaries surround an alveolus, which is the smallest unit in the lung functioning in gas exchange [73]. The wall between alveoli, the interalveolar septa, contains a single unit of capillary blood vessels, typically $5\mu\text{m}$ in diameter [90].

The pulmonary capillaries encapsulating the alveoli are sheetlike in appearance, and blood flows around “posts” within the sheet [72]. Fluid dynamics within the capillaries (not considered in this dissertation) are different from large and small vessel hemodynamics, and depend on the height of the sheet [72]. Figure 2.5 shows a link between pulmonary arterioles and venules with the alveoli, idealized using a simplified geometry as proposed by Fung [72, 73].

Hemodynamics. The average pulmonary capillary pressure is 7 mmHg [90]. The effects of hydrostatic pressure and gravity are significant for pulmonary capillary blood flow when humans are upright. As shown in Figure 2.6, capillary flow for humans in the upright position have three zones:

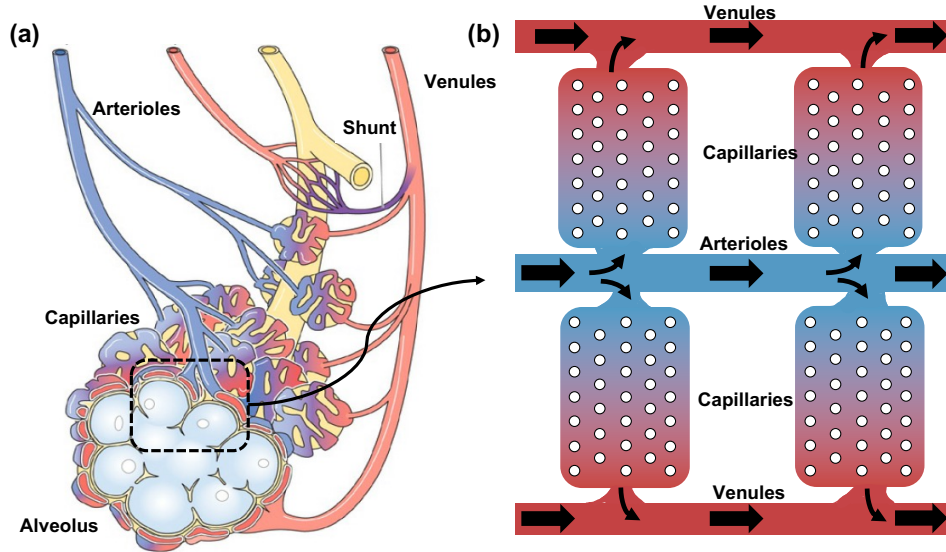


Figure 2.5 Dynamics in the pulmonary capillaries. (a) Anatomical schematic showing pulmonary arterioles distributing oxygen depleted blood to the pulmonary capillaries at the alveoli and pulmonary venules returning blood to the atrium. Adapted from [28]. (b) A simplistic depiction of blood flowing through the pulmonary alveoli originally proposed by Fung [73]. Note that a single arteriole distributes blood to more than one set of alveoli. The capillaries, located within the rectangular regions, flow by the alveolar posts, shown as circles.

- *Zone 1: no flow.* Local alveolar air pressure is consistently greater than the pulmonary capillary blood pressure.
- *Zone 2: intermittent blood flow.* The capillary blood pressure only exceeds alveolar air pressure during systole.
- *Zone 3: continuous blood flow.* The capillary blood pressure is consistently higher than alveolar air pressure throughout the cardiac cycle.

Zone 2 and zone 3 flows are typical in normotensive humans, the former are located in the apex in the lung and the latter regions are closer to the base of the lung [90]. Zone 2 flow occurs during diastole in the apex of the lung. Zone 1 flow is only present when systolic blood pressures fall below the average pulmonary capillary pressure ≈ 7 mmHg, [90].

Optimal blood-gas exchange requires that ventilation and perfusion are matched. *Ventilation* refers to the movement of air from outside the lungs to the alveoli (e.g., inhalation), whereas *perfusion* is the transport of blood carrying dissolved gasses to and from the lung [28]. Both of these processes vary within each alveolar unit and lung zone, and can be quantified by the non-dimensional ventilation-perfusion ratio, V/Q . Both perfusion and ventilation rates drop towards the lung base. The former decreases more steeply, lowering V/Q . The average V/Q is 3.3 at the apex of the lung and 0.6 at the base, giving a lung-average V/Q of 0.86 [28]. There are two unique extremes of V/Q mismatches, as shown in Figure 2.7:

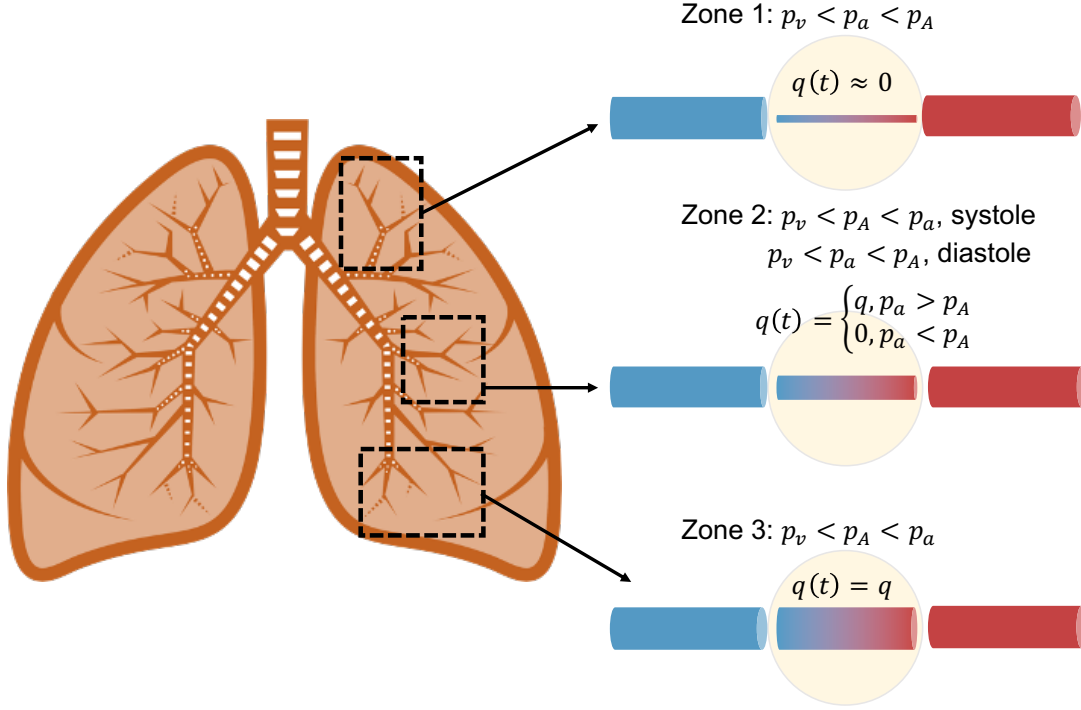


Figure 2.6 Blood flow through the physiological zones of the lung. In Zone 1, the pulmonary arterial pressure (p_a) is always smaller than alveolar pressure (p_A) due to hydrostatic forces, causing the capillaries to collapse and reduce flow to negligible values. In zone 2, $p_a > p_A$, causing blood to flow through the capillaries depending on the pulmonary venous pressure (p_v). However, during diastole $p_a < p_A$, again leading to a reduction in flow. Lastly, flow always occurs in zone 3, since $p_v < p_A < p_a$ which leads to a driving pressure gradient.

1. $V/Q = \infty \implies$ no flow (alveolar dead-space ventilation).
2. $V/Q = 0 \implies$ no ventilation (shunt).

In the former, an alveolus does not receive blood flow. One example is a pulmonary emboli, which obstructs blood from reaching a region of the lung. This leads to hyperperfusion in other unblocked regions, lowering V/Q in these alveoli (see Section 2.4 for more detail). Alveolar dead-space ventilation causes bronchiolar constriction, redistributing ventilation to better perfused areas of the lung. In the latter extreme, perfusion is normal but ventilation has ceased, causing mild hypoxia. This can arise when airways are blocked or in children with a right-to-left shunt congenital heart defect. Hypoxia causes arteriolar vasoconstriction, leading to flow diversion to regions with adequate ventilation [28]. Diagnosis of these deficiencies requires a V/Q scan, discussed in Section 2.5.

2.2.3 Pulmonary veins and venules

Morphometry. Oxygen rich blood flows out of the capillaries into the pulmonary venules and veins. Similar to the arterioles, the pulmonary venules drain from multiple alveoli, on average 17.8 [73]. Though there are less venules and veins compared to the pulmonary arterioles and arteries, the

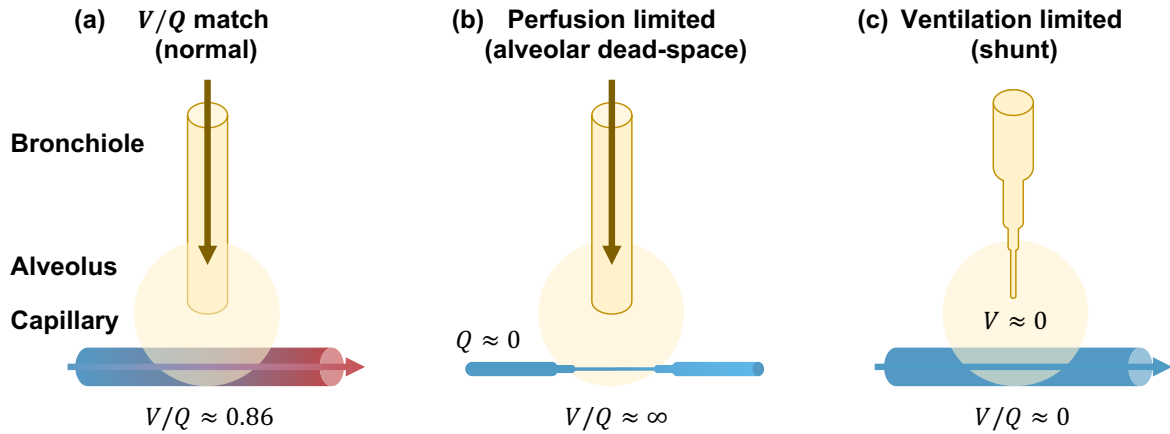


Figure 2.7 Three major ventilation-perfusion (V/Q) scenarios. (a) Normal V/Q . Vascular perfusion matches ventilation by the respiratory system. (b) An extreme case of perfusion limited V/Q , e.g., due to pulmonary emboli. The flow to the alveoli is nearly zero, leading to $V/Q \approx \infty$ even with adequate ventilation. (c) Ventilation limited V/Q , e.g., due to asthma or asphyxiation. A blockage or narrowing of the bronchioles leads to negligible ventilation with normal perfusion, resulting in $V/Q = 0$.

length and diameter ratios are similar (1.50 versus 1.58) [237]. The pulmonary venules converge rapidly from the posterior segments of the lung to the large veins connected to the left atrium. Typically, four large veins connect to the left atrium. However, there are several anatomical variants for the large pulmonary veins, which may include additional veins draining directly into the left atrium [113]. The pulmonary veins have nearly half the diameter of the pulmonary arteries [28].

Hemodynamics. The mean pressure in the pulmonary venules and veins range from 3 and 5 mmHg. One important difference between the systemic and pulmonary veins is their behavior under low or negative pressures. Systemic veins are known to collapse when transmural pressure drops below a certain threshold, giving them an irregular, elliptical shape [90]. In contrast, the pulmonary veins are tethered to the interalveolar septa, stabilizing their vascular wall and keeping them circular [73].

2.3 The pulmonary vascular wall

The arterial wall, shown in Figure 2.8, is composed of three main layers separated by a thin elastic lamina: (a) the intima, a thin monolayer of endothelial cells in direct contact with the blood; (b) the media (the middle layer), composed of smooth muscle cells (SMCs) embedded within a heterogeneous matrix of elastic and collagen fibers; and (c) the adventitia (the outermost layer), primarily composed of elastic and collagen fibers [105]. Arteries are either elastic and muscular; *elastic* arteries are larger in diameter, are located closer to the heart (e.g., the aorta and MPA), and contain large amounts of elastin [237]. *Muscular* arteries are smaller in diameter, are located closer to the lung, have a thinner wall, and contain a greater percentage of SMCs [105].

Elastic and collagen fibers are embedded in the arterial extracellular matrix. The *elastic fibers* in an artery include elastin, a polymer, and microfibrils, composed of small glycoproteins. Elastin

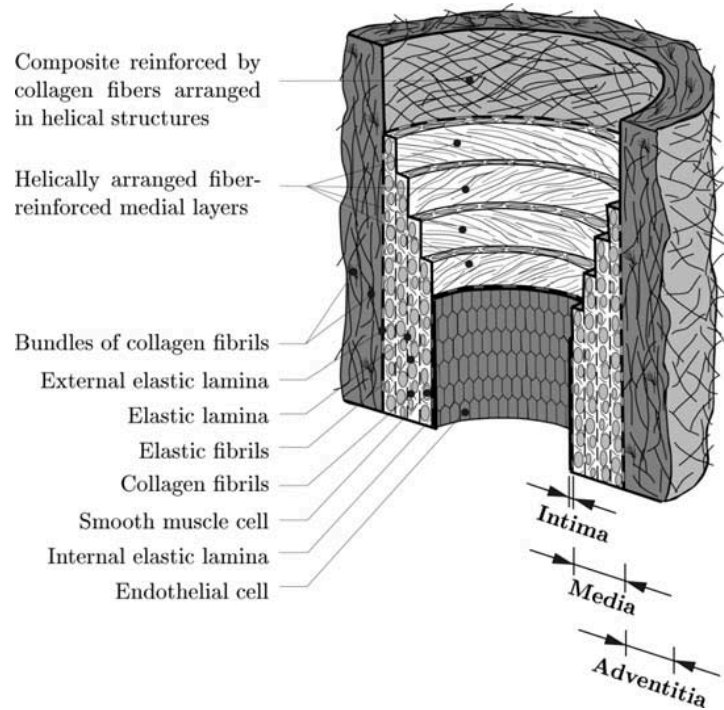


Figure 2.8 Illustration of the three layers of a healthy, elastic artery. The innermost layer, the intima, is comprised of a thin layer of endothelial cells. Next is the media, which is separated from the intima by a thin elastic lamina. The media contains predominately smooth muscle cells, which contribute the active contraction of the wall in response to changes in shear- and circumferential-stress. The media also contains collagen and elastic fibrils for structural support. The last layer, the adventitia, is composed of helically bound collagen as well as some elastin. The outer layer provides structural support under large deformations. Reproduced with permission from [97].

molecules are flexible and form an elastic fiber network, able to distend by more than 100% under physiological conditions and still return to its reference configuration [28, 105]. *Collagen fibers* serve as a structural foundation for the artery, and are less extensible (e.g., collagen can only be stretched 3-4% under physiological conditions [28]). In contrast to elastin fibers, collagen undergoes a *viscoelastic* response, with the strain varying with the history or time-course of the stress. Under large deformations, these materials do not return to their original reference configuration [240]. However, the viscoelastic behavior of excised arteries reduces after cyclic loading and unloading [74]. For this reason, arteries are modeled as *pseudo-elastic* and *hyperelastic* materials [74, 97, 105], discussed in Chapter 4. There are several types of collagen, and the most abundant types in the arterial wall are type I and III collagen. Collagen fibers are not typically under tension unless wall distension is pronounced, in which case they provide structural support for the vascular wall.

Smooth muscle cells (SMCs) have both a *passive* and an *active* contribution to wall dynamics. The passive features of SMCs are negligible compared to that of elastin and collagen fibers [97]. Nevertheless, SMCs do contribute to arterial wall stability under physiological conditions [105]. Active SMC dynamics are linked to changes in wall stress. SMCs sense both stresses on the intima (e.g., wall shear stress on the endothelial cells), and within the media and adventitia (e.g., cyclic

stretch). In response to these changes, the SMCs will induce either vasoconstriction or vasorelaxation [250]. In the pulmonary arteries, endothelial cells release vasodilators (e.g., nitric oxide (NO)) into the blood stream when wall shear stress increases. Vasodilators are absorbed through the wall and signal to SMCs to vasodilate. Conversely, low wall shear stress causes endothelial cells to release vasoconstrictive agents (e.g., endothelin-1 (ET-1)), leading to SMC contraction [77].

Arterial wall complexity limits an exact description of its stress-strain relationship. Several studies have explicitly modeled the individual layers of the vascular wall [97, 241], but in this dissertation the vascular wall is treated as a homogeneous, elastic cylinder, discussed further in Section 4.1.

The simplest descriptor of arterial wall properties is compliance, C , defined as the fractional change in volume (or area) for a given change in pressure. Another common term is distensibility, D , the compliance divided by the reference volume (or area) [252]. These are expressed as

$$C = \frac{\Delta V}{\Delta P}, \quad D = \frac{\Delta V}{V \Delta P}. \quad (2.3)$$

Compliance is inversely related to stiffness, quantified by the Young's modulus E . Experimental evidence suggests that D is constant in the normotensive pulmonary arterial network [124], but may be heterogeneous in the presence of pulmonary vascular diseases or PH [252].

2.4 Pulmonary hypertension (PH)

The 6th World Symposium on pulmonary hypertension (PH) defines the disease as a mPAP > 20 mmHg at rest (compared to the prior requirements of ≥ 25 mmHg) measured by right heart catheterization (RHC). PH is a relatively rare disease when compared to other cardiovascular ailments; however, rates are on the rise and hospitalization rates for PH in those older than 85 nearly doubled between 2001 and 2010 [247]. The disease is classified into five distinct subgroups, shown in Figure 2.9:

Group I: Pulmonary arterial hypertension (PAH)

Group II: Pulmonary hypertension secondary to left heart disease (PH-LHD)

Group III: Pulmonary hypertension due to lung disease

Group IV: Chronic thromboembolic pulmonary hypertension (CTEPH)

Group V: Pulmonary hypertension due to unknown causes

These subgroups are differentiated based on the whether they affect the pulmonary arterial system alone (pre-capillary PH) or if they affect the pulmonary veins (post-capillary PH). Pre-capillary PH is defined by a pulmonary arterial wedge pressure (PAWP) ≤ 15 mmHg, and isolated post-(or combined pre- and post-) capillary PH, where PAWP > 15 mmHg [218]. In general, PH decreases compliance (increases stiffness) by altering the composition of the pulmonary vascular wall, typically

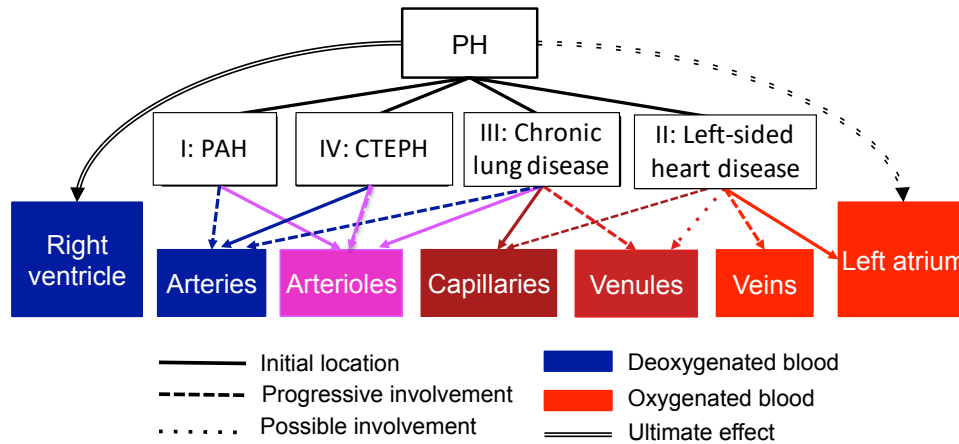


Figure 2.9 Flow chart showing the locations in the vasculature that drive PH in the first four subgroups. Group I, pulmonary arterial hypertension (PAH), initiates in the arterioles via uncontrolled vasoconstriction and remodeling, and propagates to the large arteries. Group II initiates from left-sided heart disease (LHD), affected the pulmonary veins and venules. Isolated post-capillary PH stops at the venules, though combined pre- and post-capillary PH due to PHD eventually affects the capillaries and arterial side. Group III includes PH due to lung-disease, initiating in the capillary beds and progressing the the arterioles and venules. Group IV is chronic thromboembolic pulmonary hypertension (CTEPH), and begins with thromboemboli located in either the large or small arteries. This causes hypoperfusion distal to lesions and hyperperfusion in unobstructed regions, causing subsequent vascular stiffening and remodeling. Figure provided by M. Umar Qureshi.

by increasing relative amounts of collagen through fibroblasts in the vascular wall. In contrast to collagen, elastin content typically does not change over time [237].

2.4.1 Group I: pulmonary arterial hypertension (PAH)

PAH has an incidence of 1.1 adults per 7.6 million [247]. In addition to a mPAP > 20 mmHg at rest, positive diagnosis of PAH requires a PVR ≥ 3 Wood units ($\approx 240 \text{ g/cm/s}^2$). PAH is divided into seven subtypes, including idiopathic PAH (iPAH) and PAH due to congenital heart disease [141]. As of 2020, the five-survival rate for PAH patients ranges from 61.2% to 65.4% [247].

One of the distinguished features of PAH is the narrowing and muscularization of the pulmonary arterioles. Decreased arteriolar diameter increases PVR by 4-5 times, elevating mPAP [202]. This can lead to arteriolar occlusion, when the arteriolar wall thickens to a point where blood is completely obstructed. Network remodeling in PAH is characterized by medial thickening, including an increase in SMCs and collagen. Remodeling of the large arteries includes SMC hypertrophy (increased cell size), while the small arteries and arterioles undergo SMC hyperplasia (increased cell density) and adventitial collagen deposition [177]. These factors elevate PVR, mPAP, and RV afterload. The initial onset of PAH is unknown, but is believed to initiate in the arterioles. It is hypothesized that individuals with a mutation in the bone morphogenetic protein receptor 2 gene, responsible for inhibiting proliferation of smooth muscle vascular tissue, are more susceptible to PAH. A defect in this gene can lead to uncontrolled SMC growth and wall thickening [177]. To better understand the

progression of PAH, animal models have been proposed. The most common animal PAH model is in rat, where subcutaneously injections of monocrotaline cause an overwhelming inflammatory response, leading to pulmonary vascular remodeling [80].

2.4.2 Group II: pulmonary hypertension secondary to left heart disease (PH-LHD)

PH is a common comorbidity of left-sided heart disease (PH-LHD), and is broken down into two main subgroups: isolated post-capillary PH (IPC-PH), with a PAWP > 15 mmHg and av diastolic pressure gradient < 7 mmHg or a PVR \leq 3 Wood units; and combined post- and pre-capillary PH (Cpc-PH), defined by an elevated PAWP > 15 mmHg and a diastolic pressure gradient \geq 7 mmHg or a PVR > 3 Wood units [239]. Moreover, PH-LHD can be classified as heart failure with (a) preserved ejection fraction (the percent of blood ejected from the heart during systole) (HFpEF), (b) reduced ejection fraction (HFrEF), or (c) valvular heart disease (VHD). All of these elevate left atrial pressure and cause a passive increase in pulmonary venous pressure. This is hypothesized to cause pulmonary arterial vasoconstriction, elevating mPAP [177].

The two typical causes of PH-LHD are mitral or aortic valve disease or myocardial diseases on the left heart, e.g., myocardial infarction [177]. Elevated left atrial pressure propagates through the veins to the alveoli, causing alveolar damage, fibrosis, and eventual remodeling of the small pulmonary arteries [193]. Increased mPAP attempts to match the rise in left atrial pressure. If pulmonary arterial pressure magnitude surpasses left atrial pressure, then the disease is termed CPC-PH. It is hypothesized that the transition from IPC-PH to CPC-PH is determined by the pulmonary capillaries, which remodel due to alveolar damage [193].

Animal models and experimental design for PH-LHD are still evolving. A recent study induced PH-LHD by prescribing an left ventricle myocardial infarction [179]. This involves the ligation of the coronary circulation, reducing the blood supply to the left ventricular wall and leading to cell death. This mouse model induces PH-LHD by reducing RV function and impairing vascular-ventricular interaction. A PH-LHD model in swine has also been developed, utilizing a pulmonary vein banding technique that cuts off blood supply from one vein to the LA. This experimental setup increases mPAP and elevates PVR, consistent with physiological understanding of the disease in humans [57].

2.4.3 Group III: pulmonary hypertension due to lung disease

PH due to chronic lung diseases, including hypoxia, chronic obstructive pulmonary disease (COPD), and interstitial lung disease, is the second most common form of PH representing roughly 9% of all PH cases [247]. Besides elevating mPAP > 20 mmHg, group III PH is uniquely driven for each subgroup and respiratory disease.

Hypoxia, decreased oxygen saturation in the blood, is common for people living in high elevations. This leads to an initial increase in CO followed by vasoconstriction and muscularization of the arterioles. The exact mechanisms of hypoxia-induced vasoconstriction are not well known. It is known that hypoxic environments promote the release of the vasoconstrictor ET-1 from the pulmonary arterial wall, inducing vasoconstriction [28]. This is opposite to the systemic circulation,

where a hypoxic environment induces vasodilation. Pulmonary vascular hypoxic vasoconstriction is strictly a local phenomenon, and is not regulated by the nervous or endocrine system. To better understand the pulmonary vascular response to hypoxia, experimental mouse models are used. Mice are placed in a hypobaric chamber and exposed to several weeks of low oxygen content to induce hypoxia. This model results in vascular remodeling and collagen accumulation, elevating mPAP above 20 mmHg [232, 245] (as shown in this dissertation).

The most prominent feature of PH due COPD is the enlargement of the intimal layer of the smaller, muscular arteries. This is due to hyperplasia of SMCs, requiring new layers of elastic lamina that thicken the intima. COPD induced PH was originally thought to be driven by hypoxia, yet recent evidence has shown that vascular remodeling can occur in patients with mild COPD that do not suffer from hypoxemia. Instead, damage to the endothelium due to harmful agents (e.g., cigarette smoke) are suspected to initiate a cascade of inflammatory behavior [177].

2.4.4 Group IV: chronic thromboembolic pulmonary hypertension (CTEPH)

Chronic thromboembolic pulmonary hypertension (CTEPH) is the only *curable* form of PH. CTEPH is typically preceded by an acute pulmonary embolism or deep venous thrombosis, though it can also be found in patients without preexposure to either [177]. This form of PH is more rare than Groups II and III, but is likely underdiagnosed. Prospective studies show that CTEPH develops in anywhere between 0.4% to 6.2% of patients with acute pulmonary embolism [218]. A recent study in northern France found that of 107 patients with coronavirus disease 2019 (COVID-19), 22% had pulmonary emboli, and 22% of the emboli were located in the distal, segmental branches [181]. The possible correlation between pulmonary emboli and COVID-19 motivates investigations into recurrent pulmonary emboli, CTEPH, and disease management.

Symptoms of CTEPH include dyspnea (trouble breathing) and exercise intolerance, making diagnosis of CTEPH versus other diseases difficult. Screening by echocardiography can reveal elevated RV pressure, after which patients undergo V/Q scanning. Patients presenting a unilateral perfusion defect on V/Q proceed to an expert PH center for RHC and structural imaging, with definitive diagnosis by a mPAP > 20 mmHg, a PAWP < 15 mmHg, and PVR \geq 3 Woods units [218].

The disease is typically initiated by a blockage or obstruction in the large or medium diameter pulmonary arteries [217]. Recent studies using optical coherence tomography have classified CTEPH lesions as into five main categories: (1) ring-like lesions, (2) web-like lesions, (3) subtotal occlusions, (4) total occlusions, and (5) tortuous lesions [108]. Of these, subtotal occlusions, ring-like, and web-like lesions are the most common and have the lowest probability of complication in response to BPA intervention. Ring-like lesions, shown in Figure 2.10, are short, abrupt narrowings in the vessel lumen, typically occurring at junction points, that are similar in appearance to systemic circulation stenoses. Web-like lesions consist of fibrous bands of material that more often obstruct the entirety of the vessel lumen, as shown in Figure 2.10, and appear “mesh-like” on imaging scans. Subtotal occlusions induce vessel tapering that leads to a decrease in blood velocity distal to the lesion. Total occlusions are the most severe type, blocking flow from any downstream vessels. Lastly, tortuous

lesions are located in vessels smaller than subsegmental arteries, and appear twisted and tortuous in shape [115]. The fractional flow reserve (FFR), defined as the ratio of pressures proximal-to and distal-to a lesion, is the only current metric for specifying lesion severity [108].

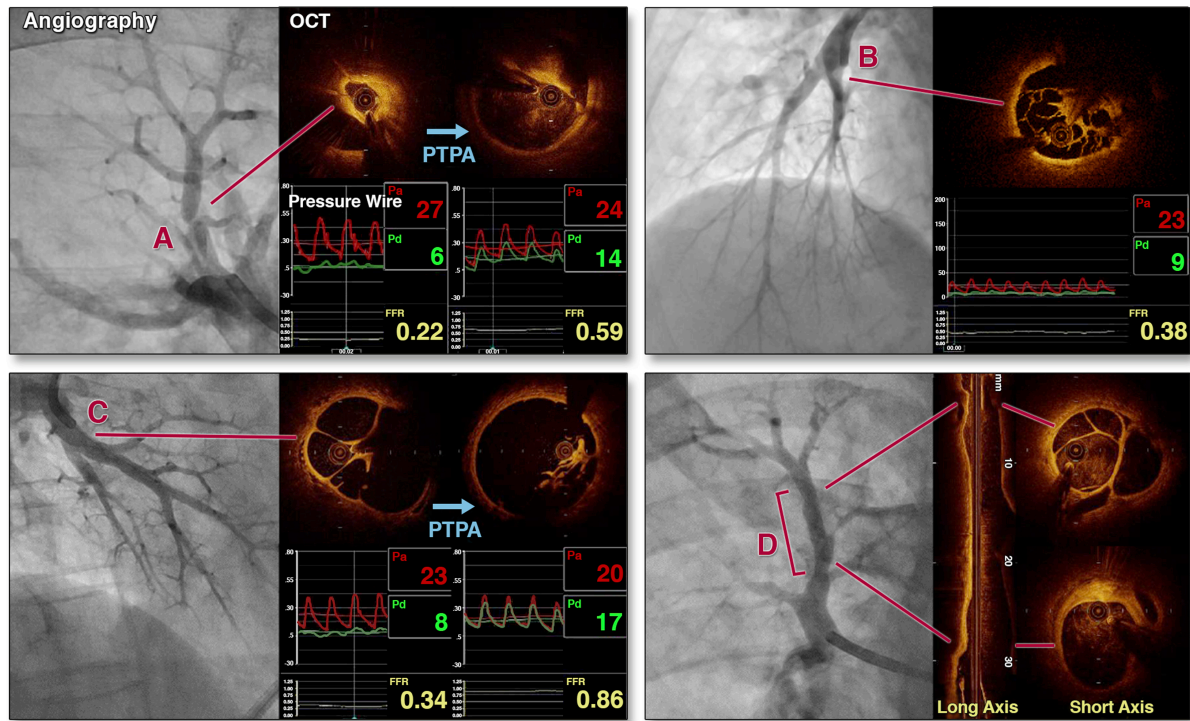


Figure 2.10 Optical coherence tomography (OCT) imaging of lesions in CTEPH. Fractional flow reserve (FFR) measures the pressure drop across the lesions. (A) OCT imaging of a vascular segment before and after percutaneous pulmonary angioplasty (PTPA, synonymous with BPA). FFR is improved, but does not reach a normotensive value near 1. (B) Web like lesion that leads to an FFR of 0.38. Note the non-symmetric, banded appearance of the lesion. (C) OCT imaging and FFR of a lesion after PTPA, with drastically improved FFR values. (D) Web-like lesion that extended throughout a vessel segment. Reproduced with permission from [108].

Large pulmonary artery occlusions induce resistance to flow, increasing mPAP and RV afterload. Current hypotheses suggest that lesion-induced flow redistribution leads to (a) decreased vascular stretch and shear stress distal to lesions and (b) elevated flow and shear stress in unobstructed pathways. These hemodynamic changes induce arteriolar muscularization and luminal narrowing, causing secondary pulmonary arteriopathy [133]. Muscularization and narrowing of small vessels are associated with an increased PVR. Narrowing of the small pulmonary arteries and arterioles increases mPAP, elevating the stress on the MPA. In severe cases of CTEPH, large, proximal arteries near the heart will dilate in response to chronic pressure overload [50].

Swine experiments can replicate the phenotypes of CTEPH using polyethylene microspheres. These microspheres are inserted into the pulmonary arteries via a catheter and occlude the distal

vasculature. Though emboli are not constrained to a specific lung region, the experiment does induce mechanical obstructions in the distal vasculature common in CTEPH. Results from this animal model are consistent with knowledge of the disease, namely that small pulmonary vessels narrow in CTEPH and cause endothelial dysfunction (e.g., imbalances in ET-1/NO) [224].

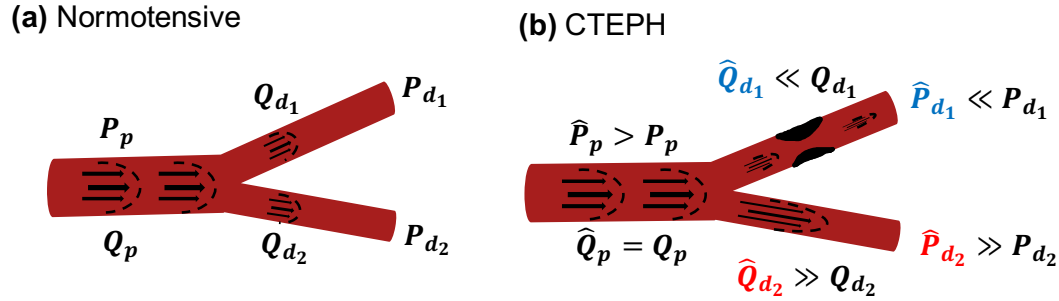


Figure 2.11 Flow and pressure changes in CTEPH. (a) Flow is distributed from a parent vessel to its two daughter vessels based on relative size of the two vessels. Pressure is relatively constant across the junction. (b) The addition of a lesion in CTEPH (in branch d_1) increases the resistance to flow, elevating the parent pressure. Pressure downstream from the lesion drops drastically due to the mechanical obstruction of the lesion. In contrast, the unobstructed vessel (branch d_2) receives a higher flow rate, increasing the pressure in this branch. \hat{P} and \hat{Q} represent the pressure and flow in CTEPH.

2.4.5 Group V: pulmonary hypertension due to unknown causes

PH due to unclear or multifactorial mechanisms are lumped into group 5. Diseases include sickle cell disease, malaria, and cardiopulmonary bypass procedures [177]. Causes of group 5 disease are divided into four disorder groups: hematologic, systemic, metabolic, or other [254]. Sickle cell disease has the unique feature that it causes similar remodeling to PAH, but has distinct differences in the appearance of narrowing lesions observed in histological studies. It is hypothesized that the driving mechanism in group 5 is increased cardiac output due to anemia, fistulas, or arteriovenous shunts, causing endothelial dysfunction and/or left-sided heart impairment [254].

2.5 Disease diagnostics

PH diagnosis requires two main types of data: *morphometric data* and *hemodynamic data*. *Morphometric data* assesses the structural integrity of the pulmonary circulation. *Hemodynamic data* quantifies in-vivo blood pressure and blood flow. Morphometric data can only be obtained from noninvasive imaging. Hemodynamic data can be obtained from either invasive or non-invasive measurements, and clinical measures are derived from these. Invasive measurements are more accurate, but have run a higher risk of injury, whereas the noninvasive are easier and more cost efficient but come with a higher measurement uncertainty. A summary of the morphometric and

hemodynamic data available is provided in Table 2.2.

2.5.1 Morphometry

Medical imaging is the most reliable technology for assessing the structure of the heart, lung, and vasculature. The main imaging modalities include *echocardiography*, *computed tomography*, *magnetic resonance*, and *ventilation-perfusion* imaging.

Echocardiography utilizes sound waves and their reflections off of the heart to provide time-dependent heart dynamics. This is the least invasive form of imaging and is usually the first step in screening those showing typical symptoms of dyspnea or difficulty exercising for PH. Outputs from echocardiography include atrial and ventricular volume, septal deformation, valve dynamics, and systolic and diastolic function [177]. Though echocardiography is the least expensive modality, it has the largest uncertainty.

Computed tomography (CT) imaging provides a three-dimensional (3D) reconstruction of the chest, with x-y plane images measured at incremental sub-millimeter thickness apart. CT imaging typically injects a contrast medium into a vein, flowing to the right atrium and pulmonary circulation. [177]. The quality of the CT image is correlated with the timing of injection; if the CT is not time-gated with an electrocardiogram (ECG), contrast may not be ejected precisely when imaging is being done. The output from CT imaging can be used to assess the size of the MPA, an independent biomarker of mortality, as well as any downstream thromboembolic material common in CTEPH (see Figure 2.12). CT imaging can provide information about the entire pulmonary tree, including vessels as small as 1 mm² in area [50]. For small animals, micro-CT imaging can be used, providing an image resolution of 30-40 μ m [245]. CT imaging is the most prominent imaging modality for assessing the state of the pulmonary vasculature.

Magnetic resonance imaging (MRI) characterizes the structure of both the heart and vasculature. MRI can generate 3D reconstructions of the heart chambers, quantify time-dependent heart contractility, and calculate area changes and flow velocity in the MPA. MRI myocardial tagging can quantify the strain in each heart chamber, crucial for understanding the progression of PH to RV dysfunction [177]. Magnetic resonance angiography (MRA) is another form of MR imaging that can be used to better identify the location of downstream lesions, reducing the uncertainty in lesion location. MRA can also capture the pulmonary arterial and venous vascular trees.

Ventilation-perfusion (V/Q) scans are separated into two separate tests: (1) the inhalation of a radio-nucleotide gas, providing insight into alveolar ventilation and any underlying bronchiole disease; and (2) the injection of radioactive albumin into a vein, illuminating perfused regions of the pulmonary capillaries. In the case of CTEPH, multiple thromboemboli lead to a redirection in blood flow. Underperfusion presents itself in V/Q scans and provides insight into regions of the lung suspected of emboli, as shown in Figure 2.13. V/Q scans have the highest sensitivity in detecting CTEPH, and are regularly used to determine if RHC is appropriate.

Table 2.2 Murine and human data collected over the course of this dissertation. ¹Provided by Dr. Naomi Chesler, previously at the University of Wisconsin, Madison and currently at University of California, Irvine. ²Provided from Dr. Sudar Rajagopal at Duke University Hospital's Center for Pulmonary Vascular Disease. ³Provided by Dr. Martin Johnson from Golden Jubilee Hospital's Scottish Pulmonary Vascular Unit.

Data	Description	Utilized in this dissertation
Morphometric imaging data		
Mouse		
Normotensive ($n = 3$)	High resolution micro-CT images of pulmonary arterial tree from excised lungs ¹	Yes
Hypertensive (HPH, $n = 3$)	High resolution micro-CT images of pulmonary arterial tree from excised lungs ¹	Yes
Human		
Normotensive ($n = 1$)	Normotensive, female chest CT image obtained from OSMSC [261]	Yes
Hypertensive (CTEPH, $n = 7$)	Chest CT images from Duke University Hospital ²	No
Hypertensive (CTEPH, $n = 7$)	V/Q scans from Duke University Hospital ²	No
Pressure data		
Mouse		
Normotensive ($n = 7$)	Dynamic MPA pressure data obtained using a pressure-tip catheter ¹	Yes
Hypertensive (HPH, $n = 5$)	Dynamic MPA pressure data obtained using a pressure-tip catheter ¹	Yes
Human		
Hypertensive (CTEPH, $n = 7$)	RHC reports from Duke University Hospital ²	No
Hypertensive (CTEPH, $n = 1$, PAH $n = 2$)	RHC reports from Golden Jubilee Hospital ³	No
Flow data		
Mouse		
Normotensive ($n = 7$)	Dynamic MPA flow obtained from ultrasound ¹	Yes
Hypertensive (HPH, $n = 5$)	Dynamic MPA flow obtained from ultrasound ¹	Yes
Human		
Hypertensive (CTEPH, $n = 7$)	Static CO measured by thermodilution from Duke University Hospital ²	No
Hypertensive (CTEPH, $n = 1$, PAH $n = 2$)	Dynamic MPA flow MRI flow from Golden Jubilee Hospital ³	No

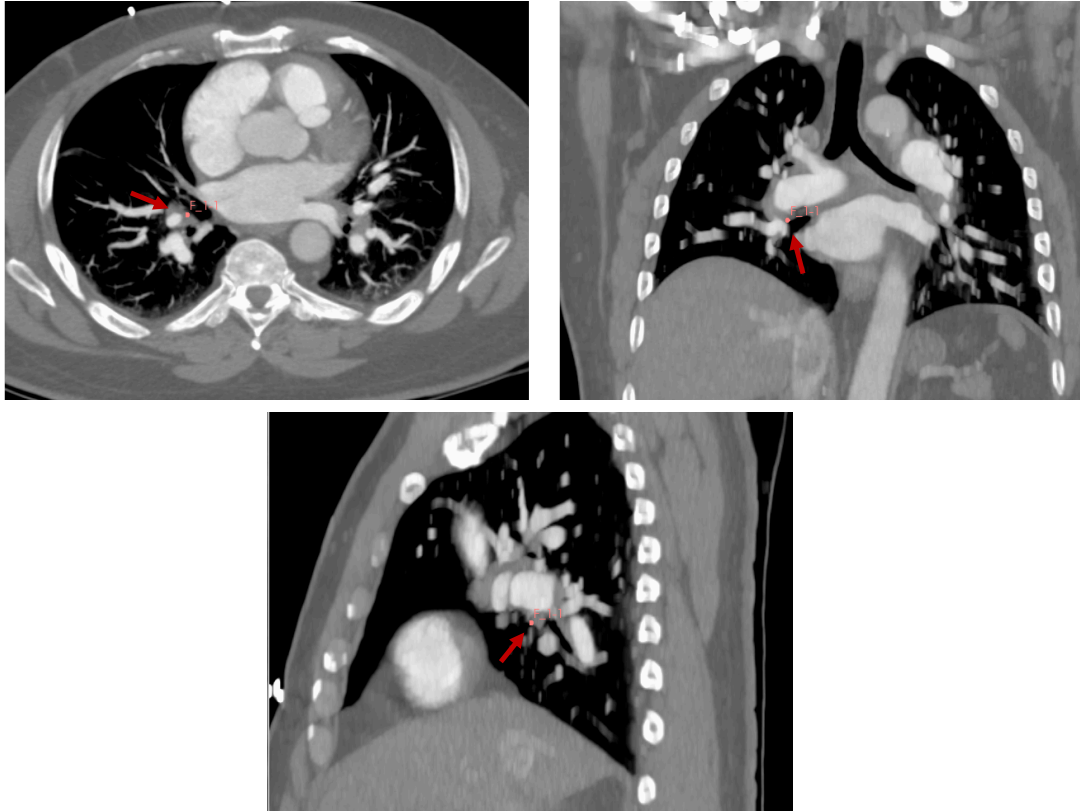


Figure 2.12 Multiplane view of a CT image from a patient with CTEPH. The red arrow indicates a region of the pulmonary arteries obstructed by a thromboembolism. Data provided by Duke University.

Mouse morphometric data. In this dissertation, retrospective data from normotensive and hypoxia-induced PH (HPH, group III) mice, made available by Dr. Naomi Chesler while at the University of Wisconsin, Madison [232], are used. All mice were 10- to 12-week old male C57BL6/J mice (Jackson Laboratory, Bar Harbor, ME). The HPH mice were placed in a hypobaric chamber and exposed to hypoxia by reducing the partial pressure of oxygen by half. These mice were exposed to hypoxic conditions for a total of 21 days. Normotensive mice were placed in a normoxia environment for the same duration of time. Morphometric data is provided for both normotensive and HPH mice via high resolution micro-CT scans, with a resolution of 30-40 μm .

Before imaging the mice, the MPA and trachea are cannulated [245]. The MPA cannula outer and inner diameter are 1.27 and 0.86 mm, respectively, which are visible in the images and used to scale the arterial network dimensions. The heart is subsequently dissected away and the lungs are ventilated. The cannulas are then clamped at their end-inspiratory volume, and a solution of perfluorooctyle bromide contrast agent is injected into the lungs. The lungs are then subjected to cyclic loading from 0 to 25 mmHg. Then, arterial pressure is fixed to one of four pressures (6.3, 7.4, 13.0, and 17.2 mmHg). While pressure is held constant, the lungs are rotated at 1° increments while under an microfocal X-ray CT system. Each planar project image is a result of averaging seven frames, reducing noise and maximizing contrast. An example image can be found in Figure 2.14. For

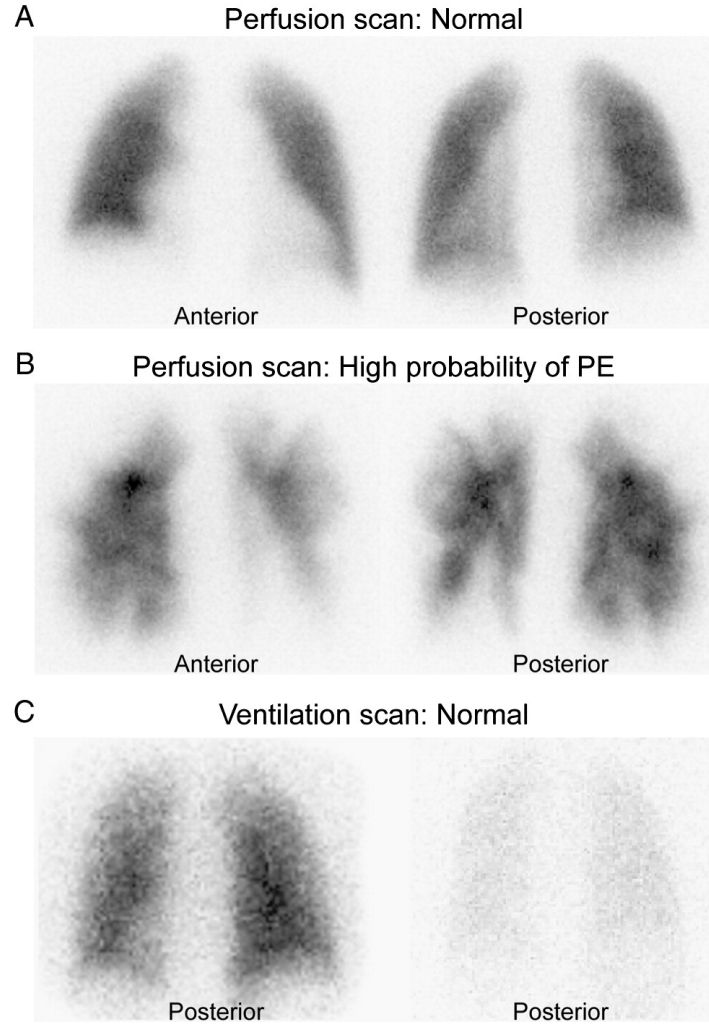


Figure 2.13 Ventilation-perfusion scan. (A) Perfusion scan from a typical, healthy individual. (B) Perfusion scan from an individual with a high probability of pulmonary embolism (PE). The patchy regions suggest flow heterogeneity, and provide insight into where lesions may be located. (C) A ventilation scan from a typical, healthy individual. Reproduced from [8] with permission.

the mouse micro-CT data, image intensities run from 0 to 255, corresponding to a typical grey scale.

Human morphometric data. For the study in Chapter 9, a normotensive CT image was obtained from SimVascular and the Open Source Medical Software Corporation's (OSMSC) database [261]. The image comes from a 67 year old female with no known health complications. The CT image consists of a $512 \times 512 \times 198$ stack of planar images, with a (0.5859, 0.5859, 1.25) mm voxel spacing. The image intensities in the CT scan are in dimensionless Hounsfield units (HU), with values between -1000 (air), 2000 (dense tissue like bone), and 3000 (for nonphysiological objects, such as metal).

Additional human data includes CT images and V/Q scans from seven patients with CTEPH, obtained from Dr. Sudar Rajagopal at Duke University Hospital.

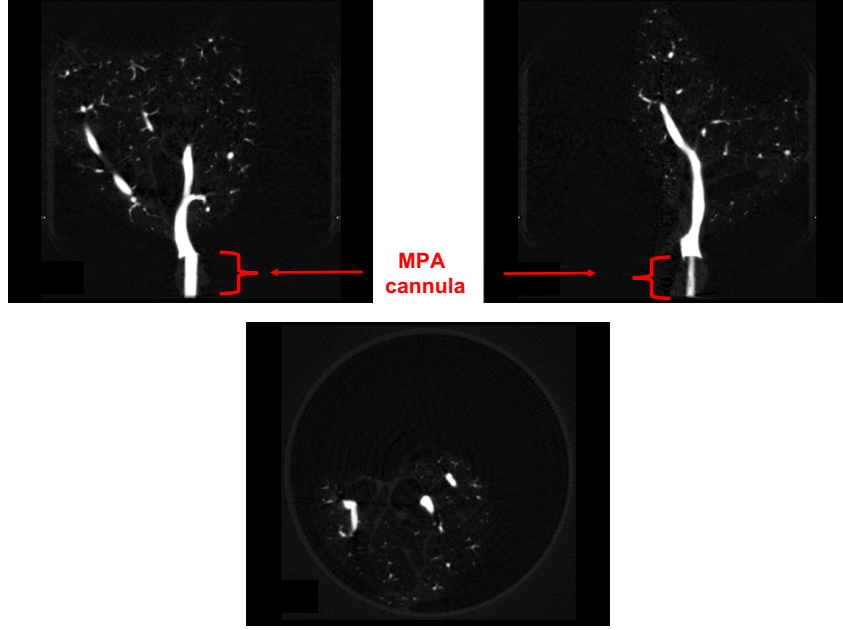


Figure 2.14 Micro-CT image from a perfused mouse lung. Note that the cannula provides an obvious, rigid shape at the MPA (shown in red) and is used to calibrate the dimensions of the vasculature.

2.5.2 Blood pressure

Echocardiography can estimate the pressure in each heart chamber. To do this, echocardiography records tricuspid regurgitant jet velocity (v_{TRV}), the velocity of blood entering the RV, using continuous-wave Doppler. The resulting maximum signal velocity is calculated with a simplified Bernoulli equation:

$$p_{RV,sys} = 4 \cdot v_{TRV}^2 + p_{RA}. \quad (2.4)$$

The above equation depends on estimated right atrial pressure, p_{RA} , constructed from dimensions of the inferior vena cava [177]. Estimating p_{RA} in this way introduces large uncertainty, however, this non-invasive measurement is typically the first step in screening for RHC and PH.

Right heart catheterization (RHC) is required to definitively diagnose PH. The first RHC was performed in 1929 by Werner Forssmann in Germany [177], who advanced a thin catheter from his own cubital vein to his right atrium, and provided him (and two others) the Nobel Prize in Physiology or Medicine in 1956. Since then, several advancements in RHC have led to the development of the standard Swan-Ganz catheter used to diagnose PH [177].

The procedure is done under local anesthesia, and requires the insertion of a catheter into the right atrium and RV (typically through the right jugular vein) while patients are supine. Once the catheter is advanced past the superior vena cava, dynamic and static pressure measurements are recorded in the right atrium, RV, MPA, and, in some instances, other lobar arteries, as shown in Figure 2.15. In addition to the large artery pressure measurements, catheters are equipped with a balloon that can be inflated and lodged into a lobar or segmental artery. Measured pressure downstream

from the balloon, PAWP, represents the pressure attributed to the pulmonary capillaries and veins, and is often used as a surrogate for left atrial pressure [177]. One important indicator of PH severity is PVR, which represents the entire resistance of the pulmonary circuit. This is immeasurable, but is approximated as $(mPAP-PAWP)/CO$ (CO measurements discussed below).

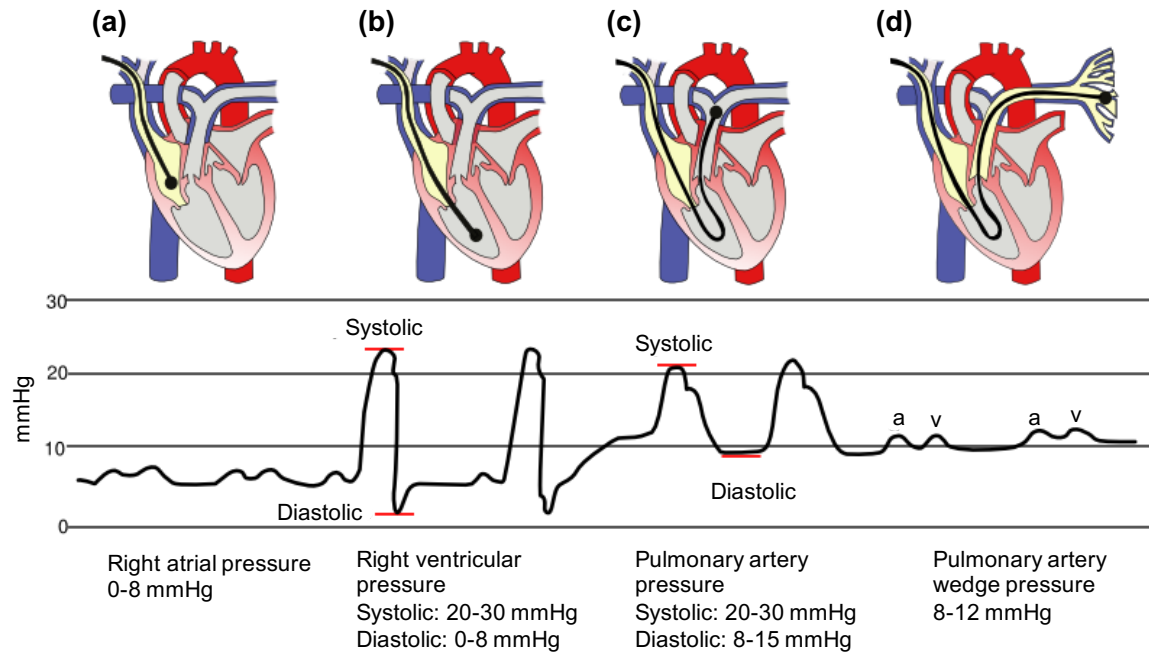


Figure 2.15 Progression of catheter placement during RHC and measured blood pressure. (a) Catheter is inserted through the superior vena cava and enters the right atrium (RA). (b) The catheter is advanced through the tricuspid valve into the RV. (c) The catheter is advanced through the pulmonary valve to record MPA pressure. (d) The balloon tip of the catheter is inserted into a smaller artery and inflated, recording the pulmonary artery wedge pressure. Reproduced and modified with permission from https://www.pcupedia.org/images/6/64/RightHeart_Waveforms_Fig1.svg.

2.5.3 Blood flow

Echocardiography can estimate RV ejection velocity and MPA area, and be converted to a flow estimate. Stroke volume of the heart can also be assessed using echocardiography, and Doppler measurements can construct estimates of flow velocity in the MPA.

Magnetic resonance imaging (MRI) can measure detailed pulmonary artery flow waveforms. This technique is rarely used in the US for PH assessment, but several clinics use velocity-encoded cine MR images to construct proximal pulmonary artery flow profiles. A benefit of these flow waveforms is their use in characterizing pulmonary arterio-ventricular coupling [177]. In addition, flow waveforms, typically computed as the product of area and velocity measurements, provide information about wave reflections [229], significant in vascular remodeling due to PH.

Thermodilution) requires the injection of cold saline, via a catheter, into the right atrium, and estimates CO. The change in fluid temperature within the MPA is measured by heat sensors in the catheter. The change in temperature between the two sites over time provides an estimate of the CO, typically averaged over three successive saline injections. Thermodilution measurement is subject to uncertainty, as bolus temperature, regularity of injection velocity, and volume of injection can vary the measured output [151].

Fick's method). Another method for estimating CO is from Fick's equation:

$$CO = \frac{V_{O_2}}{C_{O_2}^a - C_{O_2}^v} \quad (2.5)$$

where V_{O_2} is the oxygen consumption of the lungs and $C_{O_2}^a$ and $C_{O_2}^v$ are the oxygen concentrations in the pulmonary arteries and veins, respectively. Fick's equation can be applied either directly or indirectly. The *direct Fick method* measures V_{O_2} using a spirometer, and calculates the concentration difference using blood samples. Its widely acknowledged that direct Fick provides a reasonable estimate of CO [177]. *Indirect Fick* uses textbook formulas to relate body mass and oxygen consumption, and are highly subject to uncertainty [159].

Mouse hemodynamic data. This dissertation utilizes pulsatile pressure-flow data from 7 normotensive and 5 HPH mice [232], made available by Dr. Naomi Chesler while at the University of Wisconsin, Madison. Similar to the imaging data, HPH was induced using a hypobaric chamber with a reduced partial pressure of oxygen over 21 days. To obtain in-vivo hemodynamic measurements, mice were anesthetized with an urethane solution injected intraperitoneally. Mice were then intubated and placed on a ventilator, and the rest of the body was dissected to reveal the RV and lungs. A pressure-tip catheter was inserted into the apex of the RV for RHC and then advanced to the MPA just proximal to LPA and RPA. Pressure tracings were recorded at 5 kHz on a hemodynamic workstation (Cardiovascular Engineering, Noarwood, MA). The pressure waveforms were signal-averaged after aligning the waveforms' ECG signals.

Pulsatile flow was measured by ultrasound during RHC. A 30 MHz probe was used to record velocity just distal to the pulmonary valve, and the probe was angled such that the velocity measured was maximized. The flow velocity, a digitized broadband Doppler audio signal, was averaged using a spectral analysis. In addition, the MPA inner diameter was measured from leading edge to leading edge in B-mode of the Doppler imaging. The combination of flow velocity and MPA cross-sectional area was used to calculate of flow. Both pressure and flow waveforms are shown in Figure 2.16.

Human hemodynamic data. This dissertation uses a publicly available MPA flow waveform from Simvascular and the OSMSC [261]. The flow waveform was digitized using GraphClick¹. The flow waveform reaches a peak flow of approximately 300 ml/s, and has a CO of approximately 5 L/min.

Hemodynamic data available for future studies include three RHC reports from PH patients

¹<http://www.arizona-software.ch/graphclick/>

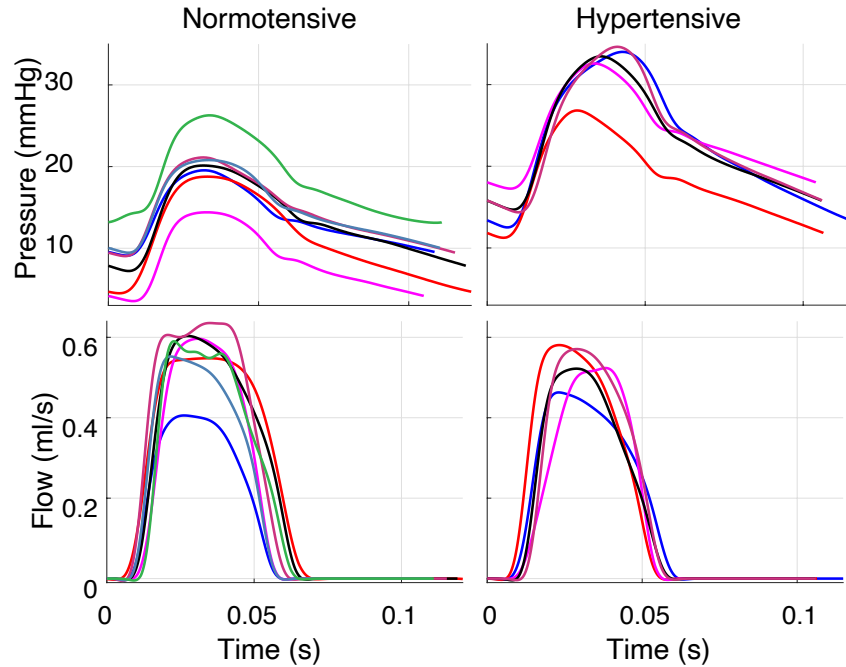


Figure 2.16 Pressure (top) and flow (bottom) data from both normotensive and hypertensive (HPH) mice. There are 7 control animals and 5 HPH.

(2 PAH and 1 CTEPH) at the Golden Jubilee Hospital System in Scotland, provided by Dr. Martin Johnson, as well as MRI flow waveforms. An additional 7 RHC reports from CTEPH patients are available from Dr. Sudar Rajagopal at Duke University Hospital. These include measures of CO by thermodilution, but do not include MRI flow waveforms.

2.6 Pulmonary hypertension treatments

PH treatment reduces mPAP and improves cardiac function, making the disease more manageable but not curing PH. For CTEPH patients, surgical intervention is also used and can cure PH. All

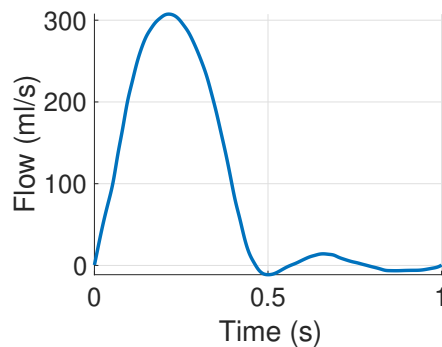


Figure 2.17 A digitized, human flow waveform in the MPA from Simvascular and the OSMSC [261].

five groups can be treated using vasodilators, which decrease PVR. For CTEPH, either pulmonary endarterectomy (PEA) or balloon pulmonary angioplasty (BPA) are used to remove or disrupt pulmonary emboli.

2.6.1 Vasodilators

Vasodilators to induce vasorelaxation in the small arteries and arterioles. Pharmaceutical drugs can do this through enhancement or inhibition of several biochemical pathways. The main target of pharmaceutical interventions is the pulmonary endothelium, which provides a mechanotransduction pathway between blood flowing in the lumen and the vascular wall. Increased wall shear stress promotes the release of ET-1, a potent vasoconstriction, which promotes SMC proliferation and collagen turnover. ET-1 acts through two main pathways on the endothelium, namely ET_A receptors on SMCs located in the media and ET_B receptors on both SMCs and the endothelium itself. When ET_A receptors are bound by ET-1, they promote malicious pulmonary vascular remodeling. In the healthy pulmonary vasculature, ET_B receptors promote the release of endothelial nitric oxide synthase (eNOS), which is converted to NO to induce relaxation. NO directly promotes cyclic guanosine monophosphate (cGMP) in SMCs, inhibiting proliferation and wall thickening. ET_B receptors also promote clearance of ET-1, reducing the amount circulating in the blood. It is hypothesized that endothelial dysfunction and an inability to rebalance the ET-1-to-NO ratio promotes the rapid remodeling seen in PAH (see Figure 2.18), making it the ideal target for drug therapy [75, 177].

Prostacyclin is another target for vasodilator drugs, which inhibits platelet aggregation and dilates blood vessels [28]. Prostanoids are potent vasodilators that promote the release of prostacyclin. For patients with severe PAH, intravenous injection of the prostanoid epoprostenol is recommended [177]. Iloprost is an inhaled prostanoid that induces pulmonary and systemic vasodilation. A recent investigation by Wang et al. [251] showed that short term use of iloprost is beneficial for those with group III PH due to COPD.

Phosphodiesterase-5 (PDE5) inhibitors can counteract an elevated ET-1/NO seen in PH. PDE5 inhibitors, including sildenafil and tadalafil, block PDE5, which degrades and inactivates cGMP. By reducing the circulating PDE5, the endothelium produces greater amounts of NO to induce vasodilation. While tadalafil is FDA approved, it can have negative systemic side-effects if mixed with other hypertensive drugs, such as systemic vasodilators [94].

Endothelin receptor agonists (ERAs) are another intervention successful in reducing vascular remodeling and mPAP. These drugs include Bosentan and macitentan, which block the binding sites for ET-1. Bosentan, which is the most commonly used PAH medication, blocks both ET_A and ET_B receptors. They also inhibit the positive vasodilatory effects of ET_B receptors [51]. These drugs also have potential side effects, including peripheral edema and anemia.

The last class of vasodilators are approved for both PAH and CTEPH: soluble guanylate cyclase stimulators [82]. The only FDA approved class of this type for both PH subgroups is riociguat, which stimulates soluble guanylate cyclase (a membrane protein that is a receptor for NO)[28]. Riociguat elevates the level of cGMP, again leading to vasorelaxation in SMCs and inhibiting proliferation.

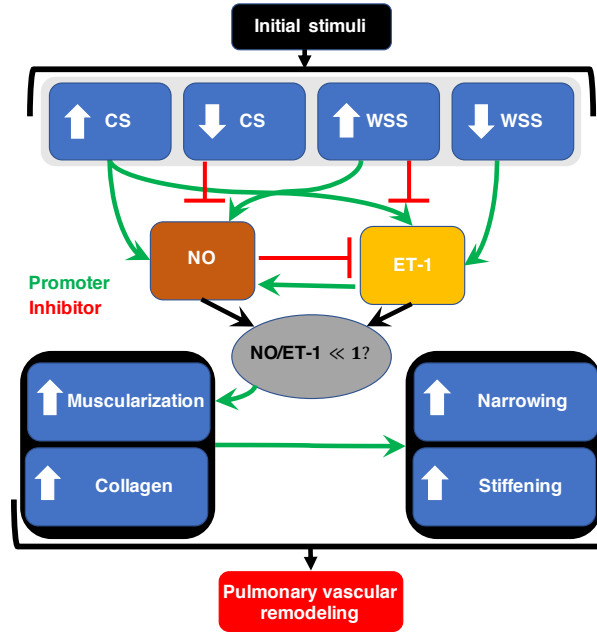


Figure 2.18 Hypothesized promoter-inhibitor relationship for NO and ET-1 in the progression of pulmonary vascular remodeling. CS: cyclic stretch; WSS: wall shear stress; NO: nitric oxide; ET-1: endothelin-1.

2.6.2 Pulmonary endarterectomy (PEA)

Since CTEPH is onset by the presence of thromboembolic material, management of the disease typically requires surgical intervention. The gold-standard CTEPH treatment is pulmonary endarterectomy (PEA) or thromboendarterectomy (PTE), an invasive procedure with a low morbidity when performed at an expert center [56]. Patients deemed “operable” for PTE are hemodynamically stable and have lesions proximal enough for intervention. The procedure involves cardiopulmonary bypass, during which the patient is put into circulatory arrest via deep hypothermia for a maximum of 20 minutes and attached to a heart-lung machine. The cardiovascular surgeon then inserts several catheters into the patient, and makes an incision into the RPA. Any loose thrombus nearby are removed, and, if necessary, the procedure is repeated in the LPA and its proximal vessels. Several possible complications include reperfusion injury (i.e., high flow areas that undergo too great of stress) after surgery and arterial rupture. Overall mortality rate is low for the procedure at approximately 2-3% [177], and the 5-year survival rate estimates after PTE are approximately 75% [234].

2.6.3 Balloon pulmonary angioplasty (BPA)

Though PTE is highly effective, between 12% to 60% of patients are inoperable due to distal lesions [115], located in the segmental and subsegmental arteries. Lesions may also be inaccessible due to other comorbidities, such as coronary artery disease or left heart failure [55]. The optimal alternative treatment for these patients is balloon pulmonary angioplasty (BPA) therapy, a minimally invasive

procedure that uses a balloon catheter to mechanically disrupt the thrombi. BPA is distinct from PEA in that occlusive lesions are not removed but altered to decrease lumen obstruction. Complete BPA therapy requires multiple interventions in various segments over several sessions [130]. BPA is a relatively novel approach, with its first two documented uses in CTEPH done in 1988 and 2001 [177].

The procedure requires inserting a guide catheter through the jugular or right femoral vein. Two operators are required for BPA: one is in charge of traversing through the arteries with a guidewire while the other manipulates the guide catheter. Pulmonary angiography assesses the hemodynamic state proximal to and distal to the catheter location. The wire and catheter are transversed past any lesion, and a balloon on the end of the catheter is inflated. This disrupts the thromboembolic material, increasing the unobstructed luminal area [130, 177]. Studies suggest a 90% 5-year survival rate for patients undergoing BPA [215, 234].

Recent studies have utilized the FFR to assess the severity of the lesions [115]. FFR values vary depending on lesion severity and location, as shown in Figure 2.10. In general, 2-4 segments of the lung are treated at each BPA session. Targets and area for treatment are decided by the surgeon's experience, and the lesion type and location within the vasculature. One approach is to prioritize the lesions in the lower lobe since these typically perfuse the largest parts of the lung. However, it is unclear using current diagnosis techniques which lesions should be treated for maximum hemodynamic improvement.

CHAPTER

3

IMAGE ANALYSIS

This chapter describes the imaging analysis used to construct pulmonary vascular networks. Prior studies have integrated imaging data with cardiovascular modeling, yet the methods described here are the first to generate large pulmonary arterial networks for 1D hemodynamic simulations. These methods construct a novel pipeline that converts patient imaging data to individual vascular segments. The final aspect of this pipeline is constructing a labeled, geometric tree and connectivity matrix that are readily passed to the 1D hemodynamics model, enabling patient specific simulations from imaging data.

Section 3.1 provides an overview of medical imaging data and prior image analysis studies. Section 3.2 provides an overview of image segmentation and Section 3.3 provides details on how the segmentation is reduced to a network of centerlines. Lastly, methods that convert the centerline network to a connected, labeled graph for the hemodynamics model are described in Section 3.4.

3.1 Medical imaging analysis

Imaging and hemodynamic data are required to diagnose PH, but there are no tools for integrating both data modalities. The structure and function of the pulmonary circulation are highly coupled, hence a tool integrating both data modalities will provide information on their coupling in normotensive and hypertensive scenarios. This approach has been utilized understanding systemic artery disease [13, 129, 207], but not for PH.

We present an image analysis pipeline involving the three main steps: (1) *image segmentation*, (2) *centerline extraction*, and (3) *network labeling*. Figure 3.1 depicts the necessary steps for converting a set of imaging data to a labeled, directed network.

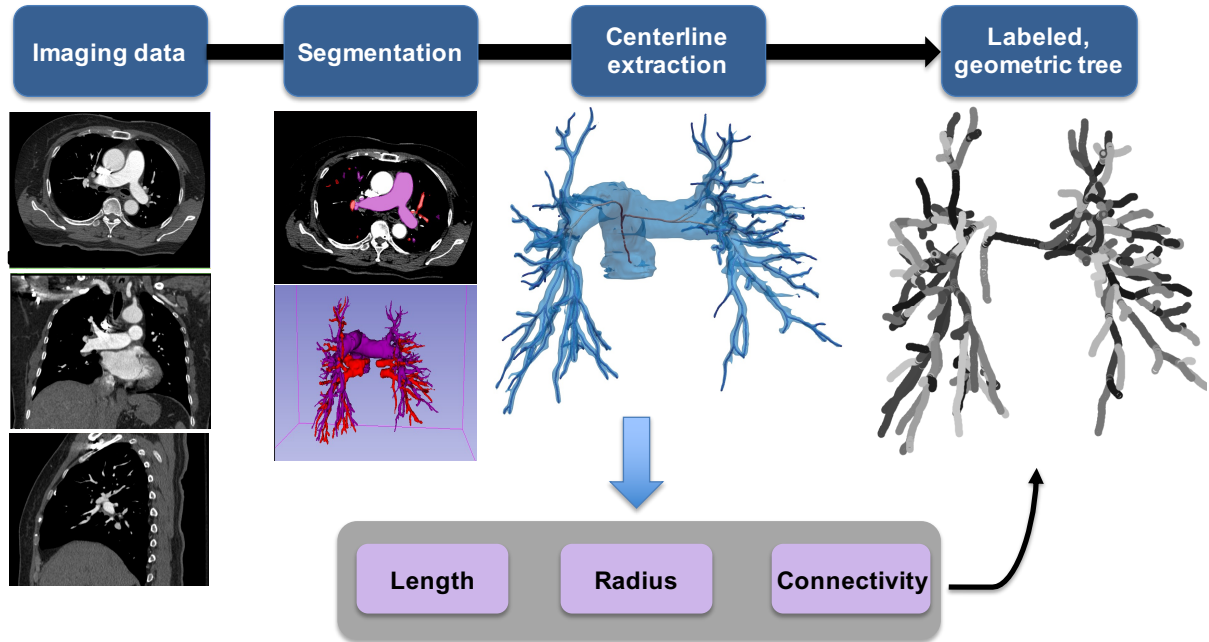


Figure 3.1 Workflow for generating connected, labeled vascular networks from imaging data. First, the imaging data must be analyzed and manually labeled as arteries or veins. Then, manual and semi-automated segmentation methods are used to reconstruct the 3D geometry. After segmenting the arteries (and veins), the resulting 3D geometry is passed into a skeletonization or centerline software (e.g., VMTK). Lastly, algorithms presented in Section 3.4 separate the individual vessel components, determine their radius and length, and define the connectivity matrix for the entire vascular network. Note that the greyscale color coding in the constructed network represent different vessels in the network.

3.2 Image segmentation

Image segmentation is the process of dividing an image into unique regions of interest. Image segmentation can be done using *manual*, *semi-automatic*, or *fully automatic* tools.

Manual segmentation includes painting regions of interest and is accurate to the level of the operator (e.g., a radiologist). These methods take substantial time especially if the goal is to obtain the pulmonary vasculature. However, manual methods are the gold-standard for validating semi- and fully automated methods [38, 203]. The review of pulmonary segmentation methods by Van Rikxoort [242] notes that all state of the art segmentation methods first require a validation dataset generated from manual segmentation.

Semi-automated segmentation requires some user input in initializing and correcting of the segmentation, but use algorithms to segment a majority of the tissue. These methods speed up segmentation by using seed- and region-growing algorithms [10, 273]. Random Forest classification is another semi-automated method readily available in the open source software ITK-SNAP [273]. Deformable, active-contour (or “snake”) algorithm are also available in ITK-SNAP [273]. These algorithms begin with a set of user painted initial seeds, and evolve a contour over the image domain by updating

the contour at each time step. The time evolution of the contour depends on both the gradient of the image intensity and the voxel intensity probability map [242, 273]. The cut-off time for the evolution problem is determined by the user, and induces operator uncertainty (investigated here). Semi-automated methods also include local and global thresholding (presented in detail later).

Fully-automated segmentation perform segmentation without user interaction. Some of the first work on automated vascular segmentation include the “vesselness” filter introduced by Frangi [69]. This method convolves the hessian of a Gaussian kernel with an image using various standard deviations, and enhances tubular structures such as vascular segments. These filters can be used in combination with shape analysis to automatically segment the lung lobes and nearby tissue [242]. Convolutional neural networks are the state-of-the-art methods for image segmentation. U-net (2D images) [203] and 3D U-Net [38] consist of multiple up- and down-convolutions that integrate whole image information with finer details obtained from convolved neural network layers.

In this work, we utilize a combination of manual and semi-automatic segmentation methods. For the mouse, the vasculature is excised from the lung, heart, and other tissue before imaging. This enables the use of global-thresholding, defined as

$$I(w) = \begin{cases} 1, & w_{\text{lower}} \leq w \leq w_{\text{upper}} \\ 0, & \text{else} \end{cases} \quad (3.1)$$

where w is the image intensity at a given voxel location. This methodology can be used to restrict intensity limits for other segmentation methods or segment all voxels in the image within these bounds. In contrast to this discrete thresholding framework, continuous methods for thresholding can also be used, as shown in Figure 3.2. ITK-SNAP has its own sigmoidal thresholding function, and maps voxel intensities to a probability map. The sigmoidal functions available, shown in Figure 3.2, are

$$I(w) = \begin{cases} \frac{1}{1 + e^{-\gamma(w - w_{\text{lower}})}}, & \text{lower threshold} \\ \frac{1}{1 - e^{-\gamma(w - w_{\text{upper}})}}, & \text{lower threshold} \\ \frac{1}{1 + e^{-\gamma(w - w_{\text{upper}})}} - \frac{1}{1 + e^{-\gamma(w - w_{\text{lower}})}}, & \text{lower \& upper threshold} \end{cases} \quad (3.2)$$

where w_{lower} and w_{upper} are lower and upper thresholding limits and γ is a smoothness parameter.

The mice images are segmented using the contour evolution algorithms in ITK-SNAP. Three representative segmentations performed using the software ITK-SNAP [273] are shown in Figure 3.3 using the same segmentation method but with different lower thresholding and smoothing parameter values.

For the human image, segmentation is carried out by first manually segmenting the pulmonary

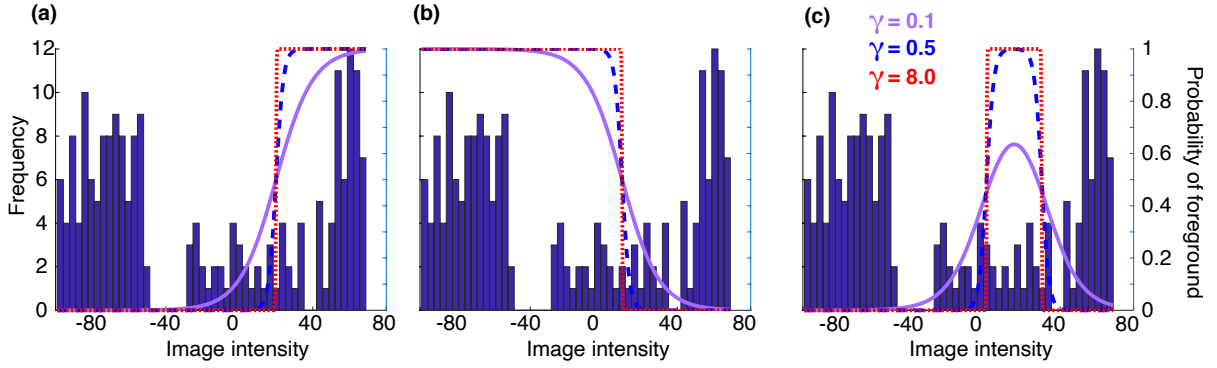


Figure 3.2 Thresholding functions used in ITK-SNAP. A histogram of image intensities (left y label) are plotting along with the thresholding functions (right y label) with a smoothing parameter value of $\gamma = 0.1, 0.5$, and 8.0 . (a) A lower threshold sigmoidal function with $w_{\text{lower}} = 30$. (b) An upper threshold sigmoidal function with $w_{\text{upper}} = 30$. (c) A combined upper and lower threshold function with $w_{\text{lower}} = 0$ and $w_{\text{upper}} = 30$.

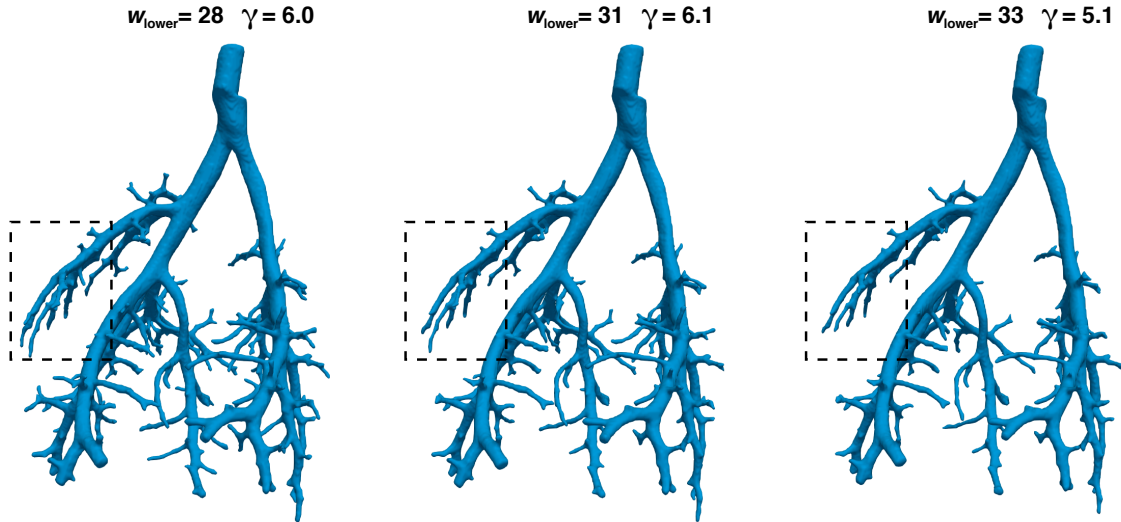


Figure 3.3 Three segmentations of the same mouse image using ITK-SNAP. Each segmentation utilizes the same number of active-contour evolutions, but has different lower threshold limits and smoothness parameters. Notice the the right pulmonary arteries (left on the page) vary in connectivity and length for differernt segmentation parameters.

arteries and veins in 3D Slicer [121]. Though the veins are not used in the computational model here, they run parallel to the large arteries and must be quantified reduce vessel misclassification, as shown in Figure 3.4. After the initial manual segmentation, a region growing operation captures the distal vasculature. Manual editing is used to add or remove any vessels not captured.

3.3 Centerline extraction

The computational domain for the mathematical model requires that 3D segmentations are translated to a labeled, geometric tree. To do this, a centerline network is first extracted. This dissertation

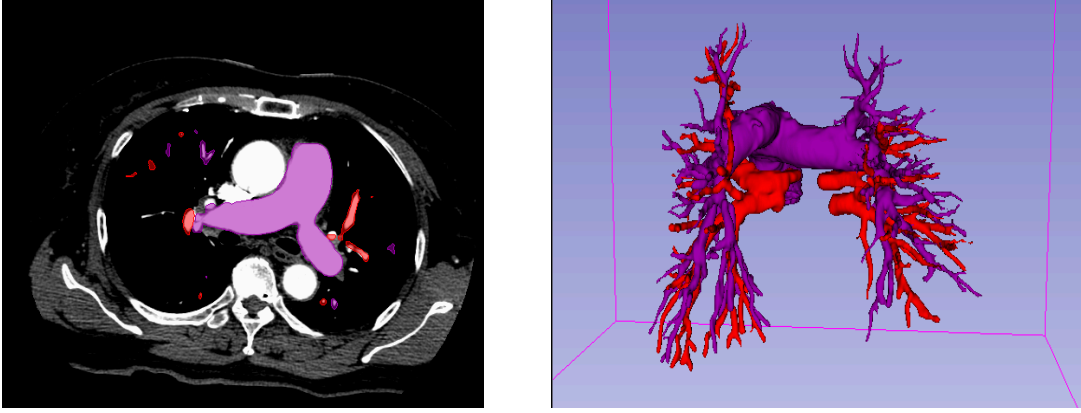


Figure 3.4 Example of a segmented human image. (a) Segmentation of the pulmonary arteries and veins shown in the axial perspective. (b) 3D rendering of segmented pulmonary arteries and veins. Images viewed in 3D Slicer.

uses the Vascular Modeling Toolkit (VMTK) to reduce the 3D geometries to a centerline network [9, 10]. Centerlines are extracted from the segmentation surface meshes using native VMTK scripts and stored in files containing (x, y, z) coordinates. In brief, centerlines are determined as the shortest weighted paths traced between an inlet and outlet point. These paths are constrained based on the Voronoi diagram of the mesh, which is the set of 3D space closest to each individual point in the mesh [10]. One of the main drawbacks of VMTK is that the user is tasked with determining the inlet point (e.g., the MPA) as well as the outlet points (e.g., all the terminal vessels in a network). For the pulmonary circulation, this task becomes manually cumbersome. Other methods, such as those pursued in [35], use automated algorithms for mapping the centerlines of the network, and have their own error-handling methods. An example centerline network constructed from the mouse arterial tree using VMTK is presented in Figure 3.5.

3.4 Labeled, geometric tree

The last stage in the image analysis pipeline is to construct a *labeled, geometric tree*. To do this, two main steps are required; the first is separating the centerlines into separate arcs connected by junction nodes, and the second is labeling those arcs with a radius and length.

Arcs and nodes. The centerlines from VMTK start at each terminal vessel and end at the inlet of the MPA; hence centerline data is duplicated in regions where two vessels merge. To determine the arcs and nodes representing vessels, a connectivity matrix must be generated. No current software exists for separating the data files from VMTK, hence custom, novel algorithms were developed. Unique centerline coordinates are determined by finding intersection points at each bifurcation, labeled as network junctions. All points between two junctions are labeled as vessels, or *arcs*, and saved as separate data structures (see Algorithm 1). The points connected two arcs are labeled as junction points, or *nodes*.

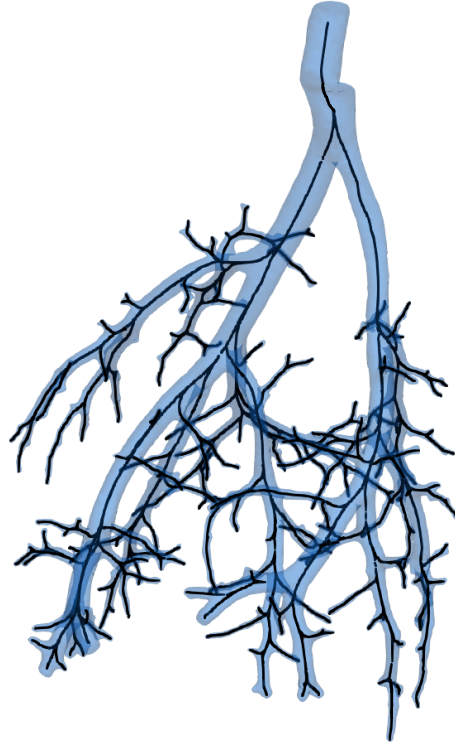


Figure 3.5 Representative segmentation of the mouse vasculature (blue) overlaid with the centerlines produced by VMTK (black). The segmentation was conducted using a deformable snake algorithm in ITK-SNAP.

Unique data points are determined using MATLAB's `unique` function. Every pathway is tracked until it reaches a point that is shared by another full pathway, and labeled as an intersection node. Arcs are determined as sets of points that align between any two nodes. The fact that any n number of nodes in a network are guaranteed to have exactly $(n-1)$ arcs between the nodes themselves limits any double counting of arcs and allows for memory pre-allocation. This methodology is described in Algorithm 2.

Labeling arcs. Both length and radii are determined for each vessel. The length is calculated as the sum of euclidean distances between coordinate points in \mathbb{R}^3 . For the radius, VMTK provides its own estimates using maximally inscribed spheres [9]. In short, a sphere is maximally inscribed if no other neighboring spheres contain it, and is directly related to the Voronoi diagram of the mesh. However, non-smoothness of the segmentation or rapidly branching structures (e.g., pulmonary arteries) induce uncertainty in the radii measurements. Moreover, radii estimates can be affected by the regions immediately before or after a junction, denoted as the "ostium" region. In this work, radii are calculated as the average value over the center 50% of points, avoiding estimates within the ostium regions. A representative example of radii estimates and the calculated mean radius from the human images is shown in Figure 3.6.

Algorithm 1: Find shared and unique points

Define C, r, U, l , and N , where C is the matrix of centerline points (x, y, z) , r is the vector of radii values, l is the vector of length values, U is the matrix of full pathways, and N is the size of the centerline file

Initialize $M = 0, K = 1$.

for $k = 1, 2, \dots, N - 1$ **do**

$d_C = \sqrt{(C(k) - C(k+1))^2}$

$d_R = R(k) + R(k+1)$

if $d_C > d_R$ **then**

 Append $C(K : k)$ to U

$M = M + 1$

$K = k + 1$

Initialize $\gamma = 10^6$, $v = 0$, and V structure of individual vessel arcs

for $k = 1, 2, \dots, M$ **do**

for $j = k + 1, \dots, M$ **do**

if $U(k) \cap U(j) \neq \emptyset$ **then**

$\gamma = \min(\gamma, \text{Size}(U(k) \cap U(j)))$

$V(v) = U(k)(0 : \gamma)$

$v = v + 1$

Algorithm 2: Determine network connectivity

Initialize $g = 0$ vessel generation, n_p to the inlet node, $E \in \mathbb{R}^{N \times 3}$ the vector of coordinates for each terminal outlet node, V the previously determine structure of vessel arcs, $V_{old} = V$ the arcs that have not yet been structured in the network, C the empty connectivity matrix, and $k = 0$ the vessel number used for storage.

Inputs V_{old}, k, C

Begin Recursive:

if $n_p \notin V$ **then**

 Mark vessel k as terminal in C and set $V_{old} = V_{old} \setminus V(k)$

RETURN C

else

 Find daughter nodes $n_d = n_p \cap V$ and set number of daughters found $N_d = |n_d|$

for $i = 1, \dots, N_d$ **do**

CALL RECURSIVE with $k = k + 1$, $g = g + 1$, and $n_p = n_d(i)$

RETURN C

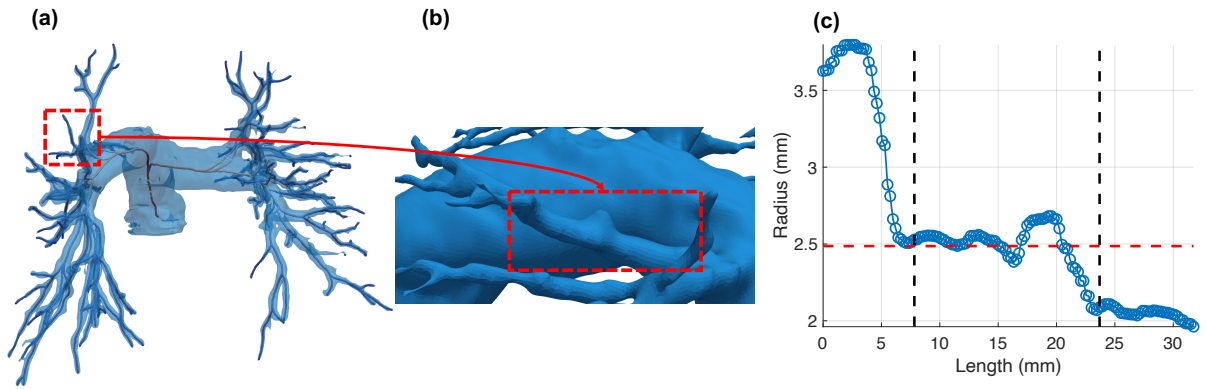


Figure 3.6 (a) Segmentation of human pulmonary arteries along with centerlines generated by VMTK. (b) Zoom in of a vessel in the right upper lobe. (c) Radius values calculated by VMTK (blue circles) along with 25% and 75% cutoffs used to calculate the mean radius (red dashed line) used in the network model.

CHAPTER

4

ONE-DIMENSIONAL FLUID DYNAMICS

This chapter provides an overview of the 1D computational hemodynamics. The core of the derivations are adapted from [166, 189]. Innovations in this thesis include a new energy loss model based on the Darcy-Forchheimer equation, integrating a radius-hematocrit dependent viscosity model in the small vessels, multiscale hemodynamic predictions using the structured tree model, and an algorithm for preserving total resistance in Windkessel boundary conditions for networks of different sizes.

Section 4.1 describes the large vessel fluid dynamics equations solved in each vessel and Section 4.2 describes energy loss lesion models. Section 4.3 describes the small vessel models, and Section 4.4 discusses the boundary conditions for each vessel. Section 4.5 details the numerical scheme for solving the 1D network model. Finally, Section 4.6 describes wave intensity analysis (WIA).

4.1 Large vessel hemodynamics

Fluid dynamics in the large pulmonary arteries are driven by the flow ejected from the RV. The force exerted on the fluid is converted to a pulse-wave and propagated from the large arteries to the capillary beds. Fluid dynamics in each vessel are modeled using the Navier-Stokes equations

$$\frac{\partial \rho}{\partial t} + \nabla \cdot (\rho \mathbf{u}) = 0 \quad (4.1)$$

$$\rho \left(\frac{\partial \mathbf{u}}{\partial t} + \mathbf{u} \cdot \nabla \mathbf{u} \right) = \nabla \cdot \boldsymbol{\sigma} + \rho \mathbf{f} \quad (4.2)$$

where ρ is the fluid density, \mathbf{u} is the fluid velocity vector in Cartesian coordinates, $\boldsymbol{\sigma}$ is the stress-tensor including both normal and shear stresses being exerted on the fluid, and \mathbf{f} are the body forces acting on the fluid (e.g., the force of gravity, $\mathbf{f} = -\rho g z \mathbf{e}_z$, where \mathbf{e}_z is a unit vector in the z direction). Assuming that the fluid is incompressible (i.e., constant density ρ), body forces are negligible (e.g., in supine position), and that blood in the large arteries is Newtonian and viscous, we get

$$\nabla \cdot \mathbf{u} = 0 \quad (4.3)$$

$$\rho \left(\frac{\partial \mathbf{u}}{\partial t} + \mathbf{u} \cdot \nabla \mathbf{u} \right) = -\nabla p + \mu \nabla^2 \mathbf{u}. \quad (4.4)$$

3D simulations of hemodynamics provide intricate flow and shear stress predictions [61, 129]. The study by Spazzapan et al. [222] predicted pulmonary artery shear stress pre- and post-surgery for CTEPH patients using a 3D fluid dynamics model, confirming an increase in shear stress after surgery. Yang et al. [266] coupled a heart model to a 3D fluid dynamics model of the pulmonary artery and predicted low shear stress in PAH patients relative to control. These detailed flow predictions, but computations are too expensive for patient-specific analyses in the clinic. An alternative to detailed 3D models are 1D models, which can predict pulse wave propagation throughout a vascular tree at a significantly lower computational cost. Several studies have validated 1D models against 3D models, concluding that flow and pressure waveform predictions are comparable to the 3D models [25, 268]. Another advantage of 1D models is that their reduced computational cost enables efficient parameter estimation and uncertainty quantification (detailed in Chapter 5), necessary for in-clinic models. For this reason, a 1D fluid dynamics model is considered here.

4.1.1 Governing equations

We assume that blood vessels are straight, cylindrical, and impermeable tubes (depicted in Figure 4.1), encouraging the use of cylindrical coordinates (r, θ, x) with $\mathbf{u} = [u_r, u_\theta, u_x]$. Assuming that the flow is irrotational and axysymmetric with no swirl, the fluid velocity is independent of the circumferential component, i.e., $\mathbf{u} = [u_r(r, x, t), 0, u_x(r, x, t)]$. Nondimensional analyses, derived in Appendix A, show that the radial velocity is negligible relative to the axial velocity, i.e. $u_r \ll u_x$. Thus, pressure only depends on the axial location and time, $p \equiv p(x, t)$. Under these assumptions, the 1D mass conservation and momentum balance equations are

$$\frac{\partial(r u_r)}{\partial r} + \frac{\partial u_x}{\partial x} = 0 \quad (4.5)$$

$$\frac{\partial u_x}{\partial t} + u_r \frac{\partial u_x}{\partial r} + u_x \frac{\partial u_x}{\partial x} = -\frac{1}{\rho} \frac{\partial p}{\partial x} + \nu \left(\frac{1}{r} \frac{\partial}{\partial r} \left(r \frac{\partial u_x}{\partial r} \right) \right) \quad (4.6)$$

where $\nu = \mu/\rho$ is the kinematic viscosity.

To predict volumetric blood flow, we integrate the system over the cross-sectional area. Beginning

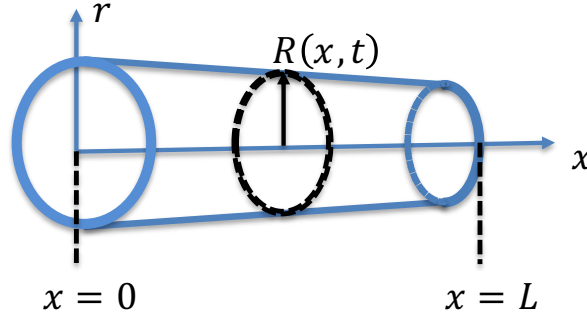


Figure 4.1 Schematic of a cylindrical blood vessel. Notice that the cross sectional area $A(x, t) = \pi R^2(x, t)$ across the vessel length L can change in both space and time.

with (4.5),

$$2\pi \int_0^R \left(\frac{\partial u_x}{\partial x} + \frac{\partial(r u_r)}{\partial r} \right) r dr = 0, \quad (4.7)$$

where $R = R(x, t)$ is the outer radius of the blood vessel at location x and time t . Applying Leibniz rule to the first term gives

$$2\pi \int_0^R \left(\frac{\partial u_x}{\partial x} + \frac{\partial(r u_r)}{\partial r} \right) r dr = 2\pi \frac{\partial}{\partial x} \int_0^R u_x r dr - 2\pi \left[\frac{\partial R}{\partial x} u_x r \right]_{r=R} + 2\pi [r u_r]_{r=R}. \quad (4.8)$$

Enforcing a no-slip condition at the boundary $r = R(x, t)$, where the fluid velocity is equal to the velocity of the wall, i.e. $u_x|_{r=R} = 0$ and $u_r|_{r=R} = \frac{\partial R}{\partial t}$, gives

$$2\pi \frac{\partial}{\partial x} \int_0^R u_x r dr - 2\pi \left[\frac{\partial R}{\partial x} u_x r \right]_{r=R} + 2\pi [r u_r]_{r=R} = 2\pi \frac{\partial}{\partial x} \int_0^R u_x r dr + 2\pi R \frac{\partial R}{\partial t}. \quad (4.9)$$

We define the volumetric flow rate over the cross-section and the time derivative of the area as

$$q(x, t) = 2\pi \int_0^R u_x r dr, \quad 2\pi R \frac{\partial R}{\partial t} = \frac{\partial A}{\partial t} \quad (4.10)$$

Inserting Eq. (4.10) in Eq. (4.9) gives

$$\frac{\partial q}{\partial x} + \frac{\partial A}{\partial t} = 0. \quad (4.11)$$

Similarly, integrating Eq. (4.6) over the cross section gives

$$2\pi \int_0^R \left(\frac{\partial u_x}{\partial t} + u_r \frac{\partial u_x}{\partial r} + u_x \frac{\partial u_x}{\partial x} \right) r dr = 2\pi \int_0^R \left(-\frac{1}{\rho} \frac{\partial p}{\partial x} + \nu \left(\frac{1}{r} \frac{\partial}{\partial r} \left(r \frac{\partial u_x}{\partial r} \right) \right) \right) r dr. \quad (4.12)$$

The first term is simplified as

$$\begin{aligned} 2\pi \int_0^R \frac{\partial u_x}{\partial t} r dr &= \frac{\partial}{\partial t} 2\pi \int_0^R u_x r dr - 2\pi \left[u_x \frac{\partial R}{\partial t} \right]_R \\ &= \frac{\partial q}{\partial t} \end{aligned} \quad (4.13)$$

where the nonslip condition $u_x|_R = 0$ and the definition of $q(x, t)$ are used. Integrating the next momentum term by parts and applying the no-slip condition gives

$$2\pi \int_0^R u_r \frac{\partial u_x}{\partial r} r dr = 2\pi \left([r u_r u_x]_0^R - \int_0^R u_x \frac{\partial}{\partial r} (r u_r) dr \right) = -2\pi \int_0^R u_x \frac{\partial}{\partial r} (r u_r) dr. \quad (4.14)$$

Using the mass balance relation, we get

$$-2\pi \int_0^R u_x \frac{\partial}{\partial r} (r u_r) dr = 2\pi \int_0^R u_x \frac{\partial u_x}{\partial x} r dr. \quad (4.15)$$

Combining Eq. (4.15) with the third term in Eq. (4.12) results in

$$2\pi \int_0^R u_x \frac{\partial u_x}{\partial x} r dr + 2\pi \int_0^R u_x \frac{\partial u_x}{\partial x} r dr = 2\pi \int_0^R \frac{\partial u_x^2}{\partial x} r dr. \quad (4.16)$$

The pressure gradient can be integrated directly, giving

$$2\pi \int_0^R \frac{1}{\rho} \frac{\partial p}{\partial x} r dr = \frac{1}{\rho} \frac{\partial p}{\partial x} 2\pi \int_0^R r dr = \frac{A}{\rho} \frac{\partial p}{\partial x}. \quad (4.17)$$

Finally, integrating the viscous shear force on the right hand side of the momentum equation gives

$$\begin{aligned} 2\pi \int_0^R \nu \left(\frac{1}{r} \frac{\partial}{\partial r} \left(r \frac{\partial u_x}{\partial r} \right) \right) r dr &= 2\pi \nu \int_0^R \left(\frac{\partial}{\partial r} \left(r \frac{\partial u_x}{\partial r} \right) \right) dr \\ &= 2\pi \nu \left[r \frac{\partial u_x}{\partial r} \right]_R. \end{aligned} \quad (4.18)$$

In summary, equations (4.13), (4.16), (4.17), and (4.18) give the 1D momentum balance equation

$$\frac{\partial q}{\partial t} + 2\pi \int_0^R \frac{\partial u_x^2}{\partial x} r dr + \frac{A}{\rho} \frac{\partial p}{\partial x} = 2\pi \nu \left[r \frac{\partial u_x}{\partial r} \right]_R. \quad (4.19)$$

4.1.2 Velocity Profile

To write the momentum equation as a function of q , we need to specify a velocity profile over the cross-section [249]. For a fully developed, parabolic flow, we have

$$u_x = 2\bar{u}_x \left(1 - \frac{r^2}{R^2}\right), \quad 0 \leq r \leq R, \quad (4.20)$$

which is a Poiseuille profile, where \bar{u}_x is the mean velocity. The maximum velocity is $2\bar{u}_x$ at $r = 0$, and $\bar{u}_x = 0$ at $r = R$, satisfying the no slip condition. This velocity profile holds for an infinite pipe without side branches. However, the branching of the vasculature inhibits a strictly Poiseuille profile [248]. Instead, most 1D models [4, 41, 223, 268] use a more general, power-law profile

$$u_x = \frac{\chi + 2}{\chi} \bar{u}_x \left(1 - \left(\frac{r}{R}\right)^\chi\right) \quad (4.21)$$

where $\chi = 2$ gives the Poiseuille profile and $\chi = 9$. Numerous authors [4, 41, 223] use $\chi = 9$, which appears more flat (see Figure 4.2).

An alternative profile resembling the in-vivo, plug-like velocity [137, 166] is the Stokes-boundary layer profile

$$u_x = \begin{cases} \bar{u}_x, & r \in [0, R - \delta) \\ \bar{u}_x \frac{R - r}{\delta}, & r \in [R - \delta, R] \end{cases} \quad (4.22)$$

where δ (cm) is the boundary layer thickness. Lighthill [137] concluded that the boundary layer can be approximated by $\delta = \sqrt{T \nu / 2\pi}$, where T (s) is the cardiac cycle length. Within this boundary layer, the velocity decreases from the mean value to zero (satisfying the no-slip condition).

Finally, a number of recent studies (e.g., [16, 22, 198]) have used *Womersley theory* to predict a profile that varies with the cardiac cycle. However, the review by van de Vosse and Stergiopolus [249] has shown that adding this component does not change flow predictions significantly. Therefore, in this study we chose the simpler Stokes boundary layer.

Using the Stokes-boundary layer profile, the right hand side of (4.19) evaluated at $r = R$ is

$$2\pi \nu \left[r \frac{\partial u_x}{\partial r} \right]_R = -\frac{2\pi \nu R \bar{u}_x}{\delta} = -\frac{2\pi \nu R}{\delta} \frac{q}{A}. \quad (4.23)$$

Using Liebniz rule, the second term in Eq. (4.19) can be written as

$$\begin{aligned} \int_0^R \frac{\partial u_x^2}{\partial x} r dr &= \frac{\partial}{\partial x} \int_0^R u_x^2 r dr - \left[u_x^2 r \frac{\partial R}{\partial x} \right]_{r=R} \\ &= \frac{\partial}{\partial x} \int_0^R u_x^2 r dr \end{aligned} \quad (4.24)$$

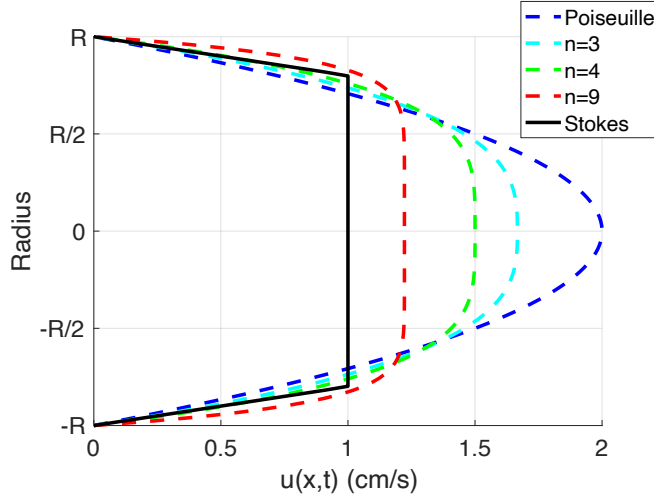


Figure 4.2 The Poiseuille, power-law, and Stokes boundary layer velocity profiles as described in equations (4.20), (4.21), and (4.22).

which holds because of the no-slip condition. Using Eq. (4.22) gives

$$\begin{aligned}
 2\pi \frac{\partial}{\partial x} \left(\int_0^R u_x^2 r dr \right) &= 2\pi \frac{\partial}{\partial x} \left(\int_0^{R-\delta} u_x^2 r dr + \int_{R-\delta}^R u_x^2 r dr \right) \\
 &= 2\pi \frac{\partial}{\partial x} \left(\int_0^{R-\delta} (\bar{u}_x)^2 r dr + \int_{R-\delta}^R \left(\bar{u}_x \frac{R-r}{\delta} \right)^2 r dr \right) \\
 &= 2\pi \frac{\partial}{\partial x} \left(\bar{u}_x^2 \left(\frac{1}{2} R^2 - \frac{2}{3} \delta R + \frac{1}{4} \delta^2 \right) \right) \\
 &= \frac{\partial}{\partial x} \left(\bar{u}_x^2 \left(\pi R^2 - \frac{4}{3} \delta \pi R + \frac{1}{2} \pi \delta^2 \right) \right). \tag{4.25}
 \end{aligned}$$

Assuming that the boundary layer is much smaller than the radius, $\delta/R \ll 1$, and using $\pi R^2 = A$ and $q = uA$, we get

$$\begin{aligned}
 \frac{\partial}{\partial x} \left(\bar{u}_x^2 \left(\pi R^2 - \frac{4}{3} \delta \pi R + \frac{1}{2} \pi \delta^2 \right) \right) &= \frac{\partial}{\partial x} \left(\bar{u}_x^2 A \left(1 - \frac{4\delta}{3R} + \frac{\delta^2}{R^2} \right) \right) \\
 &\approx \frac{\partial}{\partial x} (\bar{u}_x^2 A) \\
 &= \frac{\partial}{\partial x} \left(\frac{q^2}{A} \right) \tag{4.26}
 \end{aligned}$$

Thus, the final mass-momentum system is

$$\frac{\partial q}{\partial x} + \frac{\partial A}{\partial t} = 0 \tag{4.27}$$

$$\frac{\partial q}{\partial t} + \frac{\partial}{\partial x} \left(\frac{q^2}{A} \right) + \frac{A}{\rho} \frac{\partial p}{\partial x} = -\frac{2\pi \nu R}{\delta} \frac{q}{A}. \tag{4.28}$$

4.1.3 Constitutive law

The 1D equations above contain three unknowns: volumetric flow q , cross-sectional area A , and pressure p . To close the system, a constitutive model, i.e., a *stress-strain relationship*, for the blood vessel is needed. The stress, σ is the force per unit volume acting on the material, and the strain, ϵ , is a dimensionless measure of relative displacement from some reference point.

Assuming that the vessel is a cylinder made of a linear, elastic, homogeneous, and isotropic material, stress-strain relation is

$$\sigma_{rr} = E\epsilon_{rr} + \kappa(\sigma_{\theta\theta} + \sigma_{xx}) \quad (4.29)$$

$$\sigma_{\theta\theta} = E\epsilon_{\theta\theta} + \kappa(\sigma_{rr} + \sigma_{xx}) \quad (4.30)$$

$$\sigma_{xx} = E\epsilon_{xx} + \kappa(\sigma_{rr} + \sigma_{\theta\theta}). \quad (4.31)$$

where ϵ_{ii} and σ_{ii} are the normal strain and normal stress in the i th direction, E is the Young's modulus, and the κ is the Poisson's ratio.

For a pressurized vessel with no external force, $\sigma_{rr}|_R = -p$ and $\sigma_{rr}|_{R+h} = 0$, where p is the blood pressure in the lumen. If the wall thickness h is non-negligible relative to the lumen radius, then the radial stress σ_{rr} is significant and varies from $r = R$ to $r = R + h$ (see Figure 4.3). If the wall is thin compared to the vessel radius ($h \ll R$), then $\sigma_{\theta\theta}$ is approximately constant across the wall. As noted by Humphrey [104], the thin wall assumption allows us to approximate the mean radial stress as $\bar{\sigma}_{rr} \approx -p/2$.

The force exerted by the vessel wall must balance with the fluid pressure (shown below in Figure 4.3) at the outer radius of the lumen R in the *loaded* configuration. The pressure acting on the lumen is uniform over the area, i.e. $p \equiv p \sin(\theta)$. This balances the circumferential stress acting in the normal direction over both half-sections of the tube shown in Figure 4.3, giving

$$\begin{aligned} & \int_0^L \int_0^\pi p \sin(\theta) R d\theta dx - 2 \int_0^L \int_R^{R+h} \sigma_{\theta\theta} dr dx = 0 \\ \Rightarrow & \int_0^L \int_0^\pi p \sin(\theta) R d\theta dx = 2 \int_0^L \int_R^{R+h} \sigma_{\theta\theta} dr dx. \end{aligned} \quad (4.32)$$

Since the forces are applied uniformly, we can write

$$\begin{aligned} pR \int_0^L \int_0^\pi \sin(\theta) d\theta dx &= 2\sigma_{\theta\theta} \int_0^L \int_R^{R+h} dr dx \\ \Rightarrow 2pRL &= 2\sigma_{\theta\theta}L \\ \Rightarrow \sigma_{\theta\theta} &= \frac{pR}{h}. \end{aligned} \quad (4.33)$$

Note that this equation holds for the **loaded** configuration [104]. Since $h \ll R$, $\frac{p}{2} \ll \frac{R}{h}p$, and hence $\sigma_{rr} \ll \sigma_{\theta\theta}$. Assuming that the vessel is tethered in the longitudinal direction (along the x axis),

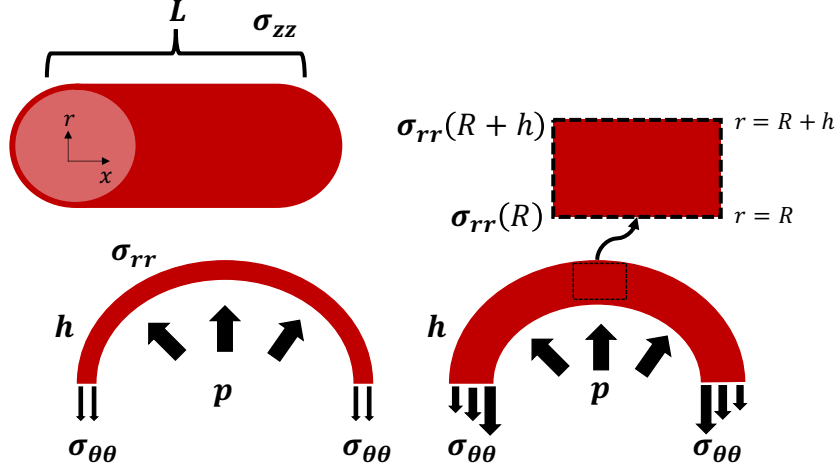


Figure 4.3 Stress exerted on a thin (left) and thick (right) walled pressurized cylinder.

$\epsilon_{xx} \ll 1$. Then, the stress-strain relationship for the axial direction is

$$\sigma_{xx} = E\epsilon_{xx} + \kappa(\sigma_{rr} + \sigma_{\theta\theta}) \approx \kappa\sigma_{\theta\theta}. \quad (4.34)$$

Using σ_{xx} in the circumferential stress gives

$$\begin{aligned} \sigma_{\theta\theta} &= E\epsilon_{\theta\theta} + \kappa\sigma_{xx} = E\epsilon_{\theta\theta} + \kappa^2\sigma_{\theta\theta} \\ \Rightarrow \epsilon_{\theta\theta} &= \frac{(1-\kappa^2)}{E}\sigma_{\theta\theta}. \end{aligned} \quad (4.35)$$

The *Lagrangian strain* in the circumferential direction of the vessel wall due to blood pressure is

$$\epsilon_{\theta\theta} = \frac{2\pi R - 2\pi r_0}{2\pi r_0} = \frac{R - r_0}{r_0} \quad (4.36)$$

where r_0 is the reference radius and R is the current radius. Combining the results from Eq. (4.33) and (4.36), we can rewrite Eq. (4.35) as

$$\begin{aligned} \epsilon_{\theta\theta} &= \frac{(1-\kappa^2)}{E}\sigma_{\theta\theta} \\ \Rightarrow \frac{R - r_0}{r_0} &= \frac{(1-\kappa^2)}{E} \frac{R}{h} p \\ \Rightarrow p &= \frac{Eh}{(1-\kappa^2)r_0} \left(\frac{R - r_0}{R} \right) \end{aligned} \quad (4.37)$$

$$= \frac{Eh}{(1-\kappa^2)r_0} \left(1 - \sqrt{\frac{A_0}{A}} \right). \quad (4.38)$$

Lastly, assuming that the vessel wall is incompressible, corresponding to $\kappa = \frac{1}{2}$, gives

$$p(x, t) = p_0 + \frac{Eh}{(1-\kappa^2)r_0} \left(1 - \sqrt{\frac{A_0}{A}} \right), \quad (4.39)$$

$$= \frac{4}{3}\beta_w(r_0) \left(1 - \sqrt{\frac{A_0}{A}} \right) \quad (4.40)$$

where p_0 is the reference pressure (in the *unloaded, stressed* configuration), and $\beta_w(r_0) = Eh/r_0$. Note that if the wall displacements are small, then

$$\frac{R-r_0}{R} \approx \frac{R-r_0}{r_0} \quad (4.41)$$

which is the *Eulerian strain*. This change in the denominator in the strain to r_0 instead of R , giving an alternative constitutive equation

$$p(x, t) = p_0 + \frac{4}{3}\beta_w(r_0) \left(\sqrt{\frac{A}{A_0}} - 1 \right). \quad (4.42)$$

Eq. (4.39) and (4.42) are approximately equivalent under the small strain assumption. As detailed in Section 2.3, the pulmonary vascular wall is heterogenous and varies with vessel caliber. To account for changes in wall composition and stiffening, vascular stiffness (shown in Figure 4.5) is modeled as [166]

$$\frac{Eh}{r_0} = k_1 e^{-k_2 r_0} + k_3, \quad (4.43)$$

where k_1 (g/cm/s²), k_2 (s), and k_3 (g/cm/s²) are parameters describing the rate at which vessels stiffen with decreasing radius. The two constitutive models listed above have been used in numerous 1D blood flow studies [3, 4, 16, 166, 168]. Some studies advocate the use of Eq. (4.39) over Eq. (4.42), as in the limit of high strains, Eq. (4.39) is bounded where as Eq. (4.42) blows up (see Figure 4.4).

However, as discussed in Section 2.3, the vessel wall consists of collagen, elastin, and smooth muscle cells, which deform in a nonlinear and viscoelastic fashion. Several 1D studies, mostly studying flow in the systemic circulation, e.g. [21, 240], have used more advanced wall models to account for this behavior. The pulmonary arteries operate under lower pressure, but only a few studies have examined the deformation of these. Examples include the study by Qureshi et al. [191], who investigated a non-linear elastic model represented by a tangent function, and showed that the nonlinear wall model provides a better fit to normotensive hemodynamics while the linear-wall model is comparable in disease when the pulmonary walls have thickened and stiffened. Previous studies have utilized viscoelastic constitutive laws in the 1D setting [21, 225], achieving similar pressure-area relationships seen during ex-vivo testing. Conditioned materials, i.e. those cyclically loaded and unloaded until the constitutive law is strain-rate independent, can be modeled as *pseudoelastic* materials [74]. In this framework loading and unloading of the material are modeled as separate elastic materials with a specific pseudo-strain energy function. Strain-energy density functions,

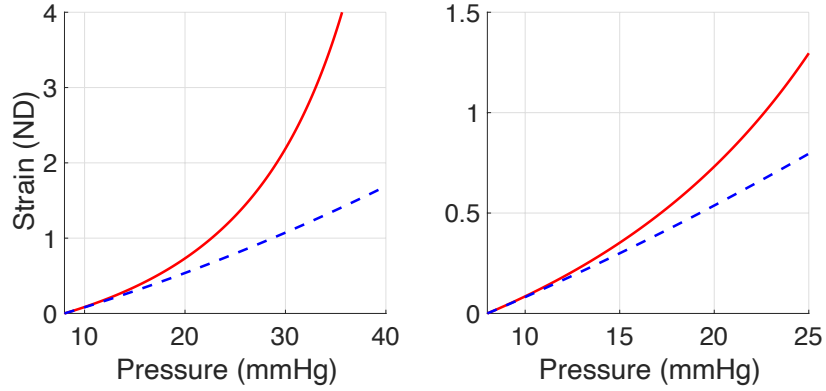


Figure 4.4 Constitutive models from Eq. (4.39) (shown in red) and Eq. (4.42) (shown in blue). For large strains (left panel), the two models deviate with Eq. (4.39) blowing up for high strains while 4.42 increases linearly. For small strains (right most panel), Eq. (4.39) and Eq. (4.42) are similar

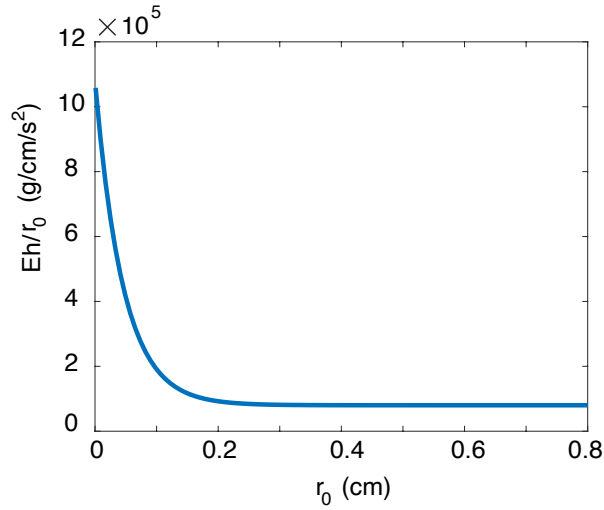


Figure 4.5 Stiffness function as described by Eq. (4.43) and originally derived in [166]. Note that smaller vessels have a greater stiffness. Plot is generated with $k_1 = 10^6$, $k_2 = 22$, and $k_3 = 8 \times 10^4$.

which relate material properties to the material deformation, can also account for wall heterogeneity and the interaction of elastin, collagen, and SMCs. These are studied as hyperelastic models [97, 104]. *Hyperelastic* models describe an elastic material that can undergo large deformations [97]. These have more recently been integrated into the 1D modeling framework for systemic vessels [44], and are an active research area.

4.1.4 Summary

Based on the above derivations, the final system of equations is

$$\frac{\partial q}{\partial x} + \frac{\partial A}{\partial t} = 0 \quad (4.44)$$

$$\frac{\partial q}{\partial t} + \frac{\partial}{\partial x} \left(\frac{q^2}{A} \right) + \frac{A}{\rho} \frac{\partial p}{\partial x} = - \frac{2\pi \nu R}{\delta} \frac{q}{A} \quad (4.45)$$

$$p(x, t) = \mathcal{F}(A, A_0, \beta_w), \quad (4.46)$$

where \mathcal{F} is the constitutive law, dependent on the material parameters β_w .

4.2 Stenosis models

Vascular stenoses are a fatal vascular wall abnormality that obstructs the vascular lumen. Modeling this abnormality is especially important when simulating emboli in the large pulmonary arteries due to CTEPH. The physics of flow through a constriction parallel ideas for gas flow through a nozzle [125]. Flow approaching the stenosis increases in velocity as the area of the vessel decreases. The sudden increase in area distal to the stenosis decreases the fluid velocity and induces a pressure (head) loss. This increases the resistance to flow, causing flow redistribution in the network, and flow separation, decreasing the wall shear stress. This is one physiological mechanism responsible for plaque rupture in most heart attacks and stroke [125].

One of the first models compared to experimental data was developed by Young and Tsai [269, 270]. Using polyester resin tubes with specified area reductions, the authors ran several experiments with both axisymmetric and nonsymmetric obstructions using steady and pulsatile flow. Young and Tsai concluded that pressure drop across the tube stenosis can be modeled by

$$\Delta p_{ring} = \frac{\mu K_v}{2r_p} u + \frac{\rho K_t}{2} \left(\frac{A_p}{A_s} - 1 \right)^2 |u|u + \rho K_u L \frac{\partial u}{\partial t} \quad (4.47)$$

or written in terms of q/A_p

$$\Delta p_{ring} = \frac{\mu K_v}{2\pi(r_p)^3} q + \frac{\rho K_t}{2(A_p)^2} \left(\frac{A_p}{A_s} - 1 \right)^2 |q|q + \frac{\rho K_u L_s}{A_p} \frac{\partial q}{\partial t}. \quad (4.48)$$

Here, $A_p = \pi r_p^2$ is the area prior to the stenosis, and L_s is the length of the stenosis. The above equation has three main components: (1) losses due to viscous forces (K_v), (2) losses due to turbulent forces due to the constriction and expansion of the tube (K_t), and (3) losses due to inertial effects (K_u). K_v is strongly dependent on the geometry of the stenosis, and can be approximated as [268],

$$K_v = 16 \frac{L_s}{r_p} \left(\frac{A_p^2}{A_s^2} \right), \quad (4.49)$$

whereas $K_t = 1.52$ and $K_u = 1.2$ are assumed to be geometry independent.

This model has been used to study the effects of stenoses on systemic artery [22, 136] and coronary artery disease [25]. Studies by Bezerra et al. [25] and Yin et al. [268] both showed that 3D fluid dynamic predictions across systemic stenoses can be captured using Eq. (4.48) in a 1D hemodynamic model. Only one previous study by Spilker et al. [223] has considered a similar pressure loss model in the pulmonary circuit. A detailed description of how these loss coefficients affect 1D model predictions can be found in [22].

Equation (4.48) is valid for ring-like, concentric lesions, but pulmonary lesions common in CTEPH take several different forms. Web-like lesions are the most common type, and have fibrous, heterogenous bands that impede flow (see Figure 2.10). As illustrated in Figure 4.6, these lesions can be paralleled to a loosely packed porous media. Noting that the flow through these lesions provide a non-negligible Reynolds number, we propose a pressure loss based on the Darcy-Forchhemeier equation

$$\Delta p_{\text{web}} = L_w \left(\frac{\mu}{K_{\text{perm}}} \frac{q}{A} + \rho K_w \left(\frac{q}{A} \right)^2 \right), \quad (4.50)$$

where L_w (cm) is the length of the obstructed area, K_{perm} (cm²) is the permeability of the web-like lesion, and K_w (dimensionless) is the pressure loss coefficient due to inertial effects. As discussed in [126], one can approximate $K_w = G / \sqrt{K_{\text{perm}}}$, used here as well.

Both Eq. (4.48) and Eq. (4.50) are enforced by solving a root-finding problem. The Jacobian is derived analytically, and provided in Appendix B.4.

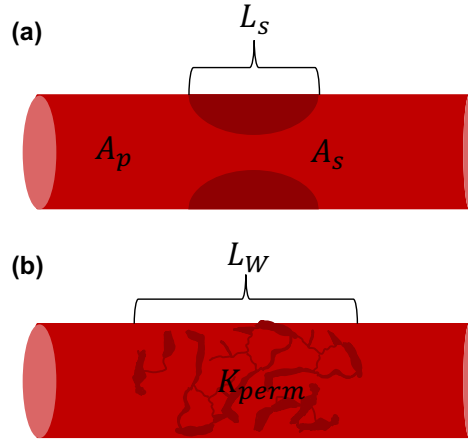


Figure 4.6 Depiction of how ring- and web-like lesions are modeled. (a) Ring-like lesions are modeled as concentric, short lesions are characterized by their unobstructed area, A_p , obstructed area A_s , and length L_s . (b) Heterogenous strands of fibrous material characterize web-like lesions. The degree of obstruction is determined by the length of the lesion, L_w , and the permeability of the web, K_{perm} .

4.3 Small vessel hemodynamics

Imaging data can provide structural information about the large vessels in the network. Since image resolution is limited, a model of the small vessels and microvasculature is required at the end of the large vessels. Systemic capillary models utilize steady, viscous dominate Stokes' flow, and account for the size of red blood cells as they transverse the capillary beds [212]. These models can account for the diffusion of substances across the capillary-tissue barrier. A simpler approach is to model the capillaries as a single, porous media, as done by Coccarelli et al. [43]. Their work lumped the capillaries into a single poro-elastic tube and attached this porous media model to a 1D network. Pulmonary capillary models following Fung's "sheet" model approach [71, 73] and have also been coupled to large vessel 1D models [40].

In this dissertation, two modeling approaches are pursued. The first is the most common approach [4, 5, 21, 58], and models the distal vasculature as an electrical circuit. Otto Frank [170] compared the elastic nature of the aorta to a German fire engine, called a "Windkessel," and is now synonymous with the electrical circuit analogy that consists of a resistor in series and a resistor and capacitor in parallel.

The other small vessel model considered here is the structured tree model, developed by Olufsen [166]. The structured tree represents the downstream vasculature as a self-similar fractal tree. The fluid dynamics in the small vessels are viscous dominant, leading to analytical pressure and flow solutions in the frequency domain. This approach models the vessels up to the capillaries, and allows for small vessel predictions in the absence of imaging data.

4.3.1 Windkessel model

The Windkessel model parallels the vascular tree to an electrical circuit, where pressure is analogous to voltage, flow to the current, vascular resistance to electrical resistance, and compliance to capacitance [259]. The 3 element Windkessel model stems from the idea that blood leaving the heart overcomes a proximal resistance R_p (mmHg s/ ml) (sometimes called characteristic impedance, Z_c) and then traverses the vasculature downstream which has some total compliance C_T (ml/mmHg) and distal resistance R_d (mmHg s/ ml), as depicted in Figure 4.7. This is modeled by an electrical R-C-R circuit, with a resistor in series and then a resistance and capacitor in parallel. The Windkessel model is represented by the ordinary differential equation

$$\frac{dp}{dt} = R_p \left(\frac{dq}{dt} \right) + q \left(\frac{R_p + R_d}{R_p R_d} \right) - \frac{p}{R_d C_T}. \quad (4.51)$$

Since the pumping of the heart is nearly periodic, we can rewrite the variables q , and p as periodic

functions using the discrete, Fourier transform:

$$q(x, t) = \sum_{k=-\infty}^{\infty} Q(x, \omega_k) e^{i\omega_k t}, \quad (4.52)$$

$$p(x, t) = \sum_{k=-\infty}^{\infty} P(x, \omega_k) e^{i\omega_k t}, \quad (4.53)$$

where $\omega_k = 2\pi k/T$ is the angular frequency. The frequency domain quantities can also be expressed in terms of their time-domain equivalent

$$Q(x, \omega) = \frac{1}{T} \int_{-T/2}^{T/2} q(x, t) e^{-i\omega_k t} dt \quad (4.54)$$

$$P(x, \omega) = \frac{1}{T} \int_{-T/2}^{T/2} p(x, t) e^{-i\omega_k t} dt, \quad (4.55)$$

In the frequency domain, the Windkessel model is

$$\begin{aligned} i\omega P e^{i\omega t} &= i\omega R_p Q e^{i\omega t} + Q e^{i\omega t} \left(\frac{R_p + R_d}{R_p R_d} \right) - P e^{i\omega t} \frac{1}{R_d C_T} \\ \Rightarrow P \left(i\omega + \frac{1}{R_d C_T} \right) &= Q \left(i\omega R_p + \frac{R_p + R_d}{R_p R_d} \right) \\ \Rightarrow \frac{P}{Q} \equiv Z &= \frac{R_p + R_d + i\omega C_T R_p R_d}{1 + i\omega C_T R_d} \end{aligned} \quad (4.56)$$

where Z (mmHg s/ml) is the impedance.

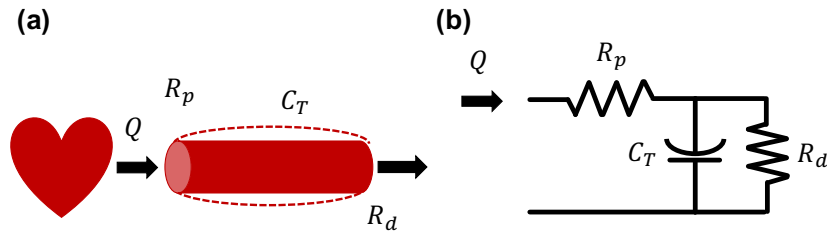


Figure 4.7 (a) Physiological depiction of the 3 element Windkessel. Blood ejected out of the heart must overcome some proximal resistance, R_p , and then flows through an artery with total compliance C_T and distal resistance R_d . (b) Electrical circuit analog for the Windkessel model. The circuit consists of a resistor in series with a resistor and capacitor in parallel.

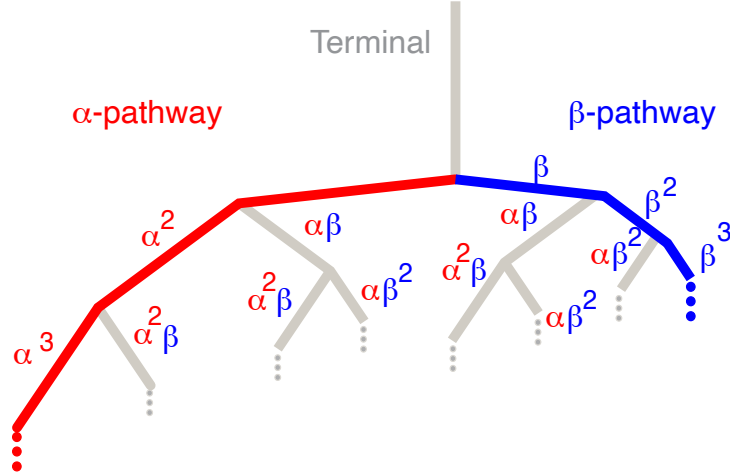


Figure 4.8 Schematic of the structured tree. At each bifurcation, daughter vessels are scaled from the parent vessel radius by the radius scaling factors α and β , $0 < \beta \leq \alpha < 1$. The “ α ” pathway (denoted in red) is the longest path in the network, whereas the “ β ” pathway (denoted in blue) is the shortest pathway.

4.3.2 Structured tree

Rather than lump the entire downstream vasculature into an electrical circuit, the structured tree model assumes that vessels distal to the large arteries are represented by fractal, self-similar trees, shown in Figure 4.8. Each daughter vessel is related to its parent via the radius scaling factors α and β , and a length to radius ratio L_{rr} . The dimensions of any vessel in the structured tree can be expressed in terms of the terminal large artery radius r_{term} proximal to the beginning of the structured tree

$$r_{n,m} = r_{term} \alpha^n \beta^m, \quad L_{n,m} = L_{rr} r_{n,m}. \quad (4.57)$$

The network is truncated once reaching a terminal radius r_{min} .

These scaling factors require either ex-vivo measurements (e.g., lungs taken out of the body) or super-high resolution imaging. Olufsen [166] determined scaling factors for the systemic circulation using literature data. As mentioned in Section 2.2, the pulmonary vasculature branches rapidly, therefore this factors are not valid for the pulmonary arterial tree. Qureshi et al. [189] used pulmonary artery literature data from multiple studies, deducing a length to radius ratio of

$$L_{rr} = \begin{cases} 15.75 r^{1.10} & r \geq 0.005 \\ 1.79 r^{0.47} & r \leq 0.005 \end{cases}. \quad (4.58)$$

The study determined $\alpha = 0.846$ and $\beta = 0.698$, similar to [166]. A recent study in mice by Chambers et al. [35] estimated these parameters from high-resolution imaging data from normotensive and HPH mice. They also found that $\alpha = 0.88$ and $\beta = 0.67$ in normotensive mice, whereas $\alpha = 0.86$ and $\beta = 0.66$ in HPH, similar to the findings of Qureshi et al. [189]. However, since mice are smaller than

humans, the length to radius ratio was determined as

$$L_{rr} = \begin{cases} 13.4e^{0.00771r_0}, & \text{normotensive} \\ 10.9e^{0.00797r_0}, & \text{hypertensive.} \end{cases} \quad (4.59)$$

Similar to the large vessels, hemodynamics are computed in the structured tree. However, fluid flow in the small arteries and arterioles is viscous dominant, hence the nonlinear inertial terms in Eq. (4.46) can be disregarding. A detailed derivation of this is provided by Olufsen [166], and is summarized here. Rewriting the momentum equation without the nonlinear inertial term gives

$$\frac{\partial u_x}{\partial t} + \frac{1}{\rho} \frac{\partial p}{\partial x} = \frac{\nu}{r} \frac{\partial}{\partial r} \left(r \frac{\partial u_x}{\partial r} \right). \quad (4.60)$$

Assuming that Q, P are periodic as before, and defining

$$u_x(x, t) = \sum_{k=-\infty}^{\infty} U(x, \omega_k) e^{i\omega_k t}, \quad (4.61)$$

$$U(x, \omega) = \frac{1}{T} \int_{-T/2}^{T/2} u_x(x, t) e^{-i\omega_k t} dt, \quad (4.62)$$

$$(4.63)$$

we can write Eq. (4.60) as

$$i\omega_k U e^{i\omega_k t} + \frac{1}{\rho} \frac{\partial P}{\partial x} e^{i\omega_k t} = \frac{\nu}{r} \frac{\partial}{\partial r} \left(r \frac{\partial U}{\partial r} \right) e^{i\omega_k t} \quad (4.64)$$

$$\Rightarrow \nu \frac{\partial^2 U}{\partial r^2} + \frac{\nu}{r} \frac{\partial U}{\partial r} - i\omega_k U = \frac{1}{\rho} \frac{\partial P}{\partial x}. \quad (4.65)$$

Eq. (4.65) is a second-order, linear, nonhomogenous differential equation, whose analytical solution is

$$U = \frac{1}{\rho} \frac{\partial P}{\partial x} \left(1 - \frac{J_0(r w_0 / r_0)}{J_0(w_0)} \right), \quad w_0 = \sqrt{i^3 \omega^2} = \sqrt{\frac{i^3 r_0^2 \omega}{\nu}}, \quad (4.66)$$

where w (nondimensional) is the Womersley number and $J_0(x)$ is the zeroth order Bessel function of the first kind. The flow Q is determined by integrating over the cross-section

$$Q = 2\pi \int_0^{r_0} U r dr = \frac{2\pi}{i\omega\rho} \frac{\partial P}{\partial x} \int_0^{r_0} \left(1 - \frac{J_0(r w_0 / r_0)}{J_0(w_0)} \right) r dr, \quad (4.67)$$

$$= \frac{2\pi}{i\omega\rho} \frac{\partial P}{\partial x} (1 - F_J), \quad (4.68)$$

where F_J is the ratio of first and zeroth order Bessel functions, i.e.

$$F_J = \frac{2J_1(w_0)}{w_0 J_0(w_0)}. \quad (4.69)$$

Note that using the linear pressure-area relation in Eq. (4.39) can be rewritten as

$$\begin{aligned} p &= p_0 + \frac{4}{3}\beta_w \left(1 - \sqrt{\frac{A_0}{A}}\right) \\ \Rightarrow A &= \left(1 - \frac{3(p-p_0)}{4\beta_w}\right)^{-2} A_0(x). \end{aligned} \quad (4.70)$$

Expanding $\frac{\partial A}{\partial t}$ in terms of p and linearizing gives

$$\begin{aligned} \frac{\partial A}{\partial t} &= \frac{\partial A}{\partial p} \frac{\partial p}{\partial t} \\ &= \frac{3}{2\beta_w} A_0 \left(1 - \frac{p-p_0}{\beta_w}\right)^{-3} \frac{\partial p}{\partial t}. \end{aligned} \quad (4.71)$$

Under the assumption that vessels are sufficiently small and stiff, i.e. $Ek \gg r_0 p$ and $p/\beta_w \approx 0$, we can approximate the compliance $C = \frac{\partial A}{\partial p}$ above as

$$C = \frac{3}{2\beta_w} A_0 \left(1 - \frac{p-p_0}{\beta_w}\right)^{-3} \quad (4.72)$$

$$\approx \frac{3}{2\beta_w} A_0 \quad (4.73)$$

giving

$$\frac{\partial A}{\partial t} = C \frac{\partial p}{\partial t}. \quad (4.74)$$

A similar approach using Eq. (4.42) gives

$$A = \left(1 + \frac{(p-p_0)}{\beta_w}\right)^2 A_0(x), \quad (4.75)$$

$$C = \frac{3}{2\beta_w} A_0 \left(1 + \frac{(p-p_0)}{\beta_w}\right) \quad (4.76)$$

$$\approx \frac{3}{2\beta_w} A_0, \quad (4.77)$$

hence, the constitutive laws given by equations (4.39) and (4.42) give the same compliance.

The mass conservation equation in the frequency domain is

$$\frac{\partial A}{\partial t} + \frac{\partial q}{\partial x} = 0 \quad (4.78)$$

$$\Rightarrow i\omega CP + \frac{\partial Q}{\partial x} = 0. \quad (4.79)$$

Analytical solutions to the two equations are obtained by first differentiating Eq. (4.79) with respect to x and solving for P , giving

$$\frac{\partial P}{\partial x} = \frac{-1}{i\omega C} \frac{\partial^2 Q}{\partial x^2}. \quad (4.80)$$

Using this in the momentum balance, Eq. (4.68), gives

$$\begin{aligned} i\omega Q &= \frac{A_0}{i\omega C\rho} \frac{\partial^2 Q}{\partial x^2} (1 - F_J) \\ \Rightarrow \frac{\partial^2 Q}{\partial x^2} + \frac{\omega^2 C\rho}{A_0(1 - F_J)} Q &= 0 \\ \Rightarrow \frac{\partial^2 Q}{\partial x^2} + \frac{\omega^2}{c^2} Q &= 0, \end{aligned} \quad (4.81)$$

where $c = \sqrt{A_0(1 - F_J)/\rho C}$. The analytical solutions for both Q and P are written as

$$Q(x, \omega) = a \cos\left(\frac{\omega}{c} x\right) + b \sin\left(\frac{\omega}{c} x\right) \quad (4.82)$$

$$P(x, \omega) = \frac{i}{g_\omega} \left(b \cos\left(\frac{\omega}{c} x\right) + a \sin\left(\frac{\omega}{c} x\right) \right), \quad (4.83)$$

$$g_\omega = \sqrt{\frac{CA_0(1 - F_J)}{\rho}}, \quad (4.84)$$

where a and b are unknown integration constants. The above solutions hold $\forall \omega_k \neq 0$. For the zeroth frequency, we revisit Eq. (4.65) and set $\omega_k = 0$

$$\begin{aligned} \frac{1}{\rho} \frac{\partial P}{\partial x} &= \frac{\nu}{r} \frac{\partial}{\partial r} \left(r \frac{\partial U}{\partial r} \right) \\ \Rightarrow \frac{\partial P}{\partial x} \frac{r}{\mu} &= \frac{\partial}{\partial r} \left(r \frac{\partial U}{\partial r} \right). \end{aligned}$$

Integrating a with respect to r twice gives

$$\frac{\partial P}{\partial x} \frac{r^2}{4\mu} = U + C_1 \ln(r) + C_2. \quad (4.85)$$

The fluid velocity must be bounded at $r = 0$, hence $C_1 = 0$. Enforcing the no-slip condition $U(r_0) = 0$ then gives

$$U = \frac{\partial P}{\partial x} \frac{r^2 - r_0^2}{4\mu} \quad (4.86)$$

$$\Rightarrow Q = 2\pi \int_0^{r_0} U r dr = -\frac{\pi r_0^4}{8\mu} \frac{\partial P}{\partial x}, \quad (4.87)$$

which is a Poiseuille flow.

To propagate the solution throughout the structured tree, we relate $P(x, \omega)$ and $Q(x, \omega)$ using

the impedance, $Z(x, \omega) = P(x, \omega)/Q(x, \omega)$. Using Eq. (4.82) and (4.83) in the impedance relation gives

$$Z(x, \omega) = \frac{P(x, \omega)}{Q(x, \omega)} = \frac{i(b \cos(\omega x/c) - a \sin(\omega x/c))}{g(a \cos(\omega x/c) + b \sin(\omega x/c))}. \quad (4.88)$$

Then impedance at $x = 0$ and $x = L$ are

$$Z(0, \omega) = \frac{i b}{g a},$$

$$Z(L, \omega) = \frac{i(b \cos(\omega L/c) - a \sin(\omega L/c))}{g(a \cos(\omega L/c) + b \sin(\omega L/c))}. \quad (4.89)$$

Combining these equations gives the impedance at $x = 0$

$$Z(0, \omega) = \frac{i g^{-1} \sin(\omega L/c) + Z(L, \omega) \cos(\omega L/c)}{\cos(\omega L/c) + i g Z(L, \omega) \sin(\omega L/c)}. \quad (4.90)$$

The zero-frequency value, $Z(0, 0)$, analogous to the DC component in electrical circuit theory, is given by

$$\lim_{\omega \rightarrow 0} Z(0, \omega) = \frac{8\mu l}{\pi r_0^4} + Z(L, 0), \quad (4.91)$$

which is the same as a Poiseuille resistance.

We assume continuity of pressure and conservation of flow at each junction in the small vessels of the structured tree. Under these assumptions, the impedance at a junction mimics resistors in parallel, i.e.

$$Z_p(L, \omega) = \left(\frac{1}{Z_{d_1}(0, \omega)} + \frac{1}{Z_{d_2}(0, \omega)} \right)^{-1}. \quad (4.92)$$

At the terminal end of the structured tree, where $r < r_{min}$, a constant terminal impedance $Z(L, 0) = Z_{trm}$ is prescribed. Previous studies assume that Z_{trm} is negligible [53, 168, 169]. However, the thousands of vessels in the structured tree lead to Q values on the order of $10^{-5} - 10^{-8}$ (ml/s) at the terminal ends. For this reason, the capillary pressure, $P_{trm} = Z_{trm} \cdot Q_{trm}$ is only non-negligible when $Z_{trm} \in [10^4, 10^9]$.

Once large vessel hemodynamics are determined, the resulting waveforms can be propagated through the structured tree. The impedance and pressure at $x = 0$ are determined by

$$P(L, \omega) = P(0, \omega) \cos(\omega L/c) - Q(0, \omega) \frac{i}{g_\omega} \sin(\omega L/c), \quad (4.93)$$

$$Z(L, \omega) = \frac{i g_\omega^{-1} \sin(\omega L/c) - Z(0, \omega) \cos(\omega L/c)}{g_\omega \cos(\omega L/c) Z(0, \omega) - \cos(\omega L/c)}, \quad (4.94)$$

for $\omega \neq 0$. The flow is calculated from the impedance relation, i.e. $Q(L, \omega) = P(L, \omega)/Z(L, \omega)$. For the

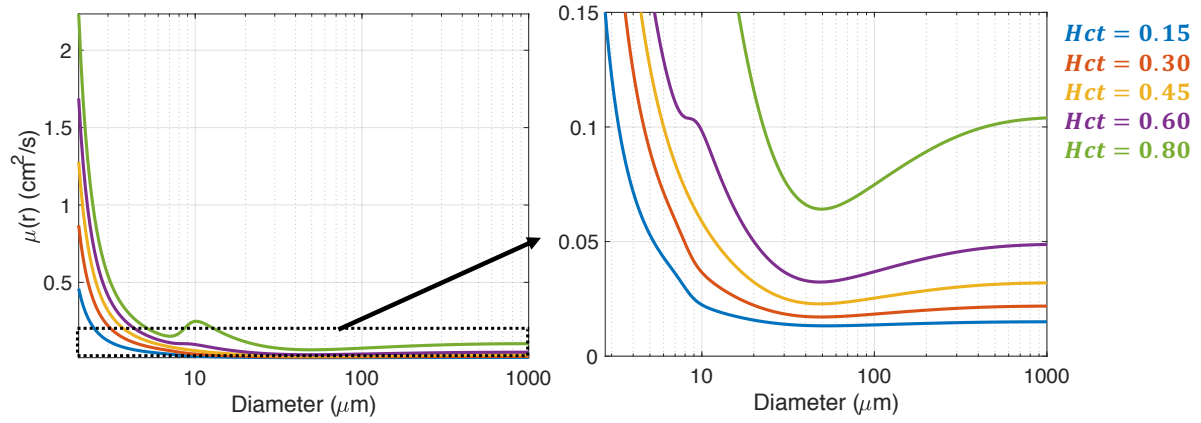


Figure 4.9 Nonlinear viscosity function originally proposed in [185] that depends on both vessel diameter and the hematocrit, Hct. Note that viscosity becomes more influential for smaller vessels and that viscosity magnitude is greater for greater Hct.

zeroth frequency, the solution is

$$P(L, 0) = P(0, 0) - Q(0, 0) \frac{8\mu L}{\pi r^4}, \quad (4.95)$$

$$Z(L, 0) = Z(0, 0) - \frac{8\mu L}{\pi r^4} \quad (4.96)$$

This enables pressure and flow predictions in any daughter vessel provided the pressure and flow of the parent are known [169]. To determine the impedance at the end of the larger arteries, Z_{trm} is used to calculate the inlet impedance $Z(0, \omega)$ at each terminal branch of the structured tree. Then, vessels are combined using Eq. (4.92). In this manner, the impedance of the entire tree is calculated recursively starting from the terminal end, giving the total impedance.

Prior studies assumed a constant viscosity in the terminal vessels [169, 189]. However, the non-Newtonian effects of blood viscosity μ (and hence kinematic viscosity ν) become more influential as the vessel radii decreases, requiring a radius dependent viscosity. The investigation by Pries et al. [185] suggested

$$\mu^*(r_0) = \left[1 + (\mu_{0.45} - 1) \left(\frac{(1 - \text{Hct})^c - 1}{(1 - 0.45)^c - 1} \right) \mathcal{D} \right] \mathcal{D}, \quad (4.97)$$

$$\mu_{0.45}(r_0) = 6e^{-0.17r_0} + 3.2 - 2.44e^{-0.12r_0^{0.645}}, \quad (4.98)$$

where $\mathcal{D} = (2r_0/(2r_0 - 1.1))^2$ and $\mu_{0.45}(r_0)$ is the relative viscosity at an average hematocrit level of 0.45. Figure 4.9 shows the viscosity five different Hct values. The addition elevates the viscous resistance in the smallest arterioles, improving the physiological relevance of the modeling framework.

4.4 Network model

The 1D equations (4.27) and (4.28) are hyperbolic PDEs, with characteristics pointing in the opposite direction. The system has three state variables p , q , and A , but only require a numerical solution for q and A , since $p \equiv p(A)$. Hence, a boundary condition at $x = 0$ and $x = L$ is only required for one of the states. The other state can be determined from the characteristic system [166].

4.4.1 Inflow condition

The network inlet can be coupled to a heart model or supplied an inflow waveform. In this work, a measured flow waveform is prescribed (see Figures 2.16 and 2.17 for mouse and human data).

4.4.2 Junction conditions

At a junction with n daughters, each vessel requires a boundary condition at the inlet and outlet. To link hemodynamics at junctions, continuity of flow is enforced:

$$q_p(L, t) = \sum_{i=1}^{n_v} q_{d_i}(0, t) \quad \forall t \in [0, T], \quad i = 1, 2, \dots, n \quad (4.99)$$

where n_v is the number of daughter vessels at a junction. In addition, continuity of static pressure is also assumed

$$p_p(L, t) = p_{d_i}(0, t), \quad \forall t \in [0, T], \quad i = 1, 2, \dots, n. \quad (4.100)$$

Note that another common junction condition is continuity of *total* pressure derived from a Bernoulli principle [158],

$$p_p(L, t) + \frac{1}{2} \rho (u_p(L, t))^2 = p_{d_i}(0, t) + \frac{1}{2} \rho (u_{d_i}(0, t))^2 + K_{\text{loss}} \frac{1}{2} \rho (u_p(L, t))^2 \quad (4.101)$$

where K_{loss} is a loss term that may arise due to the geometry of the junction (e.g., when junctions have large changes in angles or stenoses).

These junction conditions are enforced by solving a root-finding problem using a Newton-Raphson routine. Whereas prior work considered bifurcating junctions only [168, 189], this work derives the junction conditions for trifurcations, ensuring that patient specific geometries can be used. The analytical Jacobian for bifurcations and trifurcations are provided in Appendix B.3.

4.4.3 Outflow condition

At the terminal vessels, a Windkessel model or structured tree are attached. Both are coupled to the large vessel equations using the impedance relation, either Eq. (4.56) for the Windkessel model or Eq. (4.88) for the structured tree. To couple the time-domain large vessel equations to the frequency domain boundary conditions, the impedance is converted to the time domain using the discrete

inverse Fourier transform. The flow is then related to the pressure and inverse impedance (called “admittance”) via the convolution integral

$$q(L, t) = \int_0^t p(L, \tau) Z^{-1}(t - \tau) d\tau. \quad (4.102)$$

This is numerically approximated by

$$q(L, n\Delta t) = \Delta t \sum_{j=1}^n p(L, (n-j)\Delta t) Z^{-1}(j). \quad (4.103)$$

4.5 Numerical Solution

The system of equations Eq. (4.27) and Eq. (4.28) is solved using the Ritchmeyer two-step Lax-Wendroff scheme. This requires that the system be written in conservation form

$$\frac{\partial}{\partial t} \mathbf{U} + \frac{\partial}{\partial x} \mathbf{R} = \mathbf{S}. \quad (4.104)$$

The pressure gradient can be expanded as

$$\begin{aligned} \frac{\partial p}{\partial x} &= \frac{\partial p}{\partial A} \frac{\partial A}{\partial x} + \frac{\partial p}{\partial A_0} \frac{\partial A_0}{\partial r_0} \frac{dr_0}{dx} + \frac{\partial p}{\partial \beta_w} \frac{d\beta_w}{dr_0} \frac{dr_0}{dx}, \\ &= \frac{\partial p}{\partial A} \frac{\partial A}{\partial x} + 2\pi r_0 \frac{\partial p}{\partial r_0} \frac{dr_0}{dx} + \frac{\partial p}{\partial \beta_w} \frac{\partial \beta_w}{\partial x} \end{aligned} \quad (4.105)$$

where we utilize

$$\frac{\partial A_0}{\partial x} = \frac{\partial A_0}{\partial r_0} \frac{dr_0}{dx} = 2\pi r_0 \frac{dr_0}{dx}. \quad (4.106)$$

To capture all partial derivatives with respect to x , we define

$$B = \frac{1}{\rho} \int_{A_0}^A A' \frac{\partial p}{\partial A'} dA'. \quad (4.107)$$

For the tube law given in Eq. (4.39), we get

$$\begin{aligned} B &= \frac{1}{\rho} \int_{A_0}^A A' \left(\frac{1}{2} \beta_w \sqrt{\frac{A_0}{A^3}} \right) dA' \\ &= \frac{\beta_w}{\rho} (\sqrt{AA_0} - A_0). \end{aligned} \quad (4.108)$$

The second constitutive equation, Eq. (4.42), gives

$$\begin{aligned} B &= \frac{1}{\rho} \int_{A_0}^A A' \left(\frac{1}{2\beta_w} \frac{1}{\sqrt{A'A_0}} \right) dA' \\ &= \frac{\beta_w}{3\rho} \left(\sqrt{\frac{A^3}{A_0}} - A_0 \right). \end{aligned} \quad (4.109)$$

Defining B allows us to write

$$\frac{A}{\rho} \frac{\partial p}{\partial x} = \frac{\partial B}{\partial x} + 2\pi r_0 \frac{\partial p}{\partial r_0} \frac{dr_0}{dx} + \frac{\partial p}{\partial \beta_w} \frac{\partial \beta_w}{\partial x} \quad (4.110)$$

$$= \frac{\partial B}{\partial x} - B_{RHS}. \quad (4.111)$$

Using B and B_{RHS} in Eq. (4.104) gives

$$\mathbf{U} = \begin{bmatrix} A \\ q \end{bmatrix}, \quad \mathbf{R} = \begin{bmatrix} 0 \\ \frac{q^2}{A} + B \end{bmatrix} \quad (4.112)$$

$$\mathbf{S} = \begin{bmatrix} 0 \\ -\frac{2\pi \nu R}{\delta} \frac{q}{A} + B_{RHS} \end{bmatrix}. \quad (4.113)$$

The two-step Rithmeyer Lax-Wendroff scheme is second order accurate in space and time [166]. The numerical solution at the new time point $n + 1$, as illustrated in Figure 4.10, is determined by

$$\mathbf{U}_m^{n+1} = \mathbf{U}_m^n - \frac{\Delta t}{\Delta x} (\mathbf{R}_{m+1/2}^{n+1/2} - \mathbf{R}_{m-1/2}^{n+1/2}) + \frac{\Delta t}{2} (\mathbf{S}_{m+1/2}^{n+1/2} + \mathbf{S}_{m-1/2}^{n+1/2}) \quad (4.114)$$

where n is the current time step and m is the spatial step. The alf-spatial step values at $M + 1/2$ and $M - 1/2$ are determined using

$$\mathbf{U}_{m+1/2}^{n+1/2} = \frac{1}{2} (\mathbf{U}_{m+1}^n + \mathbf{U}_m^n) - \frac{\Delta t}{2\Delta x} (\mathbf{R}_{m+1}^n - \mathbf{R}_m^n) + \frac{\Delta t}{4} (\mathbf{S}_{m+1}^n - \mathbf{S}_m^n) \quad (4.115)$$

$$\mathbf{U}_{m-1/2}^{n+1/2} = \frac{1}{2} (\mathbf{U}_m^n + \mathbf{U}_{m-1}^n) - \frac{\Delta t}{2\Delta x} (\mathbf{R}_m^n - \mathbf{R}_{m-1}^n) + \frac{\Delta t}{4} (\mathbf{S}_m^n - \mathbf{S}_{m-1}^n). \quad (4.116)$$

In this dissertation, the equations are solved in non-dimensional form, as described in Appendix A. Boundary conditions utilizing this scheme require “ghost points,” which are explained in the Appendix B.1 and Appendix B.2.

4.6 Wave intensity analysis

The ejection of blood out of the ventricles leads to wave propagation, where both flow and pressure energies are transmitted down the vascular tree. Waves reaching junction points propagate backward

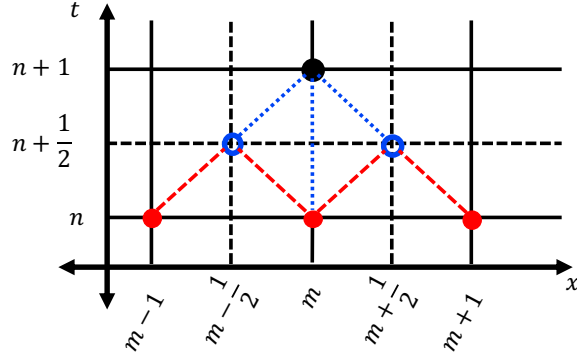


Figure 4.10 Depiction of the Lax-Wendroff method for interior points. The previous time point n (denoted in red) are used with the half-time steps (in blue) to predict the next time point at $n + 1$ (black).

as reflections. In normotensive physiology, backward, reflected waves are minimal, and nearly all waves are transmitted to the periphery. When arteries stiffen, wave propagation speed increases and causes amplified reflections. If backward traveling reflected waves meet oncoming forward waves, there can be *wave augmentation*, elevating blood pressure (see Figure 4.11). PH is known to cause mismatches in vascular properties, leading to pulmonary arterial wave reflections [244]. PH induces wall stiffening, leading to an increased pulse wave velocity, wave augmentation, and RV afterload [252].

One way to study the impact of disease is by decomposing pulse wave propagation into the transmitted and reflected parts, called wave-intensity analysis (WIA). This method quantifies both forward and backward propagating waves and their effects on proximal hemodynamics using a linearized version of Eq. (4.27) and Eq. (4.28) in the absence of viscous forces [188]. The pressure and velocity wavefronts dp and du , are determined from a hyperbolic system using Riemann's method of characteristics [171]. The characteristic paths are

$$u \pm c, \quad c^2 = \frac{A}{\rho} \frac{\partial p}{\partial A} \quad (4.117)$$

where c is the pulse wave velocity. Using Eq. (4.39) or Eq. (4.42) gives

$$c = \sqrt{\frac{2\beta_w}{3\rho} \left(\frac{A}{A_0}\right)^{1/4}}, \quad \text{or} \quad c = \sqrt{\frac{2\beta_w}{3\rho} \left(\frac{A_0}{A}\right)^{1/4}}. \quad (4.118)$$

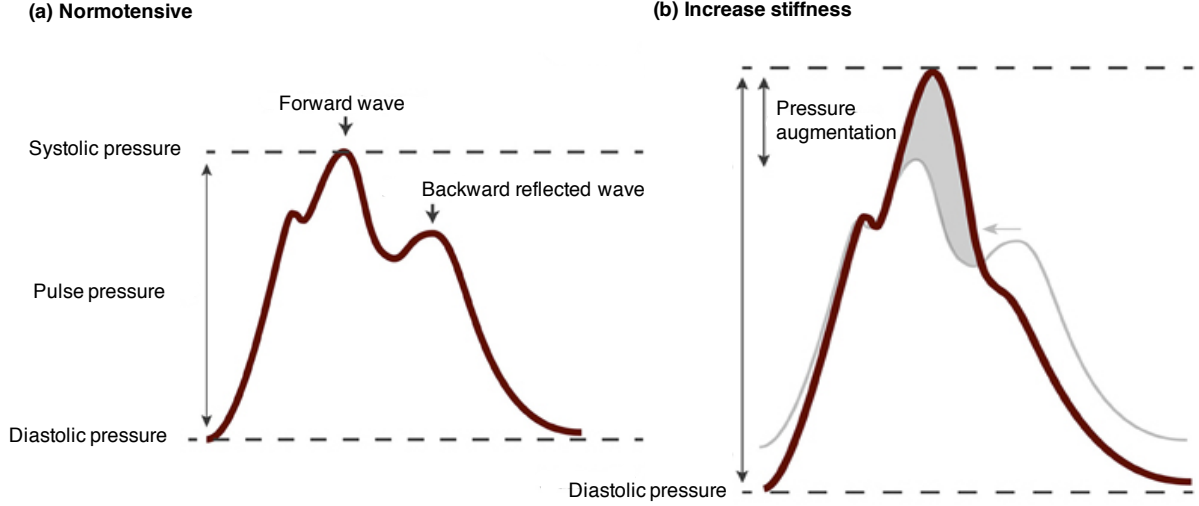


Figure 4.11 Schematic of increased wave reflections in disease. (A) A normotensive pressure waveform is composed of a forward traveling wave that propagates before the backward, reflected wave arrives. (B) Stiffer arteries increase the speed of wave propagation and cause a backward wave to occur during forward propagation, augmenting the pressure wave. Reproduced and modified from [243] with permission.

Under the assumption that $u = 0$ at diastole, the Riemann invariants R_{\pm} are

$$\begin{aligned}
 R^{\pm} &= u \pm \int_{A_0}^A \frac{c(A')}{A'} dA' \\
 &= u \pm \int_{A_0}^A \left(\frac{A'}{\rho c} \frac{\partial p}{\partial A'} \right) \frac{1}{A'} dA' \\
 &= u \pm \int_{p_0}^p \frac{1}{\rho c} dp', \tag{4.119}
 \end{aligned}$$

using Eq. (4.117). WIA represents pressure, flow, and velocity waveforms as successive wavefronts, and decomposes the waveform into unique wave types [172]. Using R^{\pm} , the pressure and velocity wavefronts are

$$\begin{aligned}
 dR^{\pm} &= du \pm \frac{dp}{\rho c} \\
 \implies dp^{\pm} &= \frac{1}{2} (dp \pm \rho c du) \tag{4.120}
 \end{aligned}$$

$$du^{\pm} = \frac{1}{2} \left(du \pm \frac{dp}{\rho c} \right). \tag{4.121}$$

The discrete forward and backward pressure and velocity waves can then be calculated as

$$p^{\pm} = p(t_0) + \sum_{t_1}^{t_N} dp^{\pm} \quad (4.122)$$

$$u^{\pm} = u(t_0) + \sum_{t_1}^{t_N} du^{\pm} \quad (4.123)$$

where $t_0 = 0$ is at the end of diastole.

The sign of these wave elements are used to classify them as accelerating ($du > 0$) or decelerating ($du < 0$) waves and compression ($dp > 0$) or expansion ($dp < 0$) waves. The product $WI = du dp$ is the wave intensity, and has units of energy flux per unit area corresponding to acoustic intensity [171]. To account for signal discretization, the time-normalized wave intensities [188]

$$WI^{\pm} = \frac{\delta p^{\pm}}{\delta t} \frac{\delta u^{\pm}}{\delta t}, \quad (4.124)$$

are used, where δp and δu are the discretized pressure and velocity wavefronts, WI^+ is the forward wave intensity, and WI^- is the backward wave intensity. A summary of the wave types are provided in Table 4.1. Figure 4.12 shows decomposed wavefronts, pressure and velocity waveforms, and WIA results for one of the normotensive mice from Section 2.5. It is imperative to note that the assumptions of WIA are a limitation, as arterial flow is not strictly inviscid [188].

Table 4.1 Classification of wave fronts and wave types.

du	wave type	dp	wavefront	dI	wave type
+	accelerating	+	compression	+	forward compression waves (FCW)
−	decelerating	+	compression	−	backward compression waves (BCW)
+	accelerating	−	expansion	−	forward decompression waves (FEW)
−	decelerating	−	expansion	+	backward expansion waves (BEW)

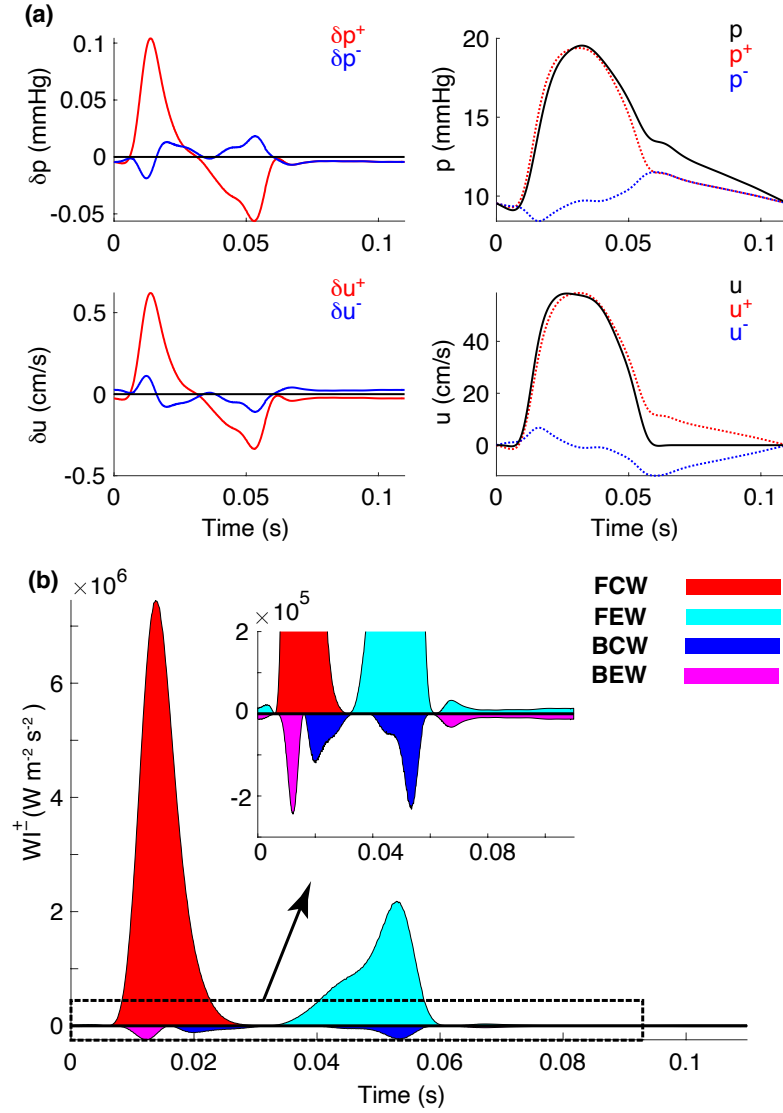


Figure 4.12 Wave intensity analysis for a normotensive control mouse. (a) Separation of the pressure (top row) and velocity (bottom row) waveforms into their wavefronts (left column) and the forward and backward running composite signals (right column). (b) Wave intensity results, showing forward compression (FCW) and expansion (FEW) waves as well as backward compression (BCW) and expansion (BEW) waves.

CHAPTER

5

PARAMETER INFERENCE AND UNCERTAINTY QUANTIFICATION

This chapter introduces mathematical and statistical aspects of inverse problems. Both frequentist and Bayesian parameter estimation methods are described and utilized in this work. The 1D hemodynamics model includes (1) parameters specifying the large artery geometry, (2) parameters describing properties of the blood and vascular wall, and (3) boundary condition parameters. Calibrating the model to measured data requires parameter inference, and some parameters are unidentifiable given the specific model and available data. This chapter gives an overview of model analysis and uncertainty quantification techniques.

Section 5.1 gives an overview of inverse problems and the general statistical theory for these problems. Section 5.2 covers the mathematical formulation of local and global sensitivity analyses. Section 5.3 discusses techniques for parameter identifiability, and Section 5.4 summarizes inference techniques. Lastly, Section 5.5 provides an overview of the methodologies for forward and inverse uncertainty quantification.

5.1 Inverse problems

Consider some measured data $\mathbf{y} \in \mathbb{R}^N$, and a mathematical model $f(t, x; \boldsymbol{\theta})$ that depends on time t , space x , and a set of physically relevant parameters $\boldsymbol{\theta} \in \mathbb{R}^{\mathcal{P}}$. The goal of an *inverse problem* is to ascertain information about the parameters $\boldsymbol{\theta}$ contributing to the data generating process. The inverse problem requires (1) observed data, (2) a mathematical model of the physical system, and

(3) statistical model for the measurement noise. There are two statistical frameworks for addressing the inverse problem.

In *frequentist statistics*, the measured data are realizations from a random process, and the parameters are fixed but unknown. The goal is to minimize the expected loss, (the mismatch between the model and \mathbf{y}) over all possible data, called the *risk*. In practice, the expectation is approximated using estimators, e.g., the maximum likelihood estimator, and then minimized. The uncertainty in the frequentist parameter estimate is determined by the *sampling distribution* of the estimator [154].

In *Bayesian statistics*, $\boldsymbol{\theta}$ is modeled as a random variable and has a distribution, determined using the fixed, known data. This idea stems from *Bayes' rule*; suppose the joint distribution of the model f is

$$p(\boldsymbol{\theta}, \mathbf{y}) = \pi_0(\boldsymbol{\theta}) \pi(\mathbf{y}|\boldsymbol{\theta}), \quad (5.1)$$

where $\pi_0(\boldsymbol{\theta})$ is the prior knowledge (i.e., density) for $\boldsymbol{\theta}$, and $\pi(\mathbf{y}|\boldsymbol{\theta})$ is the sampling distribution of the data. Bayes' rule states that the posterior density $\pi(\boldsymbol{\theta}|\mathbf{y})$ of the parameters conditioned on the data is

$$\pi(\boldsymbol{\theta}|\mathbf{y}) = \frac{\pi(\mathbf{y}|\boldsymbol{\theta}) \pi_0(\boldsymbol{\theta})}{\pi(\mathbf{y})} = \frac{\pi(\mathbf{y}|\boldsymbol{\theta}) \pi_0(\boldsymbol{\theta})}{\int_{\mathbb{R}^D} \pi(\mathbf{y}|\boldsymbol{\theta}) \pi_0(\boldsymbol{\theta}) d\boldsymbol{\theta}}. \quad (5.2)$$

This expression depends on the likelihood of the observed data given the parameters, $\pi(\mathbf{y}|\boldsymbol{\theta})$, and the marginal density of the data $\pi(\mathbf{y})$, also called the normalization constant. The goal of the Bayesian inverse problem is still to minimize the expected mismatch between the model and \mathbf{y} , but by constructing the posterior distribution $\pi(\boldsymbol{\theta}|\mathbf{y})$. The normalization factor, $\pi(\mathbf{y})$, is approximated by integrating over all possible joint densities. Samples from the posterior can be generated numerically using techniques like Markov chain Monte Carlo (MCMC), sequential Monte Carlo, expectation propagation, or the Laplace approximation [78, 112].

A common statistical model is

$$y_i = f(t_i, x; \boldsymbol{\theta}) + \epsilon_i, \quad i = 1, 2, \dots, N. \quad (5.3)$$

The above formulation assumes that the measurement errors, ϵ_i , are independent and identically distributed (iid). The errors are additive and assumed to be normally distributed with zero mean and variance σ_ϵ^2 , or $\epsilon_i \sim \mathcal{N}(0, \sigma_\epsilon^2)$.

Herein, we define the *residual*, the difference between the observed data and the mathematical model, and the scalar valued *cost functional* as

$$r_i(\boldsymbol{\theta}) = y_i - f(t_i, x; \boldsymbol{\theta}), \quad \text{for } i = 1, 2, \dots, N, \quad (5.4)$$

$$J(\boldsymbol{\theta}) = \mathbf{r}(\boldsymbol{\theta})^\top \mathbf{r}(\boldsymbol{\theta}). \quad (5.5)$$

Cardiovascular inverse problems using 3D [63, 143, 144], 1D [173, 186, 191], and 0D models [49,

80, 165] have been previously pursued. The computational complexity of 3D hemodynamics models requires innovative, cost efficient multi-fidelity or surrogate methods for inference. The study by Marsden et al. [144] determined optimal cardiovascular geometries for 3D flow simulations using a derivative free, surrogate mangement framework to overcome computational costs of explicit optimization. Moghadam and colleagues [63] determine optimal shunt placement for congenital heart disease Norwood surgery. Using 3D finite element model of the aorta and pulmonary arteries coupled to a 0D model of the heart and rest of the circulatory system, the authors determined the optimal shunt angle and diameter for the Norwood procedure. The reduced computational cost of 1D and 0D models makes direct gradient based optimization feasible for subject-specific parameter inference. Qureshi et al. [191] inferred 1D model parameters in normotensive and hypertensive mice. The study by Geringer et al. [80] estimated Windkessel parameters in rats during PAH progression, correlating increased vascular resistance with disease progression. MCMC methods capturing parameter posteriors have also been used [46, 173, 175, 186], which naturally provide measures of uncertainty in the parameter and output space. It is important to note that the above formulations do not consider *model discrepancy*, which accounts for missing physics in the modeling framework [117]. This topic is addressed by Paun et al. [175] in the context of the 1D model from Section 4.1, and show that parameter posteriors are biased and that output uncertainty is underestimated when disregarding model discrepancy. The reader is referred to [117, 221] for more details regarding model discrepancy.

5.2 Sensitivity analyses

Sensitivity analysis quantifies the parameter influence with respect to a quantity of interest, and are divided into two categories. *Local sensitivity* analysis approximates model sensitivity to the parameters in a small neighborhood around a nominal value. Local sensitivity analyses vary parameters one at a time. In contrast, *global sensitivity* analyses estimate model sensitivity throughout the admissible parameter space, varying multiple factors at a time [221]. This study uses both analyses to deduce influential, identifiable hemodynamic parameters.

5.2.1 Local sensitivity

Derivative-based sensitivity analysis approximates the partial derivative of the quantity of interest with respect to the parameters. Assume that $f(t, x; \theta)$ is the quantity of interest. The sensitivity $S_i(t_j, x; \theta)$ with respect to θ_i is defined as

$$S_i(t_j; \theta) = \frac{\partial f(t_j, x; \theta)}{\partial \theta_i}, \quad i = 1, \dots, \mathcal{P}, \quad j = 1, \dots, N, \quad (5.6)$$

where t_j is the j -th time point. The sensitivity matrix $S(t; \theta)$ is constructed by appending all the $N \times 1$ sensitivity vectors $S_i(t; \theta)$. For inverse problems, a similar approach can be applied to the residual $r(\theta)$ or cost functional $J(\theta)$. The two methods for computing local sensitivities are *adjoint*

methods and *forward sensitivity methods* [60, 88, 163].

Adjoint method. Let $J(u(\theta), t, x; \theta)$ be the cost functional that depends on the model states u , time, space, and the parameters. Define $N(u(\theta), t, x; \theta) = 0$ as the set of governing equations (either ODEs or PDEs). The Jacobian of the cost is

$$\nabla J = \frac{\partial J}{\partial \theta} + \frac{\partial J}{\partial u} \frac{du}{d\theta} \quad (5.7)$$

where $\frac{du}{d\theta}$ is the *sensitivity* of the model states with respect to the parameters. Note

$$\frac{dN}{d\theta} = \frac{\partial N}{\partial \theta} + \frac{\partial N}{\partial u} \frac{du}{d\theta} = 0. \quad (5.8)$$

If $\frac{\partial N}{\partial u}$ is invertible, then

$$\frac{du}{d\theta} = \left(\frac{\partial N}{\partial u} \right)^{-1} \left(-\frac{\partial N}{\partial \theta} \right), \quad (5.9)$$

hence

$$\nabla J = \frac{\partial J}{\partial \theta} - \frac{\partial J}{\partial u} \left(\frac{\partial N}{\partial u} \right)^{-1} \left(\frac{\partial N}{\partial \theta} \right). \quad (5.10)$$

Define the vector p

$$p^\top = -\frac{\partial J}{\partial u} \left(\frac{\partial N}{\partial u} \right)^{-1} \Rightarrow p^\top \frac{\partial N}{\partial u} = -\frac{\partial J}{\partial u}, \quad (5.11)$$

which simplifies the gradient equation to

$$\nabla J = \frac{\partial J}{\partial \theta} + p^\top \left(\frac{\partial N}{\partial \theta} \right). \quad (5.12)$$

Equation 5.11 is the *adjoint equation* and can be used to determine the gradient as follows:

1. Solve the system of equations $N(u(\theta), t, x; \theta) = 0$ for the states $u(\theta)$.
2. Solve the adjoint problem in Eq. (5.11) for p .
3. Calculate the gradient in Eq. (5.12).

Using this approach, one model evaluation and one adjoint solve determine the gradient of J . The adjoint method is beneficial for expensive models, requiring only one solution of the state equation in contrast to finite difference methods requiring multiple forward solves. Adjoint equations are typically simpler than the state equations, e.g. nonlinear PDE systems have linear adjoints [178]. Adjoint equations are derived analytically and arise from rewriting the constrained optimization problem as a Lagrange multiplier problem [88]. This approach has been utilized in cardiovascular hemodynamics. The study by Ismail et al. [109] determine Windkessel parameters coupled to a 3D-FSI model using an adjoint approach, showing improved parameter convergence. Melani [147] derived adjoint equations for 1D fluid dynamic equations, and inferred the stiffness parameter for single vessels and a network model.

Forward sensitivity methods. When adjoint solvers are not available, *forward sensitivity* methods can be used. Equation 5.9 is the *forward sensitivity equation*, and for simpler models can be derived analytically. If not, the sensitivity of the model output can be approximated using either *automatic differentiation* or *finite difference* methods. *Automatic differentiation* utilizes ideas from calculus, namely the chain rule, to decompose the derivative into forward or backward accumulations of simpler derivatives known. These algorithms are *exact* and do not incur floating-point arithmetic errors from approximations. A detailed summary of these methods for MATLAB is provided by Neidinger [160]. This is a fundamental technique in machine learning, where back propagation enables efficient gradient computation [78].

This work utilizes finite difference approximations for derivative based sensitivity. The centered finite difference method

$$\frac{\partial f}{\partial \theta_i} \approx \frac{f(t, x; \theta + \mathbf{e}_i \psi) - f(t, x; \theta - \mathbf{e}_i \psi)}{2\psi}, \quad (5.13)$$

is used, where $\psi = \sqrt{h}$ [60, 106], h step-size of the ODE or PDE numerical discretization, and \mathbf{e}_i is a unit vector in the i -th direction.

Parameters of different orders of magnitude can skew the interpretation of which parameters are more influential. To make sensitivities of similar magnitude, the log-scaled parameters $\tilde{\theta} = \log(\theta)$ (or $-\log(|\theta|)$ for negative parameters) can be used

$$\tilde{S}_i(t; \theta) = \frac{\partial f(t, x; \theta)}{\partial \tilde{\theta}_i} = \frac{\partial f(t, x; \theta)}{\partial \theta_i} \theta_i, \quad i = 1, \dots, \mathcal{P}. \quad (5.14)$$

The advantage of log-scaling is that sensitivities retain the original units of f . If the quantity of interest has multiple outputs, it may be advantageous to scale the sensitivity by f ,

$$\frac{\partial \tilde{f}(t, x; \theta)}{\partial \tilde{\theta}_i} = \left(\frac{\theta_i}{f(t, x; \theta)} \right) \frac{\partial f}{\partial \theta_i}. \quad (5.15)$$

To rank parameters from most- to least-influential for parameter fixing, the 2-norm of the sensitivity is used

$$\overline{S}_i = \|\tilde{S}_i\|_2. \quad (5.16)$$

Parameters corresponding to a value of \overline{S}_i less than some threshold are considered non-influential and can be fixed. Alternatively, non-influential parameters can be used to simplify or reduce the model [194].

5.2.2 Global sensitivity

Global sensitivity analyses quantify output uncertainty by sampling parameters throughout the feasible parameter space. Two common approaches are Morris screening [153], which provide a coarse approximation of the model sensitivity, and Sobol' indices [205], a variance based global sensitivity approach.

5.2.2.1 Morris screening

Morris' screening involves the computation of "elementary effects", the relative change of the model output with respect to a change in parameter value. The effects of θ_i on the output quantity are classified as a) negligible overall, b) linear and additive, or c) having nonlinear effects or higher order interactions with other parameters. To perform this analysis, parameters are mapped from their bounded parameter space $\Omega^{\mathcal{P}}$ to the unit hypercube $[0, 1]^{\mathcal{P}}$, where \mathcal{P} denotes number of parameters analyzed. Using a uniform, bounded prior distribution restricts the model analysis to a physiologically relevant parameter subspace without invoking a bias. The elementary effects are computed as

$$d_i(t; \theta) = \frac{f(t; \theta + \mathbf{e}_i \Delta) - f(t; \theta)}{\Delta}. \quad (5.17)$$

The step size Δ is chosen from the set $\Delta \in \{1/(\mathcal{M} - 1), 2/(\mathcal{M} - 1), \dots, (\mathcal{M} - 2)/(\mathcal{M} - 1)\}$, where \mathcal{M} denotes the number of parameter perturbations used in the screening method, i.e., the number of possible perturbation sizes. To preserve symmetry of the parameter distributions, \mathcal{M} should be even [221]. The elementary effects are computed by sampling K values from a uniform distribution for the parameter θ_i^j . To compare elementary effects for vector outputs, the 2-norm elementary effects, $\tilde{d}_i^j(\theta) = \|d_i^j(t; \theta)\|_2$, is used.

The elementary effects' mean and variance are obtained by integrating the outcomes from multiple iterations. The modified Morris' indices are calculated as

$$\mu_i^* = \frac{1}{K} \sum_{j=1}^K |\tilde{d}_i^j|, \quad \sigma_i^2 = \frac{1}{K-1} \sum_{j=1}^K (\tilde{d}_i^j - \mu_i^*)^2, \quad (5.18)$$

where μ^* quantifies the individual effect of the input on the output, i.e., the sensitivity of the model with respect to the parameters, while the variance estimate σ^2 describes the variability in the model sensitivity due to parameter interactions or nonlinearity. Parameters with a large μ^* and σ^2 have nonlinear or drastic effects on the model output. Similar inference can be made for other combinations of μ^* and σ^2 . Wentworth et al. [258] proposed a combination of the two metrics, ranking parameter influence using $\sqrt{\mu^{*2} + \sigma^2}$. The randomized Morris algorithm is an efficient algorithm for computing elementary effects and scales the step size Δ by the parameter magnitude (see Algorithm 2 in [165]).

5.2.2.2 Sobol' indices

Variance based methods like Sobol' indices decompose the variance of a quantity of interest into the variances attributed to single parameters and their higher order interactions. Consider the parameters θ with density $\pi(\theta)$, where each parameter i lies within the physiologically admissible parameter space Γ_i . The parameter domain is then $\theta \in \bigcup_{i=1}^{\mathcal{P}} \Gamma_i = \Omega^{\mathcal{P}} \subset \mathbf{R}^{\mathcal{P}}$ (note that we drop the

dependence on x and t for clarity hereon). The expectation and variance of f are defined as

$$E(f(\boldsymbol{\theta})) = \int_{\Omega^{\mathcal{P}}} f(\boldsymbol{\theta}) \pi(\boldsymbol{\theta}) d\boldsymbol{\theta}, \quad (5.19)$$

$$V(f(\boldsymbol{\theta})) = \int_{\Omega^{\mathcal{P}}} (f(\boldsymbol{\theta}) - E(f(\boldsymbol{\theta})))^2 \pi(\boldsymbol{\theta}) d\boldsymbol{\theta} = E(f(\boldsymbol{\theta})^2) - E(f(\boldsymbol{\theta}))^2. \quad (5.20)$$

We are interested in computing the conditional expectation and variance of the quantity interest when a single parameter θ_i is known. Define the operators

$$E_{\theta_{\sim i}}(f(\boldsymbol{\theta}|\theta_i)) = \int_{\Omega^{\mathcal{P}-1}} f(\boldsymbol{\theta}|\theta_i) \pi(\boldsymbol{\theta}) d\boldsymbol{\theta}, \quad \Omega^{\mathcal{P}-1} = \Omega^{\mathcal{P}} \setminus \Gamma_i, \quad (5.21)$$

which does not include θ_i , and the partial variances

$$V_{\theta_i} = V(E_{\theta_{\sim i}}(f|\theta_i)). \quad (5.22)$$

The above expression measures the variance of the expected value of the quantity of interest, conditioned on the fixed, known parameter θ_i . From this we define the *first order sensitivity measure*

$$S_i = \frac{V_{\theta_i}}{V(f)}. \quad (5.23)$$

The *total effect index* is

$$S_{T_i} = \frac{E_{\theta_{\sim i}}(V_{\theta_i}(f|\theta_{\sim i}))}{V(f)} = 1 - \frac{V_{\theta_{\sim i}}(E_{\theta_i}(f|\theta_{\sim i}))}{V(f)}. \quad (5.24)$$

The first order effects describe the influence of a single parameter on the variance of the quantity of interest. By definition, $\sum_i S_i \leq 1$, hence the difference $1 - \sum_i S_i$ describes the variance of the output attributed to higher order parameter interactions. The difference $S_{T_i} - S_i$ for θ_i quantifies the higher order effects attributed to that parameter, and $S_i = S_{T_i}$ implies only first-order effects.

The majority of prior work with time-dependent output have averaged the Sobol' indices over the time interval [221]. However, more recent work has focused on developing Sobol' indices for time-dependent output. Alexanderian et al. [7] define a *generalized Sobol' index* that accounts for the time history of evolutionary processes. Randall et al. [194] constructed a *limited memory Sobol' index*, which computes variance estimates within a fixed window of time based on the physical system's traits. These approaches are an active area of research and seek to mitigate averaging or point-wise computation effects that misconstrue model sensitivity.

5.3 Parameter identifiability

Determining whether a parameter is influential on the model output or quantity of interest is a component of *parameter identifiability*. As detailed by Miao [150], unidentifiability is separated into two types:

1. *Structural unidentifiability*. The parameters θ are structurally unidentifiable if the mapping from the model framework to the quantity of interest χ , $\mathcal{C} : f(t, x; \theta) \rightarrow \chi$, is non-injective, i.e. $\mathcal{C}(f(t, x; \theta^1)) = \mathcal{C}(f(t, x; \theta^2)) \not\Rightarrow \theta^1 = \theta^2$.
2. *Practical unidentifiability*. The parameters θ are practically unidentifiable if the mapping from the model to a finite **measured** quantity of interest y , is non-unique or non-injective.

The former characterizes the model-to-output mapping, independent of data or measurement error. The latter include stems from insufficient data or large measurement error [196]. These definitions are directly related to the quantity of interest and change if \mathcal{C} is altered.

Parameter unidentifiability leads to non-unique minima during parameter estimation [167, 182]. Unidentifiable parameters can also cause gradient based optimization to fail when the parameter Jacobian is singular [60]. Unidentifiable or correlated parameters also affect Bayesian inference methods. Correlated parameters sampling inefficiencies, requiring more realizations to construct the true posterior [78]. The goal of patient-specific modeling is to identify informative physiometers of disease. This goal is only achieved if the model parameters corresponding to the physiometers are identifiable [191]. Parameter unidentifiability is addressed using local or global analyses. The former include *asymptotic-linear analyses* and *profile-likelihood* approaches, whereas the latter include *global sensitivity* approaches or *posterior analyses*.

Asymptotic-linear analyses. Asymptotic analyses use local sensitivities to construct the Fisher information matrix, $\mathbf{F} = \mathbf{S}^\top \mathbf{S}$ [39]. In this framework, the error variance estimator s^2 is

$$s^2 = \frac{1}{N - \mathcal{P}} \mathbf{r}^\top \mathbf{r}. \quad (5.25)$$

An asymptotic covariance matrix, \mathbf{C} , of the parameter sampling distribution, and correlation matrix \mathbf{c} is then determined by

$$\mathbf{C} = s^2 \mathbf{F}^{-1}, \quad c_{ij} = \frac{C_{ij}}{\sqrt{C_{ii} C_{jj}}} \quad (5.26)$$

where $-1 \leq c_{ij} \leq 1$ for $i, j = 1, \dots, \mathcal{P}$. As in previous studies [60, 142, 182], the correlation matrix provides information about the pairwise relationships between parameters; the higher the correlation (e.g., $|c_{ij}| \rightarrow 1$) the more difficult it is to estimate parameters i and j simultaneously. For this reason, a parameter cutoff, $|c| < \gamma$, is used to fix parameters so that others can be estimated. This technique can lead to several parameter subsets, the best of which can be chosen using information criteria [48].

Note that F must be invertible to use this analysis, and a large condition number for the matrix suggests that parameters are not independent in their effects. Other local subset selection methods include the SVD-QR [167], orthogonal sensitivities [165], and eigenvalue-eigenvector subset selection [150, 221]. The review by Miao et al. [150] provides additional local-based, identifiability methods.

Profile likelihood. A robust but computationally expensive technique for identifiability analysis is profile-likelihood calculations [196]. The methods “profiles” a single parameter θ_i by fixing the parameter at a given value while inferring all other parameters $\theta_{\sim i}$. The resulting vector of cost (or likelihood) values can be used to construct so-called “likelihood-based” confidence intervals

$$\text{CI}_{\text{PL}}(\hat{\theta}_i) = \{\theta_i \mid J^* - J(\hat{\theta}_i; \theta_{\sim i}) < \Delta_\alpha\} \quad (5.27)$$

where J^* is the minimum cost (or maximum likelihood) found during the procedure and Δ_α is the α -quantile from a χ^2 distribution with \mathcal{D} degrees of freedom ($\theta \in \mathbb{R}^p$). Raue et al. [196] showed that profile-likelihood reveals structural unidentifiabilities not captured by local sensitivity approaches.

Global sensitivity approach. Sobol’ indices can also be used to determine which parameters are identifiable. Note that by definition if $S_{T_i} = 0$, then

$$\begin{aligned} \Rightarrow 1 &= \frac{V_{\theta_{\sim i}}(E_{\theta_i}(f|\theta_{\sim i}))}{V(f)} \\ \Rightarrow V_{\theta_{\sim i}}(E_{\theta_i}(f|\theta_{\sim i})) &= V(f). \end{aligned} \quad (5.28)$$

Hence, $S_{T_i} \approx 0$ means that parameter i does not affect the variance of the quantity of interest and can be fixed before performing parameter estimation [59, 231].

Posterior density. The posterior density obtained from MCMC can detect parameter unidentifiability [175, 214]. In particular, a uniform posterior distribution with no (or infinite) modality suggests that a parameter is non-influential on the likelihood, and is therefore not uniquely identifiable given the data. The study by Siekmann et al. [214] used convergence plots from MCMC to determine unidentifiable parameters in a stochastic model of ion channels. Pairwise plots of the parameter posteriors may also show linear or non-linear interactions between parameter pairs, as shown at the end of this chapter and in Chapter 7 [46]. Pairwise posteriors that show a functional dependence between two parameters may conclude practical non-identifiability.

5.4 Parameter inference

Patient-specific parameters can be determined by minimizing a cost-functional, such as the residual sum of squares

$$J(\theta) = \frac{1}{2} \mathbf{r}(\theta)^\top \mathbf{r}(\theta) \quad (5.29)$$

with \mathbf{r} defined in Eq. (5.4). If the goal is to match multiple outputs to data, the weighted or relative cost can be used

$$\tilde{J}(\boldsymbol{\theta}) = \mathbf{r}^\top \mathbf{W} \mathbf{r}, \quad (5.30)$$

where $\mathbf{W} = \text{diag}(\mathbf{y}^{-2})$ is a matrix of squared reciprocal data [48, 49, 194].

Alternatively, one could maximize a likelihood function, e.g., in the case of additive, iid errors, $\epsilon_i \sim \mathcal{N}(0, \sigma_\epsilon^2)$, the likelihood function is given by

$$L(\boldsymbol{\theta}, \sigma_\epsilon^2) = (2\pi\sigma_\epsilon^2)^{-n/2} e^{-J(\boldsymbol{\theta})/\sigma_\epsilon^2}. \quad (5.31)$$

Since most optimization packages perform *minimization*, it is common to use the negative log-likelihood. For Eq. (5.31) this gives

$$-\log(L) = \frac{n}{2} \log(2\pi) + \frac{n}{2} \log(\sigma_\epsilon^2) + \frac{1}{\sigma_\epsilon^2} J(\boldsymbol{\theta}). \quad (5.32)$$

5.4.1 Optimization

Optimization frameworks are split into global and local methods. *Global optimization* tries to determine the global minimizer of an objective function by searching throughout the admissible parameter space. These include simulated annealing, particle swarm methods, genetic algorithms, and Bayesian optimization [274]. *Local optimization* methods search for minima on a more concise, closed parameter space. These methods are broken into *gradient* and *gradient-free* methods. Gradient-free methods, including interpolation (e.g., nearest neighbors) and direct search methods (e.g., the Nelder-Mead or Hooke-Jeeves algorithm), search within a local neighborhood of a current parameter iterate by testing for improvements in $J(\boldsymbol{\theta})$ [116]. In this work, gradient-based local optimization methods are used.

Gradient based methods include first- and second-order methods; the former only utilize the gradient, whereas the latter utilize information about the curvature of the objective function. In the absence of analytical gradients, finite difference methods are used. For this reason, problems with large parameter dimensionality (such as neural networks in machine learning) utilize first-order methods. Second order methods determine the curvature of the objective function using the Hessian matrix. Newton's method constructs the Hessian explicitly, requiring more model solves to approximate but can converge quadratically close to the optimum. The approximate Hessian can also be determined using *quasi-Newton* methods, such as Broyden's method or Broyden-Fletcher-Goldfarb-Shanno (BFGS) algorithm. If the dimensionality of the system is too large to store the Hessian, matrix free methods, such as the conjugate gradient method, can be used to conjugate the Newton search direction [162]. Below is a more detailed description of line-search methods.

For first order methods, the gradient $g(\theta)$ of the cost function $J(\theta)$ with respect to the parameters is

$$g(\theta) = -(\nabla_{\theta} f)^{\top} (y - f(t, x; \theta)) = -S^{\top} r(\theta), \quad (5.33)$$

where S is the sensitivity vector. In the case of gradient descent, each parameter iterate is computed as

$$\theta^{k+1} = \theta^k - \lambda \nabla_{\theta} J(\theta^k), \quad (5.34)$$

where λ is the step length. Gradient based methods are sensitive to the initial guess θ^0 . When initial θ^0 are far from the optimum, the residual can become large and lead to over-stepping when λ is not controlled.

Line-search methods overcome this issue. A backtracking-line search that satisfies the Armijo (sufficient decrease) conditions

$$J(\theta^k + \lambda g) \leq J(\theta^k) + c g(\theta^k)(\theta^{k+1} - \theta^k), \quad (5.35)$$

where $c \in (0, 1)$ is one line-search method. Typically, $c \approx 10^{-4}$. In a backtracking line search, we start with $\lambda_0 = 1$ and try a full Newton step. If Eq. (5.35) is not satisfied, set $\lambda = \lambda_0 \cdot \xi$, where $\xi \in (0, 1)$. The routine continues with $\lambda = \lambda \cdot \xi$ until the Eq. (5.35) is satisfied. Safeguarding and polynomial based step-length control can be used to ensure λ is not too small (see Appendix B.4 for details in regard to web-like lesions). A basic Armijo-backtracking linesearch algorithm is provided in Algorithm 3. This is utilized for the root-finding problems related to the structured tree boundary conditions and web-like lesions (see Appendix B.2) [47].

Algorithm 3: General gradient descent with Armijo line search.

Input: $J, \theta^k, p^k = -g(\theta^k), \lambda_0$, and ∇f
Initialize $\lambda = \lambda_0, \xi \in (0, 1), c \in (0, 1)$.
Compute $J(\theta^k), J(\theta^k + \lambda p^k)$ and $g = \nabla J(\theta^k)$
while $J(\theta^k + \lambda p^k) > J(\theta^k) + c \lambda g^T(\theta^k) p^k$ **do**
 $\lambda = \lambda \cdot \xi$
 Compute $J(\theta^k + \lambda p^k)$
end
 $\theta^{k+1} = \theta^k + \lambda p^k$
Output: New iterate θ^{k+1}

5.4.2 Marko chain Monte Carlo (MCMC)

For Bayesian inference, both sampling methods, including MCMC, or analytical methods, such as the Laplace approximation or variational Bayesian inference [78, 112]. In this work, MCMC is used.

A Markov chain is a sequence of random variables that satisfy the Markov property

$$P(\boldsymbol{\theta}^{i+1} | \boldsymbol{\theta}_i, \boldsymbol{\theta}^{i-1}, \dots, \boldsymbol{\theta}_1) = P(\boldsymbol{\theta}^{i+1} | \boldsymbol{\theta}_i), \quad (5.36)$$

i.e., the probability of $\boldsymbol{\theta}^{i+1}$ conditioned on the prior iterate history only depends on the current iterate $\boldsymbol{\theta}^i$. The most popular MCMC algorithms include the *Gibbs sampler*, the *Metropolis-Hastings* algorithm, and the *Adaptive Metropolis* algorithm. This work utilizes the *delayed rejection adaptive Metropolis* (DRAM) algorithm, summarized below and discussed in detail in [186, 221]. The full DRAM algorithm is detailed in Algorithm 4 and utilized in MATLAB [89, 127].

The traditional Metropolis algorithm incorporates an acceptance probability α for the candidate parameter $\boldsymbol{\theta}_{\text{cand}}$ conditioned on the $(k-1)$ -th accepted parameter

$$\alpha(\boldsymbol{\theta}_{\text{cand}} | \boldsymbol{\theta}^{k-1}) = \min \left(1, \frac{\pi(\boldsymbol{\theta}_{\text{cand}} | p_{\text{data}})}{\pi(\boldsymbol{\theta}^{k-1} | p_{\text{data}})} \right) = \min \left(1, e^{-(J(\boldsymbol{\theta}_{\text{cand}}) - J(\boldsymbol{\theta}^{k-1})) / 2(s^{k-1})^2} \right), \quad (5.37)$$

where the proposal distribution for the new parameter value is assumed to be a multivariate, normal distribution with covariance C , and $(s^{k-1})^2$ is the estimated sample variance drawn from an inverse gamma distribution.

The delayed rejection (DR) component of the DRAM algorithm considers a second candidate parameter $\boldsymbol{\theta}_{\text{DR}}$ if the first candidate parameter $\boldsymbol{\theta}_{\text{cand}}$ is not accepted. The second parameter is accepted using the second acceptance probability

$$\begin{aligned} \alpha_{\text{DR}}(\boldsymbol{\theta}_{\text{DR}} | \boldsymbol{\theta}_{\text{cand}}, \boldsymbol{\theta}^{k-1}) &= \min \left(1, \frac{\pi(\boldsymbol{\theta}_{\text{DR}} | p_{\text{data}}) J(\boldsymbol{\theta}_{\text{cand}} | \boldsymbol{\theta}_{\text{DR}}) J(\boldsymbol{\theta}^{k-1} | \boldsymbol{\theta}_{\text{DR}}, \boldsymbol{\theta}_{\text{cand}})}{\pi(\boldsymbol{\theta}^{k-1} | p_{\text{data}}) J(\boldsymbol{\theta}_{\text{cand}} | \boldsymbol{\theta}^{k-1}) J(\boldsymbol{\theta}_{\text{DR}} | \boldsymbol{\theta}^{k-1}, \boldsymbol{\theta}_{\text{cand}})} \cdot \frac{1 - \alpha(\boldsymbol{\theta}_{\text{cand}} | \boldsymbol{\theta}_{\text{DR}})}{1 - \alpha(\boldsymbol{\theta}_{\text{cand}} | \boldsymbol{\theta}^{k-1})} \right) \\ &= \min \left(1, \frac{\pi(\boldsymbol{\theta}_{\text{DR}} | p_{\text{data}}) J(\boldsymbol{\theta}_{\text{cand}} | \boldsymbol{\theta}_{\text{DR}})}{\pi(\boldsymbol{\theta}^{k-1} | p_{\text{data}}) J(\boldsymbol{\theta}_{\text{cand}} | \boldsymbol{\theta}^{k-1})} \cdot \frac{1 - \alpha(\boldsymbol{\theta}_{\text{cand}} | \boldsymbol{\theta}_{\text{DR}})}{1 - \alpha(\boldsymbol{\theta}_{\text{cand}} | \boldsymbol{\theta}^{k-1})} \right). \end{aligned} \quad (5.38)$$

The second line of the above equation utilizes the symmetry of the multivariate normal proposal distribution to simplify the original fraction [221].

Lastly, the adaptive Metropolis (AM) component of the algorithm minimizes the random walk behavior by updating the parameter covariance according to a multivariate, normal distribution. The covariance is adapted after some adaptation length k_0

$$V^k = \begin{cases} V^{k-1} & \text{if } k < k_0 \\ s_p \text{Cov}(\boldsymbol{\theta}_0, \boldsymbol{\theta}^1, \dots, \boldsymbol{\theta}^{k-1}) + \zeta \mathbf{I}_{\mathcal{P}} & \text{if } k = k_0, \end{cases} \quad (5.39)$$

where s_p is a design parameter that depends on the dimension of the parameter vector, $\mathbf{I}_{\mathcal{P}}$ is the $\mathcal{P} \times \mathcal{P}$ identity matrix, and $\zeta \geq 0$ is a small perturbation parameter to ensure that C_k is positive definite. A common choice is $s_p = 2.38^2 \mathcal{P}$.

5.5 Uncertainty quantification

As detailed by Smith [221], there are two main types of uncertainty:

1. *Aleatoric uncertainty* is due to random fluctuations in the physical process, and cannot be reduced by additional physics or experimental insight.
2. *Epistemic uncertainty* is induced by simplifying model assumptions, missing physics in the modeling framework, or numerical errors (e.g., assumptions regarding a simplified mechanistic model).

There are two common approaches for handling uncertainty quantification. *Inverse uncertainty quantification* describes the uncertainty attributed to the inputs (e.g., parameters) given a model and observed data, and *forward uncertainty quantification* measures how uncertainties in input space affect the uncertainties in output space. Each of these can be addressed by methods in frequentist or Bayesian statistics. The frequentist framework constructs parameter estimator confidence intervals and model confidence and predictions intervals using an asymptotic analysis. Bayesian inverse uncertainty quantification utilizes the estimated posterior distribution, while forward propagation constructs credible intervals based on draws from the posterior [221].

5.5.1 Inverse uncertainty quantification

Frequentist methods. Confidence intervals for the model parameter estimators are constructed using an asymptotic analysis. Let $\hat{\theta}$ be the estimator that minimizes the cost function J , with the associated local sensitivity \hat{S} and error variance estimator \hat{s}^2 from Eq. (5.25). For sufficiently large data and iid Gaussian measurement errors $\epsilon_i \sim \mathcal{N}(0, \sigma_\epsilon^2)$, an asymptotic analysis can be used to construct parameter estimator sampling distributions [19]. Specifically, as the number of data $N \rightarrow \infty$, the sampling distribution for θ is a multivariate normal

$$\theta \sim \mathcal{MVN}(\theta^*, C^*), \quad C^* = \sigma_\epsilon^2 F^{-1} \quad (5.40)$$

where θ^* and C^* are the true but unknown parameters and covariance matrix. As in Eq. (5.26), C^* is approximated as the inverse of the Fisher information matrix $\hat{s}^2 \hat{F}^{-1} = \hat{s}^2 (\hat{S}^\top \hat{S})^{-1}$ [19, 154]. The parameter confidence intervals are calculated using the

$$\theta_i^{CI} \equiv \left[\hat{\theta}_i - t_{N-\mathcal{P}}^{1-\alpha/2} \sqrt{C_{ii}}, \hat{\theta}_i + t_{N-\mathcal{P}}^{1-\alpha/2} \sqrt{C_{ii}} \right], \quad (5.41)$$

where $t_{N-\mathcal{P}}^{1-\alpha/2}$ denotes a two-sided t -statistic with $N-\mathcal{P}$ degrees of freedom and a $1-\alpha/2$ confidence level, N is the number of data points, and \mathcal{P} is the number of parameters.

When there is not sufficient data for the asymptotic approach (i.e., N small), one can instead utilize *residual bootstrapping*. This approach starts by estimating $\hat{\theta}$ from the entire data set, saving the residual r_i at each data point. Since r are realizations from a random variable, new synthetic

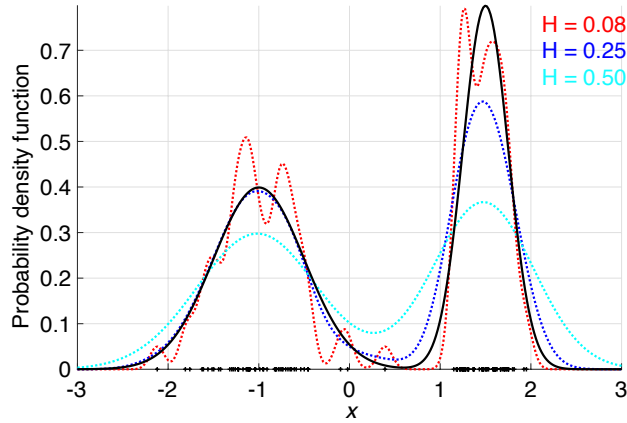


Figure 5.1 Kernel density estimation (KDE) with different bandwidths. Realizations from $x \sim \mathcal{N}(-1, 0.50^2)$ and realizations from $x \sim \mathcal{N}(1.5, 0.25^2)$ are shown as crosses, and the true distribution is shown in black. Note that a smaller bandwidth provides a more narrow kernel at each data point, whereas a large bandwidth tends to oversmooth the PDF.

data realizations can be constructed by

$$y_j^{\text{synth}} = y_j + r_m \quad (5.42)$$

where r_m is a random draw (with replacement) from \mathbf{r} . This can be iterated on multiple times to construct bootstrap estimates of the mean, covariance and standard error [18].

Confidence intervals in the frequentist framework are interpreted as follows: *given numerous experiments, we expect that the true parameter values θ will fall within $1 - \alpha/2\%$ of the constructed the confidence intervals.*

Bayesian methods. Parameter uncertainty can be directly assessed from the posterior distribution. As mentioned, algorithms including MCMC, sequential Monte Carlo, and expectation propagation can approximate the posterior density. To construct a density given the iterates of θ , the continuous version of histogram analysis called kernel density estimation (KDE) [216] is used

$$\pi(x) = \frac{1}{nH} \sum_{i=1}^n K\left(\frac{x - x_i}{H}\right), \quad (5.43)$$

where x_i is the i -th data point, n is the number of samples used for the density estimate, H is the bandwidth parameter (controlling the smoothness of the densities), and K is the kernel function. The most common kernel function (used here) is the Gaussian kernel. The bandwidth H can be determined using various methods, which are detailed in Chapter 8 [45]. Figure 5.1 shows an example problem with a bimodal distribution, and shows how a small bandwidth undersmooths the PDF while a large bandwidth misses the bimodal structure.

Parameter uncertainty is linked to the posterior variance. It is important to note that parameter

posteriors typically parallel the model sensitivity; parameters with relatively wide posteriors are typically less influential than parameters with narrow posteriors and smaller variances. The credible interval of a posterior distribution from the Bayesian perspective is more easily interpreted: *the $1 - \alpha/2\%$ parameter credible interval contains $1 - \alpha/2\%$ of the realizations of said parameter.*

5.5.2 Forward uncertainty propagation

Frequentist methods. The confidence interval for the vector quantity of interest, $f^{CI}(t)$, from a nonlinear model can be computed in a similar fashion to Eq. (7.20). The confidence interval for the mean estimate at time point t_i is

$$f^{CI}(t_i) \equiv \left[f(t_i; \hat{\theta}) - t_{N-\mathcal{P}}^{1-\alpha/2} \hat{s} \sqrt{\Gamma_i}, f(t_i; \hat{\theta}) + t_{N-\mathcal{P}}^{1-\alpha/2} \hat{s} \sqrt{\Gamma_i} \right], \quad (5.44)$$

where $\Gamma_i = G_i^T F^{-1} G_i$ and

$$G_i^T = \left(\frac{\partial f(t_i; \hat{\theta})}{\partial \tilde{\theta}_1}, \dots, \frac{\partial f(t_i; \hat{\theta})}{\partial \tilde{\theta}_{\mathcal{P}}} \right).$$

Lastly, the prediction intervals for the model response are calculated as

$$f^{PI}(t_i) \equiv \left[f(t_i; \hat{\theta}) - t_{N-\mathcal{P}}^{1-\alpha/2} \hat{s} \sqrt{1 + \Gamma_i}, f(t_i; \hat{\theta}) + t_{N-\mathcal{P}}^{1-\alpha/2} \hat{s} \sqrt{1 + \Gamma_i} \right]. \quad (5.45)$$

Bayesian methods. Sampling from the posterior using MCMC can propagate parameter uncertainties to the model output. Since the posterior distribution is typically estimated using non-parametric techniques, one cannot directly sample from the posterior using a parametric distribution. Instead, inverse transform sampling is often used, which utilizes the cumulative distribution function (CDF) and inverse CDF (iCDF). Given a random variable X and PDF $f_X(x)$, the CDF $F_X(x)$ is

$$F_X(x) = \int_{-\infty}^x f_X(x') dx'. \quad (5.46)$$

The iCDF is then $F_X^{-1}(F_X(x)) = x$. Note that $F_X(x) \in [0, 1]$, and both the CDF and iCDF are monotonically increasing functions. The inverse transform sampling procedure is then

1. Generate a draw from the uniform distribution: $u \sim \mathcal{U}(0, 1)$.
2. Compute $x = F_X^{-1}(u)$.

In this manner, non-parametric posterior densities can be sampled from by mapping a uniform random variable realization to the constructed posterior density. This also emphasizes the importance of the bandwidth parameter in KDE, since uncertainty in the posterior is directly linked to the uncertainty in output space.

It is important that parameters are sufficiently sampled so that the output uncertainty has converged. In this study, we perform forward uncertainty propagation using the explicit model. For more expensive models (e.g., 3D fluid dynamics models), this is infeasible, and other strategies

need to be used. Stochastic spectral methods, including stochastic Galerkin, collocation, or discrete projection methods, can speed up uncertainty propagation by representing the quantity of interest as a polynomial expansion [221]. The review by Eck et al. [59] examines these methods in the context of cardiovascular modeling.

5.6 Example: unidentifiability for Windkessel boundary conditions

An example of parameter unidentifiability for Windkessel parameters is presented here. Consider a fluid dynamics model with three vessels and Windkessel boundary conditions, shown in Figure 5.3. Using the radius dependent stiffness from Eq. (4.43), full parameter set is

$$\theta_1 = [k_1, k_2, k_3, R_{p,1}, R_{p,2}, R_{d,1}, R_{d,2}, C_{T,1}, C_{T,2}]. \quad (5.47)$$

Given a single pressure profile in the MPA, the goal is to uniquely identify all the parameters given the model and available data. However, it is known that resistors and capacitors in parallel are not identifiable [6], and is likely the case for a 1D model coupled to Windkessel boundary conditions.

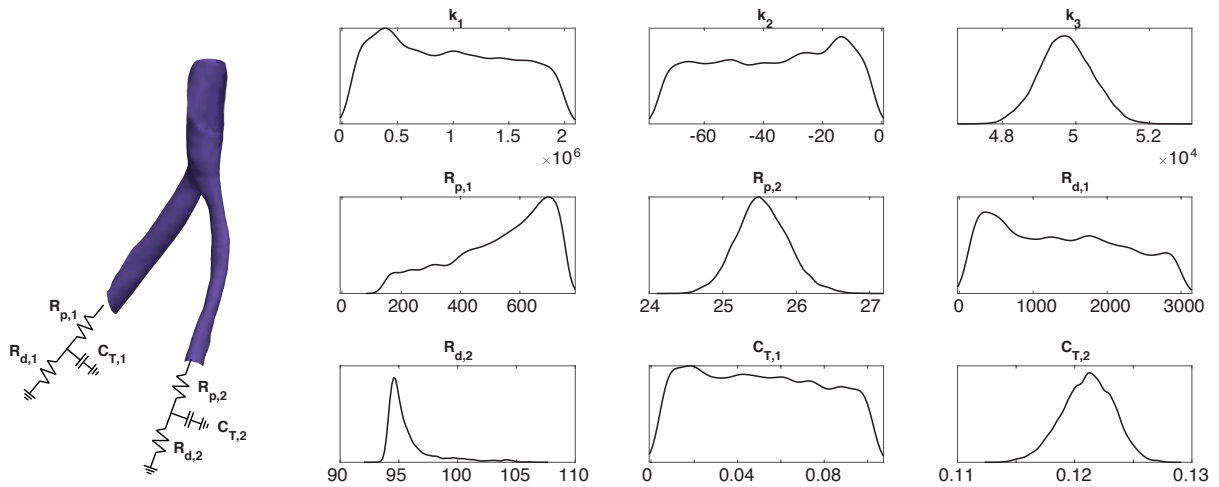


Figure 5.2 Posterior density results when estimating the full parameter set and individual Windkessel parameters. Note that some parameters have distinct modes and narrow tails, whereas others have long tails or appear nearly uniform, suggesting unidentifiability.

In this example, we use DRAM to illustrate that θ is at least practically unidentifiable. Results shown in Figure 5.2 illustrate that all nine parameters are not identifiable. It should also be noted that the Fisher information matrix, computed using a centered-finite difference method, is singular, confirming unidentifiability. Rather than cycling through possible parameter subsets that include only parts of the vasculature, we introduce the scaling factors r_p , r_d , and c , which scale the nominal Windkessel estimates (discussed and used in detail in Chapter 7 [46]). This reduces the parameter

dimensionality to

$$\theta_2 = [k_1, k_2, k_3, r_p, r_d, c]. \quad (5.48)$$

Again, DRAM is used to infer the reduced parameter set. There is still some unidentifiability in the exponential stiffness model as shown in Figure 5.3. This confirms the findings by Paun et al. [175], who also determined that k_1 and k_2 were unidentifiable. As a last step, we fix the exponential terms in the stiffness model, giving the reduced parameter set

$$\theta_2 = [k_3, r_p, r_d, c]. \quad (5.49)$$

Posterior densities for θ_2 in Figure 5.4 have a unimodal posterior distribution with finite tails. This reduced parameter subset is now identifiable given a single pressure measurement in the MPA.

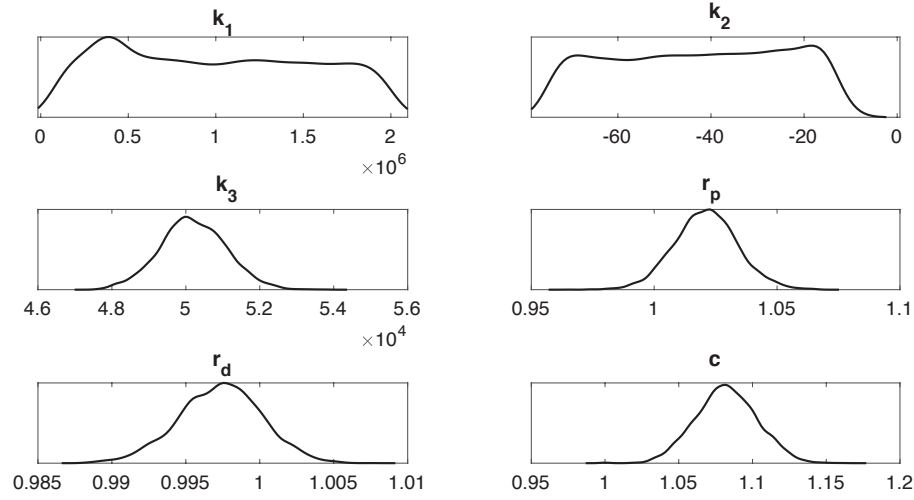


Figure 5.3 Posterior density results when estimating the individual stiffness parameters and the Windkessel scaling parameters r_p , r_d , and c . Windkessel scaling factors have a unimodal shape, as well as k_3 in the stiffness model. In contrast, k_1 and k_2 are relatively uniform, suggesting unidentifiability.

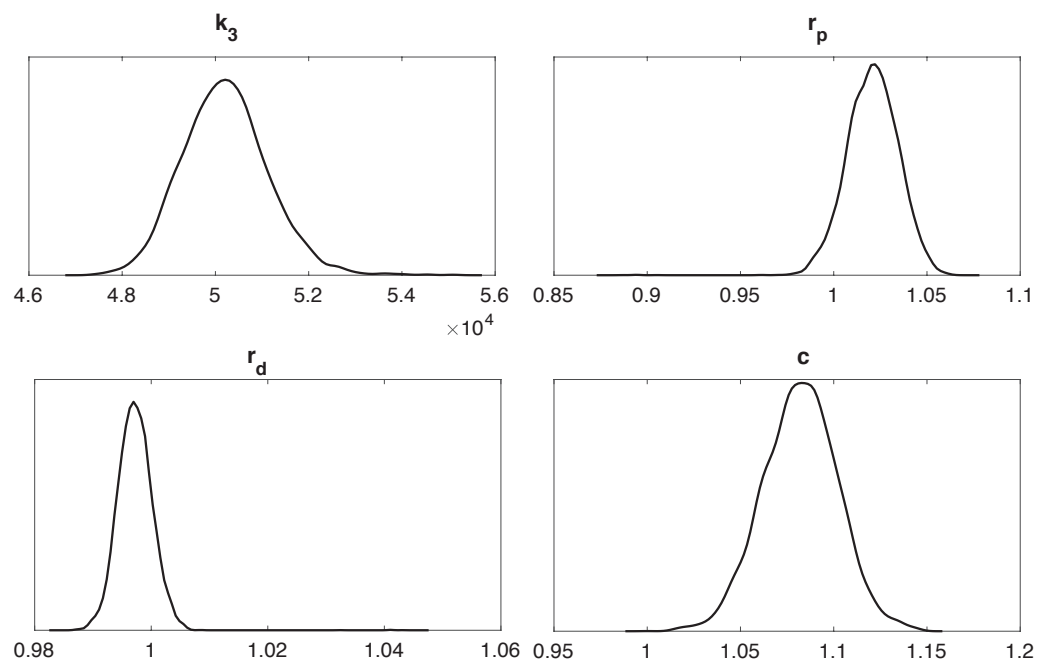


Figure 5.4 Posterior density results when estimating a single stiffness parameter and the Windkessel scaling parameters r_p , r_d , and c . Note that the posteriors are unimodal, with finite tails.

CHAPTER

6

SIMULATIONS AND INVESTIGATIONS

If left untreated, PH is a deadly disease with a high mortality rate. Diagnosis and treatment of this disease has advanced in the last several years, with image analysis and hemodynamic measurements revealing changes in vascular morphometry and function during PH. However, more work is needed to provide a synergistic tool for assessing the interactions between the structure and function of the pulmonary circulation in normotensive and PH conditions. Such a tool, as developed here, should combine imaging data with hemodynamic measurements for holistic assessment of the pulmonary circuit. Cardiovascular inverse problems provides a natural tool for clinical decision making and disease assessment. Hemodynamics models have been successfully used for planning coronary artery disease intervention [26]. Parameter inference and uncertainty quantification are understudied in computational pulmonary hemodynamics, yet this type analysis is necessary for using models in-clinic. Results in this dissertation provide a computational tool that can assess pulmonary arterial structure and function simultaneously. The next three chapters report published and submitted results focusing on cardiovascular inverse problems.

Chapter 7 includes the published study “Sensitivity analysis and uncertainty quantification of 1-D models of pulmonary hemodynamics in mice under control and hypertensive conditions,” by Colebank, Qureshi, and Olufsen. The pulmonary arterial tree includes hundreds to thousands of vessels, though it is unclear how many vessels are necessary to match model predictions to data in the MPA. This study utilizes and compares three different networks with one, three, and 21 vessels under both normotensive and PH conditions. Using both frequentist and Bayesian methods, Windkessel scaling parameters and vessel stiffness are estimated for each network. Local derivative based sensitivity analysis and Morris Screening quantify model sensitivity, showing that network size

dictates model sensitivity. Using the three network models, the following questions are addressed:

1. Given imaging and hemodynamic data, which model parameters are identifiable and influential?
2. Do the model parameters reflect physiological knowledge of the pulmonary arteries both normotensive and HPH conditions?
3. Does model sensitivity change with respect to large vessel network size or disease status?
4. Does the model sensitivity agree with physiological knowledge of HPH progression?

The novelty of this study includes performing sensitivity analyses, inferring parameter estimators and distributions, and quantifying uncertainty on different sized networks.

Chapter 8 includes the published manuscript "Influence of image segmentation on one-dimensional fluid dynamics predictions in the mouse pulmonary arteries" by Colebank, Paun, Qureshi, Chesler, Husmeier, Olufsen, and Ellwein-Fix. Image based modeling requires constructing a model domain, yet this domain is subject to uncertainties in the image segmentation pipeline. The study investigates these uncertainties in image segmentation by constructing 25 segmentations of the same micro-CT image from a normotensive mouse. Statistical properties of the network, including uncertainty in vessel geometry and uncertainty in the network connectivity, are determined. These uncertainties are then propagated through the model, revealing that network connectivity is more influential on model predictions than vessel geometry. In particular, this study examines:

1. What are the uncertainties associated with image segmentation, and how do they affect network reconstruction?
2. How are network-level, morphometric parameters affected by variability in segmentation methods?
3. Are uncertainties in individual vessel characteristics (e.g., radius and length) more or less influential than uncertainties in network size and connectivity?

This study is the first to integrate measured uncertainty due to segmentation into an expansive 1D network model. Uncertainties in pressure, flow, and wave intensity are propagated by constructing density estimates for radius and length across 25 segmentations. Another novelty is the separation of uncertainty into that attributed to vessel length and radii, and uncertainty due to network connectivity.

Chapter 9 includes the submitted manuscript "A multiscale model of vascular function in chronic thromboembolic pulmonary hypertension," by Colebank, Qureshi, Rajagopal, Krasuski, and Olufsen. This study, done in collaboration with clinicians Rajagopal and Krasuski at Duke University, proposes a multiscale model framework for group 4 PH, CTEPH. The disease is curable, but an optimal intervention strategy is not currently available. Utilizing a human image and flow data, the study

integrates pressure-loss lesion models with the 1D model coupled to a structured tree to address this issue. Normotension and four CTEPH disease cases are simulated and compared to physiological knowledge of the disease. The framework is used to simulate BPA in CTEPH patients, illustrating a possible tool in determining optimal surgical interventions. This study asks:

1. Can 1D fluid dynamics models predict in-clinic energy-losses seen in CTEPH?
2. Can large-and-small vessel disease hypotheses be observed in a hemodynamics model of CTEPH?
3. Can the model determine optimal surgical intervention be deduced?

Results from this study show that 1D model predictions can be mapped to the 3D lung tissue, providing a new quantitative metric of flow heterogeneity. The study is the first to use a combination of large and small vessel hemodynamics, and large vessel lesion models to predict improvements from simulated surgery.

The three papers are provided verbatim and may overlap with methods discussed in previous chapters.

CHAPTER

7

SENSITIVITY ANALYSIS AND UNCERTAINTY QUANTIFICATION OF 1D PULMONARY HEMODYNAMICS IN MICE UNDER CONTROL AND HYPERTENSIVE CONDITIONS

The study “Sensitivity analysis and uncertainty quantification of 1-D models of pulmonary hemodynamics in mice under control and hypertensive conditions” was published in a special issue article in the *International Journal for Numerical Methods in Biomedical Engineering*, e3242 in 2019. Contributions included determining the vascular geometry from micro-CT imaging, setting up the three network models, performing all sensitivity analyses, parameter inference, and uncertainty quantification, and writing a majority of the manuscript.

7.1 Abstract

Pulmonary hypertension (PH), defined as an elevated mean blood pressure in the main pulmonary artery (MPA) at rest, is associated with vascular remodeling of both large and small arteries. PH has several sub-types that are all linked to high mortality rates. In this study, we use a one-dimensional (1D) fluid dynamics model driven by in-vivo measurements of MPA flow to understand how model

parameters and network size influence MPA pressure predictions in the presence of PH. We compare model predictions against in-vivo MPA pressure data from a control and a hypertensive mouse and analyze model predictions in three networks of increasing complexity, extracted from micro-CT images. We introduce global scaling factors for boundary condition parameters and perform local and global sensitivity analysis to calculate parameter influence on model predictions of MPA pressure, and correlation analysis to determine a subset of identifiable parameters. These are inferred using frequentist optimization and Bayesian inference via the Delayed Rejection Adaptive Metropolis (DRAM) algorithm. Frequentist and Bayesian uncertainty is computed for model parameters and MPA pressure predictions. Results show that model predictions of MPA pressure are most sensitive to distal vascular resistance, and that parameter influence changes with increasing network complexity. Our outcomes suggest that PH leads to increased vascular stiffness and decreased peripheral compliance, congruent with clinical observations.

7.2 Introduction

Pulmonary hypertension (PH) is defined as a mean pulmonary arterial blood pressure ≥ 25 mmHg at rest and encompasses 5 main etiologies, all of which lead to right heart failure if untreated [220]. These patients experience vascular remodeling in both large and small vessels, leading to increased pulmonary arterial blood pressure and an elevated ventricular afterload, the external stress that the heart must overcome to eject blood into the aorta and main pulmonary artery (MPA). These changes ultimately alter the type, magnitude, speed, and arrival time of local pressure and flow waves [188, 249]. PH has no cure and is only diagnosed after an initial screening by echocardiogram and invasive measurement of pulmonary arterial blood pressure via right heart catheterization, resulting in delayed diagnosis of the disease and limited treatment options [220]. In this study, we develop a one-dimensional (1D) fluid dynamics model to understand how changes in network complexity and vessel stiffness impact predictions of MPA blood pressure, as this model type has potential to describe how pathology impacts the vascular structure (e.g. wall stiffness and network morphology) and function (e.g. blood pressure and flow propagation) of the pulmonary circulation. This is vital for developing better clinical tools for disease detection and monitoring progression [27, 143].

1D fluid dynamics models requires specification of four components, including 1) the geometry of the vascular network, 2) a 1D approximation of the Navier-Stokes equations, satisfying conservation of mass and balance of axial momentum, 3) a constitutive equation relating transmural pressure and vessel cross-sectional area, and 4) inlet, outlet, and junction conditions. Numerous studies have used 1D models to investigate wave propagation in the systemic circulation [4, 21, 168, 198, 226, 249] and to study how changes in vascular wall mechanics impact systemic hemodynamics [192, 225, 240]. While a majority of studies are carried out in the systemic circulation, several recent works have analyzed dynamics in the pulmonary circulation [135, 169, 189, 190]. For example, Qureshi et al. [189] developed a 1D model connecting pulmonary arteries and veins, while Lee et al. [135] and

Qureshi et al. [190] studied nonlinearity of the pulmonary arterial wall deformation. The 1D model can describe hemodynamics in both the systemic and pulmonary systems, though the systems differ significantly. The systemic network distributes blood via long vessels, forming a specialized network reaching all organs in the body, except the lungs, under a high mean pressure gradient changing from about 92 mmHg in the aorta to approximately 2 mmHg in the capillaries [146]. In contrast, the pulmonary system transports blood from the right ventricle to the left atrium, covering a relatively short distance via a rapidly branching network of highly compliant vessels, see Figure 7.1. The pulmonary system transports blood under a lower mean pressure gradient, from about 15 mmHg in the MPA to approximately 4 mmHg in the pulmonary veins [146]. These fundamental differences between the structure and function of the two systems significantly impact the parameter ranges and model behavior needed for hemodynamic predictions; a question not addressed in previous studies. A better understanding of how the model parameters impact hemodynamic predictions, i.e. the model sensitivity to parameters, is important for understanding the rapid progression of PH and eventual right heart failure. In this study, we use sensitivity analysis and uncertainty quantification to address key questions related to these aspects.

Sensitivity analysis quantifies the effects of model parameters on simulated quantities of interest by systematically perturbing parameters and quantifying their effects. This analysis can be conducted using either local [59, 60] or global [153, 205, 221] methods, providing parameter rankings [60, 165] and time-varying sensitivities [7, 148, 265]. Local sensitivity metrics are computed from explicit sensitivity equations [60] or approximated using finite differences [106, 221], automatic differentiation [60, 84], or complex step methods [17, 221]. Local methods are computationally inexpensive but are only guaranteed to be valid at a given parameter value if the model is linear and additive [205]. In contrast, global methods approximate the model sensitivity throughout a specified parameter space [34, 205, 221, 258], albeit at a much higher computational cost. Global sensitivity analysis can be conducted using variance-based methods, such as Sobol' indices [205, 258], or Morris' Screening [153]. Sobol' indices provide a more robust, finer measure of parameter influence, whereas Morris' Screening provides a coarse approximation of the global sensitivities. While the Sobol' methods perform a more extensive analysis over the entire parameter space, screening methods are less computationally expensive and are in good agreement with total indices obtained from Sobol' indices [34].

A thorough sensitivity analysis is of particular importance for network models, as the extent of the network used affects both the number of parameters in the system and their respective influence on model predictions [62, 114, 135, 152]. The effects of changing parameters in large models of the vasculature are nonlinear and complex, largely due to the complex physics of the system [58, 59]. Moreover, the physiological range for each parameter depends on both the network topology and the disease state. To address this problem, it is important to understand how the model sensitivity changes with network size and if it is possible to infer parameters given the available data. Several recent studies [12, 31, 59] have conducted sensitivity analyses and examined uncertainties in predictions for a range of cardiovascular models [37, 87, 148, 206, 264, 265]. Two studies [68,

148] have quantified how parameter influence changes with network size and complexity, and one study [37] has examined time-varying changes in model sensitivities. To our knowledge, no previous studies have examined the sensitivity of model predictions to parameters in pulmonary arterial networks, which may shed more light on differences between the systemic and pulmonary systems and assist in understanding differences between the more prevalent essential systemic hypertension and the relatively rare, yet less understood, PH.

MPA blood pressure, a signature of pulmonary hemodynamics, is vital for PH diagnosis, making it an ideal quantity of interest for sensitivity analysis. Changes in MPA pressure are attributed to proximal and distal vascular resistance and pulmonary vascular compliance [190, 220], which can serve as biomarkers for disease progression. Ideally, parameter inference would identify biomarkers using the model and available data; however, limited PH patient data leads to a naturally ill-posed inverse problem. To make the problem more well-posed, we introduce global scaling factors [186, 190] that simultaneously adjust nominal parameter estimates and reduce the parameter space by removing correlated parameters [60, 142, 165]. Once the parameter set is reduced, parameter inference is done using both frequentist and Bayesian methods. The former methods treat parameters as fixed and are less computationally expensive, while the latter treat parameters as random variables, allowing for calculation of parameter posterior distributions using numerous Monte Carlo samples [186, 221]. Once parameters are inferred, frequentist and Bayesian uncertainty quantification methods are used for both the parameters and model output, providing a measure of model robustness to natural variation in parameters and measurement error.

Our objective in this study is to analyze the sensitivity and uncertainty of MPA pressure predictions from 1D fluid dynamics models in networks of varying complexity. We perform our analysis using data from two different mice under control and hypoxic environments, the latter inducing PH. We hypothesize that it is essential to include several vessels in the network to obtain sufficiently accurate physiological information. To test our hypothesis, we compare predictions in three different networks: a single vessel model containing the MPA, a slightly more complex 3 vessel network, and a more realistic network with 21 vessels. The latter is chosen as it is the largest number of vessels that can be uniquely identified in both the control and hypoxic mouse. We introduce a reduced parameter subset using a scaling factor approach [190] and conduct sensitivity analyses to quantify the parameters' influence on pressure predictions in the MPA. We compute sensitivities using local, derivative-based [60, 142] and global screening methods [153], and investigate how sensitivity metrics change over the cardiac cycle and with network size. We use correlation analysis and posterior parameter pairwise plots from Markov Chain Monte Carlo (MCMC) sampling to determine identifiable parameters, which are inferred by minimizing the least squares error between measured and computed MPA pressure. Finally, we quantify uncertainty of the estimated parameters using asymptotic, frequentist analysis and the Delayed Rejection Adaptive Metropolis (DRAM) algorithm, and propagate this uncertainty forward to compute confidence, credible, and prediction intervals for simulated waveforms [30, 142]. The workflow for this process is shown in Figure 7.2.

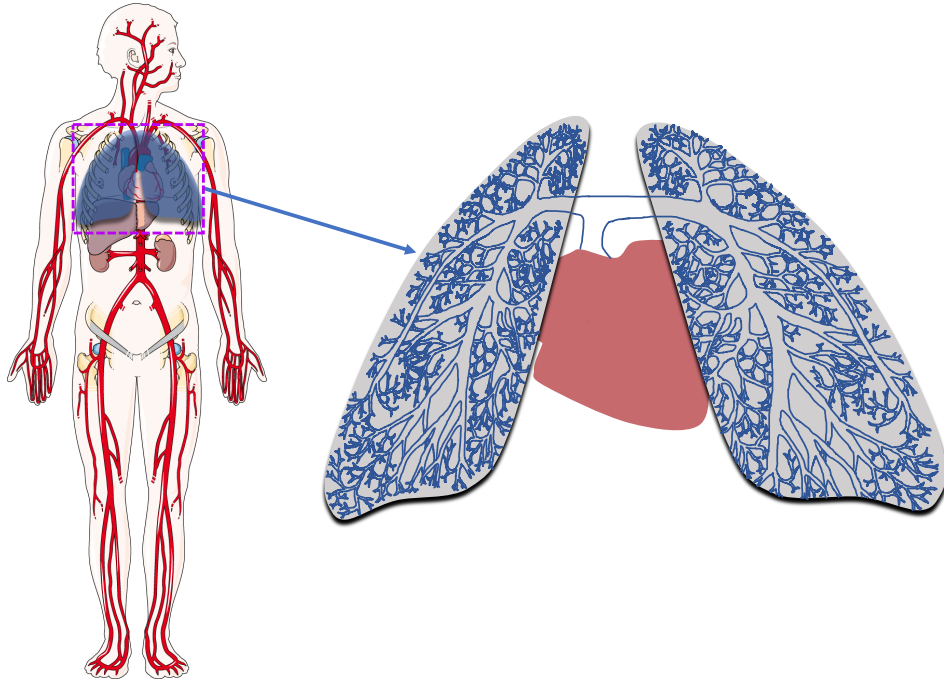


Figure 7.1 Physiological diagram illustrating (a) the systemic arterial circulation in humans compared to (b) the pulmonary circulation in the lung. The pulmonary circulation begins with the main pulmonary artery (MPA) and bifurcates into the left and right pulmonary arteries, quickly bifurcating afterwards throughout the lung.

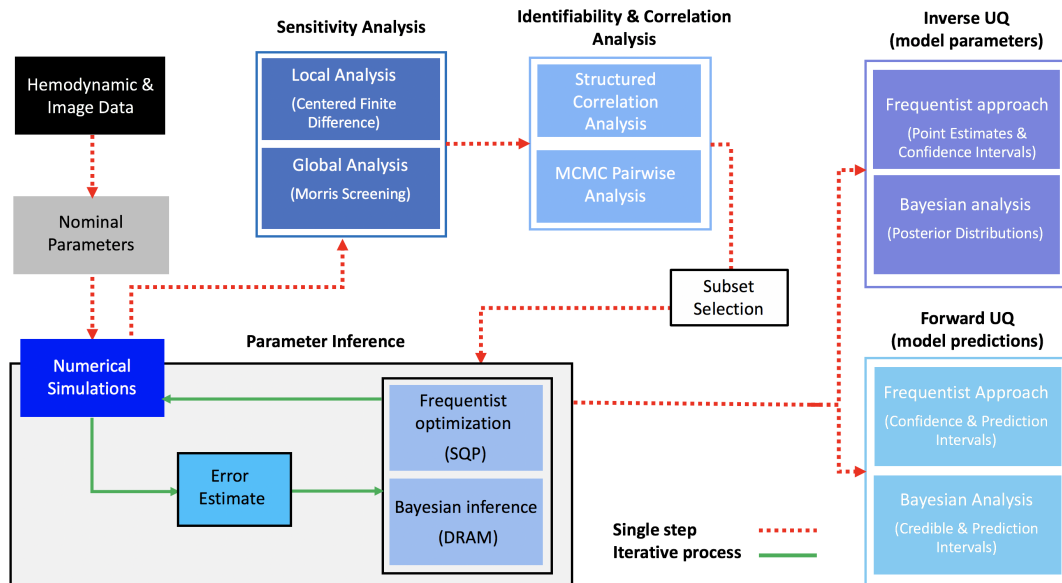


Figure 7.2 General workflow of the data analysis process. Abbreviations: MCMC: Markov Chain Monte Carlo; SQP: Sequential Quadratic Programming; DRAM: Delayed Rejection Adaptive Metropolis; UQ: Uncertainty Quantification.

7.3 Methods

7.3.1 Data

This study uses in-vivo hemodynamic and micro-computed tomography (micro-CT) imaging data from control and hypoxic mice. Detailed experimental protocols describing this data can be found in [232, 245]. All experimental procedures are approved by the University of Wisconsin Institutional Animal Care and Use Committee. Below is a brief summary of the experimental protocol and the methods for network construction.

7.3.1.1 Hemodynamic and Imaging Data

The hemodynamic data include cycle-averaged MPA pressure and flow waveforms gated to the electrocardiogram (ECG) fiducial point [232]. Blood pressure is measured at a rate of 5KHz using a 1.0F pressure-tip catheter (Millar Instruments, Houston, TX) and the flow, measured with ultrasound, is sampled at 30MHz. We examine data from one control and one hypoxic male C57BL6/J mouse (12-13 weeks, weight 24 g), selected from groups of 7 control and 5 hypoxic mice. The latter specimen is subject to a hypoxic environment for 21 days, thus creating hypoxia-induced PH in the mouse. For each group (control and hypoxia), the mice with hemodynamics closest to the group average are used for analysis in this study. The flow waveform is recorded precisely at the inlet of the MPA, while MPA pressure is recorded proximal to the first bifurcation in the network. For sake of simplicity, we assume that the pressure data corresponds to the midpoint of the MPA.

The imaging data include stacked planar X-ray micro-CT images of pulmonary arterial trees from two male C57BL6/J mice, selected from groups of 4 control and 4 hypoxic mice (10-12 weeks, weight 24 g). The hypoxic mice used for the imaging study were subject to a hypoxic environment for 10 days. The pulmonary arterial trees are imaged under a static filling pressure of 6.3 mmHg while rotating the lungs in an X-ray beam at 1° increments to obtain 360 planar images. The Feldkamp cone-beam algorithm [66] is used to render the isometric 3D volumetric dataset (497×497×497 pixels) by reconstructing and converting the 360 planar images into DICOM 3.0. See Vanderpool et al. [245] for more details on animal preparation, handling, and experimental setup, and Karau et al. [114] for details on the micro-CT image acquisition.

7.3.1.2 Network Geometry

Similar to our previous studies [186, 190], networks are extracted from DICOM images. We use ITK-SNAP [273] to segment the images and render 3D structures and Paraview (Kitware; Clifton Park, NY) to convert segmentations to Visualization ToolKit Polygonal (vtp) files. Lastly, the 3D networks are converted to data structures containing centerline coordinates, vessel radii, and orientation using the Vascular Modeling ToolKit (VMTK) [9, 11].

We use a custom MATLAB (Mathworks; Natick, MA) algorithm to construct a 1D graph representation of the network, described by a connectivity matrix linking edges (vessels) and nodes

(junctions). Each edge is associated with a series of $x y z$ -coordinates denoting points along the centerline and their corresponding radii. The radius for each edge is calculated by averaging the center 80% of the vessel radii [190] and the length L is calculated as the sum of the distances between $x y z$ -coordinates (\mathbf{x}_i)

$$r_0 = \frac{1}{N_v} \sum_{i=1}^{N_v} r_i, \quad L = \sum_{i=1}^N l_i, \quad \text{where} \quad l_i = \|\mathbf{x}_{i+1} - \mathbf{x}_i\|, \quad (7.1)$$

where N is the number of points along the vessel centerline, and N_v is the center 80% of the points. Junction points (nodes) corresponding to vessel bifurcations are identified as the intersection between two centerlines and embedded in a connectivity matrix.

Hemodynamic data is only available from the MPA, hence the simplest fluid dynamics model includes a single vessel (SV model, left panel of Figure 7.3) emanating at the root of the pulmonary vasculature and terminating at the first pulmonary junction. We compare results in the SV model with the second smallest network containing three vessels, the MPA and the left and right pulmonary arteries, (center panel in Figure 7.3). We refer to this model as the "single bifurcation" (SB) model. The advantage of the SB model is that it can predict perfusion to the left and the right lobes of the lung, enabling us to compare results with previous studies [27, 189]. Lastly, we compare results from the SV and SB networks with a more realistic network containing 21 vessels (right panel of Figure 7.3). We include 21 vessels as it is the largest number of vessels that can be identified in both the control and hypoxic mouse. This allows for comparison between disease states without the considering the influence of connectivity, as these models use the same connectivity. The vessel radii and lengths vary between the control and hypoxic mice, as shown in Table 7.1. Given that the three models are of various order, we can account for the effects of model-induced wave reflections, which are prominent in larger network models [265]. Moreover, the 21 vessel model allows us to analyze the role attributed to changes in distal vessel segments on PH progression [120, 135, 169, 220]. Ideally, we should gradually increase the network from 3 to 21 vessels; however, the computational cost associated with parameter inference and UQ is expensive and require several thousands of forward simulations for each model and disease type, hence, we limit our analysis to the three networks, shown in Figure 7.3: (a) a single vessel (SV - zero bifurcation) model, (b) a three vessel (SB - single bifurcation) model, and (c) a 21 vessel (FN - full network- ten bifurcations) model.

7.3.2 Modeling

Similar to previous studies [169, 189, 190], the 1D fluid dynamics model is derived from the continuity and Navier-Stokes equations combined with a constitutive equation relating pressure and vessel area. A measured flow waveform is prescribed at the inlet of the MPA, and outlet boundary conditions are specified by three-element Windkessel models, with nominal parameter values calculated using the hemodynamic data and network geometry.

Table 7.1 Vessel dimensions and connectivities for SV, SB, and FN networks for the control and hypoxic mice.

Vessel Index	Connectivity (Daughters)	Control		Hypoxic	
		$r_0 \times 10^{-1}$ (cm)	$L \times 10^{-1}$ (cm)	$r_0 \times 10^{-1}$ (cm)	$L \times 10^{-1}$ (cm)
1*†	(2,3)	0.47	4.10	0.51	3.58
2†	(4,5)	0.26	4.45	0.26	4.03
3†	(6,7)	0.37	3.72	0.37	3.08
4	(8,9)	0.24	2.41	0.25	2.92
5	–	0.13	0.52	0.17	0.65
6	(14,15)	0.32	2.02	0.28	1.60
7	–	0.17	2.12	0.19	0.93
8	(10,11)	0.23	3.11	0.24	2.06
9	–	0.17	1.77	0.17	0.51
10	(12,13)	0.20	2.62	0.22	2.37
11	–	0.16	0.69	0.17	0.88
12	–	0.15	1.40	0.19	1.27
13	–	0.14	0.62	0.15	0.51
14	(16,17)	0.26	0.81	0.27	1.20
15	–	0.19	1.84	0.19	1.55
16	(18,19)	0.25	0.83	0.26	0.71
17	–	0.15	3.02	0.18	1.68
18	(20,21)	0.24	4.69	0.24	3.55
19	–	0.15	1.77	0.18	1.86
20	–	0.22	1.78	0.23	2.24
21	–	0.18	0.55	0.19	1.07

* Dimensions for the single vessel (SV) model, † the single bifurcation (SB) model, and the 21 vessel full network model (FN) model. For each connectivity pair (i, j) , i refer to the left and j to the right daughter. Vessels marked with – are terminal.

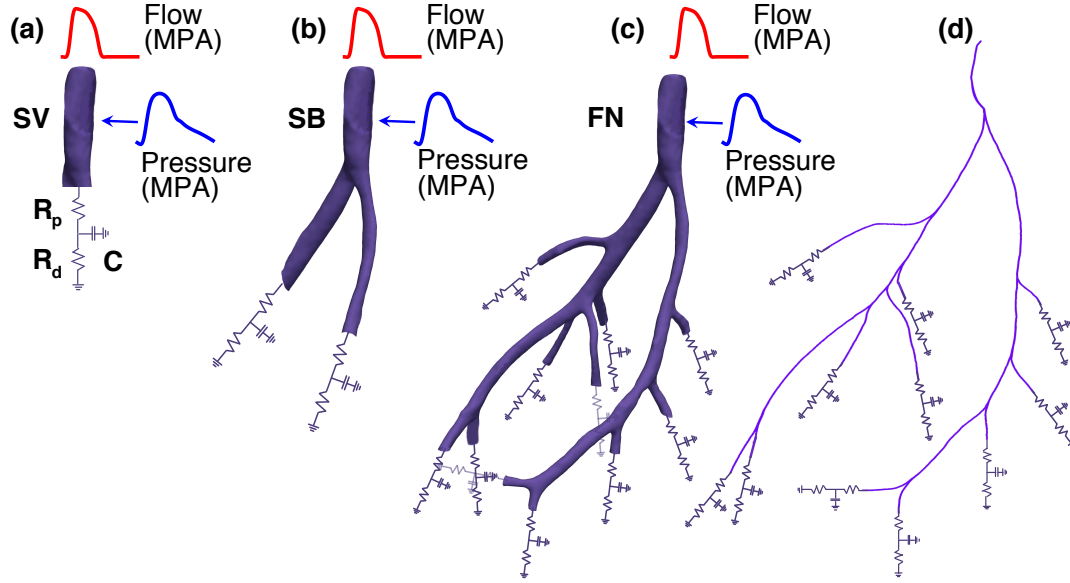


Figure 7.3 Pulmonary arterial networks constructed from micro-CT images of a control mouse. Three models are analyzed: **(a)** a single vessel model (SV), **(b)** a single bifurcation model (SB), and **(c)** a 21 vessel full network model (FN). The 1D model **(d)** is constructed by extracting centerlines from an isometric 3D volumetric surface rendered from the segmented images. The networks are represented by a connectivity matrix with nodes, edges, vessel radii, lengths, and orientation. A flow waveform obtained from data is attached at the network inlet, and at the outlets we attach three-element Windkessel models, relating flow and pressure. Pressure data is measured at the midpoint of the MPA and used for parameter inference.

7.3.2.1 1D fluid dynamics equations

The 1D model is derived under the assumptions that the vessels are cylindrical, that blood is incompressible, that flow is Newtonian, laminar, and axisymmetric (with no swirl), and that the arterial walls are impermeable. The equations for mass conservation and momentum balance are written as [168, 169, 189, 190]

$$\frac{\partial A}{\partial t} + \frac{\partial q}{\partial x} = 0, \quad \frac{\partial q}{\partial t} + \frac{\partial}{\partial x} \left(\frac{q^2}{A} \right) + \frac{A}{\rho} \frac{\partial p}{\partial x} = -\frac{2\pi \nu R}{\delta} \frac{q}{A}, \quad (7.2)$$

where x (cm) and t (s) denote the axial and temporal coordinates, $p(x, t)$ (mmHg) denotes the transmural blood pressure, $q(x, t)$ (ml/s) the volumetric flow rate, and $A(x, t) = \pi r(x, t)^2$ (cm²) the cross-sectional area, where $r(x, t)$ (cm) is the vessel radius. The blood density ρ (g/ml), kinematic viscosity ν (cm²/s), and boundary layer thickness δ (cm) are assumed constant. The momentum equation is derived under the no-slip condition, satisfied by imposing a flat velocity profile over the lumen area [168] with a thin boundary layer that decreases linearly in the vicinity of the walls, where the transition to no-slip takes place. In order to maintain consistent units in the system of equations (7.2), we convert the pressure from mmHg to units of (g/(cm s²)) using the conversion factor 1 mmHg = 1333.22 (g/(cm s²)).

To close the system of equations, we adopt a constitutive equation relating pressure and cross-

sectional area via a linear wall model [204]. The wall model is derived under the assumptions that the vessels are cylindrical and that the walls are thin ($h/r_0 \ll 1$), incompressible, homogeneous, and orthotropic [14]. We assume that the loading and deformation are axisymmetric and that the vessels are tethered in the longitudinal direction so that longitudinal strain is negligible. Under these conditions, the external force reduces to stress in the circumferential direction, yielding a linear stress-strain relation

$$p = \beta \left(\sqrt{\frac{A}{A_0}} - 1 \right), \quad \beta = \frac{E h}{(1 - \kappa^2) r_0}, \quad (7.3)$$

where β (mmHg) denotes the vessel stiffness. E (mmHg) denotes the circumferential Young's modulus, $\kappa = 0.5$ (dimensionless) the Poisson ratio, h (cm) the wall thickness, and $A_0 = \pi r_0^2$ (cm²) refers to the reference cross-sectional area [168, 204] at $p = p_0 = 0$.

7.3.2.2 Boundary conditions

The system of equations (7.2)-(7.3) is hyperbolic with characteristics that propagate in opposite directions [2], i.e. to be well-posed each vessel needs an inlet and outlet boundary conditions. We enforce this by specifying the flow at the network inlet (Figure 7.3) and conservation of flow and continuity of pressure at each junction, given by

$$p_p(L, t) = p_{d_i}(0, t) \quad \text{and} \quad q_p(L, t) = \sum_i q_i(0, t), \quad (7.4)$$

where the subscripts p and d_i ($i = 1, 2$) refer to the parent and daughter vessels, respectively. Outlet boundary conditions for each terminal vessel are described by three-element Windkessel models (an RCR circuit) relating peripheral pressure $p(L, t)$ and flow $q(L, t)$ as

$$\frac{dp(L, t)}{dt} - R_p \frac{dq(L, t)}{dt} = q(L, t) \left(\frac{R_p + R_d}{R_d C} \right) - \frac{p(L, t)}{R_d C}, \quad (7.5)$$

where $R_T = R_p + R_d$ (mmHg s/ml) is the total peripheral resistance, R_p is the proximal resistance, R_d is the distal resistance, and C (ml/mmHg) is the total compliance of the vascular region perfused by the terminal vessel (see Figure 7.3). The system of equations (7.2)-(7.5) are solved numerically in C++ using the two-step Lax-Wendroff method, described in detail in [168].

7.3.2.3 Nominal parameter values

The 1D model has three types of parameters, shown in Table 7.2, specifying the network geometry, the fluid and vascular properties, and the in- and outlet boundary conditions. Some of these can be measured or found in literature, while others must be estimated. Here, we describe how to compute nominal parameter values before performing model reduction and parameter inference using frequentist and Bayesian techniques.

Network geometry: Vessel length, radius, and connectivity are extracted from imaging data as

described in Sec. 7.3.1. While these quantities carry uncertainty, we assume that all geometric properties are constant and known. The dimensions and connectivity of the different models are given in Table 7.1.

Fluid and vascular properties: The blood density $\rho = 1.057$ (g/ml) [199], the kinematic viscosity $\nu = 0.0462$ (cm²/s), measured at a shear rate of 94 (s⁻¹) [262], and the boundary layer thickness $\delta \approx \sqrt{\nu T/2\pi}$ [249] are assumed constant. Here, T (s) denotes the length of the cardiac cycle, which is 0.112 and 0.107 (s) for the control mouse and hypoxic mouse, respectively. This difference was statistically insignificant [190] and had a negligible effect on model predictions, hence we use $T = 0.11$ for all simulations. The nominal value for the wall stiffness in the MPA (β_{MPA}) is approximated as

$$\beta_{\text{MPA}} = \frac{2(A_0 Z_c)^2}{\rho}, \quad (7.6)$$

where the characteristic impedance Z_c is estimated from the slope of the pressure-flow loop including 95% of the flow during ejection phase [191].

Inflow and outlet conditions: We specify a control and hypoxic flow waveform at the inlet of the MPA, repeated for each cardiac cycle ($T = 1/\text{HR}$ (s)), for each mouse. At the outlet of each terminal vessel, we specify a three-element Windkessel model (equation (7.5)). This model has 3 parameters, two resistors and a capacitor, given by $\theta_{wk} = \{R_p, R_d, C\}$. For each terminal vessel, the total peripheral resistance is $R_T = R_p + R_d = \bar{p}/\bar{q}$, where \bar{p} and \bar{q} denote the mean pressure and mean flow over over the cardiac cycle from the data. Similar to previous studies [21, 146] we assume that the nominal proximal resistance is $R_p = 0.2R_T$ and that the distal resistance is $R_d = R_T - R_p$. As suggested by Stergiopoulos et al. [226], the peripheral compliance is calculated as $C = \tau/R_T$, where the time-constant τ is estimated by fitting the diastolic pressure decay $p_d(t)$ to an exponential function [190, 191]

$$p_d(t) = p(t_d)e^{-(t-t_d)/\tau}, \quad (7.7)$$

where t_d denotes the onset of diastole.

For models with more than one vessel (i.e. the SB and FN models), θ_{wk} are estimated by distributing R_T to each terminal vessel j as

$$R_{Tj} = \frac{\bar{p}}{\bar{q}_j}, \quad \text{and} \quad C_j = \frac{\tau}{R_{Tj}}, \quad (7.8)$$

where \bar{q}_j is the mean flow to vessel j , determined by applying Poiseuille's law recursively at each junction. This relation gives

$$\bar{q}_{d_i} = \frac{F_{d_i}}{\sum_i F_{d_i}} \bar{q}_p, \quad \text{where } F_{d_i} = \left(\frac{\pi r_0^4}{8\mu L} \right)_{d_i} \quad \text{for } i = 1, 2. \quad (7.9)$$

Here \bar{q}_{d_i} and \bar{q}_p denote the mean flow in the daughter vessel i and parent vessel p , respectively, with viscosity μ . Similar to the SV model, the total resistance is distributed as $R_{pj} = 0.2R_{Tj}$ and

$R_{dj} = R_T j - R_{pj}$. Each outlet j requires specification of 3 parameters (R_{pj}, R_{dj}, C_j), i.e. the SV model has 3 outlet parameters, the SB model has 6 outlet parameters, and the FN model has 33 outlet parameters.

Table 7.2 List of parameter values and how they are calculated.

Parameter	Units	Control Value	Hypoxic Value	Reference
r_0	[cm]	†	†	[190]
L	[cm]	†	†	[190]
ρ	[g/ml]	1.057	1.057	[199]
ν	[cm ² /s]	0.0462	0.0462	[262]
δ	[cm]	0.03	0.03	[249]
κ	dimensionless	0.5	0.5	[190]
Z_c	[mmHg s / ml]	26.0	150.6	[191]
T	[s]	0.11	0.11	[190]
τ	[s]	0.14	0.09	[190]
R_T	[mmHg s / ml]	Eq. (7.8)	Eq. (7.8)	[190]
C	[ml / mmHg]	Eq. (7.8)	Eq. (7.8)	[190]
$\beta = Eh/r_0$	[mmHg]	*	*	-
r_p	dimensionless	*	*	-
r_d	dimensionless	*	*	-
c	dimensionless	*	*	-

† - parameters based on imaging data; * - parameters estimated

7.3.3 Parameter Reduction

Assuming that the network geometry is fixed, the model parameters can be grouped into two categories: parameters in the 1D model equations, $\theta_{1D}^i = \{T, \nu, \rho, \delta, \beta_i\}$ for $i = 1, \dots, N_{ves}$, where N_{ves} is the number of vessels, and parameters needed to specify the outlet boundary conditions, $\theta_{wk}^j = \{R_{pj}, R_{dj}, C_j\}$ for $j = 1, \dots, N_{term}$, where N_{term} is the number of terminal vessels. The models studied here have 8, 13, and 58 parameters for the SV, SB, and FN models, respectively, yet data is only available in the MPA. The lack of downstream data makes parameter inference ill-posed, as multiple parameters are to be inferred using one time-series signal. To address this problem, we introduce global scaling factors to reduce the number of inferred parameters.

As mentioned earlier, we assume that the cardiac cycle length T , the viscosity ν , the density ρ , and the boundary layer thickness δ are constant and that the parameter stiffness β is constant for all networks within each disease type [124, 135, 190]. As a result, only the Windkessel parameters R_p, R_d , and C are vessel specific. From circuit theory, it is known that resistors and capacitors in

parallel and series can be combined to compute the total resistance and capacitance for a circuit. The presence of multiple resistors and capacitors, which could be combined, leads to identifiability issues, i.e. estimated parameters may not be unique [107, 180, 182, 221]. To avoid this, we simplify the parameter inference problem by introducing global scaling factors [186, 190] r_p, r_d , and c for the Windkessel parameters at each terminal vessel j

$$\tilde{R}_{pj} = r_p R_{pj}, \quad \tilde{R}_{dj} = r_d R_{dj}, \quad \tilde{C}_j = c C_j, \quad (7.10)$$

where $\tilde{(\cdot)}$ refer to the scaled Windkessel parameters.

In summary, we fix parameters $\{T, \nu, \rho, \delta\}$ as well as the nominal Windkessel parameters $\{R_{pj}, R_{dj}, C_j\}$ for each terminal vessel j , leaving the reduced parameter set $\theta = \{\beta, r_p, r_d, c\}$ to be inferred.

7.3.4 Parameter Inference

Inferred parameters $\hat{\theta} = \{\hat{\beta}, \hat{r}_p, \hat{r}_d, \hat{c}\}$ are determined by minimizing

$$\min_{\theta} J = \min_{\theta} \left(\frac{1}{N} \chi(t; \theta)^T \chi(t; \theta) \right), \quad \chi(t; \theta) = \begin{bmatrix} p_m(L/2, t_1) - p_{data}(t_1) \\ \vdots \\ p_m(L/2, t_N) - p_{data}(t_N) \end{bmatrix}, \quad (7.11)$$

where N is the number of data points, $p_{data}(t_i)$ is the MPA pressure data measured at $t = t_i$, and $p_m(L/2, t_i)$ is the corresponding model prediction at the midpoint of the MPA for a given value of θ . Throughout this paper, we use $\hat{(\cdot)}$ to denote quantities that are estimated using either the frequentist or Bayesian techniques described in Section 3. Moreover, the scaling factors shown in equation (7.10) always adjust the nominal parameter estimates R_{pj}, R_{dj} , and C_j , which are calculated using equation (7.9).

7.4 Model Analysis

To determine the influence of model parameters on the MPA pressure, we use local and global sensitivity methods. We analyze parameter correlations and pairwise parameter distributions to determine a subset of parameters that can be estimated given the model and available data. We use both frequentist and Bayesian inference methods to infer point-estimates and posterior parameter distributions by minimizing the least squares error between model predictions and MPA pressure measurements. Subsequently, we use forward uncertainty propagation to quantify the uncertainty of model predictions in the MPA and downstream vasculature.

7.4.1 Sensitivity Analysis

Sensitivity analysis characterizes the influence of parameters on the model output. This type of analysis provides insight into future data collection methods and experimental designs, as parame-

ters that are more influential should be prioritized for experimental measurement [91]. Conversely, a lack of agreement between sensitivity analysis and physiological knowledge can imply missing model physics or a need for different measurements. In this study, we use derivative-based local sensitivity analysis [60] and Morris screening [231] (global) to quantify the parameter influence on MPA pressure predictions; the quantity of interest. Local sensitivity analysis is computationally efficient and valuable if accurate nominal parameter values are known, whereas global sensitivity analysis provides a more robust analysis of the model at a much higher computational cost. Since MPA pressure varies in time, we compute both the averaged and time-varying model sensitivities.

7.4.1.1 Local sensitivity analysis

Derivative-based sensitivity analysis computes the model sensitivity with respect to a single parameter value within a small neighborhood of the nominal estimate value [164, 165, 182]. For a given quantity of interest $f(t; \theta)$, the sensitivity $S_i(t_j; \theta)$ is defined as

$$S_i(t_j; \theta) = \frac{\partial f(t_j; \theta)}{\partial \theta_i}, \quad i = 1, \dots, P, \quad j = 1, \dots, N, \quad (7.12)$$

where θ_i denotes the parameter of interest, P is the number of parameters in the model, t_j is the j -th time point, and N is the number of time steps in the model output. The sensitivity matrix $S(t; \theta)$ is constructed by appending all the $N \times 1$ sensitivity vectors $S_i(t; \theta)$.

In this study, we approximate the model sensitivity using the centered finite difference method

$$\frac{\partial f}{\partial \theta_i} \approx \frac{f(t; \theta + \mathbf{e}_i \psi) - f(t; \theta - \mathbf{e}_i \psi)}{2\psi}, \quad (7.13)$$

where ψ is the step size and \mathbf{e}_i is a unit vector with a 1 in the i -th entry and 0's elsewhere. Finite difference methods for sensitivity equations are limited by the accuracy of the numerical solver for the given system of ODE's/PDE's [106], but are more computationally efficient [17, 60, 84, 165]. We choose a relatively larger number of time-steps per period, 8192 here, to ensure numerical stability and satisfaction of the CFL condition in every vessel, making $\psi = \sqrt{\Delta t} \approx 10^{-3}$ for the second-order accurate Lax-Wendroff scheme.

To make sensitivities of similar magnitude and prevent negative parameter values, we log scale the parameters, $\tilde{\theta} = \log(\theta)$. The resulting log-scaled sensitivities are given by

$$\tilde{S}_i(t; \theta) = \frac{\partial f(t; \theta)}{\partial \tilde{\theta}_i} = \frac{\partial f(t; \theta)}{\partial \theta_i} \theta_i, \quad i = 1, \dots, P. \quad (7.14)$$

Local sensitivities are computed as functions of time over one cardiac cycle and ranked sensitivities \bar{S}_i are computed by averaging sensitivities over one cardiac cycle using the 2-norm

$$\bar{S}_i = \|\tilde{S}_i\|_2. \quad (7.15)$$

It should be noted that sensitivity computations are done over one cardiac cycle after the system has reached steady, oscillatory behavior, i.e. effects of initial conditions have dissipated.

7.4.1.2 Global sensitivity analysis

We use Morris' screening [153] to compute global sensitivity metrics, which is of similar accuracy as Sobol' based total sensitivities computed using variance-based methods [34, 258]. Morris' screening involves the computation of "elementary effects", which determine the relative change of the model output to a relative change in parameter values. The screening method quantifies the effects of a parameter θ_i on the output quantity as a) negligible overall, b) linear and additive, or c) having nonlinear effects or higher order interactions with other parameters. To perform this analysis, parameters are mapped from their bounded parameter space $\Theta \in \mathbb{R}^P$ to the unit hypercube $[0, 1]^P$, where P denotes number of parameters analyzed. Using a uniform, bounded prior distribution restricts the model analysis to a physiologically relevant parameter subspace without invoking a bias. The elementary effects are computed as

$$d_i(t; \theta) = \frac{f(t; \theta + \mathbf{e}_i \Delta) - f(t; \theta)}{\Delta}, \quad (7.16)$$

where \mathbf{e}_i is the unit vector in the i -th direction, $i = 1, 2, \dots, P$. The step size Δ is chosen from the set $\Delta \in \{1/(\mathcal{M} - 1), 2/(\mathcal{M} - 1), \dots, (\mathcal{M} - 2)/(\mathcal{M} - 1)\}$, where \mathcal{M} denotes the number of parameter perturbation levels used in the screening method, i.e. the number of possible perturbation sizes. To preserve symmetry of the parameter distributions, we choose \mathcal{M} to be even [34, 153, 221]. The elementary effects are then computed by sampling K values from a uniform distribution for the parameter θ_i^j . To compare elementary effects at different points in the parameter space, we compute 2-norm elementary effects, denoted by $\tilde{d}_i^j(\theta) = \|d_i^j(t; \theta)\|_2$. We employ the algorithm by Wenthworth et al. [258] scaling the step size Δ by the parameter magnitude.

The elementary effects' mean and variance are obtained by integrating the outcomes from multiple iterations. The modified Morris' indices are calculated as

$$\mu_i^* = \frac{1}{K} \sum_{j=1}^K |\tilde{d}_i^j|, \quad \sigma_i^2 = \frac{1}{K-1} \sum_{j=1}^K (\tilde{d}_i^j - \mu_i^*)^2 \quad (7.17)$$

where μ^* quantifies the individual effect of the input on the output, i.e. the sensitivity of the model with respect to the parameter selected, while the variance estimate σ^2 describes the variability in the model sensitivity due to parameter interactions or nonlinearity. Parameters with a large μ^* and σ^2 have large effects on the model output and are highly nonlinear in the model. Similar inference can be made for other combinations of μ^* and σ^2 . Following work by Wenthworth et al. [258], we compute the metric $\sqrt{\mu^{*2} + \sigma^2}$ to rank the parameters, which takes into account the magnitude and variability of the elementary effects.

For the randomized Morris' algorithm, we set the number of samples $K = 50$, the number of levels of the parameter space $\mathcal{M} = 20$, and the step size $\Delta = \frac{\mathcal{M}}{2(\mathcal{M}-1)} \approx 0.526$. The parameter

bounds are $\beta_{control} \in [7.5, 75]$ and $\beta_{hypoxic} \in [75, 750]$ mmHg for the control and hypoxic mice, and $(r_p, r_d, c) \in [0.05, 3]^3$ for both the control and hypoxic animals. These bounds ensure that model predictions are within the physiological range for each disease type without invoking a strong bias in the prior parameter distributions.

7.4.2 Correlation Analysis

To identify pairwise parameter correlations and find a reduced parameter subset, we analyze the covariance matrix V , which for a constant observation variance s^2 can be approximated asymptotically [19] as

$$V = s^2 [\tilde{S}(t; \theta)^T \tilde{S}(t; \theta)]^{-1}, \quad s^2 = \frac{1}{N-P} [\chi(t; \theta)^T \chi(t; \theta)], \quad (7.18)$$

where $\chi(t; \theta)$ is the residual defined in equation (7.11), \tilde{S} is the sensitivity matrix defined in equation 7.12, and P is the number of parameters. We calculate correlations as

$$v_{ij} = \frac{V_{ij}}{\sqrt{V_{ii} V_{jj}}}, \quad (7.19)$$

where v_{ij} is a symmetric matrix with diagonal elements $v_{ii} = 1$ and $|v_{ij}| \leq 1$. High pairwise parameter correlations can cause optimization routines to fail finding a unique (local) minimum [68, 164, 165, 221]. Smaller parameter sets benefit from higher correlation cutoffs, whereas large parameter sets can cause issues with parameter inference for lower correlation values. We consider a cutoff of 0.9, which is within the normal cutoff range reported previously [30, 142, 167, 221].

7.4.3 Optimization

Identifiable model parameters are estimated using a sequential quadratic programming (SQP) algorithm, minimizing (7.11) within specified parameter bounds [186]. The complexity of the 1D fluids model introduces a need for parameter bounds, ensuring that the numerical solver converges without violating the CFL condition. The physiological interpretation of parameter values also provide bounds, which may be more restrictive than the numerical bounds.

The SQP algorithm is executed via the MATLAB function `fmincon`. For the control mouse, the parameter bounds were set at $\beta \in [7.5, 75]$ mmHg and $(r_p, r_d, c) \in [0.05, 3]^3$, and for the hypoxic mouse we set $\beta \in [75, 750]$ mmHg and $(r_p, r_d, c) \in [0.05, 3]^3$. For each optimization, eight initial values are sampled from a uniform distribution spanning the intervals given above. Using eight initial conditions ensured that the optimization converged to the same local minimum within the parameter bounds. Optimization was run on an iMac (3.4 GHz Intel Core i7, 16GB RAM, OS 10.13.4). The algorithm is iterated until the least squares minimization problem has converged, i.e. $|J_N - J_{N-1}| < 10^{-8}$.

7.4.4 Uncertainty Quantification

Given the limited data available from PH patients, it is important to understand how uncertainties in model parameters propagate to model predictions. We use frequentist and Bayesian methods to propagate uncertainty predictions through each model. Frequentist methods treat parameters as fixed and unknown, encouraging traditional optimization-based parameter inference and model confidence intervals as discussed in [221]. In contrast, the Bayesian framework treats parameters as random variables and incorporates a priori knowledge, via prior parameter distributions, and a likelihood function to construct posterior distributions that best explain the observed data. Sampling from the posterior distributions can then propagate uncertainties forward and construct model confidence and credible intervals. Bayesian methods provide more detailed uncertainty but are more computationally expensive than frequentist method. However, frequentist parameter inference can fail if parameters are non-identifiable or highly correlated, whereas the Bayesian methods can expose these relationships while still providing information about parameter uncertainty. Below we describe both methods, highlighting the advantages and disadvantages for each.

7.4.4.1 Frequentist analysis

In the frequentist framework, confidence and prediction intervals are constructed for both the parameters and the model predictions where data is available. To compute the confidence intervals for a given parameter, we consider estimated parameters $\hat{\theta}$ that minimize the cost function J defined in equation (7.11) and the associated local sensitivity matrix $\hat{S} = \tilde{S}(t; \hat{\theta})$. Using this framework and the constant, estimated observation variance \hat{s}^2 from equation (7.18), the parameter confidence intervals are calculated as

$$\theta_i^{CI} \equiv \left[\hat{\theta}_i - t_{N-P}^{1-\alpha/2} \hat{s} \sqrt{(\hat{S}^T \hat{S})^{-1}}, \hat{\theta}_i + t_{N-P}^{1-\alpha/2} \hat{s} \sqrt{(\hat{S}^T \hat{S})^{-1}} \right], \quad (7.20)$$

where $t_{N-P}^{1-\alpha/2}$ denotes a t -statistic with $N - P$ degrees of freedom and a $1 - \alpha = 0.95$ confidence level, N is the number of data points, and P is the number of parameters. The confidence interval for the model response, $y^{CI}(t)$, can be computed in a similar fashion

$$y^{CI}(t_i) \equiv \left[y(t_i; \hat{\theta}) - t_{N-P}^{1-\alpha/2} \hat{s} \sqrt{\Gamma_i}, y(t_i; \hat{\theta}) + t_{N-P}^{1-\alpha/2} \hat{s} \sqrt{\Gamma_i} \right], \quad (7.21)$$

where $\Gamma_i = G_i^T (\hat{S}^T \hat{S})^{-1} G_i$ and

$$G_i^T = \left(\frac{\partial y(t_i; \hat{\theta})}{\partial \tilde{\theta}_1}, \dots, \frac{\partial y(t_i; \hat{\theta})}{\partial \tilde{\theta}_p} \right).$$

Lastly, the prediction intervals for the model response are calculated as

$$y^{PI}(t_i) \equiv \left[y(t_i; \hat{\theta}) - t_{N-P}^{1-\alpha/2} \hat{s} \sqrt{1 + \Gamma_i}, y(t_i; \hat{\theta}) + t_{N-P}^{1-\alpha/2} \hat{s} \sqrt{1 + \Gamma_i} \right]. \quad (7.22)$$

It should be noted that since data is only collected at the inlet of the MPA, we cannot estimate the variance \hat{s}^2 that would be needed to construct accurate confidence and prediction intervals in other vessels of the network.

7.4.4.2 Bayesian analysis

In contrast to the frequentist framework, Bayesian credible and prediction intervals are computed from the posterior distributions of the parameters in question. In this study, we employ the Delayed Rejection Adaptive Metropolis (DRAM) algorithm [89, 127, 186] to determine posterior parameter distributions and study pairwise parameter correlations (see Appendix C for more details on the algorithm).

The parameter posterior, $\pi(\theta|y)$ is computed using Bayes' formula

$$\pi(\theta|y) = \frac{\pi(y|\theta)\pi_0(\theta)}{\pi(y)} = \frac{\pi(y|\theta)\pi_0(\theta)}{\int_{\mathbb{R}^p} \pi(y|\theta)\pi_0(\theta)d\theta} \quad (7.23)$$

for the data y , where $\pi(y|\theta)$ is the likelihood function, $\pi_0(\theta)$ is the prior distribution, and $\int_{\mathbb{R}^p} \pi(y|\theta)\pi_0(\theta)d\theta$ is a normalization factor. We assume that the prior distribution $\pi_0(\theta)$ is flat (i.e. uniformly distributed) over the physiological bounds, and that the likelihood function $\pi(y|\theta)$ in (7.23) can be specified and reflects statistical properties of the data. We assume that the measurement errors, ϵ_i , are normally distributed, independent and identically distributed (iid) random variables with mean zero and constant variance σ_ϵ^2 , i.e. $\epsilon_i \sim \mathcal{N}(0, \sigma_\epsilon^2)$. Under these assumptions the likelihood function is given as

$$\mathcal{L}(\theta, \sigma_\epsilon^2|y) = \pi(y|\theta) = \frac{1}{(2\pi\sigma_\epsilon^2)^{N/2}} e^{-\chi^T \chi / 2\sigma_\epsilon^2}, \quad (7.24)$$

where χ is the residual defined in equation (7.11).

For MCMC methods, convergence to the true posterior distribution is only guaranteed for an infinite number of samples, i.e. $M \rightarrow \infty$. In practice, the number of samples should be large enough to ensure that the chains have visibly converged. In this study, we use the Geweke test [81], which determines convergence of a MCMC chain by comparing the first 10% and last 50% of the chain for significant differences in the mean and computes a p-value from a Z-statistic. p-values close to zero indicate that the null hypothesis of equal means between the two chains should be rejected, suggesting non-convergence.

Subsequently, the posterior distribution $\pi(\theta|y)$ is used to compute credible and prediction intervals for the model response. To do so, we draw 2,000 samples from the posterior distribution propagating uncertainties forward through the model computing both credible and prediction intervals for the pressure in the MPA [89, 221].

7.5 Results

7.5.1 Sensitivity Analysis

Figure 7.4 shows the sensitivity of MPA pressure predictions for the 4 parameters in the control and hypoxic mouse. Normalized pressure and flow waveforms are plotted in the background to help identify which sections of the cardiac cycle (e.g., systole from (b)-(d) or diastole from (a)-(b) and (d)-(a)) are most sensitive to these parameters. Results indicate that r_d is the most influential parameter throughout the cycle for all networks in both mice. Analysis of the remaining parameters show that the vessel stiffness β becomes more influential as more branches are added, while the proximal resistance r_p scaling factor becomes less influential, indicating that model sensitivity to the proximal resistances R_p is reduced. The compliance scaling factor c hardly changes for the control mouse whereas the hypoxic mouse shows a decrease in influence as more vessels are added. Analysis of the sensitivities over the cardiac cycle reveals that model predictions are more sensitive to r_p than β during systole (between (b) and (d)) for the SV model, but switch in the FN model. Moreover, r_d has the greatest influence on the model prediction during diastole (from (a)-(b) and (d)-(a)), i.e. the sensitivity value decreases with increasing flow and pressure. The model sensitivity to the scaling factor c oscillates over the cardiac cycle, having the largest relative influence on model predictions at the start and end of systole (from (b)-(c) and (d)-(a)). The sensitivity curves illustrate a change in behavior over time for increasing network sizes, e.g. the peak of the β sensitivity curve occurs later in the cardiac cycle in the FN model in comparison to the SV model.

Figure 7.5 shows the scaled average elementary effects compared to the standard deviation from the global sensitivity analysis. Both the control and hypoxic models are plotted against each other for the SV, SB, and FN networks. These results agree with the local analysis, as the global sensitivity analysis shows that the r_d scaling parameter has the largest influence (characterized by μ^*) and the largest variability in influence (characterized by σ) regardless of the network size or disease. The value of σ for c in the control mouse is consistently larger than the average influence of μ^* regardless of model, yet the hypoxic mouse has a relative decrease in σ when moving from the SV model to the SB and FN models. Results show that r_d has the largest interaction and/or nonlinear effect while r_p has the smallest σ , regardless of the disease or model type.

In summary, the global analysis shows that the stiffness parameter β (for both control and hypoxic mice) becomes more influential as more vessels are added, while the compliance scaling factor c has a high variance across all three model types. These results indicate that the influence of compliance on MPA pressure is highly dependent on the parameter space for β , r_p , and r_d . Overall, the parameter rankings, shown in Figure 7.6, are consistent between the local and global methods with the exception of the compliance scaling factor c , which is shown to be more influential when doing global sensitivity analysis. The discrepancy between the two methods arises because the global rankings account for the variability in the model influence, and c tends to have large values of σ .

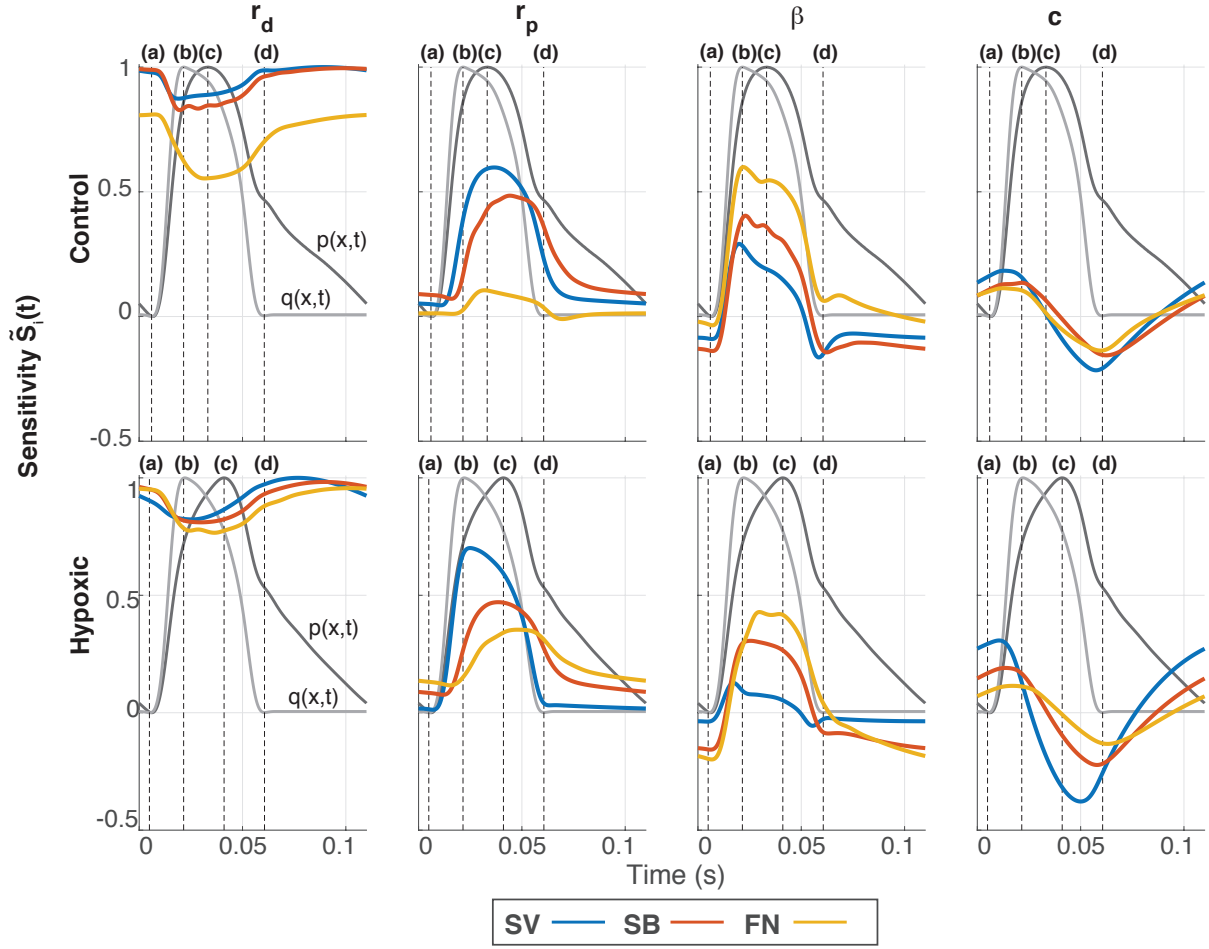


Figure 7.4 Normalized local sensitivities in the root of the MPA, pressure during the cardiac cycle for the SV (blue), SB (red), and FN (yellow) models. Light and dark gray lines denote the normalized flow and pressure predictions, respectively. Dashed vertical lines indicate (a) the start of systole, (b) the time of maximum flow, (c) the time of maximum pressure, and (d) the start of diastole. Results show that r_d is the most influential parameter regardless of model or disease type and that vessel stiffness β increases in influence as more vessels are added to the system.

7.5.2 Correlation Analysis

The local parameter sensitivities are used to compute the covariance (equation (7.18)) and correlation matrices for each model. For the control model, no parameters are above the correlation cutoff $|v_{ij}| \leq 0.90$. However, for all three hypoxic networks β and r_p are correlated above 0.9. To explore this correlation over a larger parameter space, we conducted a DRAM simulation on each model for the control and hypoxic mouse and plotted pairwise parameter posterior distributions. Results for the hypoxic FN model, shown in Figure 7.7a, agree with the local covariance analysis that β and r_p are correlated, providing a correlation value of 0.97 between the two parameters. While correlations are the strongest for the hypoxic FN model, some correlation persisted in all networks ($0.85 < |v_{ij}|$).

We fixed β at its nominal value and repeated DRAM simulations, shown in Figure 7.7b, which

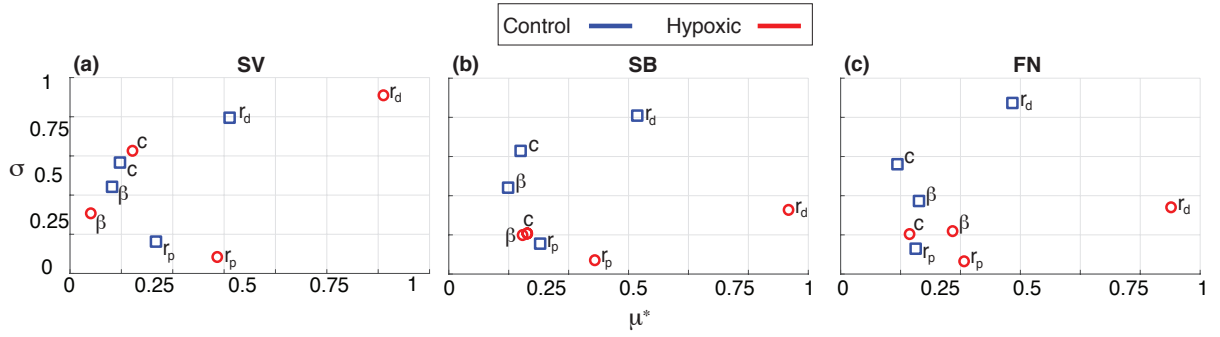


Figure 7.5 Normalized Morris' indices μ^* and σ for the (a) SV, (b) SB, and (c) FN models in the control (blue squares) and hypoxic (red circles) mice. For both mice, r_d has the largest value of μ^* and σ . The global sensitivities show that the parameter β increases in influence as more vessels are added to the network.

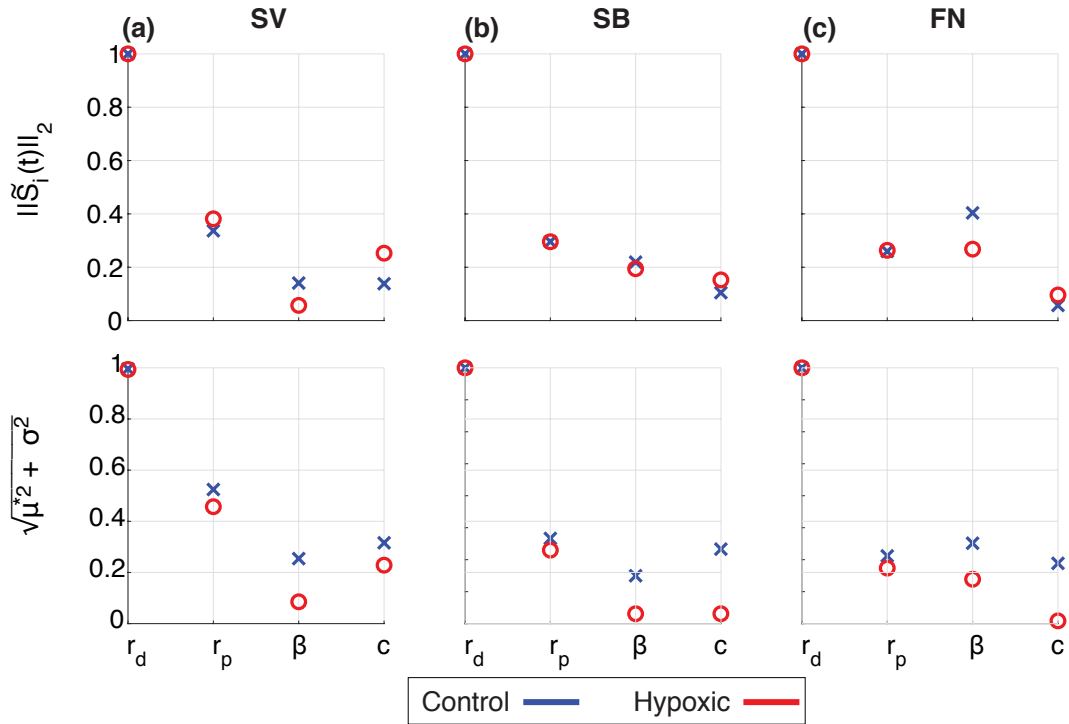


Figure 7.6 Ranking of parameters in the (a) SV, (b) SB, and (c) FN models based on their local and global sensitivity results. All ranking metrics were scaled to the rank value of r_d , which was largest in magnitude. Blue x's indicate control models while red circles indicate hypoxic models.

reduced parameter correlations below our threshold 0.9. As a result of this analysis, we let β vary between groups (control and hypoxic) but assume it is constant for all three networks. This is advantageous, as it allows us to compare models where the large vessel stiffness is the same within each disease type.

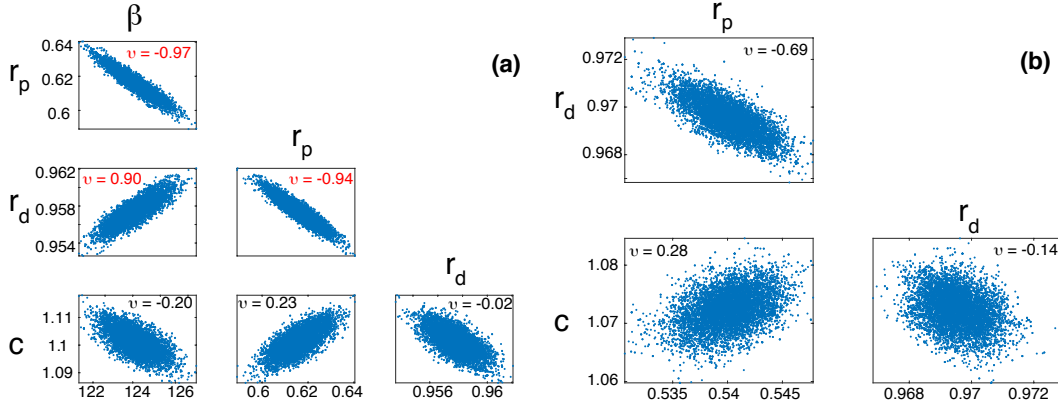


Figure 7.7 (a) Pairwise plots from 10,000 iterations in DRAM for the hypoxic FN model using the full parameter set $\theta = (\beta, r_p, r_d, c)$; (b) Pairwise plots from DRAM when β was fixed at its nominal value. (a) shows that the parameters β and r_p are highly correlated, as was indicated by the structured correlation results. By fixing β (panel (b)), the correlation between parameters, denoted by ν , decreases.

7.5.3 Frequentist analysis

As noted in Sec. 7.5.2, we estimate a single β value and individual scaling factors for each network, i.e. we estimate a total of 10 parameters

$$\hat{\theta}_0 = \{\hat{\beta}, \hat{r}_p^{SV}, \hat{r}_d^{SV}, \hat{c}^{SV}, \hat{r}_p^{SB}, \hat{r}_d^{SB}, \hat{c}^{SB}, \hat{r}_p^{FN}, \hat{r}_d^{FN}, \hat{c}^{FN}\} = \{\hat{\beta}, \hat{\theta}^{SV}, \hat{\theta}^{SB}, \hat{\theta}^{FN}\} \quad (7.25)$$

minimizing the least squares cost defined in (7.11) for the control and hypoxic mouse.

To ensure convergence, we propagate eight initial values sampled from a uniform parameter distribution over the intervals given in Sec. 7.5.1. Nominal and optimal model predictions are depicted in Figure 7.8 (panels (a),(b) and (c),(d), respectively) and the optimal parameter values are given in Table 7.3. Results depicted in Figure 7.8 show that all models fit the data well after optimization, significantly improving the costs, provided in Table 7.4, from the nominal parameter fits. First, we note that all three models provide an equally good fit within disease type, as the least squares error is of the same order of magnitude for each network. However, simulations do reveal that the hypoxic model fits the data better than the control model, as the least squares error is an order of magnitude smaller, 10^{-2} vs. 10^{-1} .

Table 7.3 reports estimated vessel stiffness β , optimal values for the scaling factors r_p, r_d and c , the ratio of peripheral to total network resistance R_p/R_T , the total peripheral resistance R_T^{WK} , and the peripheral compliance C^{WK} for each network and each mouse pre and post optimization. The latter is done using the optimized scaling factors in equation (7.10). The R_p/R_T ratio decreases as the number of vessels in the network is increased for both the control and hypoxic mouse. The total resistance R_T^{WK} was consistently higher in the hypoxic mouse, whereas the compliance C^{WK} was higher for the control mouse. For both the control and hypoxic mice, the total peripheral resistance

R_T^{WK} decreased as more vessels were added to the network. Confidence intervals (Table 7.5) for the parameters are calculated around the optimized values $\hat{\theta}$ obtained from the SQP algorithms. Results show that the intervals for the control model parameters are larger than those found for the hypoxic parameters, a result of the larger residual obtained with the control models. For the FN model, we calculated frequentist prediction intervals for MPA pressure using the optimized parameter values and equation (7.21) (compared to Bayesian results in Figure 7.10).

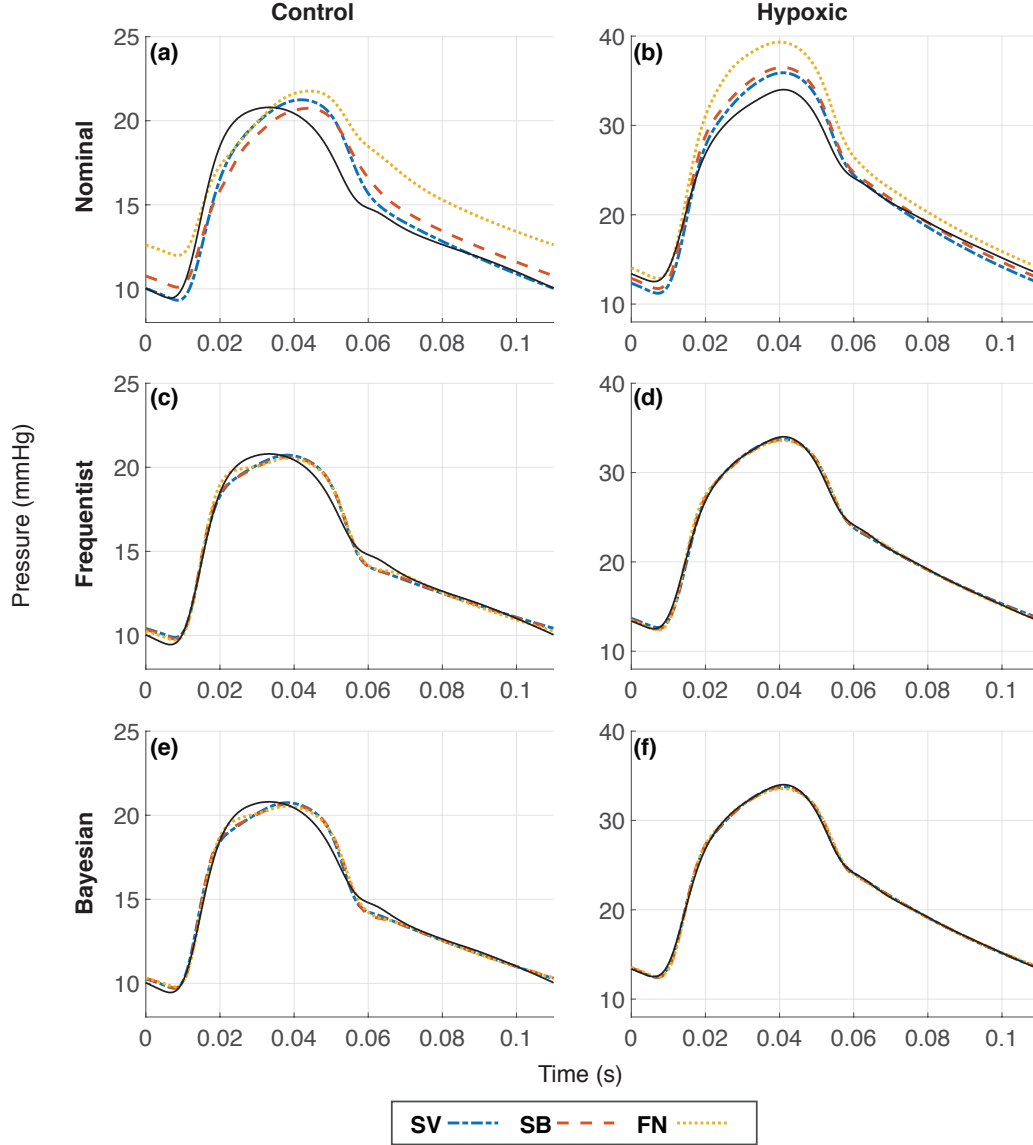


Figure 7.8 The MPA pressure data (black, solid curve) and predictions with the SV (dash-dot, blue line), SB (dashed, red line), and FN (dotted, yellow line) models. MPA pressure waveforms for the control (left column) and hypoxic (right column) models are plotted using the nominal parameters ((a) and (b)), the optimized parameter values ((c) and (d)), and the maximum a posteriori parameters ((e) and (f)).

Table 7.3 Nominal and optimized parameter values and the relative change to the nominal estimates after optimization. The wall parameter β was the same for all three models in each mouse.

Model	Parameter	Control			Hypoxic		
		Nominal Estimate	Optimized Value	Relative Change (%)	Nominal Estimate	Optimized Value	Relative Change (%)
-	β	26.0	42.9	65	150.9	136.6	-10
SV	r_p	1	8.84×10^{-1}	-12	1	8.86×10^{-1}	-12
SV	r_d	1	1.02	2	1	1.02	2
SV	c	1	1.44	44	1	1.21	21
SV	R_p/R_T	0.2	0.18	-11	0.2	0.18	-11
SV	R_T^{WK}	78.4	77.6	-1	147	146	-0.7
SV	C^{WK}	1.7×10^{-3}	2.5×10^{-3}	44	5.9×10^{-4}	7.1×10^{-4}	21
SB	r_p	1	8.00×10^{-1}	-20	1	8.21×10^{-1}	-18
SB	r_d	1	9.95×10^{-1}	-0.5	1	1.00	0.3
SB	c	1	1.34	34	1	1.14	14
SB	R_p/R_T	0.2	0.17	-17	0.2	0.17	-15
SB	R_T^{WK}	78.4	74.9	-4	147	142	-3
SB	C^{WK}	1.7×10^{-3}	2.3×10^{-3}	34	5.9×10^{-4}	6.7×10^{-4}	14
FN	r_p	1	1.34×10^{-1}	-87	1	5.40×10^{-1}	46
FN	r_d	1	8.82×10^{-1}	-12	1	9.70×10^{-1}	3
FN	c	1	1.62	62	1	1.07	7
FN	R_p/R_T	0.2	0.04	-82	0.2	0.12	-39
FN	R_T^{WK}	78.4	57.4	-27	147	130	-12
FN	C^{WK}	1.7×10^{-3}	2.8×10^{-3}	62	5.9×10^{-4}	6.3×10^{-4}	7

Units: β (mmHg), R_T^{WK} (mmHg s/ml), C^{WK} (ml/mmHg), and $r_p, r_d, c, R_p/R_T$ (dimensionless)

7.5.4 Bayesian analysis

DRAM simulations were initialized using the estimated parameters from the SQP optimization. The stiffness parameter was fixed at its optimal value $\hat{\beta}$, while the scaling parameters $\{r_p, r_d, c\}$ were allowed to vary. Each simulation used a 2,000 iteration burn-in period to initialize a 10,000 iteration chain, which allowed for convergence to the posterior distribution. We prescribed a uniform prior distribution spanning $\pm 50\%$ of the optimized value for each parameter, facilitating adequate exploration of the parameter space. The posterior densities for all three models are shown in Figure 7.9, with initial point-estimates (the optimized values from the SQP optimization, $\hat{\theta}$) marked with asterisks on the density curves. We used the Geweke test statistics for each DRAM chain to test that the iteration chains had converged. All chains had a p -value ≥ 0.98 for all models and both animals (control and hypoxic), suggesting convergence.

Results show that the maximum a posteriori (MAP) parameter value corresponding to the maximum value of the posterior density aligns with the SQP optimization results and that the posterior distributions are unimodal, indicating an agreement between frequentist and Bayesian methodologies. This is also observed in Figure 7.8, as the frequentist and Bayesian parameter

estimates (panels (c),(d) and (e),(f), respectively) produce nearly identical predictions of MPA pressure. The width of the parameter posteriors, calculated from the variance of the distribution σ_{θ}^2 , are larger for the control model than for the hypoxic model (shown in Table 7.5). This result is similar to the frequentist analysis, as the larger residual in the control prediction leads to wider parameter confidence intervals. These results also agree with the local sensitivity analysis; the width of c is largest, indicating less impact on the model predictions within the physiological parameter space, while r_p and r_d are more influential and hence have narrower distributions. The variance estimates for each parameter are given in Table 7.5.

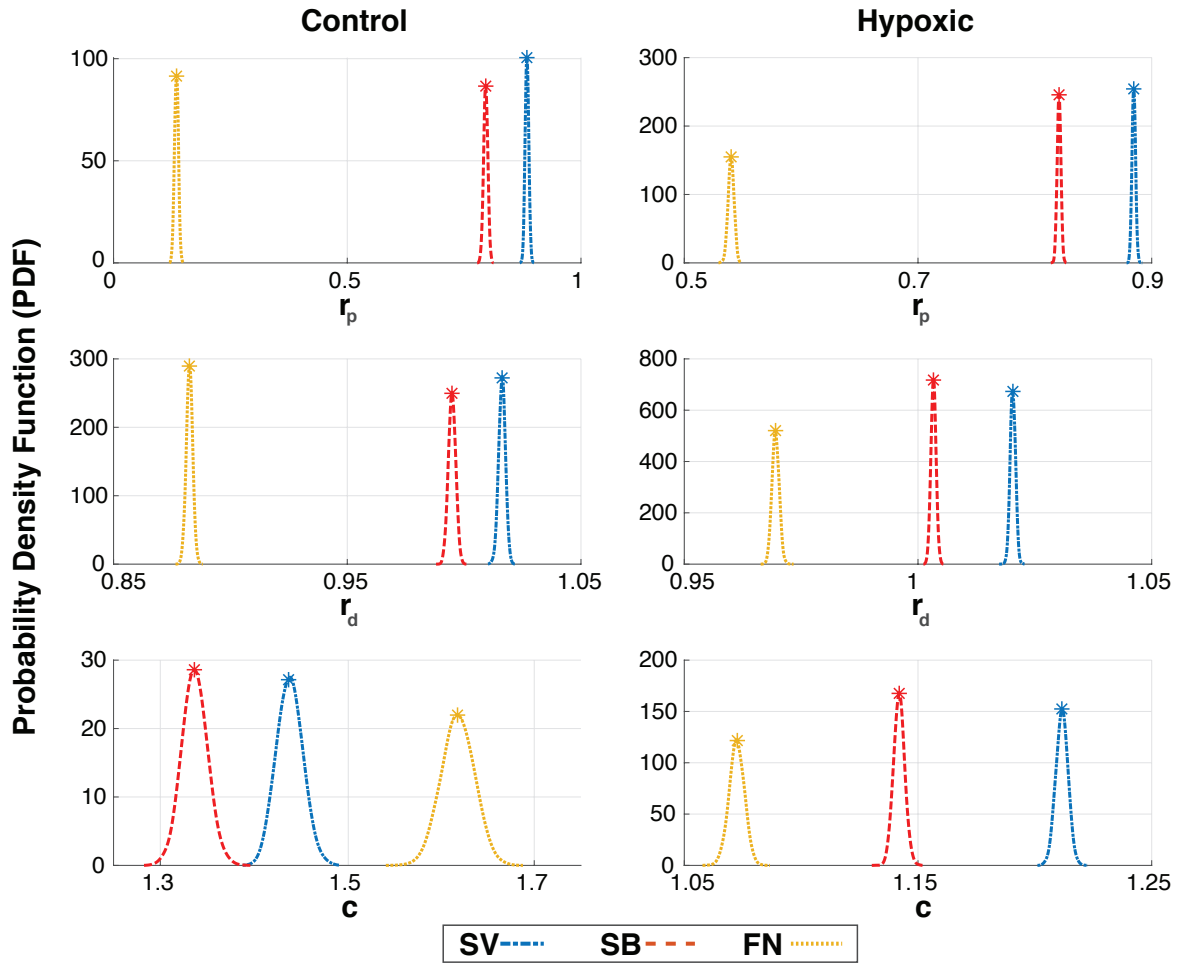


Figure 7.9 Posterior densities obtained from 10,000 chain iterations of DRAM from the SV (dash-dot, blue curve), SB (dashed, red curve), and FN (dotted, yellow curve) models for the control and hypoxic mice. Graphs show results after discarding the 2,000 iteration burn-in period. The parameter values obtained from the SQP optimization are plotted with asterisks on the density curves. Values on the abscissa denote the parameter values for the respective scaling factors.

We draw 2,000 realizations from the parameter posterior densities to construct Bayesian credible

Table 7.4 Least squares cost for all simulations using both frequentist and Bayesian methods.

	Control		Hypoxic	
Model	J_{opt}	J_{DRAM}	J_{opt}	J_{DRAM}
SV	1.71×10^2	1.53×10^2	6.08×10^1	2.12×10^1
SB	1.79×10^2	1.76×10^2	5.28×10^1	5.16×10^1
FN	1.44×10^2	1.38×10^2	7.97×10^1	7.03×10^1

and prediction intervals for MPA pressure. The confidence, prediction, and credible intervals for MPA pressure predictions are shown in Figure 7.10 using the FN model. Results shows that the frequentist and Bayesian intervals agree and that the data lies within the confidence bounds. Similar results are obtained for the SV and SB models, yet it should be noted that intervals are larger in the control mouse than the hypoxic, indicating a greater uncertainty in MPA predictions.

Table 7.5 Frequentist confidence intervals for the optimized Windkessel parameters $\hat{\theta}_{WK} = \{r_p, r_d, c\}$ and Bayesian posterior variances for the control and hypoxic models.

		Control			Hypoxic		
Model	Parameter	Optimized Value	Confidence Interval	Posterior σ_θ^2	Optimized Value	Confidence Interval	Posterior σ_θ^2
SV	r_p	8.84×10^{-1}	$[8.76, 8.93] \times 10^{-1}$	7.93×10^{-5}	8.85×10^{-1}	$[8.81, 8.88] \times 10^{-1}$	1.56×10^{-5}
SV	r_d	1.02	[1.01, 1.02]	1.25×10^{-5}	1.02	[1.02, 1.02]	2.54×10^{-6}
SV	c	1.44	[1.42, 1.46]	9.20×10^{-4}	1.21	[1.21, 1.22]	3.98×10^{-5}
SB	r_p	7.96×10^{-1}	$[7.85, 8.08] \times 10^{-1}$	1.06×10^{-4}	8.21×10^{-1}	$[8.17, 8.24] \times 10^{-1}$	1.53×10^{-5}
SB	r_d	9.95×10^{-1}	$[9.92, 9.98] \times 10^{-1}$	1.45×10^{-5}	1.00	[1.00, 1.00]	1.57×10^{-6}
SB	c	1.34	[1.32, 1.36]	1.15×10^{-3}	1.14	[1.14, 1.15]	4.05×10^{-5}
FN	r_p	1.35×10^{-1}	$[0.75, 1.95] \times 10^{-1}$	2.76×10^{-4}	5.40×10^{-1}	$[5.31, 5.49] \times 10^{-1}$	3.04×10^{-4}
FN	r_d	8.82×10^{-1}	$[8.79, 8.86] \times 10^{-1}$	9.93×10^{-6}	9.70×10^{-1}	$[9.68, 9.71] \times 10^{-1}$	1.04×10^{-5}
FN	c	1.62	[1.60, 1.64]	1.85×10^{-4}	1.07	[1.07, 1.08]	1.16×10^{-4}

7.5.5 Network Predictions

Figure 7.8 illustrates that all three models can predict nearly identical dynamics in the MPA. However, due to the limited number of vessels, both the SV and SB models cannot predict pressure multiple generations away from the MPA, while with the FN model we can predict pressure in all 21 vessels. We used Bayesian uncertainty propagation to understand how parameter uncertainty affects pressure predictions downstream. Figure 7.10 shows the pressure data in the MPA compared to frequentist and Bayesian prediction intervals, along with uncertainty bounds for seven vessels in the FN model for both the control and hypoxic mouse.

Model predictions in vessels immediately distal to the MPA retain a similar systolic and pulse

pressure (the difference between the maximum and minimum pressure) as the MPA. In contrast, the distal vessel predictions show a decreased pulse pressure, especially in the control mouse. The pulse pressure decreased by 68% in the control vs. 28% in the hypoxic mouse, indicating larger pressure dissipation in the control mouse.

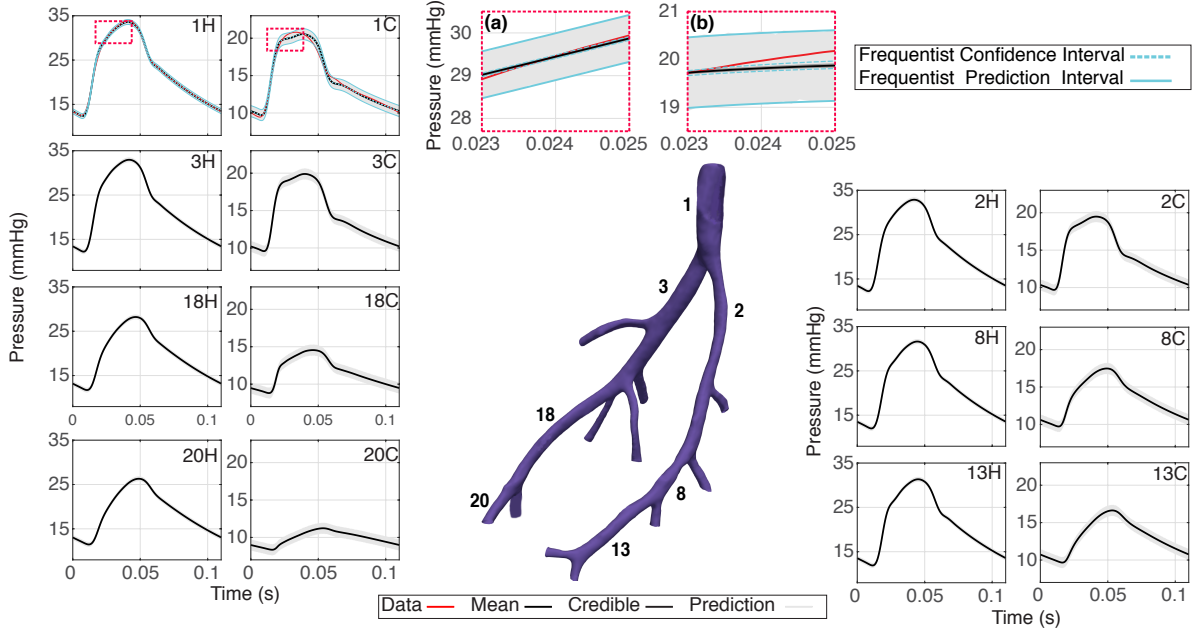


Figure 7.10 MPA pressure uncertainty in the proximal and downstream vasculature computed using frequentist and Bayesian techniques. For each vessel blood, pressure predictions in the left column are for the control mouse (denoted by a C) while the right column show pressure predictions in the hypoxic mouse (denoted by an H). Panels (a) and (b) show a zoom in during systole, illustrating that the frequentist analysis agrees with Bayesian estimates and that the data lies within the uncertainty bounds. These panels show that the uncertainty bounds are wider for the control mouse than the hypoxic mouse agreeing with observations that the hypoxic model fits the data better.

7.6 Discussion

This study investigates how the behavior of a 1D fluids model changes with network size and pathology. We used local and global sensitivity analysis to determine parameter influence and model sensitivity under different network sizes, and then used local correlation analysis and MCMC pairwise plots to quantify parameter correlations. Subsequently, we used parameter inference and uncertainty quantification to identify optimal parameter values and study the effects of inherent parameter uncertainty. Overall, our results show that the peripheral vascular resistance r_d is the most influential parameter, and that the large vessel stiffness β increases in influence with network size, while the model sensitivity to peripheral vascular compliance c and resistance r_p decreases

with network size.

Sensitivity Ranking

The three representative networks (SV, SB, FN) studied here contain different 1D to 0D model ratios. Results shown in Figure 7.6 show that the vessel stiffness β becomes more influential in determining model dynamics as more vessels are added to the network. As we add more vessels, we approximate less of the downstream vasculature via Windkessel models, hence minimizing their influence on MPA predictions. Specifically, the scaling factors r_p and c become less influential, especially in the hypoxic mouse, suggesting that inferring β is more important in large networks, while inferring r_p and c is less critical. The one exception to this is the compliance scaling factor c for the control mouse, which is ranked more influential by the global analysis. The large nonlinear/interaction effects that are attributed to compliance play a larger role in the control mouse because the large vessels are less stiff (i.e. β is smaller), which likely makes the model predictions more sensitive to changes in peripheral compliance. We recall that the parameter r_p scales the proximal resistance R_p , representing the characteristic peripheral impedance, and c scales the peripheral compliance C . These results suggest that larger networks encompassing more of the pulmonary arteries may be less sensitive to changes in proximal resistance, allowing for a fixed value of R_p at each terminal vessel or a simpler boundary condition. This would substantially reduce the dimensionality of the problem when doing parameter inference.

Quantifying the influence of the Windkessel parameters can assist in understanding which parameters provide more information for the optimization routine, especially when the dimensionality of the network is large compared to the amount of data available. Similar to previous findings [37], the high sensitivity of R_d suggests that more detailed modeling of the peripheral vasculature may be beneficial. Moreover, we showed that the number of vessels in the model dictates how influential Windkessel parameters are, which could ultimately lead to changes in estimates during parameter inference. From a clinical perspective, this could change the interpretation of PH severity and could alter hypothesized treatment strategies such as target pharmaceutical therapies [220] as regions of high distal resistance (i.e. R_d) might change with network size. Overall, the local and global sensitivity methods give similar parameter rankings, as shown in Figure 7.6, suggesting that the local sensitivity analysis, which is less computationally expensive, provides accurate information about the model sensitivity.

Time-varying Sensitivities

As depicted in Figure 7.4, the parameter β has the largest effect on pressure predictions during systole, where the volume changes are the largest, thereby increasing vessel strain and blood pressure. These results are similar to the findings by Xiu et al. [265] who showed that pressure wave reflections returning at peak systole are affected by vessel stiffness. The proximal resistance, $\hat{R}_p = \hat{r}_p R_p$, has a maximum influence aligned with the maximum systolic pressure in the SV model, but achieves its maximum influence towards the start of systole in the control FN model and the end of systole in the

hypoxic FN model. This result suggests that both the large artery stiffness and proximal downstream resistance have an immediate effect on the pressure for the SV model, but that their effect on larger network pressure predictions is altered. This indicates that features of the larger network are shifting the peak components of the sensitivity curves to other points in the cardiac cycle. Similarly, the c sensitivity curves show a shift in where their maxima and minima occur when adding vessels to the system. One possible explanation of this phenomenon is that adding more vessels to the network introduces impedance mismatches at vessel junctions and at the boundary, introducing wave reflections in the pulse-wave propagation. This would make the time-varying sensitivities shift in time, since changes in model parameters now change the propagation of pressure downstream. A more advanced global sensitivity metric for the variance of the time-varying sensitivities may indicate how sensitivities are changing with network size and over the cardiac cycle [58].

The peripheral resistance $\hat{R}_d = \hat{r}_d R_d$ has the largest influence on pressure during diastole and shows decreased influence during systole, obtaining its largest values during periods of minimal flow. Physiologically, we expect that distal vascular resistance should be the most influential parameter during diastole, as this would indicate a greater diastolic pressure maintained due to higher resistance to flow downstream. This result agrees with the previous studies [37, 148] in the systemic circulation which showed that the influence of boundary resistance was greatest during diastole. The model sensitivity to compliance oscillates between systole and diastole, but decreases for an increased number of vessels in the system, indicating a stronger dominance of model behavior from 1D model parameters (i.e. β).

Parameter Inference

The 1D models presented here include at most 21 vessels with 11 terminal vessels (giving 21 stiffness parameters β and 33 outlet boundary conditions). As discussed in the methods section, resistors and capacitors in series and parallel can be unidentifiable and highly correlated, making it nearly impossible to estimate individual outlet parameters without additional data [107, 165, 180, 182, 221]. We introduced scaling factors r_p and r_d for the proximal and distal resistance (R_p and R_d) and c for the total peripheral compliance (C) to remedy this issue. We argue that this method of parameter reduction is advantageous in comparison to traditional subset reduction techniques [60, 165, 182] because it maintains the ability to draw inference about the entire pulmonary circulation, rather than reducing the parameter space to a subset that is not characteristic of the entire vasculature. If additional data are available downstream, e.g. in the left and right pulmonary artery, scaling factors may be identified for each distal vascular bed.

Both the correlation analysis and the DRAM posteriors showed that the hypoxic parameter set had significant correlations between β and r_p ($|v_{ij}| > 0.95$ vs. $|v_{ij}| > 0.85$ for the control mouse). We chose to fix β at a constant value for each disease type across all three models, i.e. we set up an optimization scheme where we estimated a common value of β in each mouse along with estimates of r_p, r_d, c for each network size. This favors previous pulmonary modeling studies [124, 169, 186, 191] which showed physiological results using a fixed, vessel-independent stiffness. The agreement

between local and global correlation analysis reinforces the idea that the computationally cheaper local analysis can assist in parameter reduction before performing any global, Bayesian analysis [142, 164, 182].

For the Bayesian parameter inference (DRAM) we kept β constant at the optimized value, allowing for better construction of the scaling factor parameter posterior distributions. Results show that the hypoxic mouse has a lower peripheral compliance than the control mouse [186, 190]. An interesting observation is the ratio of proximal to total resistance (i.e. R_p/R_T) is nearly the same between disease type in the SV and SB model, but the control FN model shows a drastic reduction in the ratio (0.04, see Table 7.3). Moreover, the total resistance for all three models in each disease type is well approximated by the nominal values, whereas the compliance estimates for the control mouse are much larger than the nominal values. The increased value of c is likely due to an inability to capture the exact dynamics of the control data, indicating more complex vascular wall mechanics and inviting further investigation into complex constitutive equation [135, 190, 192, 225, 240].

The DRAM and uncertainty quantification results support the frequentist analysis results. The overlap between the MAP estimates and the frequentist estimates, as well as the uni-modality of the posterior distributions, indicates that no other local minima exist within the parameter bounds sampled. Frequentist optimization takes significantly less computation time (on the order of hours to days) compared to a Bayesian analysis like DRAM (on the order of weeks), which encourages the use of the frequentist analysis. However, the parameter posteriors provided from DRAM can be used to quantify uncertainty without performing asymptotic analysis, making it a more robust estimate of parametric uncertainty. Likewise, the prediction intervals indicate that both the control and hypoxic models have minimal uncertainty in MPA predictions, as the 95% prediction intervals reveal a ± 1 mmHg band around the mean prediction. Further analysis of the parameter distributions showed that the control mouse has wider bands of uncertainty due to the larger data-misfit.

Physiological Insight

The pulmonary circulation consists of an expansive network of blood vessels, which branch in rapid succession from the MPA to the capillaries, encapsulating the alveoli. It is known that the distal pulmonary vasculature is modulated by disease, both structurally by changing the network morphometry [169, 220] and materially by changing vessel stiffness [120, 135, 245]. Current classification of PH and its progression is based on assessing if the pathophysiology is located in the proximal or peripheral vasculature. A model for a specific PH etiology may only require the proximal arteries (e.g. for studying blood flow in the first pulmonary bifurcation [27]) or might require analysis of dynamics in the entire network, e.g. modeling the influence of downstream thrombosis in chronic thromboembolic PH (CTEPH) on MPA dynamics [119]. Our results indicate that models of different complexity can provide similar predictions of pressure with different physiological parameters. This provides insight into how to develop a multi-scale model that can distinguish characteristics of proximal pulmonary arteries and those of downstream, distal segments. Optimization results (shown in Table 7.4) show that parameters estimated in the hypoxic mouse provide a better fit to

data than those estimated for the control mouse. We hypothesize that this is due to stiffer vessels in the hypoxic model, leading to smaller and more linear area deformation. This makes the linear wall model more appropriate for describing the vessel deformation. Conversely, the control model does not provide as accurate of a fit, likely due to the high compliance in the pulmonary tissue, inducing complex area dynamics. This agrees with previous findings [135, 225, 240] that arterial vessel deformation is nonlinear and viscoelastic in healthy controls. Finally, results from the optimization indicate that the control FN model can better describe the dynamics *in-vivo* than the SV and SB model. The addition of terminal vessels in the system allows for more accurate calibration of the network compliance. However, the hypoxic model best fits the data when only using the SV model, though the magnitude of the cost is of similar magnitude for the SB and FN models.

It is not obvious how to distinguish between “large” and “small” peripheral vessels making it difficult to determine the cutoff between explicit and lumped representation of the vasculature. Three previous studies [62, 68, 148] have examined how model predictions and parameter influence may change when reducing the size of the vascular network in the systemic circulation, showing that model predictions converge at a certain number of vessels. To our knowledge, no previous studies have analyzed the pulmonary circulation in this manner. When using a model of this type for analyzing clinical data, it may not always be advantageous to use the simplest possible model, especially when disease progression initiates global network remodeling. For example, while the SV model is able to match data in the MPA, it cannot characterize features along the pulmonary vasculature, which are essential to study the effect of progressing PH. This point was discussed by Kheifets et al. [119], who highlighted the importance of network size by showing a change in predicted distal wall shear stress due to a change in distal vascular geometry. Moreover, wave propagation cannot be analyzed adequately without considering downstream sites for wave reflections [68, 189, 249] encouraging the use of larger networks. In addition, the interpretation of downstream parameter estimates changes with different network sizes. For example, R_d in the SV model describes the distal resistance of the entire downstream vasculature, while R_d in larger network models describes the lumped vascular resistance immediately distal to the terminal vessels, providing a more specific location for the downstream resistance. In summary, this study reveals that characteristics of the model (i.e. model sensitivity to changes in parameter values) change in larger networks, and encourages a network complexity that best answers the physiologically hypothesis in question. Moreover, the incorporation of a 1D fluids model in clinical decision making must utilize the fact that uncertainties arise when hemodynamic data and image resolution are limited.

Limitations

A limitation of this analysis is that we did not consider the variation in network dimensions within disease type, nor did we account for the uncertainties in topology associated with inaccurate image segmentation. Previous studies have shown that the uncertainty in dimensions can be significant [37, 148, 152, 206, 249], for instance, in the prediction of coronary dynamics around a blockage [61, 206]. However, this analysis has not been done in the case of the pulmonary circulation and invites

similar studies. These results do not account for the uncertainty in measured inflow, which has been addressed previously [31] and can be accounted for using techniques such as Karhunen-L  ve expansions, allowing for discrete representations of continuous random-fields. We hypothesize that the inflow profile is highly influential in predictions of pressure in the pulmonary system; however, this analysis is beyond the scope of the current study and invites future research. We assumed a constant vessel stiffness throughout the network as has been done previously [124, 169, 189]. Stiffness of the proximal pulmonary arteries has been shown to be heterogeneous in control mice [135], yet this change in stiffness has little effect on pressure predictions. In the case of PH, vascular stiffness might be vessel dependent and could provide insight into which vessels are the largest contributors to increased MPA pressure. In addition, the assumption of constant arterial stiffness may very well breakdown if small arteries or arterioles are included in the model, and should be addressed by having an adaptive, non-constant vessel stiffness [135, 168, 169, 225]. Performing a sensitivity analysis on this function may provide a radius dependent model sensitivity to vascular stiffness.

The assumption of iid errors is often made for simplicity when defining the likelihood function (equation (7.24)) for MCMC routines, yet a plot of the residuals in Figure 7.11 shows that the residuals are not independent, as indicated by the oscillatory behavior. In future studies, we propose to address this, e.g. by employing a log-likelihood $\log(\mathcal{L})$, defined as

$$\log(\mathcal{L}) = -\frac{1}{2} \log(\det(2\pi\Sigma)) - \frac{1}{2} \chi^T \Sigma^{-1} \chi, \quad (7.26)$$

where Σ is the covariance matrix between the data points of the time series.

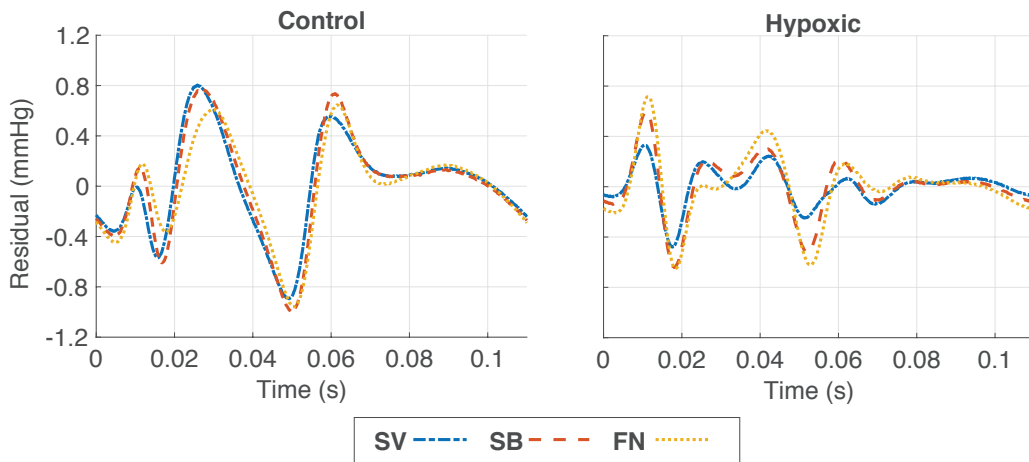


Figure 7.11 Residuals from the model predictions with the optimized parameters. The residual curves indicate that errors are not independent, violating the simplifying assumptions often made about physical models when performing parameter inference.

Results presented here depend on the model analyzed and data available for model validation.

Another limitation in this work is the inability to verify downstream predictions, as data is only measured in the MPA. If more data are available, which is typically the case in systemic cardiovascular disease [4, 21, 27, 62, 68, 157], more parameters may be inferred. Moreover, physiological constraints, such as assumptions of a non-negligible pressure drop, could be enforced to increase the number of identifiable parameters. Larger networks encompassing arterioles could have variable viscosity due to Fahraeus Lindqvist effect [lighthill1975mathematical], which could be addressed using the method proposed in this study.

7.7 Conclusion

The objective of this study is to analyze the sensitivity and uncertainty of a coupled 1D-0D model of pulse wave propagation in the pulmonary circulation using a new reduced parameter set. We analyzed model sensitivity and parameter correlation, estimated identifiable model parameters, determined uncertainty bounds in model predictions, and studied how changing network complexity affects parameter influence. To fit the model to data, we estimated vessel stiffness and global scaling parameters that adjust Windkessel parameters for a control and a hypoxic mouse in three networks of varying complexity. Results showed that the hypoxic mouse has stiffer vessels, with both proximal (parameterized by β) and peripheral (parameterized by C) vessels being stiffer. Moreover, we showed that distal resistance R_d has a larger influence on model predictions than other parameters, and that the influence of vascular stiffness β increases as more vessels are added to the network. The observation that the parameters' effect on the model output (MPA pressure) varies with network complexity is essential to account for when developing models that delineate proximal vs. peripheral vascular disease. Future studies will investigate how these results play a role in human models and whether a similar analysis can be used for full models of the pulmonary circulation, including arterial and venous structures.

CHAPTER

8

INFLUENCE OF IMAGE SEGMENTATION ON 1D PULMONARY HEMODYNAMICS

The study “Influence of image segmentation on one-dimensional fluid dynamics predictions in the mouse pulmonary arteries” was published in the *Journal of the Royal Society Interface*, volume 16, issue 159, in 2019. Contributions included the image segmentation (done jointly with a high school intern at NC State), creation of network analysis algorithms, design of an adaptive 1D model framework, model simulations and uncertainty quantification, and writing a majority of the manuscript. Second author Mihaela Paun contributed the results and text regarding Gaussian process (GP) regression.

8.1 Abstract

Computational fluid dynamics (CFD) models are emerging tools for assisting in diagnostic assessment of cardiovascular disease. Recent advances in image segmentation has made subject-specific modelling of the cardiovascular system a feasible task, which is particularly important in the case of pulmonary hypertension (PH), requiring a combination of invasive and non-invasive procedures for diagnosis. Uncertainty in image segmentation propagate to CFD model predictions, making quantification of segmentation induced uncertainty crucial for subject-specific models. This study quantifies the variability of one-dimensional (1D) CFD predictions by propagating the uncertainty of network geometry and connectivity to blood pressure and flow predictions. We analyse multiple segmentations of a single, excised mouse lung using different pre-segmentation parameters. A custom algorithm extracts vessel length, vessel radii, and network connectivity for each segmented pul-

monary network. Probability density functions are computed for vessel radius and length and then sampled to propagate uncertainties to hemodynamic predictions in a fixed network. In addition, we compute the uncertainty of model predictions to changes in network size and connectivity. Results show that variation in network connectivity is a larger contributor to hemodynamic uncertainty than vessel radius and length.

8.2 Introduction

Definitive diagnosis of pulmonary hypertension (PH), defined as a mean pulmonary arterial blood pressure ≥ 25 mmHg, requires a series of medical tests including invasive right-heart catheterization and non-invasive computed topography (CT) imaging of the heart and lungs [131]. Diagnostic protocols interpret each data source independently to make an ultimate decision about disease classification and severity [70], but recent studies [191, 235] have proposed assimilation of hemodynamics and imaging data with CFD modelling, providing insight into the structure and function of the pulmonary system.

Medical imaging and image segmentation have emerged as powerful non-invasive tools for disease diagnostics [11, 54, 176], providing an abundance of data for analysing the structure and function of the cardiovascular system under physiological and pathological conditions [131]. Advances in image segmentation include semi- and fully-automated algorithms for geometric reconstruction of complex vascular regions [93, 242]. However, inherent uncertainty is present as most image segmentation software require manual specification of the image intensity thresholds (pre-segmentation parameters) between background and foreground. For example, van Horssen et. al [100] showed that variation in image resolution affected the cumulative volume of a cast of the coronary arterial tree after segmentation. Rempfler et. al [197] compared segmentation algorithms on retinal images, showing that posterior probability estimates for foreground pixels varied with different segmentation techniques when compared to the true segmentation or so-called “ground-truth”. In contrast to the aforementioned studies, in-vivo images are only captured up to a finite resolution, which makes ground-truth rendering impossible. These two studies quantified variability in segmented networks but did not investigate how this uncertainty affected pulsatile hemodynamics.

Hemodynamic predictions (e.g., cross-sectional averaged flow and pressure) [120] in the pulmonary vasculature are often computed using either three-dimensional (3D) or one-dimensional (1D) [191] CFD models. 3D models predict local flow patterns with more precision [235] but are computationally expensive, making it difficult to perform multiple forward model evaluations for uncertainty quantification, i.e. UQ [103]. For instance, Sankaran et al. [206] computed 3D CFD model sensitivity to coronary stenosis diameters, using surrogate model approximations to combat high computational cost. However, they did not account for possible changes in network connectivity (i.e. location of bifurcations or trifurcations) nor for the uncertainty from the initial segmentations of the vasculature. In contrast, 1D models are more computationally efficient, reducing the need for surrogates and allowing for investigations into variability of network connectivity. Moreover, a

recent study [5] of the coronary vasculature showed that 1D models attain similar hemodynamic predictions as 3D when using appropriate boundary conditions. Recent studies analysed 1D systemic arterial models [100, 201] to understand how uncertainty in network structure impacts hemodynamics. Fossan et al. [68] devised an optimisation strategy to determine the number of vessels needed to match hemodynamic predictions in the coronary arteries, and Huberts et al. [103] used polynomial chaos expansion to quantify the sensitivity of flow predictions to variations in vessel radius. In contrast to the systemic circulation, the pulmonary vasculature is more compliant, branches more rapidly, and operates at a much lower mean pressure, indicating that results from the systemic circulation may not be valid for comparison.

The total uncertainty in the hemodynamic prediction is a combination of uncertainty in the model parameters and uncertainty from the modelling framework. As noted above, several previous studies have studied uncertainty with respect to prescribed hemodynamic parameters and the 1D approximation, but to our knowledge this is the first known investigation of the impact of uncertainties in network reconstruction on CFD simulations in the pulmonary vasculature. Specifically, in this chapter it is examined how pre-segmentation parameters impact estimated vessel radius, vessel length, and network connectivity, and this uncertainty is propagated to hemodynamic predictions in the pulmonary circulation. To do so, multiple segmentations of a microcomputed tomography (micro-CT) image from a mouse pulmonary arterial tree are analysed. The uncertainty resulting from the multiple segmentations is propagated using a 1D CFD model by constructing the model domain from each segmentation. Inverse UQ is performed by constructing probability density functions (pdfs) for vessel radii and lengths from network segmentations, and then propagating their uncertainty through to the model outputs, pulmonary blood flow and pressure (forward UQ) via Monte Carlo sampling. Uncertainty in hemodynamic predictions is quantified by analysing three sets of predictions (depicted in Figure 8.1 predictions using 25 segmented networks (total variation); 2) predictions from a representative network with fixed connectivity when drawing realisations of length and radius perturbations (geometric parameter variation); and 3) predictions from the same representative network when geometric parameters are fixed, but connectivity and network size are varied (network variation). UQ is an essential component of the model analysis when computational models are integrated into clinical protocols. The animal dataset used here [232, 245] serves as a preliminary step in understanding disease progression and has potential for extrapolation to human PH.

8.3 Materials and methods

8.3.1 Experimental data

This study uses existing micro-CT and hemodynamic data from two male C57BL6/J control mice aged 10-12 weeks. A detailed description of experimental protocols for the imaging and hemodynamic data can be found in [245] and [232], respectively. Briefly, hemodynamic data includes a flow waveform ensembled over 20 cardiac cycles measured using an in-line flow meter (Transonic

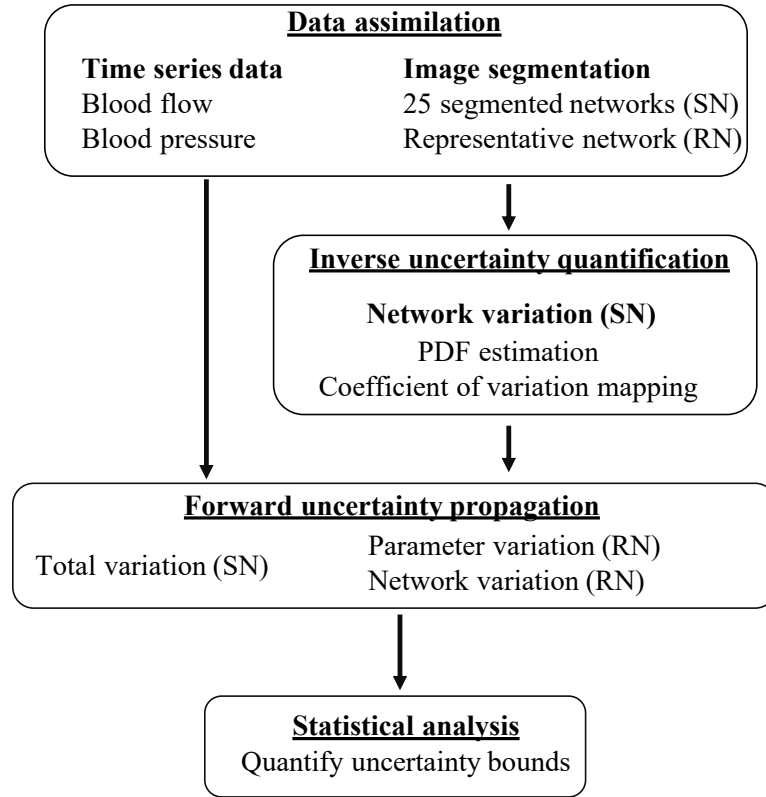


Figure 8.1 Workflow for uncertainty quantification of hemodynamics. Multiple segmentations were performed to construct the segmented networks (SNs), of which one network was selected as the representative network (RN). Inverse uncertainty quantification (UQ) was performed on the 25 SNs by constructing probability density functions (pdfs) for vessel radius and length measurements. The 25 SNs were used in model simulations to understand the total variation, while the pdfs for the vessel radii and lengths were used to propagate uncertainty in the parameter variation study of a representative network. Lastly, the structure of the representative network was changed to understand the variation induced by network connectivity. Pressure and flow predictions are compared from the three sources of variation.

Systems, Ithaca, NY) in the main pulmonary artery (MPA). The imaging data is obtained after euthanasia and inflation of the mouse lung at 17.2 mmHg. A cannula with outer diameter 0.127 cm and inner diameter of 0.086 cm is attached to the MPA before 360-degree imaging and reconstruction to DICOM 3.0 files. Both procedures were approved by the University of Wisconsin-Madison Institutional Animal Care and Use Committee.

8.3.2 Image analysis

8.3.2.1 Image segmentation

The micro-CT image is stored as a DICOM 3.0 file with voxel dimensions $497 \times 497 \times 497$. The gray-scale image (shown in Figure 8.4a) is transformed to a binary map identifying the vascular ("foreground") and non-vascular ("background") regions using global thresholding and image segmentation in ITK-SNAP [272]. Global thresholding is a pre-segmentation technique requiring a

priori selection of thresholds to specify the image intensity bounds of the foreground. Threshold bounds are traditionally selected in an ad hoc manner to ensure that the foreground is captured [61, 161, 191]. In addition, ITK-SNAP requires specification of a smoothing parameter to determine the boundary between the foreground and background (see figure 8.3). Due to the experimental protocol and use of perfused contrast, the image segmented in this study does not contain high intensity voxels from other anatomical features (e.g., the veins or the heart) within the region of interest. Therefore, only the lower threshold (θ_1) and smoothing (θ_2) pre-segmentation parameters require specification.

Acceptable intervals for (θ_1, θ_2) are determined to preserve the foreground for the large vessels across segmentations. To study segmentation induced uncertainty, we assume a uniform distribution for the two parameters, with $20 \leq \theta_1 \leq 45$ and $3 \leq \theta_2 \leq 8$, and draw 25 realisations of pre-segmentation parameter sets (θ_1, θ_2) (given in Table 8.1) using the `rand` function in MATLAB (Mathworks, Natick, MA). As shown in Figure 8.3, the foreground for distal vascular segments changes significantly when (θ_1, θ_2) are varied, but maintains features for the large, proximal vessels.

We use active contour evolution, a semi-automated segmentation algorithm available in ITK-SNAP, to segment the micro-CT image. We consistently use 2000 iterations of the contour evolution, ensuring that the largest arteries carrying the majority of the blood volume are captured. The contour evolution algorithm used for the segmentation is initialized by placing seed points within the region of interest. The algorithm iteratively updates a parametric contour representing the boundary of the segmented image (see [273] for more detail). We place a seed point at the inlet of the MPA for each segmentation and allow the active contour to evolve over 2000 iterations. The active contour evolution equation contains several parameters that allow for tuning in the evolution process. To best simulate the effects that might be captured by other researchers, we left these values at their nominal values. Other methods of pre-segmentation are available in ITK-SNAP, such as tissue classification, edge detection, and clustering. Global thresholding is the best fit for the one-tissue class image used in this study, but also holds for most imaging obtained via contrast, making it the ideal method for the present investigation. The use of 2000 iterations for the active contour evolution ensured that the largest, proximal pulmonary arteries were kept across segmentations, while smaller arteries captured varied based on the pre-segmentation parameters chosen. Since the full structure of the pulmonary arterial tree in-vivo is unknown, this protocol captures the variability in networks obtained from segmentation.

The imaging protocol described in [245] has a spatial resolution between $30\text{--}40\mu\text{m}$, providing a lower bound of $40\mu\text{m}$ for the measurement uncertainty diameter ($20\mu\text{m}$ for radius).

8.3.2.2 Network reconstruction

Segmented geometries were exported as surface meshes and converted to VTK polygonal files using *Paraview* [238] (Kitware, Clifton Park, NY, USA). Surface mesh VTK files were imported into *VMTK*¹ [11] to extract vessel segment centrelines, lengths, and radii using native scripts. Custom Matlab algorithms, which can be found in

¹(www.vmtk.org)

Table 8.1 Summary of pre-segmentation parameters and network features.

pre-segmentation parameters (θ_1, θ_2)	number of vessels	number of generations	number of terminal vessels	total volume (cm ³)
(22,5.0)	276	15	149	21.0871
(25,6.0)	422	17	226	21.3407
(26,4.7)	415	17	219	22.3524
(26,4.8)	425	18	227	22.8591
(26,5.1)	441	17	234	22.7031
(27,5.8)	450	17	240	22.9599
(28,6.0)	333	15	178	20.6542
(30,4.6)	428	16	230	21.7283
(30,5.7)	461	17	245	23.0039
(30,6.5)	476	18	252	23.1922
(30,8.0)	409	16	220	21.7642
(31,5.6)	462	18	246	23.3346
(31,6.1)	310	15	164	18.2311
(32,4.1)	419	16	220	22.2851
(33,4.2)	446	18	239	23.0664
(33,5.1)	505	18	269	24.6089
(34,3.3)	495	18	265	24.1804
(34,3.4)	474	17	257	24.2923
(35,3.6)	459	17	242	23.2488
(35,4.8)	470	17	250	23.0868
(35,6.8)	404	17	214	22.7536
(36,4.0)	419	17	226	22.0391
(36,4.1)	376	16	197	22.5833
(37,3.9)	409	17	221	21.6596
(44,7.6)	185	12	98	20.4368

https://github.com/mjcolebank/Segmentation_CFD were used to extract the network connectivity from the extracted quantities and identify all the vessels in each network. Subsequently, a connectivity matrix identifying the geometry of the tree was constructed and used in the 1D fluid-dynamics model. Figure 8.4 illustrates the workflow starting from the micro-CT image segmentation and ending with the connected network representation.

Voxels are converted to cm using a scaling factor based on the known diameter of the cannula (0.086 cm). The MPA radius is estimated using measurements distal to the cannula before the left (LPA) and right (RPA) pulmonary arterial bifurcation. Figure 8.5 shows an example network with radii estimates at each point along the network and within a single vessel. Measured values for radii vary within each vessel segment, limiting our inference of tapering. To proceed with calculations, we fix the vessel radius to be the mean over the centre 80% of the individual estimates, which mitigates the impact of extreme diameters in the ostium regions at either end of each segment.

We construct connected graphs using the centreline data and create a connectivity matrix linking vessels, represented by their length and radius, and bifurcations. In addition, we capture global network features including the number of vessels, the number of bifurcations (i.e. generations), and the total vascular volume. The CFD model used for hemodynamics modelling assumes a binary structure, with each generation of the

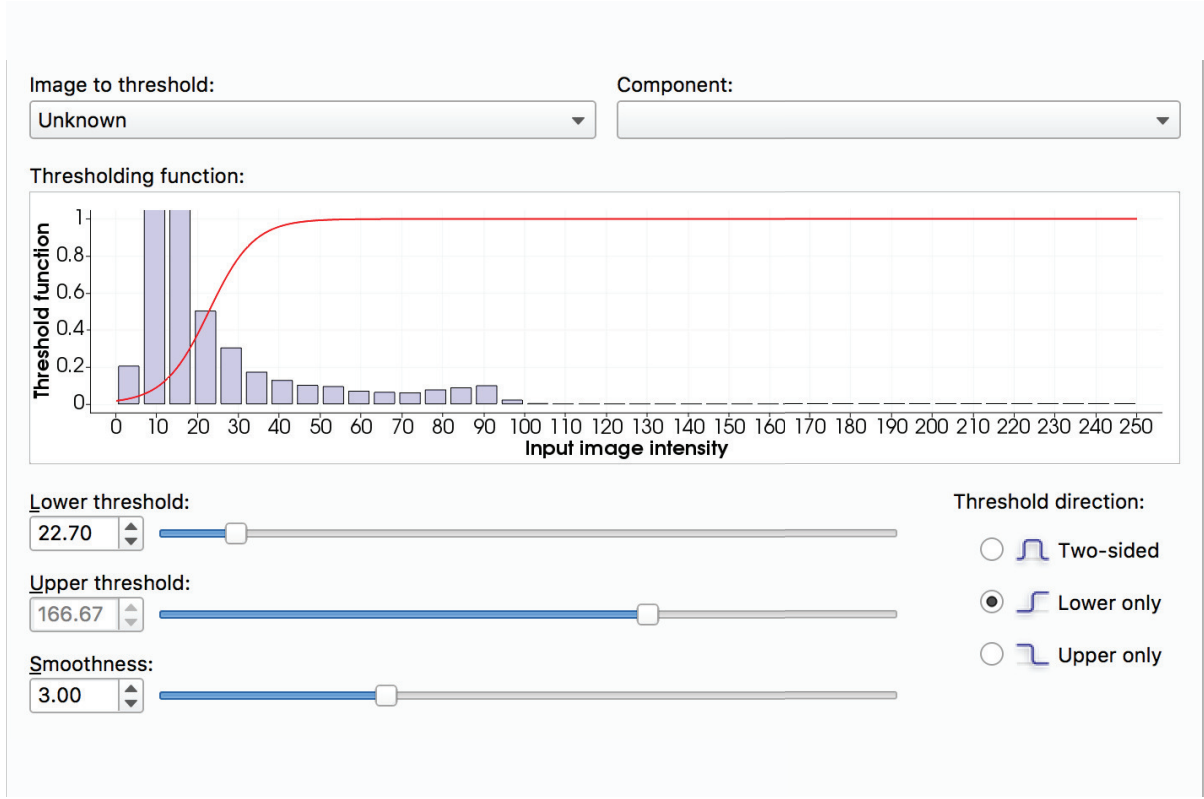


Figure 8.2 *ITK-SNAP* interface for prescribing pre-segmentation parameters (lower threshold, smoothness). Voxel intensities (x-axis) are converted to probabilities via the threshold function (y-axis). Different pre-segmentation parameters change the form of the red curve, based on which discrimination between the foreground and background is done. Here, a lower threshold on image intensities was assumed, as shown by the constant value of one in the threshold function for all values greater than the lower threshold.

tree being formed by a new set of vessels. The resulting networks were found to have no loops within the region of interest studied here. To characterize branching properties, we compute morphometric indices for each network including structured tree scaling parameters (see Section 4.3), as well as an asymmetry and area ratio, and Murray's exponent. These latter three are defined as

$$\gamma = r_{d_2}^2 / r_{d_1}^2, \quad \eta = (r_{d_1}^2 + r_{d_1}^2) r_p^2, \quad r_p^\zeta = r_{d_1}^\zeta + r_{d_2}^\zeta \quad (8.1)$$

where the subscripts p , d_1 and d_2 represent the parent and daughter branches.

8.3.3 Mathematical model

Similar to previous studies [168, 169, 191], we use a 1D CFD model to predict time-varying flow, pressure, and area in each vessel. The model is derived under the assumptions that vessels are cylindrical, blood is incompressible, and flow is laminar, axisymmetric, and Newtonian. The model equations are obtained by integrating over the cross-sectional area of the vessel, described in detail in [191]. Mass conservation and

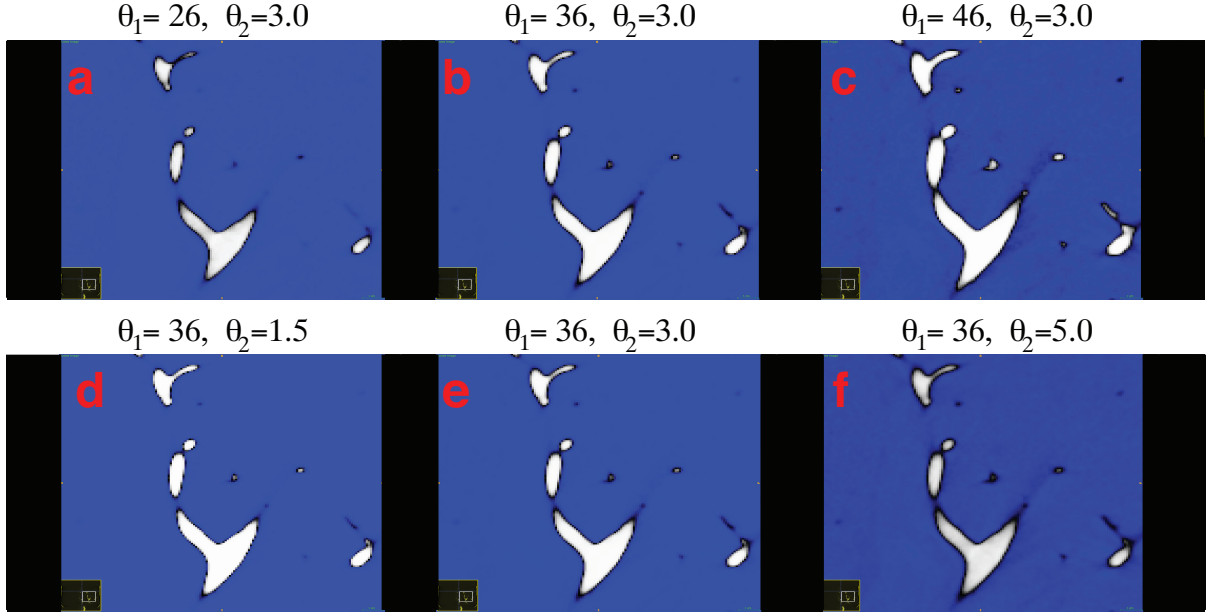


Figure 8.3 Qualitative differences in foreground (white) of distal vascular segments when changing the lower threshold for the voxel intensities (θ_1) and the smoothing parameter (θ_2). Top: changes in foreground with θ_1 ; bottom: changes in foreground with θ_2 .

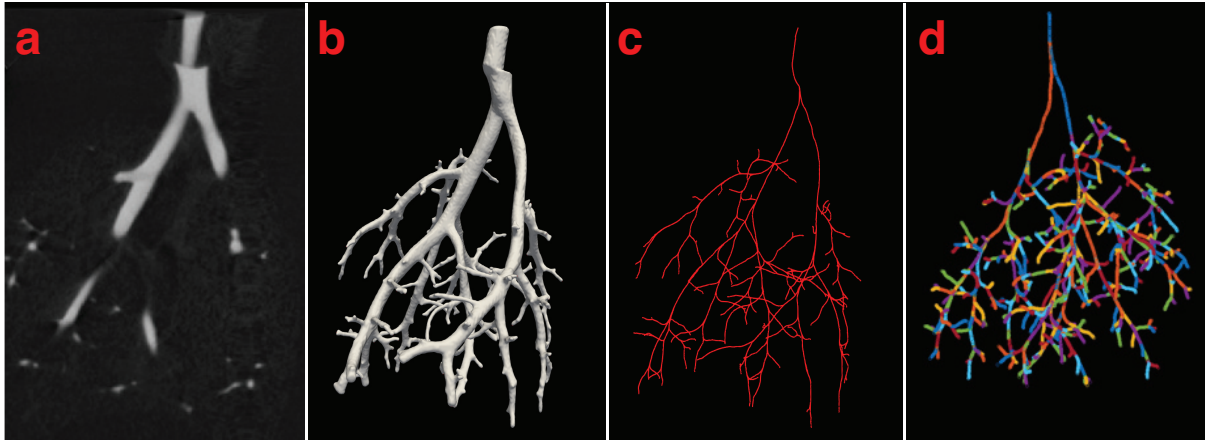


Figure 8.4 Image to network workflow. a) The foreground visible in the image file; b) The 3D rendering of the vascular foreground; c) Centrelines obtained using VMTK; d) A graph representation of the network used in the 1D model with vessels (edges) and bifurcations (nodes) identified using custom MATLAB algorithms, which can be found in https://github.com/mjcolebank/Segmentation_CFD (the different colours are used to distinguish where the vessels begin and end).

momentum balance are then given by

$$\frac{\partial A}{\partial t} + \frac{\partial Q}{\partial x} = 0 \quad (8.2)$$

$$\frac{\partial Q}{\partial t} + \frac{\partial}{\partial x} \left(\frac{Q^2}{A} \right) + \frac{A}{\rho} \frac{\partial P}{\partial x} = \frac{-2\pi \nu R}{\delta} \frac{Q}{A} \quad (8.3)$$

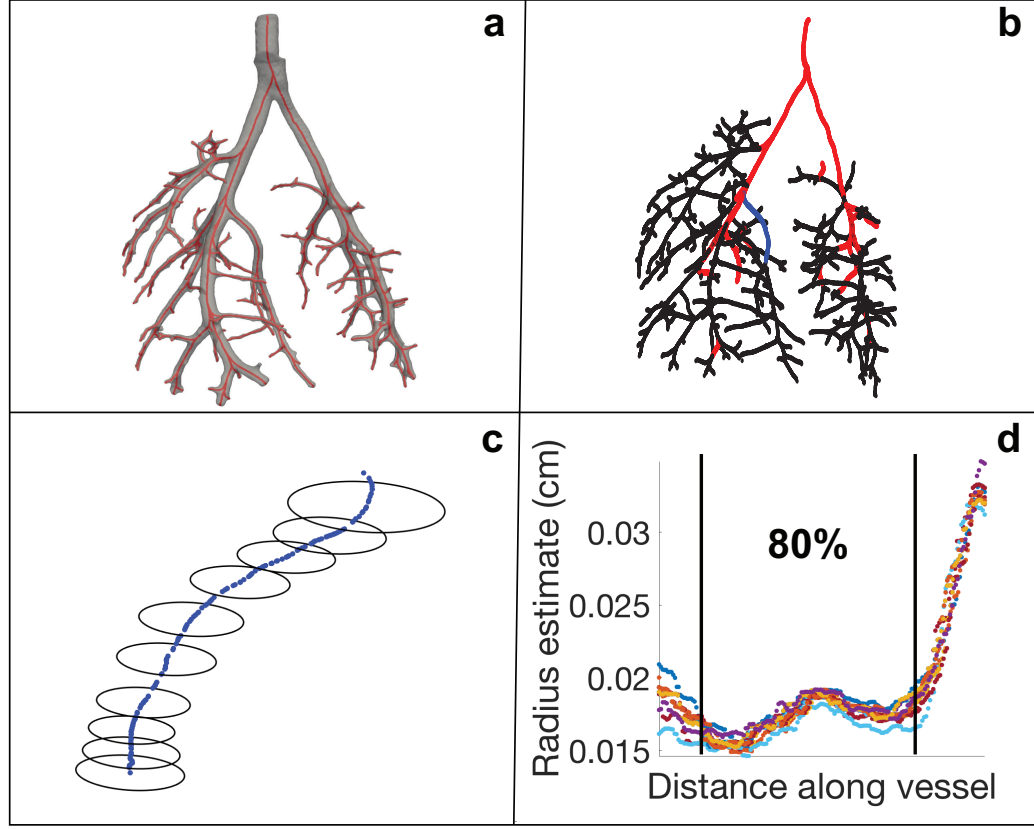


Figure 8.5 Components of an arterial tree. a) 3D segmentation of network; b) centerline representation of a tree with the 32 vessel-subset (red and blue); c) magnification of the vessel in blue depicting radius estimates; d) radius estimates along the vessel in blue, where the center 80% of points were used to calculate the mean radius.

where x (cm) and t (s) denote the axial and temporal coordinates, $A(x, t)$ (cm²) denotes the cross-sectional area, $Q(x, t)$ (cm³/s) the volumetric flow rate, $P(x, t)$ (mmHg) is the transmural blood pressure, and $R(x, t)$ (cm) the vessel radius. The blood density $\rho = 1.057$ (g/cm³) and the kinematic viscosity $\nu = 0.0462$ (cm²/s) are assumed constant [199, 262]. The right-hand side of Eq. (8.3) accounts for the frictional losses by assuming a flat velocity profile

$$u_x = \begin{cases} \bar{u}_x, & r \in [0, R - \delta) \\ \bar{u}_x \frac{R - r}{\delta}, & r \in [R - \delta, R] \end{cases} \quad (8.4)$$

with a linearly decreasing boundary layer with thickness $\delta = \sqrt{\nu T / 2\pi}$ (cm), where T (s) is the length of the cardiac cycle extracted from data [189, 191]. To close the system of equations, we consider a constitutive law relating blood pressure and vessel cross-sectional area. We model vessels as thin walled, incompressible, homogeneous, and isotropic cylinders tethered in the longitudinal direction. Under these conditions, the

linear stress-strain relation [186, 191] is given by

$$P - P_0 = \frac{4}{3} \beta_w \left(1 - \sqrt{\frac{A_0}{A}} \right) \quad (8.5)$$

where $\beta_w = E h r_0 = 37.5$ mmHg describes the arterial stiffness, E (mmHg) is the Young's modulus in the circumferential direction, h (cm) the wall thickness, and $A_0 = \pi r_0^2$ (cm²) is the reference area obtained at the reference pressure P_0 (mmHg).

The system (8.2) - (8.5) is solved using the two-step Lax-Wendroff finite difference scheme in C++ [166] with a temporal resolution of 1.3×10^{-5} (s) and a spatial resolution of 0.025 (cm) ensuring that the Courant-Fredrich-Lewy (CFL) condition is not violated. To ensure stability and convergence of the numerical scheme, the lengths of any vessels shorter than the spatial resolution of the solver are artificially augmented to be the size of two grid points.

8.3.3.1 Wave intensity analysis

Wave propagation in the pulmonary system can be characterized using wave intensity (WI) analysis [228]. Briefly, considering $Q = AU$, where U is the blood flow velocity (cm/s) in the vessel under the assumption of negligible frictional losses, we define the forward and backward components of WI as

$$WI_{\pm} = \left(\frac{\delta P_{\pm}}{\delta t} \right) \left(\frac{\delta U_{\pm}}{\delta t} \right) \quad (8.6)$$

Where '+' and '-' indicate the direction of the local waves, and δP_{\pm} and δU_{\pm} are the associated pressure and velocity "wavefronts", [191, 228]. The wave separation depends on the local pulse wave velocity

$$c(P) = \sqrt{\frac{A}{\rho} \frac{\partial P}{\partial A}} \quad (8.7)$$

Local waves can either be compressive or decompressive. Wave reflections are current clinical indicators for pulmonary vascular disease and PH progression, and can be attributed to impedance mismatch at both proximal and distal vessel junctions [172, 228].

8.3.4 Inflow and outflow boundary conditions

The 1D system is hyperbolic with characteristics pointing in opposite directions, thus two boundary conditions are needed at each vessel inlet and outlet. At the network inlet (the MPA) we prescribe a measured flow waveform from a single cardiac cycle. At network bifurcations we impose two conditions ensuring conservation of flow and a continuity of pressure. Lastly, we impose a three element Windkessel model at the outlet of terminal vessels to characterize the downstream vasculature, which relates pressure and flow via an RCR circuit model

$$\frac{dP}{dt} = R_p \left(\frac{dQ}{dt} \right) + Q \left(\frac{R_p + R_d}{R_p R_d} \right) - \frac{P}{R_d C_T}. \quad (8.8)$$

where R_p is the proximal resistance, R_d is the distal resistance, and C_T is the total compliance [186, 198].

8.3.4.1 Parameterization

The hemodynamics modelling parameters include those describing the vascular structure (radius, length, and stiffness), the fluid dynamics (including ν , ρ , and δ), and the inflow and outflow boundary conditions. We assume that inflow, ν , ρ , and β_w are fixed and independent of the network geometry [124, 189, 191], while parameters specifying the vessel radius, length, and Windkessel outflow boundary conditions (R_p , R_d , C_T) depend on the network structure [68, 191].

For each network, vessel radii and length are determined from the segmentation, while estimates are needed for Windkessel parameters. Similar to our previous study [191], we assume that the total compliance C_T can be determined from the diastolic decay time constant $\tau = R_T C_T$, where $R_T = R_p + R_d$ is the total vascular resistance [191]. R_T is computed as the ratio of mean pressure to mean flow, i.e. $R_T = \bar{P}/\bar{Q}$, and as discussed in our previous studies [46, 191], a priori resistance values for each terminal vessel can be calculated using Poiseuille's equation, relating mean pressure and flow via the vessel dimensions.

Define the inductance

$$G_i = \frac{1}{R_i} = \frac{\pi r_i^4}{8\mu L_i}, \quad (8.9)$$

which is the inverse of the Poiseuille resistance. For Poiseuille flow, $\Delta P_i = Q_i/G_i$. Continuity of pressure at a vessel junction can then be written as

$$\frac{Q_p}{G_p} = \frac{Q_{d_1}}{G_{d_1}} = \frac{Q_{d_2}}{G_{d_2}} \quad (8.10)$$

$$\implies Q_{d_1} = Q_p \frac{G_{d_1}}{G_p} \text{ and } Q_{d_2} = Q_p \frac{G_{d_2}}{G_p}. \quad (8.11)$$

Conductance in a parallel circuit follow $G_p = G_{d_1} + G_{d_2}$. Then the flows to each daughter branch are

$$Q_{d_1} = Q_p \frac{G_{d_1}}{G_{d_1} + G_{d_2}}, \text{ and } Q_{d_2} = Q_p \frac{G_{d_2}}{G_{d_1} + G_{d_2}}. \quad (8.12)$$

Using the definition of resistance from Poiseuille's law to gives

$$Q_{d_1} = Q_p \frac{\xi_{d_1}}{\xi_{d_1} + \xi_{d_2}} \text{ and } Q_{d_2} = Q_p \frac{\xi_{d_2}}{\xi_{d_1} + \xi_{d_2}}, \quad (8.13)$$

where $\xi_i = \pi r_i^4 L_i$. Finally, we set $R_p = 0.2R_T$ and $R_d = 0.8R_T$ [191].

8.3.5 Inverse uncertainty quantification

We employ inverse UQ to estimate vessel length and radius PDFs over the 25 segmented networks. To compare measurements across segmentations, PDFs are computed for radius and length from a 32-vessel subset after data standardization. Two estimation techniques, kernel density estimation (KDE) and Gaussian process (GP) density estimation, are used to compare estimated PDFs. Weighted least squares regression and GP regression are used to remedy the issues of non-constant variance, i.e. heteroscedasticity, in vessel dimensions.

8.3.5.1 Data standardisation

A subset of 32 pulmonary vessels of various calibre (see panel (b) of Figure 8.5) was selected from the 25 segmented networks. The 32 vessels were visible in all 25 networks and contained radius and length measure-

ments that encompass the full range of measurements in the networks. Length and radius measurements were standardised using

$$s_{i,j}^* = \frac{s_{i,j} - \bar{s}_i}{\sigma_{s_i}} \quad (8.14)$$

where $s_{i,j}$, $s = r, l$ are the measured radii or lengths from the i -th vessel and j -th segmentation, and s_i and σ_{s_i} are the mean and the standard deviations of the radii or lengths of the i -th vessel across the 25 networks.

8.3.5.2 Density estimation

Kernel density estimation (KDE) [216] is a non-parametric technique for estimating unknown probability distributions. KDE constructs the PDF π for vessel length and radius using

$$\pi(s^*) = \frac{1}{NH} \sum_{i=1}^N K\left(\frac{s^* - s_i^*}{H}\right) \quad (8.15)$$

where s_i^* denotes the standardized measurement of the i -th vessel, N is the number of samples used for the density estimate, H is the bandwidth parameter that controls the smoothness of π , and K is the kernel function, assumed to be a Gaussian kernel.

Two approaches for finding the optimal KDE bandwidth were considered: Silverman's rule-of-thumb [216] and maximum likelihood leave-one-out cross-validation (MLCV) [86]. The former calculates the bandwidth under the assumption that the underlying density being estimated is Gaussian, and uses the median absolute deviation. This has been shown to minimize the integrated mean squared error of the density estimate. These estimates were calculated using the `ksdensity` function from Matlab's Statistics and Machine Learning Toolbox. The latter (MLCV) leaves one point out at a time and computes the probability density estimate for the point left out based on all the other points (see eq (8.16)). Leaving one point out affects the calculation of the standardised quantities and requires re-calculation of the standardised measurements for each iteration.

$$\pi(s_i^*) = \frac{1}{(N-1)H^{\text{MLCV}}} \sum_{j=1, j \neq i}^N K\left(\frac{s_j^* - s_i^*}{H^{\text{MLCV}}}\right) \quad (8.16)$$

where s_i^* denotes the data point which was left out of the sample. The optimal bandwidth parameter H^{MLCV} that maximises the log-likelihood of the KDE:

$$H^{\text{MLCV}} = \max_{H>0} \left(\frac{1}{N} \sum_{i=1}^N \log \left(\sum_{j=1, j \neq i}^N k\left(\frac{s_j^* - s_i^*}{H}\right) \right) - \log((N-1)H) \right). \quad (8.17)$$

8.3.5.3 Statistical models for length and radius variance

The PDFs constructed from the 32-vessel subset are representative of the overall variation in the length and radius across all the segmented networks. However, the magnitude of $\sigma(L_i)$ and $\sigma(r_i)$ vary from vessel to vessel and need to be modeled explicitly before forward UQ. We use the coefficient of variation,

$$\phi(s_i) = c_v(s_i) = \frac{\sigma_{s_i}}{s_i} \quad (8.18)$$

to compare these measurements' variability.

The statistical model $\phi(s_i)$ relates the average measurements of radius and length across segmentations

to their coefficient of variation. The variance of the measurements exhibits heteroscedasticity, as smaller vessel segments are more sensitive to pre-segmentation parameters leading to non-constant variance. This violates the assumptions of ordinary linear regression; hence we consider weighted least squares regression and GP regression with input-dependent noise (contributed by Paun) [83]. Deterministic weighted least squares regression iteratively fits regression models by updating weights for each data point. The optimal weights (optimal in a maximum likelihood sense) are given by the inverse of the variance of the response $\phi(s_i)$ [92]. Since this variance is unknown, we approximate the weights as ϵ_i^{-2} , the squared residual from the unweighted regression model, reducing the impact of highly variable observations on the regression prediction. We consider exponential, logarithmic, square root, and linear weighted least squares regression models. For GP regression, Paun employed a GP for the response, $c_\nu^{s_i}$, and for the latent variance of $c_\nu^{s_i}$. In addition, the Matérn covariance function [195]

$$k_\nu(s_i, s_j) = a^2 \frac{2^{1-\nu}}{\Gamma(\nu)} (m\sqrt{2\nu})^\nu J_\nu(m\sqrt{2\nu}), \quad m = \sqrt{\sum_{k=1}^N \frac{(s_{i,k} - s_{j,k})^2}{\ell_k^2}} \quad (8.19)$$

with a smoothness parameter $\nu = 5/2$ and a correlation length ℓ_k for each set of measurements.

8.3.6 Forward uncertainty quantification

Forward UQ propagates model and parameter uncertainties to simulated quantities of interest. To analyse the variability in model predictions, three sets of simulations were set up that determine (i) the total variation of hemodynamic predictions associated with segmentation, (ii) the variation to changes in vessel radius and length (geometric parameters), and (iii) the variation to changes in network size and connectivity. The first set of simulations (i) used the 25 segmented networks, whereas the last two (ii-iii) were conducted in a representative network.

8.3.6.1 Total variation

We predict hemodynamics using each of the 25 segmented networks to quantify the total variation of flow and pressure predictions in the MPA, LPA, and RPA. The observed variation is attributed to several sources of uncertainty, including the parameters of the model and the size and connectivity of the network. Once the total variation is calculated, we quantify the relative contributions from the parameter and network variation.

8.3.6.2 Representative network

A representative network is used to examine the variation in vessel radius and length and changes in network size and connectivity. We first compute the MPA pressure waveform for each of the 25 segmented networks, then we ensemble average these to determine a mean MPA pressure. The network with the smallest least squares cost between its MPA pressure waveform and the ensemble averaged waveform is designated as the representative network.

8.3.6.3 Geometric parameter variation

We assume that density, viscosity, and vessel stiffness are constant while parameters impacted by image segmentation, including vessel length and radius, vary. The outflow boundary conditions are dependent on

vessel length and radius; thereby, we analyze the variation in model predictions associated with changes in vessel dimensions.

We compute inverse cumulative distribution functions (iCDFs) for the length and radius PDFs. The iCDF $F_s^{-1}(\alpha)$, is a nondecreasing function defined on the interval $[0, 1]$ that provides values from the original PDF, allowing for inverse transform sampling for forward UQ [103]. Briefly, let u be a realization from a uniform distribution, $u \sim U(0, 1)$, and define the realization from the iCDF as $F_s^{-1}(u)$. There exists a mapping from the realization to the iCDF for the radius and the length via $\gamma_r = F_r^{-1}(u)$ and $\gamma_L = F_L^{-1}(u)$, hence we draw samples from the iCDF to provide standardized measurements L^* and r^* .

We define a mapping from the iCDF of \bar{s}_i in vessel i to the perturbed values \hat{s}_i (cm). Writing

$$F_s^{-1}(u) = \frac{(\hat{s}_i - \bar{s}_i)}{\sigma_{s_i}}, \quad \sigma_{s_i} = \phi \bar{s}_i \cdot s_i \quad (8.20)$$

where ϕ is the statistical model for the coefficient of variance, we get

$$\hat{s}_i = (1 + F_s^{-1}(u) \cdot \phi(\bar{s}_i)) \cdot \bar{s}_i \quad (8.21)$$

for each average measurement \bar{s}_i in vessel i . The values \hat{s} are used as the dimensions for each vessel in the 1D model when doing the forward UQ. We set $\bar{s}_i = s_i^{\text{rep}}$, where s_i^{rep} are the measurements from the representative network. To ensure convergence of the posterior predictions [186], we draw $M = 10^4$ realizations using Monte Carlo sampling. The pseudo algorithm for UQ propagation is as follows:

1. Draw $u \sim \mathcal{U}(0, 1)$.
2. Obtain the standardised measurements s^* , thus the original measurements s as:

$$s^* = F_{s^*}^{-1}(u) \implies F_{s^*}^{-1}(u) = \frac{s - \bar{s}}{\sigma_s} = \frac{s - \bar{s}}{c_v^s \bar{s}}, \quad (8.22)$$

$$\implies \hat{s} = (1 + F_s^{-1}(u) \cdot \phi(\bar{s}_i)) \cdot \bar{s}_i. \quad (8.23)$$

3. Run 1D CFD model with new radius and length measurements \hat{s}_r and \hat{s}_L and new Windkessel parameters (they depend on radius and length).
4. Repeat steps 1-3 $M = 10^4$ times.

8.3.6.4 Network variation

The effect of network variation (i.e. truncation) was simulated by iteratively eliminating terminal vessel pairs from the representative network, i.e. starting at the smallest branches and moving towards the proximal vasculature, vessels with the smallest volume ($V = \pi r^2 l$) were eliminated, while ensuring that Windkessel boundary conditions were adjusted for each simulation.

8.4 Results

We analyse the total variation of flow and pressure predictions and identify the relative contributions from variations in vessel parameters and in the network. Variation in model predictions is quantified by comparing simulations in the MPA, LPA, and RPA.

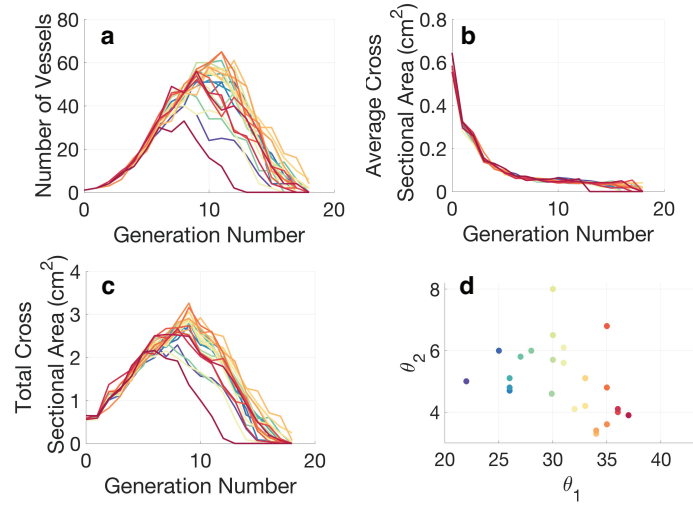


Figure 8.6 Morphometric features from the 25 segmentations marked by different colored lines. The number of vessels (a) is consistent between segmentations until the 5th generation. The average cross-sectional area (b) decreases rapidly after the 1st generation, while the total cross-sectional area (c) varies significantly between segmentations. The segmentation parameters are plotted against each other in (d), with a clear outlier present at (44, 7.6) (in pink) indicating a set of pre-segmentation parameters that have marked effects on the network structure. The outlier has lower number of vessels and total cross-sectional area as depicted in the pink curve in panels (a) and (c).

Table 8.2 Estimated structured tree parameters

Parameter	Definition	Value	Coefficient of variation
α	Large daughter scaling	0.84 ± 0.01	1%
β	Small daughter scaling	0.66 ± 0.02	3%
γ	Asymmetry ratio	0.66 ± 0.02	4%
η	Area ratio	1.21 ± 0.03	3%
ξ	Radius exponent	2.92 ± 0.01	0%

8.4.1 Network statistics

Figure 8.6 summarizes network characteristics obtained from the 25 segmented networks, including number of vessels (panel a), average cross-sectional area (panel b) and total cross-sectional area (panel c) in each generation. The average number of vessels across the networks is 437 with a standard deviation of 76 and the mean number of generations across segmentations is approximately 17. The number of vessels and total cross-sectional area of the networks are consistent across segmentations up until the 6th generation, after which the results deviate. Most segmentations achieve a maximum number of vessels and cross-sectional area between generations 8 and 14, while the average cross-sectional area rapidly decreases until the 5th generation, and then remain fairly constant afterward. Analysis across all networks in panel d shows that one network (corresponding to $(\theta_1, \theta_2) = (44, 7.6)$) is an outlier, having significantly fewer vessels and a lower total cross-sectional area. Table 1 includes all pre-segmentation parameter sets used in the repeated segmentations as well as network level features. Results of calculating morphometric indices show that the parent to daughter area ratio is greater than 1 and that Murray's exponent is approximately 3 (shown in Table 8.2), consistent with literature findings [46, 102].

8.4.2 Inverse uncertainty quantification

Figure 8.7 shows the length and radii KDE for the 32 representative vessels computed using Silverman's rule, maximum likelihood cross-validation, and GPs. Before density estimation, the standard deviation for each of the 32 vessels is used to normalize the data. The maximum coefficient of variation is 21% for the radius and 49% for the length estimate. The bandwidth estimates for Silverman's rule are $H_L^S = 2.038 \times 10^{-1}$ and $H_r^S = 1.573 \times 10^{-1}$, while for the maximum likelihood cross validation the estimated bandwidths are $H_L^{\text{MLCV}} = 1.808$ and $H_r^{\text{MLCV}} = 6.887 \times 10^{-1}$ for the length and radius densities, respectively. Computations using Silverman's rule exhibit overfitting, while the maximum likelihood cross validation over-smooths the density relative to the GP. In summary, the GP density estimation provides the most robust approximation for the KDE, which is therefore chosen in the forward uncertainty propagation.

Weighted least squares with exponential, logarithmic, square root, and linear regression functions are unable to resolve the heteroscedastic nature of the data (plots not shown). Instead, we use the GP regression model with input dependent noise to estimate $\phi(\tilde{s}_i)$, resolving the issue of heteroscedasticity. Figure 8.8 panels (a) and (b) show the GP regression for $c^v(\tilde{r}_i)$ and $c^v(\tilde{L}_i)$, respectively, while panels (c) and (d) depict the latent variance. The coefficient of variation for vessel measurements across segmentations increases as vessels get smaller. The mean variance for c_v^L increases as the length decreases, yet the mean variance of c_v^r has a sharp decrease for the smallest vessels. Both GP models stay above the minimum variability of $20\mu\text{m}$.

8.4.3 Forward uncertainty quantification

The MPA flow data is used as an inflow boundary condition, hence it does not change in any of the simulations. The ensemble averaged pressure predictions in the MPA, LPA, and RPA along with $\pm 2\sigma$ are shown in the first column of figure 9. Mean, systolic, diastolic and pulse pressure and max flow, min flow, and total volume, are given in Table 8.3. The flow distribution to the LPA is much larger than the RPA, a consequence of the larger radius of the LPA that allows for greater fluid flow. This deviation in flow is apparent in the WI plots in Figure 8.10, showing a more complex series of wave reflections in the RPA than the LPA and MPA. The ensemble averaged pressure waveform calculated from the 25 networks identifies the network generated by $(\theta_1, \theta_2) = (33, 5.1)$ as the representative network.

For the parameter variation component of the study, we use the inverse sampling methodology to propagate 10^4 realizations of perturbed radius and length values in the representative network. The second column of Figure 8.9 shows the model predictions along with the mean $\pm \sigma$. The variation in the MPA, LPA, and RPA systolic and pulse pressure is significantly larger than the mean and diastolic pressures (see Table 8.3). The flow predictions in the LPA and RPA have larger variability in mean and max flow in comparison to the minimum flow. The variation attributed to network size and connectivity is calculated by fixing each vessel's radius and length in the representative network before reducing the full network iteratively. We reduce the network starting at the smallest branches and moving towards the proximal vasculature while ensuring that Windkessel boundary conditions are adjusted for each simulation (see Figure 8.9). Overall, reducing the number of vessels from 219 in the largest network to 3 in smallest network introduces a discrepancy of approximately 10 mmHg in the pressure predictions of all three pulmonary arteries.

WI analysis results in Figure 8.10 show that all vessels have two forward waves at the beginning and end of systole. The MPA and LPA have a pronounced backward wave during peak flow and the MPA and RPA have a secondary backward wave later in systole. The RPA also has an additional backward wave that occurs towards the end of diastole. The connectivity study in the last column of Figure 8.10 shows that the MPA and LPA achieve their largest forward and backward WI value for the smallest network, while the opposite is true

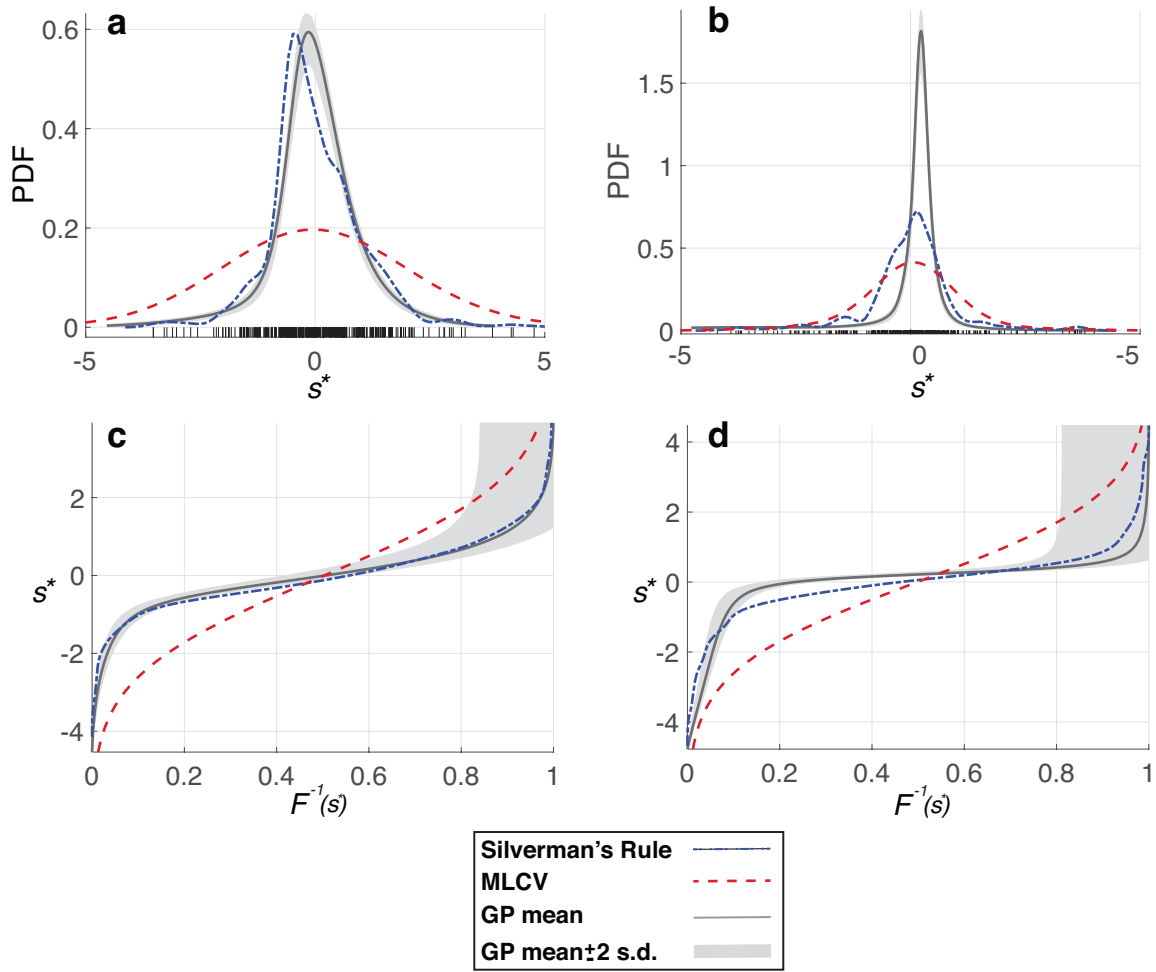


Figure 8.7 Density estimates (a) and (b) and inverse cumulative distribution functions (c) and (d) for the standardised radius and length values, respectively, measured in the 32-vessel subset. The bandwidth parameters used for the length and radius KDEs were determined using Silverman's rule (blue, dash dot) and maximum likelihood cross-validation (MLCV, red, dashed). The Gaussian process (GP) mean and 95% confidence interval are shown as a solid curve with grey bands. Standardised values are denoted by the black tick marks in panels (a) and (b).

for the RPA. Time averaged PWV in the MPA was 4.83 ± 0.0054 m/s for the total variation, 4.83 ± 0.0037 m/s for the parameter variation, and 4.84 ± 0.0054 m/s for the network variation. The mean PWV was slightly larger in the network variation study, but overall the three studies maintain the same magnitude with regard to the mean and standard deviation in PWV.

8.5 Discussion

Recent advances in image segmentation have made subject-specific modelling of PH feasible, yet the modelling process still comprises segmentation-induced uncertainty that propagates through to simulation results. This is the first known study to explicitly quantify the variability of 1D CFD blood flow and pressure predictions arising from uncertainty in pre-segmentation parameterisation. Three types of segmentation-induced varia-

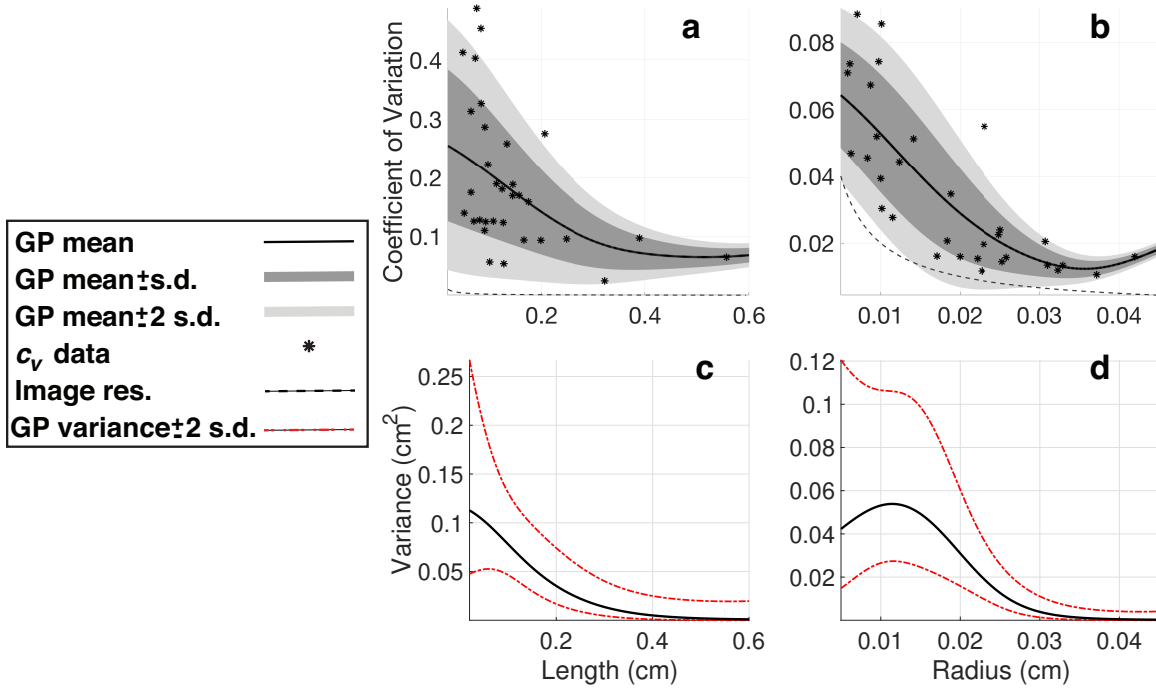


Figure 8.8 Gaussian Process (GP) regression using non-constant variance for the relationship between length and radius and their coefficient of variation (c_v). The GP means and standard deviations were computed from the c_v data obtained from the 32-vessel subset (asterisks) and plotted against the analytical bound of the image resolution (dash-dot curve), as given in [245]. The mean of the GPs and \pm one and two standard deviations (s.d.) from the mean are shown in (a) and (b) in black, dark grey, and light grey, respectively. The variance of the GPs in (c) and (d) were predicted using an additional GP and provided a mean (black) and variance (dashed curve) for the variance estimate. Both mean curves in (a) and (b) are above the uncertainty bound of the imaging protocol.

tions were investigated: the total variation arising from changes in pre-segmentation parameters, variation due to changes in vessel length and radius (geometric parameter variation), and variation with respect to network connectivity and size (network variation). Results suggest that variation in network structure is the greater contributor to uncertainty in hemodynamic predictions, consistent with what is known of the pulmonary vascular physiology. Moreover, the methodology developed herein can be used to generate a 1D model network for any vascular system.

8.5.1 Segmentation and construction of network graphs

Results show that pre-segmentation parameters drastically influence the number of vessels in the network, while the number of generations attainable remains relatively consistent. It is apparent that the network obtained from image segmentation is strongly linked to the range of image intensities considered in the foreground via choice of (θ_1, θ_2) . Most notably, the segmentation parameter set (31, 6.1) gives a volume that is significantly smaller, suggesting that even slight changes in pre-segmentation parameters can reduce the number and size of small vessels captured. The largest vascular tree used in this study contains 500 vessels, a small fraction of the thousands of blood vessels that comprise the full pulmonary arterial system [93, 235]. We expect the trends seen in Figure 8.6 to continue if more vessels are obtained from the segmentation.

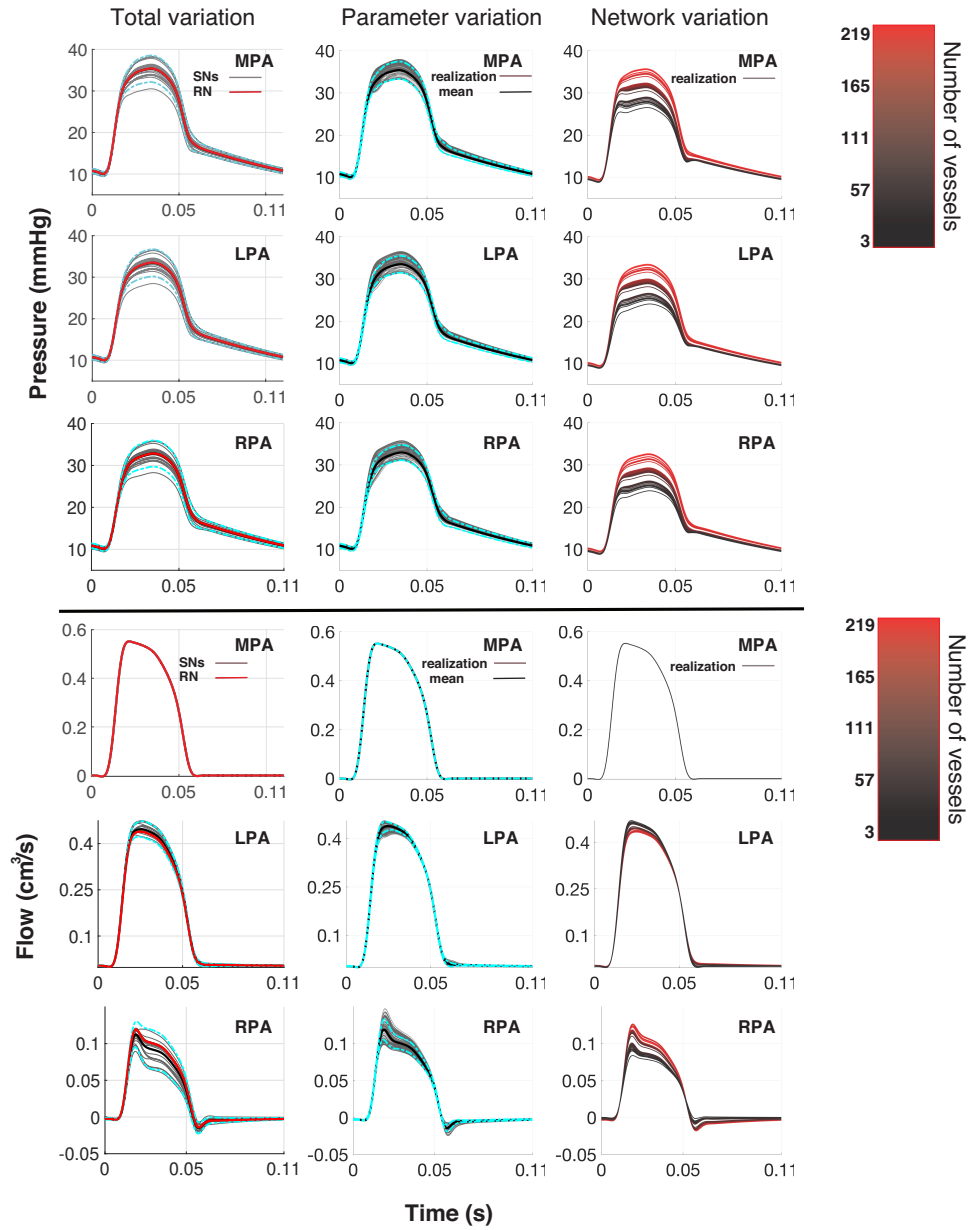


Figure 8.9 Pressure and flow predictions in the first pulmonary bifurcation when studying total variation, parameter variation, and network variation. Predictions from the total variation (1st column) include simulations in the 25 segmented networks (SNs), the representative network (RN, in red), and \pm two standard deviations (s.d.) from the mean (blue, dash-dot). The parameter variation plots (2nd column) show the 10,000 Monte Carlo realisations (grey) along with the mean (black) \pm two s.d. from the mean (blue, dash-dot). Lastly, the network variation predictions (3rd column) show the predictions when using 219 vessels in the network (bright red) up until the network is reduced to the MPA, LPA, and RPA (black).

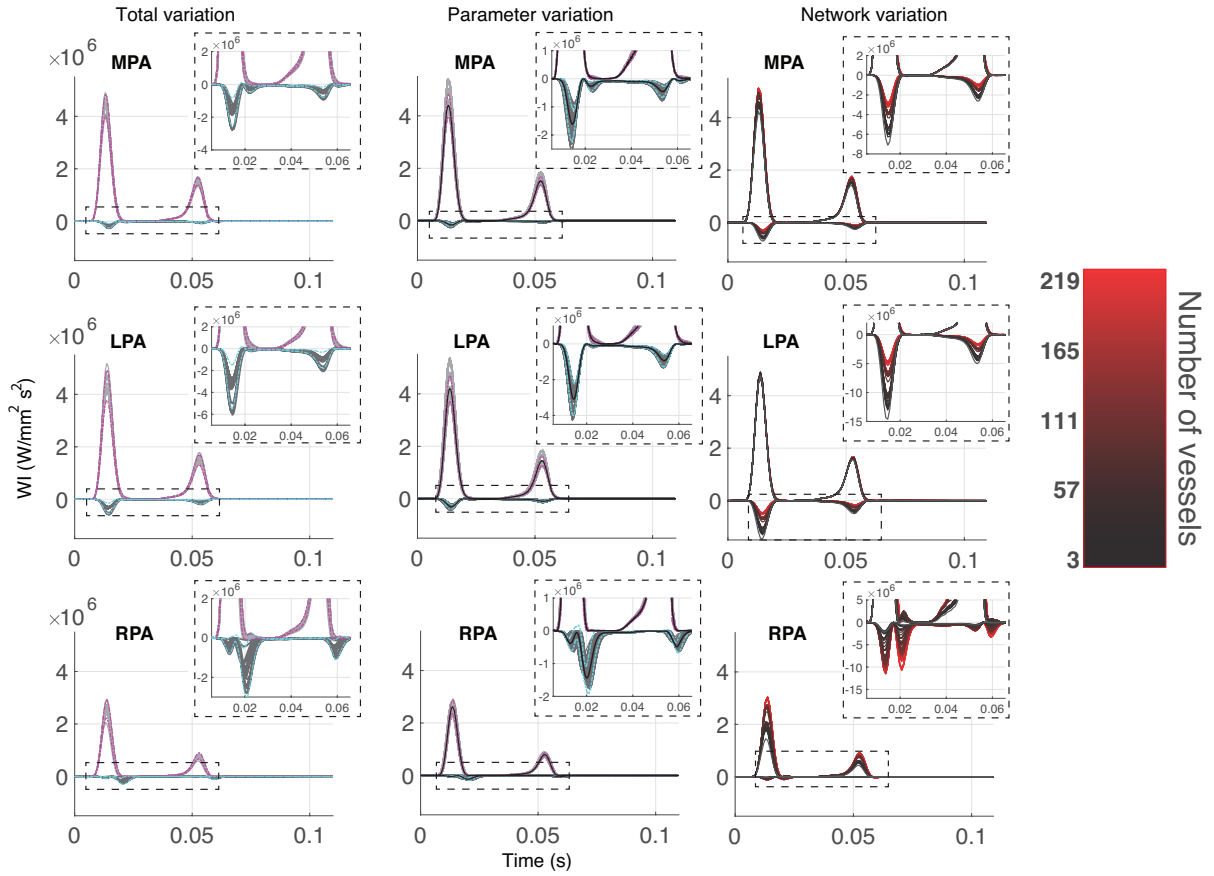


Figure 8.10 WI analysis in the first pulmonary bifurcation. Forward (positive values) and backward (negative values) waves are calculated for the total variation and parameter variation (grey lines) along with ± 2 s.d. from the mean (forward waves, magenta; backward waves, cyan). Predictions from the network variation study are colour coded according to network size, as described in Figure 8.9.

Table 8.3 Results from simulations. Values are expressed as means \pm s.d. Pressure values are in units of mmHg, flow values are in units of $\text{cm}^3 \text{s}^{-1}$ and volume values are in units of cm^3 .

Pressure				
	Mean pressure	Systolic pressure	Diastolic pressure	Pulse pressure
Total variation				
MPA	20.36 ± 0.78	35.35 ± 1.63	10.02 ± 0.27	25.33 ± 1.39
LPA	19.66 ± 0.79	33.46 ± 1.67	10.00 ± 0.27	23.45 ± 1.43
RPA	19.52 ± 0.78	32.83 ± 1.60	10.10 ± 0.28	22.74 ± 1.34
Parameter variation				
MPA	20.38 ± 0.54	35.37 ± 1.03	10.04 ± 0.23	25.33 ± 0.82
LPA	19.68 ± 0.53	33.46 ± 0.99	10.02 ± 0.23	23.43 ± 0.78
RPA	19.56 ± 0.50	33.46 ± 0.90	10.11 ± 0.24	22.80 ± 0.69
Network variation				
MPA	18.29 ± 0.84	31.70 ± 2.07	9.08 ± 0.18	22.63 ± 1.91
LPA	17.44 ± 0.86	29.34 ± 2.13	9.08 ± 0.17	20.27 ± 1.97
RPA	17.31 ± 0.83	28.71 ± 1.96	9.15 ± 0.20	19.56 ± 1.77
Flow				
	Mean flow	Max flow	Min flow	Volume
Total variation				
LPA	0.142 ± 0.004	0.447 ± 0.013	-0.000 ± 0.000	0.016 ± 0.000
RPA	0.027 ± 0.004	0.113 ± 0.009	-0.015 ± 0.004	0.003 ± 0.000
Parameter variation				
LPA	0.140 ± 0.001	0.439 ± 0.006	0.000 ± 0.015	0.015 ± 0.000
RPA	0.029 ± 0.001	0.119 ± 0.007	-0.014 ± 0.002	0.003 ± 0.000
Network variation				
LPA	0.141 ± 0.001	0.447 ± 0.009	-0.001 ± 0.001	0.016 ± 0.000
RPA	0.027 ± 0.001	0.009 ± 0.010	-0.014 ± 0.004	0.003 ± 0.000

Our techniques study uncertainty induced by global thresholding, but could be applied when other pre-segmentation techniques are used, as global thresholding is commonly used [61, 161, 191] but is only one of many segmentation methods.

The variability in the total number of vessels for a given network highlights the variation attributed to segmentation. This would be expected in other networks that exhibit dispersive branching patterns, such as the coronary arteries [100] or cerebral vasculature [198]. We employed a generation-based (Wiebel) ordering scheme to describe the branching structure, where each bifurcation is considered a new generation of blood vessels. In contrast, other authors have used other ordering systems, e.g., Strahler [102] schemes, to identify structural properties of the pulmonary system, though these methods are not as compatible with CFD network models.

8.5.2 Inverse uncertainty quantification

KDEs and GPs are commonly used techniques for density estimation [148, 200], but this study is the first to use GPs in density estimation for vascular measurements. Typically, prior assumptions are forced on the unknown parameter distributions by assuming a parametric parameter distribution. By estimating the density directly

from repeated measurements, a non-parametric density was constructed, describing the uncertainty of the measurements across segmentations without prior assumptions.

As shown in Figure 8.7, the three density estimates are similar in the mode of the distribution (approximately zero); however the GP density estimation allows for additional UQ in both the PDF and CDF estimates [200]. The PDFs for radius and length were constructed independently, thus ignoring any correlation between the radius and length measurements. A PDF estimation method that accounts for correlation between the measurements of the two quantities should be investigated further, e.g. 2D GP density estimation [200].

The GP regression analysis of the coefficient of variation against the (standardised) measurements of radius and length revealed that the coefficient of variation for the measurements increased as the measurements decreased in value. This suggests that smaller vessels are subject to larger fluctuations in measurements when varying pre-segmentation parameters, i.e. across different segmentations. Similar conclusions have been made in simulations of coronary arteries [100], as the smaller regions of the vasculature were susceptible to higher segmentation error.

8.5.3 Forward uncertainty quantification

KDEs and GPs are commonly used techniques [148, 200], but this study is the first to use GPs in density estimation for vascular measurements. Forward UQ is typically carried out by assuming a parametric parameter distribution a priori, forcing prior assumptions on the unknown parameter distributions. By estimating the density directly from repeated measurements, we construct a nonparametric, representative density describing the uncertainty of the measurements across segmentations without prior assumptions.

The standardized measurements allow us to generalise the uncertainty of the 32-vessel subset to the entire vascular network, increasing the robustness of the density estimate. As shown in Figure 8.7, the three density estimates are similar in the mode of the distribution (approximately zero); however the GP density estimation allows for additional UQ in both the density and CDF estimates [200]. We construct marginal density estimates for the PDFs of radius and length, which assumes independence among the two quantities. PDF estimation methods that account for correlation between radius and length measurements should be investigated further.

GP regression is necessary for the data considered, as weighted least squares cannot correct the heteroscedastic variance. The coefficient of variation for the measurements increased as the measured dimensions decreased in value, suggesting that smaller vessels are subject to larger fluctuations in estimated dimensions when varying pre-segmentation parameters. The gradual increase in coefficient of variation indicates that the variance of the vessel dimensions across segmentations increases as vessels get smaller. Similar conclusions have been made in simulations predicting the fractional flow reserve in coronary crowns [100], as the smaller regions of the vasculature were susceptible to higher segmentation error. However, our work is the first to consider estimated, nonparametric densities for UQ propagation, and does not require a priori distribution assumptions.

8.5.4 Total variation of model simulations

The total network size obtained from the segmentation procedure has several effects on the model output. As shown in Table 8.3, changes in network topology due to segmentation induced a variation in systolic pressure that was nearly 6 times larger than the variation of diastolic pressure. Moreover, we observe that the total variation for the systolic and pulse pressure is larger in comparison to the mean and diastolic pressure. All four of these pressure metrics are typically used in diagnostic tools of diseases such as PH [70]. Though

systolic pressure and pulse pressure have a small standard deviation (approximately 5% relative to the mean), studies investigating coronary related mortality found that these pressure quantities were important for risk assessment in patients with congenital heart disease [123]. This further indicates a need for UQ when using these models for cardiovascular disease diagnostics and risk assessment.

8.5.5 Geometric parameter variation

The standard deviation of diastolic pressure resulting from parameter (radius and length) variation is greater than that resulting from network (size and connectivity) variation. This suggests that changes in vessel dimensions and nominal boundary conditions can ultimately raise the diastolic pressure of the system, which is expected in the case of chronic vascular remodelling [70]. Parameter variation only accounted for approximately 30% of the total variation in the pulse pressure and had less of an effect on all other pressure and flow quantities when compared to the network variation. Larger networks encompassing the entire pulmonary tree will increase the parameter uncertainty, as they correspond to more vessels and more uncertain estimates of radius and length. This would in turn bias hemodynamic parameter estimates, since network predictions would be based on the initial segmentation results [206].

8.5.6 Network variation

The largest effects on pressure and flow waveform predictions in the network are attributed to changes in network connectivity and size, as seen in Figures 8.9 and 8.10. Quantitative metrics provided in Table 8.3 also show that network variation produces larger standard deviations in systolic and pulse pressures vs parameter variation, suggesting that the configuration of vessels in the pulmonary system plays an important role in hemodynamic predictions. It is known that the highly compliant pulmonary system utilizes its rapidly branching structure to perfuse the lung under a low-pressure gradient and varying cardiac outputs, and that network remodeling is common with pulmonary vascular disease [70, 235]. For example, Rol et. al [202] concluded that changes in vessel diameter with PH cannot solely explain the increase in vascular resistance, and further hypothesized that network rarefaction may be a larger contributor to increased pulmonary arterial pressure. Olufsen et. al [169] investigated this computationally by altering structured tree boundary conditions, effectively reducing the size of the microvasculature and increasing pulmonary artery pressure. Our model analysis agrees with clinical hypotheses that vascular rarefaction and associated changes in network size and connectivity contribute more to changes in pulmonary arterial pressure than vessel narrowing.

The Poiseuille relation used to distribute network resistance introduces an impedance mismatch at each terminal vessel. Reflected pressure waves due to this mismatch become more prevalent as successive vessels are added to the system, leading to an increased pressure [201, 253]. While other studies have considered non-reflective boundary conditions [5, 62], it is hypothesised that wave reflections occur in the pulmonary system when PH is present [228], illustrating the appropriateness of reflective boundary conditions in the model.

Our results show three instances where reducing part of the network causes a larger change in pressure, which agree with a previous investigation by Epstein et al. [62] that showed a critical threshold in the number of vessels that lead to larger discrepancy in hemodynamic predictions. It is often the case that hemodynamic data is only available in select locations of the vascular system [46, 186, 191]. Changes in network size will lead to changes in optimal parameter values during parameter inference, making the problem ill-posed as estimated parameters describing stiffness, compliance, and vascular resistance will depend on the size of the network used in CFD simulations. This further indicates that uncertainty in the network structure must be

taken into account when using 1D CFD models for clinical decision making [46].

8.5.7 Limitations and future work

Several potential limitations of this study can be addressed in future investigations. First, we assume negligible tapering in each vessel, which could play a role in proximal artery dynamics. Second, our model assumptions ignore radius dependent stiffness and the effects of wall-viscoelasticity, which may be important in pulmonary arteries [253] and could change the model sensitivity to network size and vessel dimensions. However, the focus of this study was to quantify how changes in the model domain attributed to pre-segmentation parameters impact hemodynamic predictions for fixed material parameters. Similar to previous studies [46, 186, 191], nominal parameters are calculated under the assumption of steady flow and that pressure does not drop in the large vessels. However, in the 1D domain we solve non-linear equations, which account for inertial and viscous losses resulting in a pressure drop along the vessels. Similar to the systemic circulation, we assume a negligible pressure drop along the large pulmonary vessels. Yet no experimental studies have measured pressure beyond the first few generations, hence validation of this assumption in the pulmonary circulation is difficult

Additional limitations involved model construction and quantified results. The length of the smallest vessels was augmented during simulations to ensure the CFL condition is not violated. The CFL condition could also be met by either increasing the number of time-steps, which increases computational cost, or devising a numerical scheme using adaptive time-stepping, extending the scope of the study. We also provided conventional mean and standard deviation calculations as familiar metrics for comparison. An alternative approach is to perform formal global sensitivity analysis. State-of-the-art methods are based on Sobol indices defined via conditional variances of different order [46, 103, 148, 206]; however, their computation via Monte Carlo or quasi-Monte Carlo simulations is computationally expensive. This computational complexity is aggravated by the fact that the image segmentation includes manual inspection and the parameter space can therefore only be sampled at a coarse level. A potential way to alleviate this problem is to use statistical emulation, e.g. using GPs, to compute first order and total effects indices. This can, in principle, follow the method described in [148], by adapting and extending existing approaches and software tools; see <https://github.com/samcoveney/maGPpy>. However, this exploration is beyond the scope of the present study and provides an interesting direction for future research.

We consider the frequently-used three-element Windkessel model as the boundary condition for the 1D model, yet this model greatly simplifies the physiological resistance beyond the segmented vessels. In contrast, structured tree boundary conditions [168, 169, 189] can provide an additional level of complexity for approximating downstream resistance and attempt to capture network structure beyond the limits of image segmentation. In addition, the experimental protocol inhibited the same mouse from being used for both the hemodynamic and imaging data. While this is a limitation for possible parameter inference, our methodology still captures variability in model predictions due to uncertainty in the vessel dimensions and network structure. Future human-based studies could incorporate non-invasive flow and imaging data from the same patient in the model. Finally, future subject-specific models of the pulmonary vasculature would be enhanced by allowing for trifurcations (done in Chapter 9) and considering branching angles in the vascular tree, thus accounting for more of the physiological traits of the network.

8.6 Conclusions

Uncertainty of model predictions must be accounted for in the absence of ground truth. We have presented the first known investigation of the impact of uncertainties in imaging-based network reconstruction on CFD simulations in the pulmonary vasculature. This work identifies the uncertainties pertaining to image pre-segmentation parameters by explicitly measuring the variation in radius and length measurements of a subset of vascular segments. Another novelty of this work is in estimating densities of radius and length from data obtained using state-of-the-art nonparametric techniques, rather than assuming a fixed and potentially biased functional form of the distribution a priori. Moreover, our study is the first to perform UQ on the dimensions and network topology of a 1D CFD model in an expansive pulmonary vascular network. Our results show that the network variation has the most influence on predictions of blood pressure and flow while changes in vessel length and radius have less impact on hemodynamic predictions.

CHAPTER

9

A MULTISCALE MODEL OF CTEPH PRE- AND POST-SURGERY

The study “A multiscale model of vascular function in chronic thromboembolic pulmonary hypertension” has been submitted to *American Journal of Physiology - Heart and Circulatory Physiology*. Contributions include segmenting the human image, developing new web-like lesion energy loss models, all simulations in the large and small pulmonary arteries, and writing a majority of the paper.

9.1 Abstract

Chronic thromboembolic pulmonary hypertension (CTEPH) is caused by recurrent or unresolved pulmonary thromboemboli, leading to perfusion defects and increased arterial wave reflections. CTEPH treatment aims to reduce pulmonary arterial pressure and reestablish adequate lung perfusion, yet patients with distal lesions are inoperable by standard surgical intervention. Instead, these patients undergo balloon pulmonary angioplasty (BPA), a multi-session, minimally invasive surgery that disrupts the thromboembolic material within the vessel lumen using a catheter balloon. However, there still lacks an integrative, holistic tool for identifying optimal target lesions for treatment. To address this insufficiency, we simulate CTEPH hemodynamics and BPA therapy using a multiscale fluid dynamics model. The large pulmonary arterial geometry is derived from a computed tomography (CT) image, whereas a fractal tree represents the small vessels. We model ring- and web-like lesions, common in CTEPH, and simulate normotensive conditions and four CTEPH disease scenarios; the latter includes both large artery lesions and vascular remodeling. BPA therapy is simulated by simultaneously reducing lesion severity in three locations. Our predictions mimic severe CTEPH, manifested by an increase in mean proximal pulmonary arterial pressure above 20 mmHg and prominent wave reflections. Both flow and pressure decrease in vessels distal to the lesions and increase in unobstructed vascular regions. We use the main pulmonary artery (MPA) pressure, a wave reflection index,

and a measure of flow heterogeneity to select optimal target lesions for BPA. In summary, this study provides a multiscale, image-to-hemodynamics pipeline for BPA therapy planning for inoperable CTEPH patients.

9.2 Introduction

Pulmonary hypertension (PH), defined as a mean pulmonary arterial pressure (mPAP) > 20 mmHg at rest [218], degrades pulmonary vascular function. The disease is associated with vascular wall thickening and decreased vessel compliance, elevating pulmonary arterial pressure. If untreated, PH progressively leads to vascular-ventricular decoupling and right ventricular dysfunction [252]. PH encompasses five etiologies: (1) pulmonary arterial hypertension (PAH); (2) PH due to left heart disease; (3) PH due to lung disease, including hypoxia and chronic obstructive pulmonary disease; (4) chronic thromboembolic pulmonary hypertension (CTEPH); and (5), PH due to unclear or multifactorial mechanisms [218]. Though vasodilator therapy can be used to treat several PH subclasses, only CTEPH (group 4) is curable via surgical intervention [115, 145]. Recently, a less invasive approach has emerged, known as balloon pulmonary angioplasty (BPA), that opens the blood vessels using cardiac catheterization [130]. However, it is unclear if this more novel treatment has the same hemodynamic improvements as the gold-standard surgical methods. To this extent, this study develops a multi-scale, computational fluid dynamics (CFD) model to predict hemodynamics in CTEPH and simulate the impact of balloon pulmonary angioplasty (BPA) treatment.

CTEPH affects 3–30 people per million worldwide [132]. However, its prevalence is likely underestimated due to the diagnostic complexity and generic nature of its two vital symptoms: dyspnea and fatigue [149]. CTEPH etiology involves recurrent obstruction of the pulmonary arteries, leading to perfusion deficits and pulmonary vascular remodeling. In addition to elevated mPAP, clinical manifestations of CTEPH include increased flow heterogeneity and elevated right ventricular afterload [65, 208]. Diagnosis requires a combination of medical imaging (e.g., chest computed tomography (CT) or magnetic resonance imaging (MRI)), ventilation-perfusion (V/Q) scanning, and invasive right heart catheterization. CT images provide information regarding pulmonary vascular structure, while V/Q scans display blood flow and oxygen delivery to the alveoli. Right heart catheterization measures dynamic pulmonary arterial blood pressure in the main, left, and right pulmonary arteries (MPA, LPA, and RPA, respectively). Catheterization also estimates left atrial pressure by calculating pulmonary arterial wedge pressure (PAWP), which is ≤ 15 mmHg for CTEPH and other pre-capillary PH [218]. Cardiac output is measured during catheterization via thermodilution or Fick's method. CTEPH diagnosis requires a pulmonary vascular resistance (PVR) ≥ 3 Woods units [218] (1 Wood unit = 0.06 mmHg s/ml), approximated using mPAP, PAWP, and cardiac output. Also, positive diagnosis requires at least one large uni- or bilateral perfusion defect, identified on a V/Q scan or CT image [145, 260]. Recent studies using optical coherence tomography [108, 115] sub-classified CTEPH lesions as (1) ring-like, (2) web-like, (3) subtotal occlusions, (4) total occlusions, and (5) tortuous lesions. Of these, subtotal occlusions, ring-like, and web-like lesions are the most common and have the lowest probability of complication in response to BPA intervention [115].

CTEPH is a rare, progressive disease that is typically preceded by an acute pulmonary embolism. Disease advancement begins with vascular remodeling of the arterioles but ultimately affects the proximal pulmonary arteries [50]. Current hypotheses suggest that lesion-induced flow redistribution leads to (a) decreased vascular stretch and shear stress in obstructed pathways and (b) increased flow and shear stress in unobstructed pathways. These hemodynamic changes induce arteriolar muscularization and luminal narrowing, causing secondary pulmonary arteriopathy [55, 118, 130]. Muscularization and narrowing of small vessels are associated with increased PVR, causing pronounced wave reflections and increased mPAP [213, 244]. This narrowing

of the small pulmonary arteries and arterioles is typically linked to the dilation of the large, proximal arteries [50, 257]. These features typically emanate after months to years of elevated PVR, hence early diagnosis and proper treatment are crucial for preventing the progression to irreversible CTEPH. However, current data analyses and treatment selection protocols lack quantifiable metrics for holistic analysis and interpretation of imaging and hemodynamic data.

Surgical interventions for CTEPH aim to reduce mPAP and increase lung perfusion [67]. Pulmonary thromboendarterectomy (PTE) is the gold standard therapeutic intervention with a five-year survival rate >83% [187]. Though PTE is highly effective, between 12% to 60% of patients are inoperable due to distal lesions [115], located in the segmental and subsegmental arteries [113]. The optimal alternative treatment for these patients is BPA therapy, a minimally invasive procedure that uses a balloon catheter to mechanically disrupt the thrombi [67]. However, complete BPA therapy requires multiple interventions in various segments over several sessions [130, 260]. The variability in lesion morphology, severity, and location makes the selection of lesions challenging for the interventionalist. Hence there is a need for a patient-specific procedural planning tool. Though the location and morphology of lesions are known to influence BPA outcome [139], the only quantifiable metric for assessing these lesions' significance is the fractional flow reserve (FFR) [115]. This necessitates additional physiomarkers for quantifying lesion severity. The incidence of CTEPH is expected to grow in the coming decade; therefore, predictive tools integrating multi-modality data will be crucial to improve the safety, efficacy, and efficiency of BPA.

CTEPH affects both the proximal and distal vasculature [111, 224]. The geometry of the large pulmonary arteries can be analyzed and reconstructed from CT images or MRI, yet image resolution makes it impossible to extract a patient-specific geometry of the small arteries and arterioles. However, the structure and function of the small pulmonary arteries and arterioles are imperative in understanding CTEPH and its treatment. For instance, clinical studies demonstrate a negative correlation between long-term survival rates and elevated PVR post-PTE [79]. The study by Jujo et al. [111] concludes that severe arteriopathy in pulmonary arterioles is linked to recurrent CTEPH after PTE. Imaging limitations encourage developing new tools for assessing small vessel function and its link to proximal artery hemodynamics. Computational modeling, used here, is one such tool that can fuse idealistic small vessel structure with image-driven large artery geometries to predict cardiovascular dynamics.

Numerous computational studies use image-based CFD modeling to predict hemodynamics in proximal vessels (e.g., [222, 266, 268]). Spazzapan et al. [222] combine patient-specific CT pulmonary angiography images with a three-dimensional (3D) CFD model to predict pulmonary hemodynamics before and after PTE. They predict low wall shear stress (WSS) distal to stenoses in the LPA and RPA, but show that WSS increases in post-PTE simulations. They also document a relatively homogeneous, bilateral flow distribution to both lungs after simulated PTE. These findings agree with the patient-specific 3D CFD study by Yang et al. [266], which predicts WSS in the proximal pulmonary arteries of pediatric patients with no PH, moderate PH, and severe PH. They describe a negative correlation between PH severity and WSS magnitude in the MPA, LPA, and RPA. While 3D CFD models provide significant insight into WSS in PH, they are computationally intensive, making it challenging to integrate them into clinical practice.

In contrast to 3D models, several studies use one-dimensional (1D) CFD models to predict wave propagation and wave reflections in the large vessels at a fraction of the computational cost. Most of these studies use 1D subject-specific models predict systemic hemodynamics. The study by Yin et al. [268] use a 1D model to predict energy losses due to stenoses in the coronary arteries. They compare 1D and 3D computations of coronary FFR in the same geometry, finding a maximum error of 3% between the two model types. Likewise, Bezerra et al. [25] predict nearly identical FFR from 3D and 1D models for multiple coronary artery patient

geometries. These studies suggest that 1D models provide nearly identical results to higher fidelity 3D models in both normotensive and hypertensive scenarios.

The models referenced above lump small vessel hemodynamics into boundary conditions. Most use the so-called Windkessel boundary condition [222, 268], a circuit analog that lumps the resistance and compliance of the microvasculature. Though this is adequate for examining large vessel dynamics, it is essential to utilize a multiscale approach including the large and small vessels. Several studies address this using a morphology-based, fractal-tree model and simplified fluid dynamic equations for the distal vasculature [42, 223]. Spilker et al. [223] use this boundary condition with a 1D CFD model to predict pulmonary hemodynamics in a porcine and a human model. Their approach utilizes the Strahler ordering scheme [102] to generate distal vascular beds and an impedance boundary condition, showing that the computed impedance is similar to the measured impedance spectra. Clipp and Steele [42] use the structured-tree boundary condition, originally developed by Olufsen [166], to predict pulmonary hemodynamics during inspiration and expiration in lambs. Their results show that the zero-frequency component of the impedance (Z) can be adjusted and matched to pressure data during respiration. While these studies account for the distal vascular structure to determine impedance boundary conditions, they do not predict hemodynamics within the distal vasculature itself.

Several studies predict multiscale hemodynamics, imperative for understanding the interactions between the large and small vessels during PH [35, 40, 169, 266]. Yang et al. [266] use the impedance boundary condition previously implemented by Spilker et al. [223] in a 3D pulmonary circulation model. They predict mean WSS in a Strahler-based distal vascular structure, and illustrate that severe PAH increases mean WSS in the smallest arteriolar branches. Clark and Tawhai [40] use a wave-transmission model of the pulmonary arterial and venous trees and couple it to a capillary sheet model to predict hemodynamics throughout the pulmonary circulation. They use imaging to obtain arteries and veins to the subsegmental level, whereas the arterioles and venules are generated using a space-filling algorithm. Their multiscale study also provides qualitative predictions of lung perfusion, showing increased flow heterogeneity with reduced pulmonary vascular compliance. The study by Olufsen et al. [169] solves nonlinear, inertia-driven 1D flow equations in the large pulmonary arteries and a linearized wave-equation in the arterioles of the structured tree model. The authors use the model framework to investigate pulmonary microvascular rarefaction and show that reducing the number of arterioles increases mPAP. A similar modeling approach is used in Chambers et al. [35], which compares control and hypertensive (PH induced by hypoxia - PH group 3) mice. Their study uses large artery geometry from micro-CT imaging, whereas the small arterial and arteriolar networks are constructed from fractal trees with scaling parameters extracted from high-resolution imaging data.

To our knowledge, no previous studies incorporate pressure loss models to study the effect of lesions in CTEPH, nor do they attempt to predict large and small vessel fluid dynamics in CTEPH. To address this critical gap in the literature, we propose a novel multiscale approach that predicts large and small vessel hemodynamics. We conduct the former simulations in a patient-specific geometry extracted from CT images, whereas the latter simulations are done in asymmetric, structured trees. We combine this computational model with two energy loss models for ring- and web-like thromboembolic lesions to predict pressure, flow, and area in normotensive and CTEPH scenarios. To understand how lesions and pulmonary vascular remodeling affect pulmonary hemodynamics, we compute mPAP, FFR, and a wave reflection index, as well as lung perfusion. We compute these quantities under normotensive and four physiologically-driven CTEPH conditions. The flow distribution within the lung is converted to a quantitative flow heterogeneity index utilizing the Kullback-Leibler (KL) divergence [24]. Finally, we simulate "virtual BPA" by modulating lesion severity in multiple vessels and identify the most significant set of lesions for percutaneous intervention. This study develops a proof-of-concept modeling tool, which can assist the interdisciplinary team of cardiologists,

pulmonologists, and radiologists in determining the optimal intervention strategy for BPA therapy.

9.3 Materials and Methods

9.3.1 Network geometry

In this study, the pulmonary arterial geometry consists of an image-based large artery network generated from a CT image and a self-similar, fractal-tree representing the small arteries and arterioles.

9.3.1.1 Large vessel geometry

We generate a network of large pulmonary arteries from a publicly available chest CT scan (from Simvascular¹). The CT image is from a healthy, 67-year-old female volunteer, captured using Omnipaque 350 contrast agent. Similar to our previous study [35], we segment and reconstruct the pulmonary arterial network and lung cavity using the open-source segmentation software 3DSlicer² [64]. When segmenting the geometry, we first identify the MPA, LPA, and RPA, and then manually segment all lobar, segmental, and subsegmental vessels. We generate the 1D network by reducing the 3D vessel geometry to centerlines using the Vascular Modeling ToolKit (VMTK)[11] and use our network extraction algorithm to generate a directed graph from the centerlines [45]. This algorithm converts the network to a series of arcs (vessels) and nodes (junctions), encoded by a connectivity matrix. For non-terminal arteries, each vessel's outlet is connected to either two or three vessel inlets, deemed the parent and daughter vessels, respectively. Terminal vessels are prescribed a structured tree model at their outlet, as defined below. Each vessel has a constant radius and a length. Radii are computed as the mean within the center 80% of the vessel, and the lengths are computed as the Euclidean distance between each point in the vessel. Figure 9.1 illustrates this process showing three planes in the CT image, the segmented network and lung cavity, and the 1D network.

9.3.1.2 Small vessel geometry

It is difficult to obtain high-fidelity measurements of the small arteries and arterioles from CT images. To circumvent this, we represent the small vessels with fractal, self-similar structured trees [166, 169]. We assume that each daughter vessel is related to its parent via the radius scaling factors α and β , and a length to radius ratio L_{rr} . The dimensions of any vessel in the structured tree can be expressed in terms of the terminal large artery radius r_{term} proximal to the beginning of the structured tree

$$r_{n,m} = r_{term} \alpha^n \beta^m, \quad L_{n,m} = L_{rr} r_{n,m}. \quad (9.1)$$

Following [189], who use a combination of pulmonary artery literature data, the length to radius ratio used in this study is

$$L_{rr} = \begin{cases} 15.75 r^{1.10} & r \geq 0.005 \\ 1.79 r^{0.47} & r \leq 0.005 \end{cases}. \quad (9.2)$$

The structured tree is terminated after a specified minimal radius, r_{min} , has been reached. We use parameter values from a previous investigation from high-resolution micro-CT scans of control and hypertensive

¹<http://simvascular.github.io/>

²<http://www.slicer.org>

mice [35], and set $\alpha = 0.88$ and $\beta = 0.68$. The terminal radius of the structured tree is based on anatomical literature and set to $7.5\mu\text{m}$ [237].

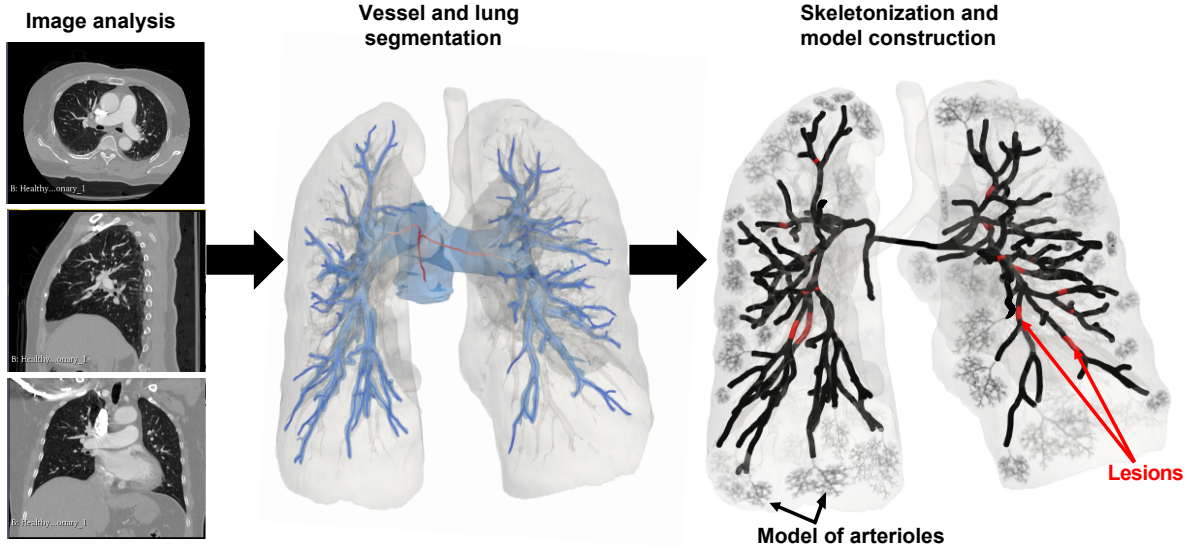


Figure 9.1 Schematic of model development, starting from image analysis and image segmentation and ending in construction of the skeletonized network and computational domain.

9.3.2 Fluid dynamics

The 1D model consists of the large pulmonary arteries segmented from the CT image, and the small pulmonary arteries and arterioles represented by structured trees. In the large arteries, we predict inertia-driven hemodynamics using a system of nonlinear partial differential equations (PDEs), while fluid dynamics in the network of small vessels are predicted by solving a linearized wave equation.

9.3.2.1 Large vessel hemodynamics

Similar to previous studies [46, 189, 191], we compute flow $q(x, t)$ (mL/s), pressure $p(x, t)$ (mmHg), and cross-sectional area $A(x, t)$ (cm^2) in each large vessel by enforcing conservation of volume

$$\frac{\partial A}{\partial t} + \frac{\partial q}{\partial x} = 0, \quad (9.3)$$

and the balance of momentum

$$\frac{\partial q}{\partial t} + \frac{\partial}{\partial x} \left(\frac{q^2}{A} \right) + \frac{A}{\rho} \frac{\partial p}{\partial x} = -\frac{2\pi\nu R}{\delta} \frac{q}{A}, \quad (9.4)$$

where $\rho = 1.055$ (g/mL) is the blood density and ν (cm^2/s) is the kinematic viscosity. The right hand side of equation (9.4) is derived under the assumption that the fluid velocity profile, $u_x(r, x, t) = q/A$ (cm/s), has a

linearly decreasing boundary layer thickness δ (cm), i.e.,

$$u_x = \begin{cases} \bar{u}_x, & 0 \leq r \leq R - \delta \\ \bar{u}_x / (R - \delta), & R - \delta \leq r \leq R. \end{cases} \quad (9.5)$$

The boundary layer δ is approximated by $\sqrt{\nu T / 2\pi}$, where T (s) is the cardiac cycle length [137]. Under this assumption, the shear stress in the large vessels is

$$\tau(x, t) = -\mu \left. \frac{\partial u_x}{\partial r} \right|_{r=R} = \mu \frac{\bar{u}_x}{\delta}. \quad (9.6)$$

To close the system of equations, we impose a pressure-area relation governing the interaction between the vascular wall and the blood. Under the assumption that vessels are thin-walled, linearly elastic, homogenous, and isotropic [166, 268], we get

$$p(x, t) = p_0 + \frac{4}{3} \frac{E h}{r_0} \left(\sqrt{\frac{A}{A_0}} - 1 \right), \quad (9.7)$$

where p_0 (mmHg) is the reference pressure at which $A = A_0 = \pi r_0^2$, E (mmHg) is Young's modulus in the circumferential direction, and h (cm) is the wall thickness. For clarity, simulations are conducted in cgs units but the results are provided in mmHg using the conversion $1 \text{ mmHg} = 1333.22 \text{ g/cm/s}^2$.

Previous investigations [128] suggest that pulmonary vascular wall properties, e.g., Young's modulus (E) and wall thickness (h), change with vessel caliber. To account for these varying wall properties, we assume that the wall-stiffness $E h / r_0$ can be represented by

$$\frac{E h}{r_0} = k_1^{la} e^{r_0 k_2^{la}} + k_3^{la} \quad (9.8)$$

as described by Olufsen [166]. Here k_1^{la} (mmHg), k_2^{la} (cm^{-1}), and k_3^{la} (mmHg) are stiffness parameters for the large arteries. Normotensive values of $k_1^{la} = 2.5 \times 10^6$, $k_2^{la} = -15$, and $k_3^{la} = 6.4 \times 10^4$ are based on our previous investigation [189, 191].

The nonlinear system of PDEs is hyperbolic with characteristics pointing in the opposite direction; thus, we require boundary conditions at each vessel inlet and outlet ($x = 0$ and $x = L$, respectively). We digitize an average control flow waveform, available from Simvascular, using GraphClick³ to provide an inflow boundary condition at the inlet of the MPA. The cardiac output is scaled to match the flow values used in [169]. At non-stenotic vessel junctions, we prescribe continuity of static pressure and conservation of flow

$$p_p(L_p, t) = p_{d_1}(0, t) = p_{d_1}(0, t), \quad (9.9)$$

$$q_p(L_p, t) = q_{d_1}(0, t) + q_{d_2}(0, t) \quad (9.10)$$

which holds $\forall t \in [0, T]$. Lastly, we couple the terminal large arteries to the structured tree model, as described later.

9.3.2.2 Stenosis models

As discussed earlier, CTEPH progression is attributed to multiple emboli and vascular proliferation, which are grouped into five types [115]: ring-like, web-like, subtotal occlusion, total occlusive, and tortuous lesions. In

³<http://www.arizona-software.ch/graphclick/>

this work, we model ring-like lesions (accounting for approximately 30% of all lesions) and web-like lesions (accounting for approximately 64% of all lesions) [115].

We model the former lesion type using the pressure loss term derived from Young and Tsai's work [271]

$$\Delta p_{\text{ring}} = \frac{\mu K_v}{2\pi(r_p)^3} q + \frac{\rho K_t}{2(A_p)^2} \left(\frac{A_p}{A_s} - 1 \right)^2 |q|q + \frac{\rho K_u L_s}{A_p} \frac{\partial q}{\partial t}, \quad (9.11)$$

where K_v , K_t , and K_u (dimensionless) are the loss coefficients due to viscous, turbulent, and inertial forces, respectively. Moreover, r_p (cm) and A_p (cm²) denote the unobstructed radius and area proximal to the lesion, and L_s is the length of the ring-like lesion. This stenosis model has been implemented in 1D models and validated against 3D models in the systemic circulation [25, 183, 268]. The viscous loss K_v , related to the stenosis geometry, is given by [268]

$$K_v = 16 \frac{L_s}{r_p} \left(\frac{A_p}{A_s} \right)^2. \quad (9.12)$$

Ring-like lesions are typically located proximal to vascular junctions [115], hence we prescribe these lesions and their energy loss proximal to vessel junctions.

We model web-like occlusions as semi-porous structures, which only partially occlude the vascular lumen [108]. The pressure drop in web-like lesions is modeled as

$$\Delta p_{\text{web}} = L_w \left(\frac{\mu}{K_{\text{perm}}} \frac{q}{A} + \rho K_w \left(\frac{q}{A} \right)^2 \right), \quad (9.13)$$

where L_w (cm) is the length of the obstructed area, K_{perm} (cm²) is the permeability of the web-like lesion, and K_w (dimensionless) is the pressure drop due to inertial effects. Equation (9.13), the Darcy-Forchheimer equation, is used for fluid flow through porous media at moderate Reynold's numbers (i.e. > 10) [275]. Previous work [126, 275] assumes that $K_w \approx G/K_{\text{perm}}^{1/2}$, where G (cm) depends on the material in question. Since material properties are unknown, we assume $G = 0.10$ for all simulations involving web-like lesion and place them at the vessel midpoint as these lesions can extend throughout a single vessel [108].

We compute the FFR for each lesion to quantify the pressure-losses due to lesion type and severity. As done in prior coronary studies [26], the FFR is calculated as

$$\text{FFR} = \frac{\bar{p}_{\text{dist}}}{\bar{p}_{\text{prox}}} \quad (9.14)$$

where \bar{p}_{prox} and \bar{p}_{dist} are the mean pressure proximal to and distal to the lesion, respectively.

9.3.3 Small vessel hemodynamics

While inertial effects dominate large vessel hemodynamics, blood flow in the small arteries and arterioles is dominated by viscous forces. For this reason, we solve linearized forms of equations 9.3 and 9.4. The linearized equations are converted to a discrete, frequency domain Fourier series, resulting in a wave-equation with analytical pressure and flow solutions, $P(x, \omega)$ and $Q(x, \omega)$, for each frequency ω . These are related via the impedance, $Z(x, \omega) = P(x, \omega)/Q(x, \omega)$. The input impedance at $x = 0$ can then be written as

$$Z(0, \omega) = \frac{ig^{-1} \sin(\omega L/c) + Z(L, \omega) \cos(\omega L/c)}{\cos(\omega L/c) + igZ(L, \omega) \sin(\omega L/c)} \quad (9.15)$$

for any frequency $\omega \neq 0$, whereas the zero frequency value, $Z(0, 0)$, analogous to the DC component in electrical circuit theory, is given by

$$\lim_{\omega \rightarrow 0} Z(0, \omega) = \frac{8\mu\ell_{rr}}{\pi r_0^3} + Z(L, 0). \quad (9.16)$$

The above equations depend on the frequency domain quantities g_ω and c , which are defined in Section 4.3. These terms depend on Eh/r_0 , which has the same form as equation 9.8, but with parameters k_1^{sa} , k_2^{sa} , and k_3^{sa} .

Noting that $Q(L, \omega) = P(L, \omega)/Z(L, \omega)$ for each frequency, we can predict impedance, pressure, and flow using

$$P(L, \omega) = P(0, \omega) \cos(\omega L/c) - Q(0, \omega) \frac{i}{g_\omega} \sin(\omega L/c), \quad (9.17)$$

$$Z(L, \omega) = \frac{i g_\omega^{-1} \sin(\omega L/c) - Z(0, \omega) \cos(\omega L/c)}{g_\omega \cos(\omega L/c) Z(0, \omega) - \cos(\omega L/c)}, \quad (9.18)$$

for $\omega \neq 0$. For the zeroth frequency, the solution is

$$P(L, 0) = P(0, 0) - Q(0, 0) \frac{8\mu L}{\pi r^4}, \quad (9.19)$$

$$Z(L, 0) = Z(0, 0) - \frac{8\mu L}{\pi r^4} \quad (9.20)$$

This enables us to predict pressure and flow in any daughter vessel provided the pressure and flow of the parent are known [169].

The non-Newtonian effects of blood viscosity μ (and hence kinematic viscosity ν) become more influential as the vessel radii decrease towards the arterioles. Following [184], and our previous study [35], we model the viscosity in the small arteries and arterioles by a nonlinear radius dependent function of the form

$$\mu^*(r_0) = [1 + (\mu_{0.45} - 1)\mathcal{D}] \mathcal{D}, \quad (9.21)$$

$$\mu_{0.45}(r_0) = 6e^{-0.17r_0} + 3.2 - 2.44e^{-0.12r_0^{0.645}}, \quad (9.22)$$

where $\mathcal{D} = (2r_0/(2r_0 - 1.1))^2$ and $\mu_{0.45}(r_0)$ is the relative viscosity at an average hematocrit level of 0.45 [184]. We assume a typical healthy blood hematocrit of 0.45.

We assume continuity of pressure and conservation of flow at each junction in the small vessels of the structured tree. Under these assumptions, the impedance at a junction parallels resistors in parallel, i.e. $Z_p^{-1} = Z_{d_1}^{-1} + Z_{d_2}^{-1}$. At the terminating end of the structured tree (i.e., $Z(L, 0)$ at the last generation branches), the terminal impedance $Z_{trm} = \text{constant}$ is prescribed. Since the structured tree results in thousands of vessels, the flow at the end of the structured tree's are on the order of $10^{-5} - 10^{-8}$. For this reason, the capillary pressure, $P_{trm} = Z_{trm} \cdot Q_{trm}$, requires the magnitude of Z_{trm} to be on the order of $10^5 - 10^9$ to achieve non-negligible pressure values. Once we reach the terminal structured tree branch, all proximal impedance values in the tree are computed. Knowing the impedance at the root of the tree provides an interface between the large and small vessels. The large artery predictions are then used to simulate structured tree hemodynamics using the impedance relations above.

9.3.4 Numerical solution

Large vessel hemodynamics (equations (9.3, 9.4, B.95)) are solved using the Ritchmeyer two-step Lax-Wendroff scheme [166], which is second order accurate in space and time. At non-stenotic junctions, pressure continuity and flow conservation are enforced via a Newton-Raphson root finding routine. Pressure losses due to ring-like lesions, located proximal to bifurcations, are also solved using a Newton-Raphson routine. For web-like lesions, located at vessels' midpoint, we minimize residual equations using gradient-descent with a backtracking line search algorithm [116]. To increase numerical accuracy at the junctions and lesion locations, we derive and utilize the analytical Jacobian of the residuals.

To couple the large vessels to the structured tree, the frequency impedance is convolved with the pressure at the end of the large arteries. This is numerically approximated as

$$q_L^n = \Delta t \sum_{k=1}^n p_L^{n-k} (Z^k)^{-1}, \quad (9.23)$$

where q_L^n and p_L^{n-k} are the numerical solutions of flow and pressure at the end of the large terminal arteries, and Z^k is the vascular impedance of the whole structured tree calculated using equation (9.15).

9.3.5 Wave intensity analysis

Wave intensity analysis (WIA) is a time-domain decomposition of forward and backward waves and is utilized in understanding the progression of cardiovascular disease [189, 191, 230]. The so-called pressure and velocity 'wavefronts' [172] δp^\pm and δu^\pm are calculated as

$$\delta p^\pm = \frac{\delta p \pm \rho c(p) \delta u_i}{2}, \quad \delta u^\pm = \frac{1}{2} \left(\delta u \pm \frac{\delta p}{\rho c(p)} \right), \quad (9.24)$$

where the notation \pm indicates the forward ('+') or backward ('-') running wave components, and δp and δu are the incremental changes in pressure and velocity, respectively. The wave speed $c(p)$ is calculated from the pressure-area relation

$$c(p) = \sqrt{\frac{A}{\rho} \frac{\partial p}{\partial A}} = \sqrt{\frac{Eh}{r_0} \frac{1}{2\rho} \left(\frac{A}{A_0} \right)^{1/4}}. \quad (9.25)$$

Both forward and backward waves are classified as compression ($\delta p^\pm > 0$) or decompression ($\delta p^\pm < 0$) waves. Forward compression waves (FCW) originate from the right ventricle, increasing pressure and accelerating flow as blood travels towards the periphery. Forward expansion waves (FEW) also originate in the proximal arteries but decrease the pressure and flow velocity. In contrast, backward compression waves (BCW) and expansion waves (BEW) propagate from the periphery, the former increasing pressure while decelerating flow, while the latter does the opposite. The wave intensity W^{I_\pm} is calculated as a product of the velocity and pressure wavefronts. Since wavefronts are not continuous but discrete approximations, we use the time-normalized wave intensity

$$W^{I_\pm} = \frac{\delta p^\pm}{\delta t} \frac{\delta u^\pm}{\delta t}. \quad (9.26)$$

After determining the type and nature of the waves, a wave reflection coefficient, \mathcal{R} , can be calculated. In this study, we use

$$\mathcal{R} = \frac{\Delta p_-}{\Delta p_+}, \quad (9.27)$$

where Δp_+ and Δp_- are the sums of the backward and forward compression waves, respectively [156].

9.3.6 Lung perfusion and heterogeneity

We map flow predictions from the large arteries to the 3D geometry [35] to predict lung perfusion. To do so, we first determine which vessels are closest to the lung tissue using a nearest-neighbor algorithm in MATLAB (Mathworks, Natick, MA). Then, we project the 1D flow predictions onto the lung tissue and generate a lung perfusion map. These predictions are converted to a probability distribution function (PDF) using kernel density estimation; we use the `ksdensity` function in MATLAB. To quantify flow heterogeneity in control, CTEPH, and post-surgical intervention simulations, we compute the KL divergence, a measure of relative entropy between two probability distributions [24], for the flow PDFs.

The KL divergence is a probabilistic measure between two distributions [24]. Let \mathcal{A} and \mathcal{B} be discrete probability distributions defined on some probability space \mathcal{W} , where \mathcal{A} is our reference or target distribution. Then, the KL-divergence is defined as

$$D_{KL}(\mathcal{A} \mid \mathcal{B}) = \sum_{w \in \mathcal{W}} \mathcal{A}(w) \log \left(\frac{\mathcal{A}(w)}{\mathcal{B}(w)} \right), \quad (9.28)$$

where $D_{KL} \rightarrow 0$ indicates identical distributions, while increasing values of D_{KL} indicates a bigger mismatch between the two distributions.

In summary, we compute the perfusion map and quantify flow heterogeneity as follows:

- (1) project the 1D flow predictions to the centerline network in 3D;
- (2) determine the terminal vessels closest to the segmented lung tissue via a nearest-neighbor algorithm;
- (3) prescribe the flow to the entire portion of tissue;
- (4) construct the flow PDF, \mathcal{B} , via kernel density estimation; and
- (5) compute $D_{KL}(\mathcal{A} \mid \mathcal{B})$.

9.3.7 Chronic thromboembolic pulmonary hypertension (CTEPH)

To simulate CTEPH, we add ring-like (concentric stenosis) and web-like (longitudinal narrowing within a vessel) [115] lesions to the proximal pulmonary arteries. We also introduce arterial vasoconstriction and progressive remodeling of the distal vasculature [50]. The former is done by decreasing the radii of vessels segmented from the CT image, while the latter is done by increasing terminal PVR (Z_{trm}) and vessel stiffness in the structured trees. We set up a normotensive simulation and four disease cases and examine changes in hemodynamic predictions. These disease cases are summarized in Table 9.1 and parameter values are given in Table 9.2. To simulate the effects of BPA, we reduce both stenosis and downstream vasoconstriction severity in three lesions and quantify improvements in hemodynamics after BPA.

9.3.7.1 Disease cases

9.3.7.1.1 Case a: Lesions only

This scenario represents a CTEPH patient without pulmonary vascular remodeling, illustrating the sole effects of arterial obstructions (ring- and web-like lesions). We add a total of 20 lesions in the network: 9 ring-like and 11 web-like. Ring-like lesions have an area reduction of 90% and spread over 25% of the original vessel. These lesions are placed proximal to vessel junctions [115]. Web-like lesions have a permeability parameter

$K_{perm} = 0.009$ and a lesion length parameter, which is 50% of the vessel's length [115]. Vessels that contain either lesion type are ten fold stiffer to account for wall stiffening due to thromboembolic material.

9.3.7.1.2 Case b: Lesions with local remodeling

In this scenario, the disease has progressed downstream to the lesions. Remodeling narrows the vascular lumen and moderately thickens the vascular walls, decreasing vessel compliance. Parameters k_1 , k_2 , and k_3 are increased in all vessels (both large and small) distal to the lesion while reducing the reference vessel radius r_0 by 40%. We also increase pulmonary vascular resistance by increasing Z_{trm} in terminal vessels that are narrowed.

9.3.7.1.3 Case c: Lesions with small vessel arteriopathy

Prolonged exposure to CTEPH is associated with secondary arteriopathy throughout the pulmonary vasculature, affecting vessels with cross-sectional areas $\leq 5\text{mm}$ [50, 130]. In particular, long-term elevation in flow and shear stress in non-obstructed vessels leads to endothelial dysfunction and increased PVR [217]. We model this by inducing global small vessel remodeling, i.e., reducing the reference radius r_0 in all vessels with a cross-sectional area $< 5\text{mm}^2$ by 40% and increasing vessel stiffness. We also increase Z_{trm} in the structured trees.

9.3.7.1.4 Case d: Lesions with proximal dilation and global small vessel arteriopathy

In the most severe cases of CTEPH, small vessel arteriopathy causes large artery dilation and stiffening [115, 130]. This scenario includes the global small vessel remodeling described in case c, with dilation and thickening of arteries with cross-sectional areas $\geq 10\text{mm}^2$ by 10%, as documented previously [50]. We further increase stiffness and raise PVR in all terminal vessels.

9.3.7.2 BPA therapy

Inoperable CTEPH patients with inaccessible distal lesions for PTE are ideal candidates for BPA. We simulate BPA intervention by decreasing lesion severity simultaneously in three locations at a time. BPA does not completely remove the lesions; hence, we still include them in the model but reduce their severity. Specifically, we reduce the stenosed area A_s and lesion length L_s from 90% to 50% for ring-like lesions and increase K_{perm} (equation (9.13)) from 0.009 to 0.05 for web-like lesions. We also return vessel reference radii, r_0 , to 90% of their original value in the obstructed pathways, mimicking decreased vasoconstriction due to lung reperfusion.

Since multiple interventions must be performed to improve hemodynamic function, the most severe lesions are prioritized for treatment to optimize increases in lung perfusion and decreases in mPAP, PVR, and wave reflections. This study uses simulations to select the "optimal" interventional option by quantifying flow heterogeneity, MPA pressure, wave reflection coefficients, along with post-BPA perfusion maps. We perform all virtual procedures in disease case (d), and compare hemodynamic indices pre- and post-BPA.

9.4 Results

The large pulmonary arterial network includes 226 vessels including the MPA, LPA, and RPA, and all visible segmental and subsegmental branches. Centerlines constructed by VMTK are processed and implemented in the 1D model. With the exception of one trifurcation, all network junctions are bifurcations. Vessels with a

Table 9.1 Summary of disease scenarios simulated in this study.

Disease scenario	Description	Modeling approach
Control	Typical pulmonary vasculature	<ul style="list-style-type: none"> - Low stiffness - Minimal PVR
(a) Lesions only	Mechanical obstructions due to ring- and web-like lesions	<ul style="list-style-type: none"> - 90% area reduction in 9 ring-like lesions - 0.009 permeability in 11 web-like occlusions
(b) Lesions with local remodeling	Increased vascular stiffness, narrowing of vessels distal to lesions, and increased PVR	<ul style="list-style-type: none"> - Increased stiffness in vessels distal to lesions - 40% reduction in radius in vessels distal to lesions - Increased PVR in terminal vessels distal to lesions
(c) Lesions with global small vessel arteriopathy	Narrowing, stiffening, and increased resistance of all small vessels	<ul style="list-style-type: none"> - 40% reduction in radius in vessels with $A_0 < 5\text{mm}^2$ - Increased stiffness in narrowed vessels - Increased PVR in affected terminal vessels
(d) Lesions with proximal remodeling and small vessel arteriopathy	Narrowing and stiffening of small vessels, dilation and stiffening of large proximal vessels, and increased PVR	<ul style="list-style-type: none"> - Small vessel remodeling from (c) - Dilation of proximal arteries with $A_0 \geq 10\text{mm}^2$ - Increased network stiffness - Increased PVR in all terminal vessels

length ≤ 1.25 mm (3 of the 226 vessels) are elongated to match the spatial resolution of the fluid dynamics solver.

We simulate normotensive hemodynamics and four disease cases with increasing CTEPH severity (cases a-d). CTEPH is induced by including 20 lesions in the segmental and subsegmental vessels and by increasing the stiffness of the large and small arteries. We compare large and small vessel hemodynamics, network perfusion, and wave intensities for all simulations. Using case (d) as our baseline for BPA, we perform virtual treatments by reducing lesion severity and stenosis induced vasoconstriction in three lesions at a time. We select an optimal procedure based on improvements in flow heterogeneity, MPA pressure, and the wave reflection coefficient.

9.4.1 Effects of lesion severity

To understand how lesions affect pulmonary hemodynamics, we increase the stenosis area of ring-like lesions and reduce the permeability of the web-like lesions. We increase the relative stenosis area, A_s/A_p , from 0% to 90%, and decrease K_{perm} from 1.5 to 0.003. Figure 9.2 shows changes in mean MPA pressure along with FFR

Table 9.2 Parameter values for simulating the five different disease scenarios described in section 9.3.7. k_3 and Z_{trm} values are listed for vessels both in unobstructed and obstructed paths (in parentheses).

Parameter	Disease case				
	Normotensive	a	b	c	d
k_1^{la} (g/(cm s ²))	2.5×10^6	2.5×10^6	2.5×10^6	2.5×10^6	1.0×10^7
k_2^{la} (1/cm)	-15	-15	-20	-20	-10
k_3^{la} (g/(cm s ²))	6.4×10^4	6.4×10^4	8.0×10^4	8.0×10^4	2.0×10^5
	—	—	(1.6×10^5)	(1.6×10^5)	(4.0×10^5)
k_1^{sa} (g/(cm s ²))	2.5×10^7	2.5×10^7	5.0×10^7	5.0×10^7	5.0×10^7
k_2^{sa} (1/cm)	-15	-15	-20	-20	-20
k_3^{sa} (g/(cm s ²))	8.0×10^5	8.0×10^5	1.6×10^6	1.6×10^6	1.6×10^6
	—	—	(1.6×10^7)	(1.6×10^7)	(1.6×10^7)
k^{lesion} (g/(cm s ²))	—	6.4×10^5	8.0×10^5	8.0×10^5	2.0×10^6
Z_{trm} (g/(cm ⁴ s))	1.0×10^5	1.0×10^5	1.0×10^6	1.0×10^7	1.0×10^8
	—	—	(1.0×10^8)	(1.0×10^8)	(1.0×10^8)

Table 9.3 Parameters describing ring- and web-like lesions and their values.

Stenosis parameters	Description	Value
K_t (ND)	Turbulent pressure loss coefficient	1.52
K_u (ND)	Inertial pressure loss coefficient	1.2
L_s (cm)	Ring-like lesion length	$L_i/4$
K_{perm} (cm ²)	Darcy loss coefficient for web-like lesion permeability	0.009
G (cm)	Inertial loss coefficient for web-like lesions	0.10
L_w (cm)	Length of web-like lesion	$L_i/2$

estimates at all lesion locations. Overall, increase ring-like lesion severity increases the mean MPA pressure from 12 to ~18 mmHg. Decreasing the permeability of web-like lesions is less influential on MPA pressure, raising it by approximately 0.5 mmHg. The minimum FFR for ring-like lesions is 0.16 when the area reduction is 90%, while the minimum FFR in web-like lesions is 0.66 for $K_{perm} = 0.003$. The average FFR for ring-like lesions at 90% area reduction is 0.25, whereas the average FFR is only 0.86 for the most web-like lesions when $K_{perm} = 0.003$.

We also map flow predictions from the 1D model to the segmented lung tissue. Figure 9.3 shows changes in perfusion when ring-like lesions' area reduction rise from 0% to 90%. Flow heterogeneity, quantified by the KL-divergence, increases with lesion severity. Results show larger perfusion deficits in the lower and

upper lobes than other regions of the lung. Changing K_{perm} in web-like lesions alone does not alter perfusion predictions substantially (results not shown). The flow PDF's for each simulation are shown in Figure 9.3. These PDFs are constructed using kernel density estimation with a bandwidth of 0.009 and a reflection boundary correction.

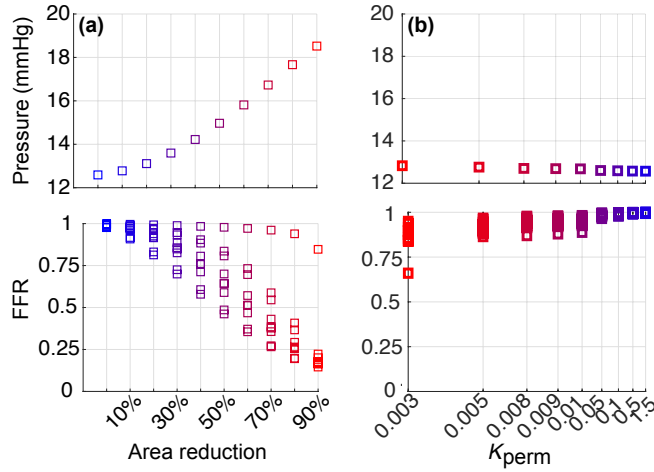


Figure 9.2 Predictions of mean MPA pressure (top), and fractional flow reserve (FFR, bottom) when increasing lesion severity in ring-like (left) or web-like (right) lesions. FFR predictions correspond to 9 ring-like lesions and 11 web-like lesions. Overall, ring-like lesions have a greater effect on MPA pressure and FFR than web-like lesions.

9.4.2 Large vessel hemodynamics

Normotensive and CTEPH predictions of pressure, flow, and shear stress at the midpoint of the MPA, LPA, and RPA are displayed in Figure 9.4. Simulations from case (a) (normotensive parameters with lesions only) result in a mean MPA pressure of 22.5 mmHg. The downstream stiffening and narrowing in case (b) have a negligible effect on pressure from case (a). Including global small vessel stiffening in case (c) elevates systolic and diastolic pressures slightly. In contrast, severe CTEPH, case (d), raises the pulse pressure (the difference between systolic and diastolic values), with systolic pressures ≈ 45 mmHg and diastolic pressures ≈ 5 mmHg.

Flow predictions are oscillatory during diastole in normotension and case (a), while increased vessel stiffness, cases (b)-(d), dampens the oscillations. All simulations have a larger flow distribution to the RPA than the LPA; normotensive predictions have a 43/57 flow split to the LPA/RPA, while in severe CTEPH, case (d), the ratio is 22/78. MPA and LPA Shear stress magnitude is greater in normotension than in any of the CTEPH simulations, while RPA shear stress is largest in case (d).

Figure 9.5 shows pressure predictions throughout the large pulmonary arteries in normotension, case (a), and case (d) at different times within the cardiac cycle. Yellow vessel segments denote lesion locations. Results show a dramatic rise in pressure proximal to lesions for cases (a) and (d), while pressure drops downstream to the lesions. For case (a), the average FFR is 0.33 (range [0.16 0.95]) for ring-like lesions and 0.95 (range [0.88 0.94]) for web-like lesions. In case (d), the average FFR is 0.37 (range [0.19 0.95]) for ring-like lesions and 0.94 (range [0.81 0.99]) for web-like lesions. Note that the pressure magnitude in vessels downstream to the lesions in case (d) are similar to normotension. Finally, we observe that peak systolic pressure trails

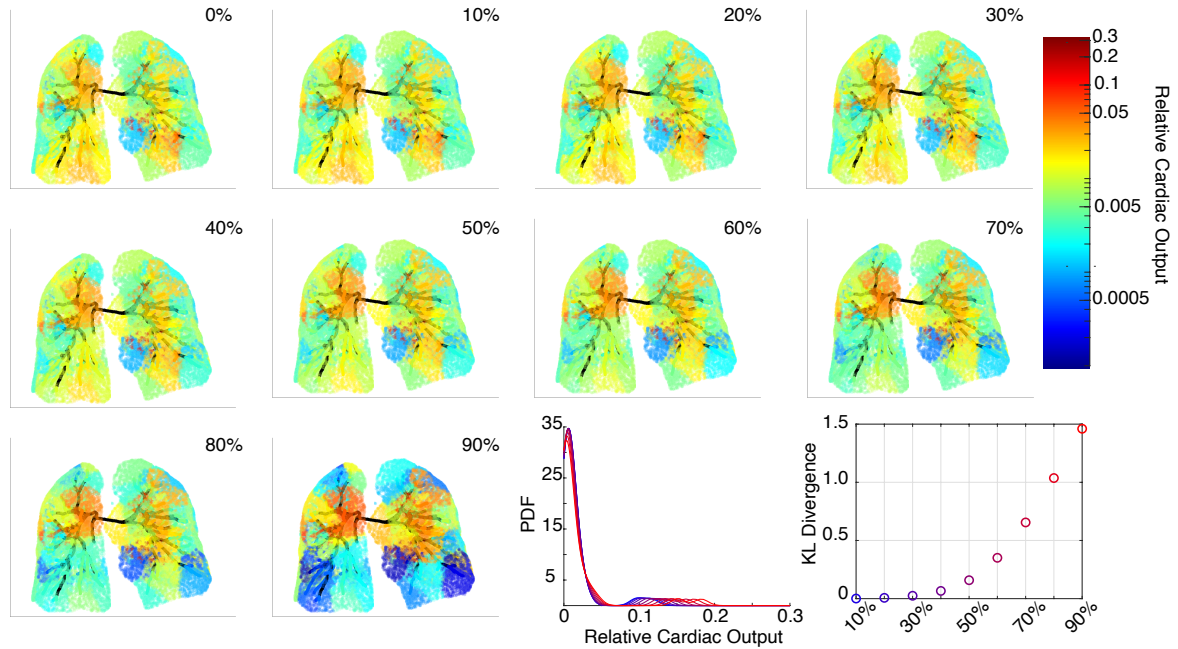


Figure 9.3 Perfusion maps for increasing ring-like stenosis severity. The top left panel (0%) shows the normotensive perfusion map, while the bottom right perfusion map shows 90% severity. The Kullback–Leibler (KL) divergence, constructed from the flow probability density function (PDF), quantifies the flow heterogeneity.

maximal MPA flow in all three simulations.

Figure 9.6 shows pressure and flow predictions along two pathways: one obstructed by lesions and one unobstructed. Pressure and flow results are reduced significantly in vessels distal to the lesion in the obstructed pathway. For case (d), stiffening and narrowing of the small vessels causes a pressure increase downstream to the lesion, yet the pressure has a smaller magnitude compared to normotensive simulations. Besides, the flow is significantly reduced in all CTEPH cases once lesions are included, though the flow does increase slightly in the terminal vessel when moving to case (d).

In contrast, all CTEPH simulations illustrate elevated pressure in the unobstructed pathway. The flow to the terminal vessel increases when lesions are added in case (a), but decreases in cases (c) and (d). Terminal vessel systolic pressure in case (d) is ~45 mmHg in vessels in the unobstructed path, whereas the terminal systolic pressure is 10 mmHg in the obstructed pathway.

9.4.3 Small vessel hemodynamics

The structured tree model predicts pressure and flow in the smaller arteries and arterioles. Figure 9.7 shows normotensive predictions as well as CTEPH simulations in six large terminal arteries: three that are downstream to a lesion and three that are not. Mean pressure and flow are shown along the α and β pathways, the longest and shortest pathways in the structured tree.

In the obstructed pathway, we see a significant drop in mean pressure and mean flow in case (a). This is consistent in both the α and β pathways. In contrast, flow redistribution to the unobstructed vessels cause an increase in pressure and flow. Vasoconstriction of the terminal arteries and stiffening of the microvasculature in case (d) increases pressure, yet flow in this pathway does not increase. Moreover, the mean pressure

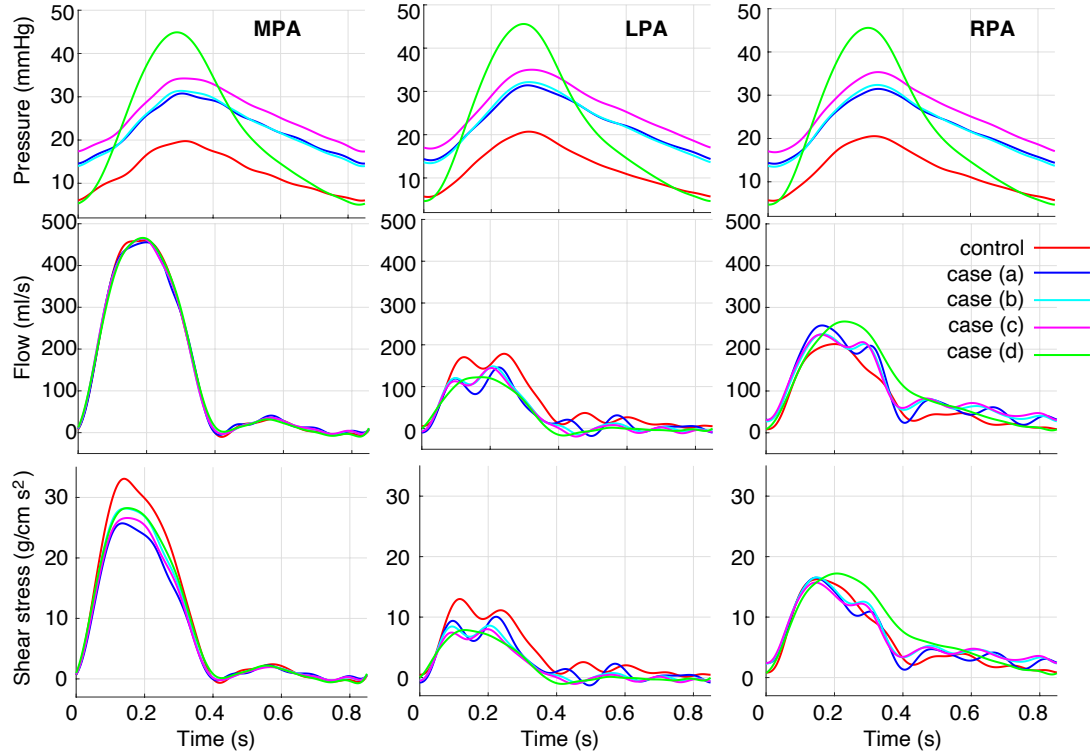


Figure 9.4 Pressure, flow, and shear stress in the main, left, and right pulmonary arteries in each disease scenario.

magnitudes in the unobstructed pathway are similar in both case (a) and case (d), though the systolic pressures (not shown) increase from 30 mmHg to 40 mmHg.

9.4.4 Wave intensity analysis (WIA)

Figure 9.8 presents wave intensity profiles in the MPA, LPA, and RPA for the normotensive and four disease cases. The wave reflection coefficient for each case is reported in Table 9.4. Normotensive simulations have a predominant FCW in all three branches, followed by a minor BCW. Overall, normotensive expansion waves are negligible. The wave reflection coefficient in the MPA is 0.47, smaller than the LPA and RPA (0.76 and 0.89). Adding lesions in case (a) leads to a prominent second FCW in the MPA and LPA, while RPA forward and backward compression waves have a bimodal profile that occur consecutively. Case (a) also produces a distinct bimodal BCW in both the MPA and LPA. In all three branches, both the forward and backward expansion waves are more oscillatory. The wave reflection coefficient increases in case (a) in the MPA and LPA, but decreases in the RPA.

Small vessel stiffening in case (b) dampens expansion wave oscillations. The wave intensity profile is similar to case (a) but shows an elevated FCW across the three branches. A diminished BCW magnitude decreases the MPA and RPA reflection coefficients; the LPA reflection coefficient is the same in case (a) and (b). Downstream narrowing in case (c) has a negligible effect on the wave intensities, but slightly intensifies BCW magnitudes, increasing the reflection coefficient in all three vessels. For case (d), the most severe CTEPH, the peak wave intensity increases for all four wave types and the bimodal FCW and BEW are gone. Though the compression wave peak increases, the wave reflection coefficient decreases in all three vessels, suggesting a

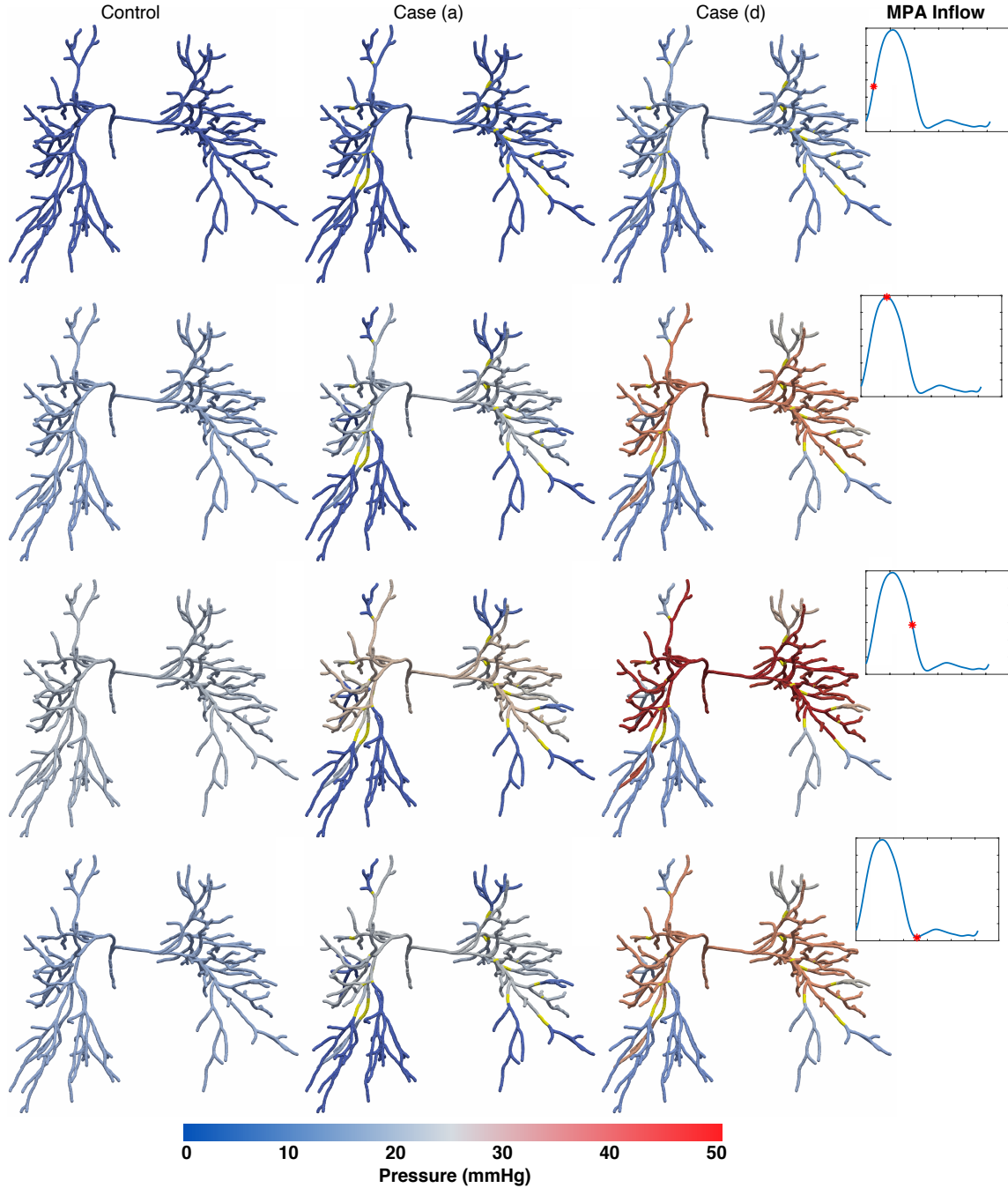


Figure 9.5 Pressure predictions in normotension and disease cases (a) and (d) throughout the network at different time points. Yellow segments indicate regions where lesions are present.

greater increase in magnitude for the FCWs than the BCWs.

9.4.5 BPA therapy

BPA therapy for inoperable CTEPH typically addresses 3-5 lesions per session; therefore, we target 3 lesions for the virtual BPA. This provides ${}_{20}C_3 = 1140$ possible lesion combinations, which are all analyzed. We choose

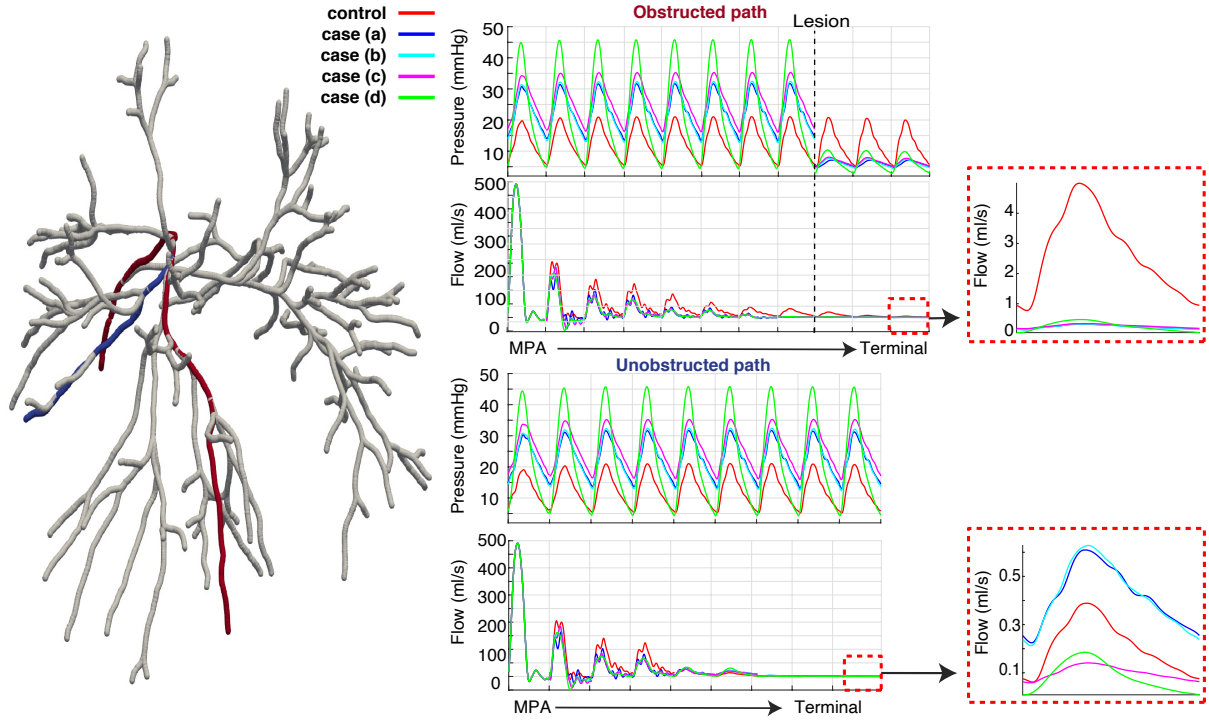


Figure 9.6 Representative obstructed (red) and unobstructed (blue) pathways in the pulmonary vasculature, along with predictions of pressure and flow for the normotensive and four CTEPH disease scenarios. A zoom in of the flow predictions in the most distal vessels of the tree are shown to the right. Results are consistent with other pathways in the network.

Table 9.4 Wave reflection coefficient in the main, left, and right pulmonary arteries (MPA, LPA, and RPA) in each disease case. The coefficient is calculated using equation 9.27.

Wave reflection coefficient			
Disease case	MPA	LPA	RPA
normotensive	0.47	0.76	0.89
case (a)	0.74	0.88	0.86
case (b)	0.68	0.88	0.83
case (c)	0.74	0.90	0.86
case (d)	0.49	0.83	0.67

the optimal BPA using a combination of MPA pressure, WIA results and flow heterogeneity (KL-divergence), and want to minimize all three quantities. These three metrics are shown in Figure 9.9 for both the pre- (case (d)) and post-BPA simulations. Results show that the optimal treatment targets three ring-like lesions: two in the right lower lobe and one in the left upper lobe (here, anatomical left and right are opposite to the left and right sides of the figure). Lung tissue perfusion maps show reperfusion to both regions, and the flow PDF shifts leftward towards a more uniform network flow. The KL-divergence decreases from 3.05 to 2.95, signifying a smaller distance between the control and post-BPA flow PDF. Systolic MPA pressure decreases from 45 to 42 mmHg after BPA, and mean pressure decreases from 22 mmHg to 19 mmHg, below the diagnostic PH cutoff. Lastly, wave intensity results illustrate a decrease in BCWs and an increase in FEWs post-BPA. The wave reflection index is reduced in all three proximal arteries after BPA, changing from 0.49, 0.83, and 0.67 to

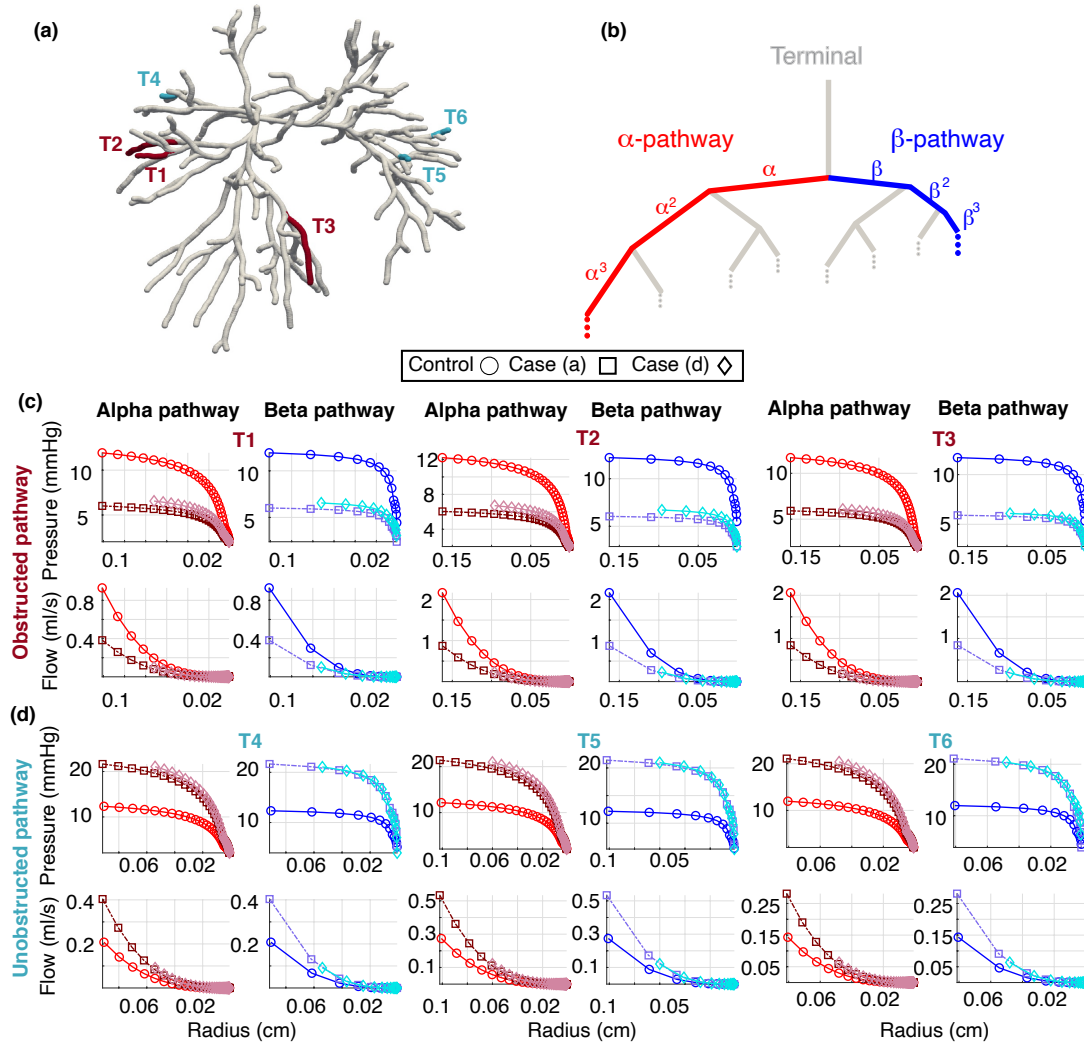


Figure 9.7 Hemodynamic predictions in the α and β pathways of the structured tree in the normotensive case and CTEPH cases (a) and (d). (a) Large vessel network with terminal vessels in obstructed (T1-T3, red) and unobstructed (T4-T6, blue) pathways. (b) Schematic of the structured tree (grey branches) and the α and β pathways (red and blue paths, respectively). (c) Mean pressure and flow predictions in the α and β pathways in terminal vessels T1-T3 as a function of radius. (d) Mean pressure and flow predictions in the α and β pathways in terminal vessels T4-T6 as a function of radius.

0.48, 0.76, and 0.61 in the MPA, LPA, and RPA, respectively. The pre-BPA FFR in these lesions are 0.44, 0.32, and 0.30, which improve to 0.88, 0.76, and 0.59, respectively, post-BPA.

9.5 Discussion

Computational hemodynamics is emerging as a useful clinical tool for cardiovascular disease. While several previous studies employ modeling to quantify treatment strategies for systemic artery disease [26, 268], less attention has been given to pulmonary vascular disease. In this study, we solve a patient-specific, 1D hemodynamics model in the large pulmonary arteries constructed from a CT image. The large vessels are

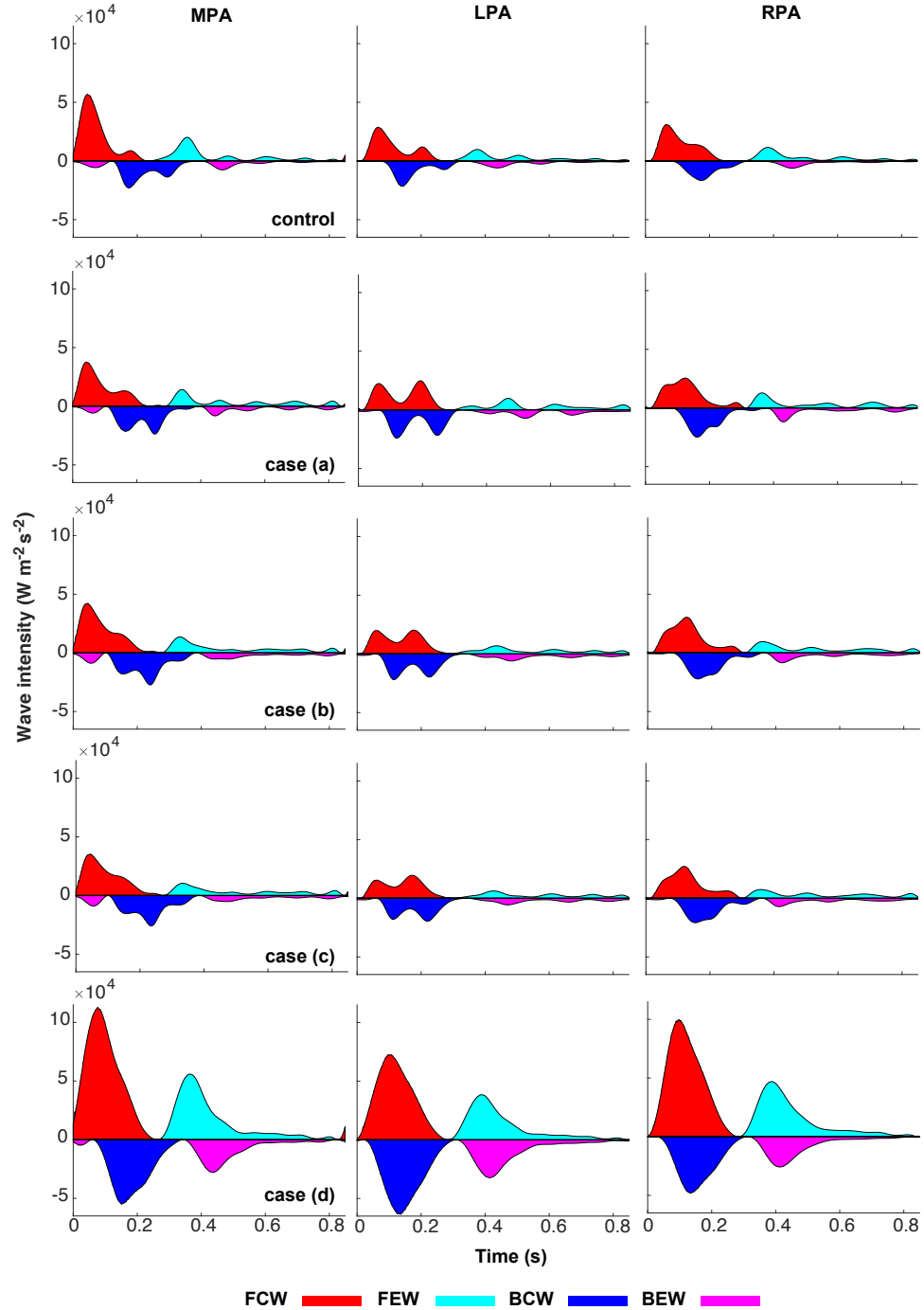


Figure 9.8 Wave intensity analysis (WIA) at the midpoint of the main, left, and right pulmonary arteries (MPA, LPA, and RPA, respectively). Forward and backward running compression waves (FCW, BCW) are distinguished from forward and backward running expansion waves (FEW, BEW).

coupled to a fractal-based small vessel model, enabling hemodynamic predictions at multiple scales. Our previous studies utilize a similar approach [35, 45, 46], yet this study is the first to utilize these methods with pressure loss models to generate perfusion maps and study CTEPH and BPA treatment strategies.

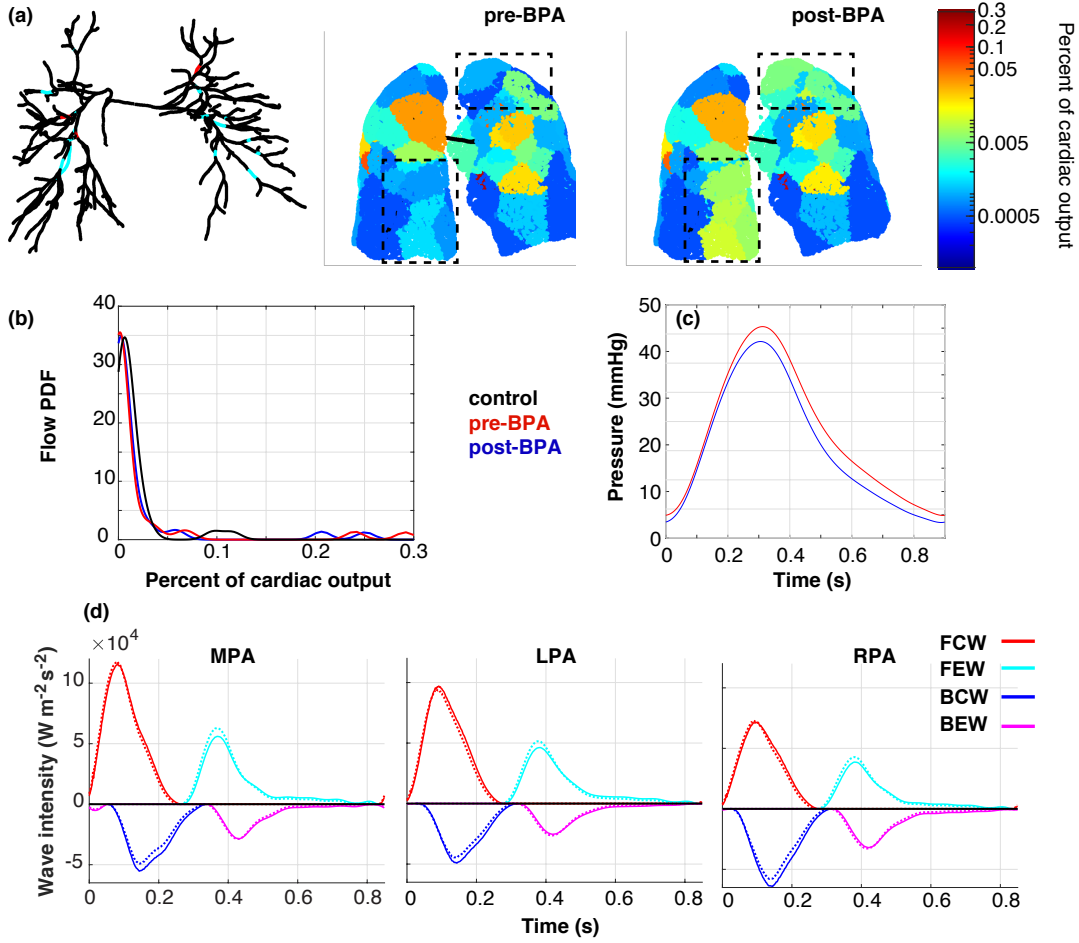


Figure 9.9 Pre and post-BPA metrics used to select the most effective treatment strategies. A total of 1140 interventions are considered. (a) Network of vessels with untreated lesions (cyan) and lesions treated in the best BPA simulation (red) along with pre and post-BPA perfusion maps. The region of the tissue most affected by BPA is identified within the black, dash-dot boxes. (b) Flow probability distribution functions (PDFs) for the normotensive (black), pre-BPA (red), and post-BPA (blue). (c) Pressure in the MPA pre-BPA (red) and post-BPA (black). (d) Wave intensities in the MPA, LPA, and RPA, pre-BPA (solid line) and post-BPA (dotted line).

9.5.1 Large artery hemodynamics

We consider five scenarios, ranging from normotensive to severe CTEPH. Figure 9.4 shows that lesions alone, case (a), elevate pressures above 20 mmHg and into the PH range. This agrees with results reported by Burrowes et al. [32], who use a steady flow, Poiseuille flow model to predict hemodynamics with and without pulmonary emboli. They argue that pulmonary vasoconstriction and stiffening are necessary to elevate mean arterial pressures above 25 mmHg. We observe similar trends in cases (b) and (c), which introduce narrowing and stiffening of the small vessels. Though cases (a)-(c) increase the mean MPA pressure, typical CTEPH patients have a systolic MPA pressure > 55 mmHg [230]. We approach this in case (d), which also dilates and stiffens the large pulmonary arteries. In addition to elevated pressure, our results show that the LPA/RPA flow imbalance increases with disease severity. This parallels results by Spazzapan et al. [222], which compare simulations between stenosed and non-stenosed geometries.

WSS in the MPA and LPA decreases in case (a), while the RPA shear stress increases. An elevated pressure without a change in wall stiffness leads to a larger area deformation, decreasing the flow velocity and WSS in the MPA. Case (a) leads to a larger flow and WSS in the RPA but reduces the WSS in the LPA. Shear stress does not increase significantly in case (d), a result of the proximal artery dilation which increases area (in the denominator of equation (9.6)). Results by Yang et al. [266] show a reduced time-averaged wall shear stress in pediatric patients with severe PH, congruent with our findings. Another study by Tang et al. [233] shows that proximal and distal WSS magnitude is smaller in PAH when compared to normotensive measurements, a consequence of MPA, LPA, and RPA dilation, also shown in this study. Though the mechanisms of PAH and CTEPH are different, both lead to proximal artery dilation [50, 266] and distal vascular narrowing [50, 145], hence a comparison of our results with PAH and CTEPH is appropriate.

A benefit of our model is the ability to project 1D network predictions onto surrounding lung tissue. Figure 9.3 shows a conversion of 1D model simulations to a 3D flow map, providing a meaningful and qualitative tool for physicians studying the effects of CTEPH. A recent study by Clark et al. [40] use a transmission line model to simulate large vessel hemodynamics and subsequently construct a lung perfusion map, similar to our work. However, their study did not account for perfusion deficits due to pulmonary lesions nor did it quantify flow heterogeneity, both of which are done here. Our model couples nonlinear, large arterial hemodynamics to both a linearized small vessel fluid dynamics model and a pressure loss term, capturing the complex relationship between pulmonary lesions and pulmonary hemodynamics. Figure 9.3 demonstrates the capability of our methodology in predicting large perfusion deficits in obstructed regions, as seen in vivo [108].

Our ring-like lesion model is based on the work by Young and Tsai [271] utilized in prior studies. The studies by Bezerra et al. [25] and Yin et al. [268] show that the combination of 1D CFD modeling with the aforementioned energy loss model is nearly identical to 3D stenosis model predictions in the coronary circulation. Only one prior pulmonary study (Spilker et al. [223]) utilized this energy loss model with a 1D framework in pigs; their results show that RPA stenosis leads to a drastic reduction of flow to the right lung and 25 mmHg increase in systolic pressure. However, none of these studies consider the effects of multiple distal lesions in an expansive pulmonary tree. In addition, we introduce a novel web-like lesion pressure loss term based on the Darcy-Forchheimer equation [267], which is a significant contribution to modeling CTEPH. These lesion types have not been modeled before, but are characteristic of a majority of CTEPH lesions [115].

Hemodynamics simulations throughout the pulmonary vasculature are feasible using our 1D CFD model framework. Figure (9.5) shows the mean pressure in each large pulmonary artery in both normotension and CTEPH, cases (a) and (d), during the cardiac cycle. While control simulations shows a relatively consistent pressure throughout the vasculature at each time point, cases (a) and (d) illustrate a significant pressure drop downstream to lesions. This pressure drop, quantified by the FFR, is measured in CTEPH patients in two previous studies [108, 246] using optical coherence tomography. These studies report FFR values ranging from 0.22 to 0.90, similar to the FFR magnitudes provided here. Our results in Figure 9.2 show that ring like lesions have a larger pressure drop than web-like lesions, but that both lesion types have varied effects on MPA pressure. Pressure drops across different types of pulmonary lesions have only recently been documented [108, 115], and these studies suggest that web-like lesions are more common and easier to treat with BPA than other lesion types. These studies also show that the changes in pressure and flow downstream of web-like lesions are more volatile than other lesion types. To date, the properties of web-like lesions have not been investigated, but more information regarding the structure and composition of web-like lesions may be used to inform our loss model. Overall, our model shows that both lesion types contribute to a decrease in pressure downstream, with ring-like lesions playing a larger role.

Current hypotheses suggest that secondary arteriopathy is a determining factor in CTEPH recovery [55, 130, 145]. As shown in Figure 9.6, model predictions in both obstructed and unobstructed pathways are affected in the different disease cases. Clearly, blood pressure drops downstream from the lesion while resistance to flow increases, leading to underperfusion in these vessels. Conversely, flow and pressure both increase in the unobstructed pathways. The study by Lang et al. [133] claims that decreased flow, and hence decreased shear stress, promotes pulmonary arterial remodeling downstream to a lesion. The authors also argue that increased flow and shear stress in unobstructed pathways leads to flow vasculopathy and, consequently, pulmonary vascular remodeling. This remodeling of both obstructed and unobstructed arterial pathways explains why all small arterial vessels, i.e. with an area $\leq 5\text{mm}^2$, narrow in CTEPH [50, 130]. Our results agree with these hypotheses and illustrate underperfusion in obstructed pathways and hyperperfusion in unobstructed pathways. Predictions in the obstructed path do not return to their original normotensive values, but they gradually approach these values as we introduce stiffening and narrowing in cases (b) through (d). Simulations from case (d) are consistent with the physiological conclusions that stiffening and narrowing of the pulmonary tree partially corrects pressure and flow imbalances due to CTEPH lesions [133].

9.5.2 Small vessel hemodynamics

Our multiscale approach utilizes the structured tree model to simulate arteriolar hemodynamics distal to the large subsegmental arteries. In CTEPH, lesions in segmental and subsegmental arteries decrease flow to the microvasculature, leading to small vessel remodeling [111, 130]. We simulate this in cases (b), (c), and (d) by decreasing the area of the terminal vessels and, consequently, the radii and number of branches in the structured tree. Results in Figure 9.6 show hemodynamic predictions in three structured trees in an obstructed path (T1, T2, and T3) and three structured trees in an unobstructed path (T4, T5, and T6). As expected, flow and pressure decrease substantially in the obstructed pathway with the addition of vascular lesions in case (a), whereas flow redistribution leads to an increase in flow and pressure in unobstructed terminal vessels and their arteriolar beds. Flow within the obstructed pathways does not increase when stiffness and PVR (Z_{term}) are increased, though flow in the unobstructed pathway decreases as a result of stiffening. These results and methods agree with previous physiological studies. For example, the study by Stam et al. [224] induced CTEPH in swine, showing that animals with pulmonary lesions have increased wall-thickness and decreased microvascular luminal area compared to control. We model both these phenotypes of CTEPH in cases (b), (c), and (d), increasing MPA pressure. The review by Lang et. al [130] also supports the idea that an increase in flow in unobstructed pathways leads to secondary arteriopathy and wall thickening in the pulmonary arterioles.

Decreasing the radii of terminal arteries leads to a smaller arteriolar tree, shown in Figure 9.7 for case (d), as r_{min} is held constant. A reduced microvascular density, also called microvascular rarefaction, is a known consequence of both CTEPH and PAH [36]. An imaging study by Come et al. [50] concludes that CTEPH patients have a reduced volume distribution of small arteries when compared to control, and suggests pruning of the pulmonary arterioles. This phenomenon is modeled by Olufsen et al. [169] who simulate rarefaction of the pulmonary microvasculature and consequently predict increased mean and diastolic pressure in the MPA. The study by Yang et al. [266] uses a 3D-0D coupled model of the proximal and distal vasculature and predicts increased right ventricular pressure and distal WSS as a consequence of the pruned pulmonary microvasculature. However, these distal vascular predictions, as well as our own here, are hypothetical, as current imaging technologies cannot capture dynamics in vessels of this magnitude. This model type can test large and small vessel disease hypotheses, and can be validated if measurements are available in both the large and small pulmonary arterial vessels.

9.5.3 Wave intensity analysis

WIA is increasingly recognized as a measure of pulmonary vascular function [213, 230]. Results in Figure 9.8 show how the addition of lesions and vascular stiffening affects forward and backward traveling waves. Results from the normotensive simulations show a large FCW in the MPA during systole followed by a smaller magnitude BCW and FEW, which rapidly decay in magnitude during diastole, and that the BEW is relatively negligible. In contrast, wave intensity magnitudes in scenario (d) nearly double in all four wave types. This agrees with the study by Su et al. [230], who measure area-velocity signals in both normotensive and PH patients, and show that wave intensity magnitudes nearly double in PH. Similarly, they show that FCWs in PH are approximately twice the magnitude of FEWs and BCWs, and that BEWs do not dissipate as quickly as in the normotensive patients. A similar conclusion is drawn in the study by Lau et al. [134]; PAH patients in the study have a much larger BCW than control subjects, ultimately leading to an increased wave reflection coefficient. In this study, we define the wave reflection coefficient as the sum of forward and backward compression waves in the time domain. However, the wave reflection coefficient can be calculated using other methods [156, 230], including impedance analysis, either in the frequency or time domain [190].

Our results suggest that wave reflection coefficients increase with disease severity. However, dilating proximal vessels leads to a decreased reflection coefficient in the MPA, LPA, and RPA, as shown in Table 9.4. Though the reflection index is decreased in case (d), BCW magnitude increases significantly. This is shown to correlate with right ventricular dysfunction in the study by Schafer et al. [210]. The authors' of this study also argue that BCWs are more indicative of increased proximal stiffening, agreeing with our results in case (d) after stiffening the large proximal arteries. The alignment between our disease scenarios and previously published in-vivo WIA suggest that this model framework is suitable for addressing wave-propagation in PH and, more specifically, CTEPH. It is reported that proximal arteries both stiffen and dilate in long term PH [50], which is accounted for in case (d) in this study. Our simulations show that this physiological phenomenon decreases the wave reflection coefficient. This suggests that dilation of the MPA attempts to reduce the load on the heart by minimizing the mismatch between right ventricular ejection and reflected waves from the arterial periphery.

9.5.4 Computational treatment planning

For inoperable CTEPH patients, a combination of drug therapy and BPA is the best alternative for improving vascular function. BPA is a physician dependent strategy and varies with both lesion location and severity of the disease [260]. One common treatment strategy is to target the lobe with the largest perfusion deficit [140], yet there may be multiple lesions within each lobe. For this reason, an integrated mathematical model of CTEPH hemodynamics with patient-specific imaging can rank lesion importance in procedural planning. Image-based computational hemodynamics modeling is already recognized as a useful tool in surgical planning for coronary artery disease [26, 268], and this study is a first step in utilizing the same framework for understanding CTEPH and hemodynamic improvement after BPA intervention.

We utilize three indices to determine the best treatment strategy: the mean MPA pressure, the wave reflection coefficient in the MPA, and the KL-divergence of the flow field. The former two quantify how BPA affects vascular-ventricular coupling and ventricular afterload, while the latter quantifies improvements in perfusion. Our results show that a combination of all three indices leads to a best treatment for improving proximal hemodynamics and lung perfusion. Within our treatment framework, we reduce stenosis severity through A_s for ring-like lesions or K_{perm} for web-like lesions, but do not remove lesions. This is important to consider, as BPA does not remove the lesions completely [108, 130]. In addition to targeting the lesions

directly, we also decrease the degree of vasoconstriction in vessels downstream from a lesion, returning their radii to 90% of their original value. This is supported by the study by Boulate et al. [29] who show that distal artery thickness in pigs can regress to typical values seen in shams after removing lesions. Their study also analyzes arterial thickness 6 weeks after reperfusing the obstructed lung tissue, demonstrating that surgical removal of clots reestablishes a normal lumen area after surgery.

Results shown in Figure 9.9 illustrate that the combination of pressure predictions, WIA, and flow heterogeneity lead to an optimal BPA treatment. The optimal treatment here reperfuses the right lower lobe and restores some flow to the periphery in the right middle lobe and left upper lobe. Though physicians typically target the lobes of the lung with the largest perfusion deficit seen on V/Q scans [130], advances in new imaging technologies (such as optical coherence tomography) also assist in determining which lesions will best improve hemodynamics [115, 118]. Our virtual BPA targets a region that is underperfused, but does not identify the most flow deficient region (the left lower lobe) as the optimal location. There are several lesions located in this lobe, hence addressing only 3 lesions has little effect on redistributing the flow. Our optimal BPA treatment also identifies proximal lesions rather than distal lesions, consistent with clinical practice [130]. Panel (b) in Figure 9.9 displays the relative cardiac output PDF for the normotensive control and pre- and post-BPA simulations, which are used to compute the KL-divergence. The control PDF has a bimodal structure, signifying two levels of perfused tissue as seen in Figure 9.3. Both pre- and post-BPA have a similar trend, but show a small area of lung that is hyperperfused relative to normotensive simulations.

Our simulation results show that both MPA pressure and wave intensities change only minutely in response to the single BPA treatment. However, improvements in hemodynamics post-BPA are typically reported over the course of months or years and after multiple sessions [130, 138]. Improvements immediately after BPA have only been reported in terms of FFR improvement [108, 140]. Our optimal BPA treatment increased FFR from 0.44, 0.32, and 0.30 to 0.88, 0.76, and 0.59, respectively. These improvements are similar to recordings from the study by Ishiguro et al. [108], which discover an improved FFR after BPA. Their study shows that FFR increases from 0.22 to 0.59 and 0.34 to 0.86 in two different lesions, similar in magnitude to our results. The long-term effects of BPA likely include decreased vasoconstriction in small arteries and normalized wall thickness [29], but only in the case of reversible PH. Recent investigations into success rates in CTEPH treatment find that the severity of small vessel disease correlates negatively with successful surgical outcomes, suggesting that the degree of small vessel arteriopathy dictates whether PH is persistent after intervention [79]. Histological data on arterioles after BPA would provide insight into the remodeling process after surgery, and could be reflected in our simulations of post-BPA hemodynamics.

9.5.5 Limitations and future work

We acknowledge several limitation in this study. We compute the wave reflection coefficient as the ratio of the cumulative forward and backward compression pressure waves. This is only one possible way of computing the wave-reflection coefficient in the time-domain [156], and can also be calculated in the frequency domain [190]. It is unclear which index best captures features of the vasculature, yet all these metrics would support our conclusion that large vessel stiffening and the presence of pulmonary lesions increase BCWs and wave reflections.

This study implements a novel web-like lesion energy loss model; however, it is unclear if this model captures proximal and distal hemodynamic features in human web-like lesions. Future studies will be devoted to validating this model type by obtaining catheter measurements prior to and after web-like lesions [115]. Moreover, we plan to investigate the sensitivity of model outputs, such as the wave reflection coefficient, mean MPA pressure, and flow heterogeneity index, to lesion and boundary condition parameters. In this

manner, we will determine which parameters influence outputs after BPA and use this to guide parameter inference in patient-specific modeling studies for patients with CTEPH.

Though we provide hemodynamic predictions immediately after BPA and hypothesize some degree of vasodilation after an intervention, it is unclear what the immediate effects of a single BPA session are. Data collection immediately after single BPA procedures may provide more insight into the immediate remodeling process. To this point, we do not attempt to predict the long term remodeling of the pulmonary vasculature after intervention, which will be investigated in future studies via a growth and remodeling framework [241]. Lastly, this proof-of-concept study models CTEPH in a control geometry by placing lesions in the segmental and subsegmental branches. Future studies will integrate CTEPH images, including lesion location, type, and severity.

9.5.6 Conclusion

This study provides a framework that integrates patient-specific CT imaging with both large and small vessel fluid dynamics to predict multiscale hemodynamics in CTEPH. We model normotensive hemodynamics and four CTEPH disease cases, the latter driven by physiological hypotheses including large and small vessel remodeling. We utilize two lesion models representing ring-like and web-like lesions, common in CTEPH and imperative for simulation studies. Our results show that combining thromboembolic lesions with pulmonary vascular remodeling increases pulmonary pressures to the CTEPH range and mimics clinical observations. We predict perfusion in the lung tissue and provide a novel, quantitative metric for measuring perfusion heterogeneity, which is essential in understanding the link between flow deficits in the lung and disease severity. WIA results from the model framework are akin to prior measurements of wave intensities in CTEPH patients. Small vessel predictions are in agreement with clinical knowledge of CTEPH progression, and illustrate that lesions lead to downstream underperfusion as well as hyperperfusion in unobstructed territories. We propose a combination of indices predicted by the model, and utilize these in prioritizing lesions for BPA therapy. Our modeling framework shows improvements in hemodynamics post-BPA, laying the foundation for future patient-specific investigations and validation studies using CTEPH data.

CHAPTER

10

DISCUSSION

This dissertation develops a framework integrating pulmonary artery imaging data with a 1D computational fluid dynamics model. The image-to-model pipeline consists of image segmentation, centerline extraction, and graph labeling, accomplished using novel algorithms. The reconstructed networks representing the large pulmonary arteries are used as the domain for nonlinear, inertially driven hemodynamic simulations performed under normotensive and PH conditions. Predictive variability due to uncertainty in the model parameters and large vessel geometry is determined. Parameter estimators and distributions constituting vessel stiffness, downstream resistance, and vascular compliance are inferred using hemodynamic data from normotensive and PH mice. Hemodynamics in CTEPH are determined by integrating a novel web-like lesion model with previously utilized ring-like lesion energy loss models. Improvements in CTEPH model predictions after BPA are calculated using a new quantitative metric for lung perfusion.

Image-based modeling

Image-based modeling is an emerging tool in the diagnosis and management of cardiovascular disease. The image analysis pipeline presented here uses open-source image segmentation software to reconstruct the pulmonary vasculature and VMTK [11] for centerline construction. Novel algorithms developed in this work decompose the centerline network into a labeled graph, consisting of length, radii, and network connectivity. These components are essential in describing the domain for the 1D fluid dynamics model. The methods were used to analyze both mouse micro-CT images and human CT images.

A limitation to the above framework is determining the vessel radii. The algorithms in VMTK provide robust estimates of radii throughout a segmentation. However, VMTK requires manual identification of all terminal branches (or *leaves*) in the network. Alternative automatic tools for constructing skeletonized networks include thinning algorithms provided in 3DSlicer [35, 95], but these require equispaced imaging data not common in human imaging. Both algorithms have uncertainty associated with radius estimates at

branch points near junctions. This limitation makes it difficult to determine if vessels taper along their length, as the proximal pulmonary arteries are known to mildly taper [248]. A recent 1D fluid dynamics investigation by Abdullateef et al. [1] showed that tapering in the aorta plays a substantial role in the waveform shape and should be including in large vessel geometries. An investigation by Paun et. al [186] (in collaboration with the author) estimated pulmonary arterial tapering in normotensive and PH conditions, revealing that inferring a taper factor improves normotensive predictions to data, but not for PH predictions. A possible remedy for this issue may include using change-point algorithms [122] to determine inlet and outlet radii or by performing hypothesis testing for different tapering models based on measured data.

Fluid dynamics model

The 1D fluid dynamics model used here has been utilized in several other studies [168, 169, 189]. However, this work is the first to consider an expansive network of blood vessels based on imaging data. Both Windkessel and structured tree boundary conditions are considered. For the Windkessel model, a novel, total resistance preserving algorithm for distributing resistance parameters is presented and used to study the effects of network uncertainty. A radius and hematocrit dependent viscosity function is implemented in the structured tree model. The structured tree model enables predictions beyond the image segmentation domain down to the precapillary level. Previous studies by Cousins [52] and Yang et al. [266] include a radius dependent viscosity, but this study includes the hematocrit term as this changes with disease [211].

The 1D model uses an MPA inflow profile to drive hemodynamics, yet PH alters right heart function and CO. The large arteries should be coupled to a heart model to understand changes in flow, CO, and arterio-ventricular coupling during PH progression [3, 198]. PH also induces arterial remodeling, especially in PAH, group III PH, and CTEPH. This can be captured by vasoconstricting and stiffening the vessels in the structured tree. However, the pulmonary capillaries surrounding the alveoli likely remodel in response to elevated pulmonary artery pressure in PH [177]. The structured tree could be coupled to a pulmonary capillary sheet model [40, 73] and used to understand the interaction between the arterioles and capillaries.

In this work the arterial walls are treated as a linear, elastic material, but could also be modeled using a nonlinear constitutive model, similar to Quershi et al. [191] (in collaboration with the author). Viscoelastic [21] and hyperelastic [44] wall models have been used in modeling 1D systemic hemodynamics, but not pulmonary hemodynamics. These topics should be further investigated.

Parameter inference and uncertainty quantification

A major component of patient-specific modeling is inferring parameter estimators or posterior distributions that are surrogates for non-measurable, in-vivo properties of the circulation. Most models have many parameters and sparse data; therefore, it is typically impossible to infer all unknown parameters. One way to determine what parameters are influential or identifiable is to use sensitivity analysis. This work shows that standard Windkessel parameters are unidentifiable given a single pressure profile. To overcome this, a set of Windkessel scaling factors is introduced, which are both influential and identifiable on model predictions of pressure. These parameters are inferred in Chapter 7. Concurring with physiological knowledge [177], results show that pulmonary arteries stiffen, distal resistance increases, and pulmonary compliance decreases in PH relative to normotensive values. Both local and global sensitivity analyses reveal that large vessel parameters (stiffness) become more influential with increasing network size, and that distal vascular resistance is consistently the most influential parameter on model predictions.

Uncertainty in hemodynamic predictions linked to uncertainties in model and network parameters are investigated in Chapters 7 and 8. Using MCMC, posterior densities for vessel stiffness and Windkessel scaling factors are constructed, and agree with similar pulmonary studies [175, 186]. This work is the first to study uncertainty in arterial network segmentation by using multiple segmentations of the same image. The separation of output uncertainty (i.e., the total variation) into network variation and geometric variation is novel, and this work carries out uncertainty propagation by sampling from density estimates based on data from multiple segmentations.

Uncertainty related to structured tree parameters was not investigated here and hasn't yet been pursued. The study by Chambers et al. [35] (in collaboration with the author) is the only one to quantify effects of these parameters, and concluded that uncertainty in L_{rr} is less influential than α or β on mPAP. This dissertation did not investigate model discrepancy, though recent results by Paun et al. [175] show that incorporating model-design uncertainty leads to a larger uncertainty band in pressure predictions. The larger uncertainty bounds in the study agree with the typical variability in pressure due to the respiratory cycle. It should be noted that segmentation uncertainty would directly affect ring-like lesion severity, as determined by Yin et al. [268]. These authors concluded that uncertainty related to lesion segmentation has significant effects on 1D hemodynamic simulations in the coronary arteries. This necessitates a similar study using both of the ring- and web-like lesions presented here.

The parameter inference results in Chapter 7 used a multi-start optimization procedure to determine optimal point estimates for MCMC. The results of MCMC are dependent on the prior distributions and initial estimates, and may be biased towards the optimization results. A way to circumvent this is to use multiple initializations of the DRAM algorithm, and could be used to test for multimodality in the posterior. The methods presented in the chapter compare asymptotic frequentist methods and non-asymptotic Bayesian inference techniques. However, there are non-asymptotic frequentist techniques, such as bootstrapping, that can be used to construct confidence and prediction intervals. Similarly, Bayesian asymptotic methods, such as the Laplace approximation [78] could also be used in place of non-asymptotic methods. Lastly, the results from Chapter 7 [46] show that the iid assumption for the residuals is violated. To circumvent this, the covariance matrix of the residuals can be determined, though this would increase the number of parameters to be estimated. Instead, one could use a Gaussian process, as done by Paun et al. [175], to estimate the covariance structure of the residuals.

Hemodynamics in CTEPH

Another innovative result in this dissertation is a 1D hemodynamics model of CTEPH. The disease is characterized by five lesion types, including ring- and web-like, integrated in the model. The ring-like lesion model was derived by Young and Tsai [269, 270], whereas the web-like lesion pressure loss model follows the Darcy-Forchheimer equation [267], a new addition. Both lesion models are integrated into a segmented, normotensive, large artery geometry. Combining both lesion types with vascular stiffening and vasoconstriction produces elevated mPAP and increased wave reflections consistent with clinical data [229]. Small artery predictions in the structured tree are consistent with the clinical hypotheses of (1) underperfusion in obstructed vasculature and (2) overperfusion in unobstructed territories [133, 224]. To construct meaningful indices for clinicians, this work produced a novel flow-heterogeneity index utilizing the KL-divergence. By combining mPAP, the flow-heterogeneity index, and a wave reflection index, an optimal BPA surgery was determined. This is the first study to construct an expansive, multiscale 1D model that produces common CTEPH phenotypes and predicts optimal intervention strategies. This proof-of-concept investigation was

done using a CT image from a normotensive human. A current study by the author is expanding the methods in this dissertation to use imaging and hemodynamic data from CTEPH patients at Duke.

10.1 Future work

RV dysfunction is the most common cause for PH mortality. RV adaptation been studied in isolation [15, 179], but simulating hemodynamics during RV deterioration has not been investigated. This motivates the development of a closed loop model of the circulation, where the pulmonary circulation is explicitly represented by a two-sided structured tree model of the arteries and veins [189], and the heart and other circulations are represented by a 0D circuit analogy [157, 198]. A more detailed model of the pulmonary capillaries, using Fung's sheet model [40, 73], would provide insight into the coupling between the large arteries, arterioles, and capillaries in disease.

Only one study by Guan et al. [85] has formally investigated the difference between structured tree and Windkessel boundary conditions in the systemic circulation. This study concluded that proximal hemodynamic conditions are comparable between the two boundary conditions, but discrepancies in distal hemodynamics are evident between the two. Olufsen [166] showed that the impedance amplitude and phase between structured tree and Windkessel boundary conditions differ for larger frequencies, and that higher frequency impedance values from the structured tree better agree with physiological measurements. However, a formal statistical mapping from one set of boundary conditions to the other has not been determined. Moreover, a future study using different sized networks, as done in Chapter 7, but with structured tree boundary conditions is warranted.

The effects of different network size are compared qualitatively using optimal parameter estimates, posterior distributions, and sensitivity analyses. A more rigorous approach to this would be to treat networks with more vessels as higher fidelity models and those with less as *lower fidelity* models. This could be investigated using *multi-fidelity* Bayesian optimization, where higher fidelity models (more vessels) are replaced by a lower fidelity model (less vessels) with an learned correction factor, e.g., a Gaussian process [268]. This would overcome two main obstacles encountered in this work: (1) the computation time for running network model with numerous vessels, and (2) the physical time required to segment an expansive network.

For the CTEPH model, a sensitivity analysis and parameter identifiability study on the model to determine which parameters are uniquely determined by RHC data is the next step. The study in Chapter 9 places lesions in the segmental and sub-segmental arteries based on the literature. Patient-specific, CTEPH CT images will require lesion detection and estimates of lesion severity. This could be determined by segmenting the visible vasculature and then analyzing radius estimates throughout the tree, flagging vessels that have an abnormal drop in radius as lesion sites. Also, the lesion models used here have not been validated in the pulmonary circulation. Recent advances in catheter technology allow physicians to measure pulmonary arterial pressure during BPA [108, 115], and data proximal and distal to the lesion site providing pressure estimates could validate the two lesion models. BPA treatment requires multiple sessions before patient mPAP decreases below 20 mmHg. However, improvements after a single BPA session are not typically reported. A future study with clinicians at Duke University is planned, where RHC data from each BPA session will be recorded. This will give snapshots of hemodynamics post-BPA and give insight into recovery after BPA.

BIBLIOGRAPHY

- [1] Abdullateef, S. et al. "Impact of tapering of arterial vessels on blood pressure, pulse wave velocity, and wave intensity analysis using one-dimensional computational model". *Int J Numer Method Biomed Eng* (2020), pp. 1–17.
- [2] Acosta, S. et al. "Numerical Method of Characteristics for One-Dimensional Blood Flow". *J Comput Phys* **294** (2015), pp. 96–109.
- [3] Acosta, S. et al. "Cardiovascular mechanics in the early stages of pulmonary hypertension: a computational study". *Biomech Model Mechanobiol* **16.6** (2017), pp. 2093–2112.
- [4] Alastruey, J et al. "Lumped Parameter Outflow Models for 1-D Blood Flow Simulations: Effect on Pulse Waves and Parameter Estimation". *Commun Comput Phys* **4.4** (2008), pp. 317–336.
- [5] Alastruey, J. et al. "On the impact of modelling assumptions in multi-scale, subject-specific models of aortic haemodynamics". *J R Soc Interface* **13.119** (2016), p. 20160073.
- [6] Alavi, S. M. M. et al. "Identifiability of generalized randles circuit models". *IEEE Trans Control Syst Technol* **25.6** (2016), pp. 2112–2120.
- [7] Alexanderian, A. et al. "Variance-based sensitivity analysis for time-dependent processes". *Reliab Eng Syst Saf* **196** (2020), p. 106722.
- [8] Amini, B. et al. "Diagnostic nuclear medicine in the ED". *Am J Emerg Med* **29.1** (2011), pp. 91–101.
- [9] Antiga, L. & Steinman, D. A. "Robust and objective decomposition and mapping of bifurcating vessels". *IEEE Trans Med Imaging* **23.6** (2004), pp. 704–713.
- [10] Antiga, L. et al. "Computational geometry for patient-specific reconstruction and meshing of blood vessels from MR and CT angiography". *IEEE Trans Med Imaging* **22.5** (2003), pp. 674–684.
- [11] Antiga, L. et al. "An image-based modeling framework for patient-specific computational hemodynamics". *Med Biol Eng Comput* **46.11** (2008), p. 1097.
- [12] Arnold, A. et al. "Uncertainty Quantification in a Patient-Specific One-Dimensional Arterial Network Model: EnKF-Based Inflow Estimator". *J Verif Valid Uncertain Quantif* **2.1** (2017), p. 011002.
- [13] Arthurs, C. J. et al. "CRIMSON: An Open-Source Software Framework for Cardiovascular Integrated Modelling and Simulation". *bioRxiv* (2020), p. 2020.10.14.339960.
- [14] Atabek, H. B. "Wave Propagation through a Viscous Fluid Contained in a Tethered, Initially Stressed, Orthotropic Elastic Tube". *Biophys J* **8.5** (1968), pp. 626–649.
- [15] Avazmohammadi, R. et al. "A Computational Cardiac Model for the Adaptation to Pulmonary Arterial Hypertension in the Rat". *Ann Biomed Eng* **47.1** (2019), pp. 138–153.

- [16] Azer, K. & Peskin, C. S. "A one-dimensional model of blood flow in arteries with friction and convection based on the Womersley velocity profile". *Cardiovasc Eng* **7.2** (2007), pp. 51–73.
- [17] Banks, H. et al. "The complex-step method for sensitivity analysis of non-smooth problems arising in biology". *Eurasian J Math Comput Appl* **3.3** (2015), pp. 1–41.
- [18] Banks, H. T. et al. "Standard error computations for uncertainty quantification in inverse problems: Asymptotic theory vs. bootstrapping". *Math Comput Model* **52.9-10** (2010), pp. 1610–1625.
- [19] Banks, H. T. et al. "Parameter selection methods in inverse problem formulation". *Mathematical modeling and validation in physiology*. Springer, 2013, pp. 43–73.
- [20] Bartolo, M. A. et al. "Numerical predictions of shear stress and cyclic stretch in the healthy pulmonary vasculature". *arXiv preprint arXiv:2103.05754* (2021).
- [21] Battista, C. et al. "Wave propagation in a 1d fluid dynamics model using pressure-area measurements from ovine arteries". *J Mech Med Biol* **16.02** (2016), p. 1650007.
- [22] Bessems, D. "On the propagation of pressure and flow waves through the patient specific arterial system". 2007.
- [23] Betts, J. G. et al. *Anatomy and Physiology*. Houston, TX: OpenStax, 2013.
- [24] Birolleau, A. et al. "Adaptive bayesian inference for discontinuous inverse problems, application to hyperbolic conservation laws". *Commun Comput Phys* **16.1** (2014), pp. 1–34.
- [25] Blanco, P. J. et al. "Comparison of 1D and 3D Models for the Estimation of Fractional Flow Reserve". *Sci Rep* **8.1** (2018), p. 17275.
- [26] Bom, M. J. et al. "Non-invasive procedural planning using computed tomography-derived fractional flow reserve". *Catheter Cardiovasc Interv* **97.4** (2020), pp. 614–622.
- [27] Bordones, A. D. et al. "Computational Fluid Dynamics Modeling of the Human Pulmonary Arteries with Experimental Validation". *Ann Biomed Eng* **46.9** (2018), pp. 1309–1324.
- [28] Boron, W. F. & Boulpaep, E. L. *Medical physiology*. English. Philadelphia, PA : Elsevier, [2017], 2017.
- [29] Boulate, D. et al. "Pulmonary microvascular lesions regress in reperfused chronic thromboembolic pulmonary hypertension". *J Heart Lung Transplant* **34.3** (2015), pp. 457–467.
- [30] Brady, R. et al. "Personalized mathematical model of endotoxin-induced inflammatory responses in young men and associated changes in heart rate variability". *Math Model Nat Phenom* **13.5** (2018), pp. 1–20.
- [31] Brault, A. et al. "Uncertainty quantification of inflow boundary condition and proximal arterial stiffness–coupled effect on pulse wave propagation in a vascular network". *Int J Numer Method Biomed Eng* **33.10** (2017), e2859.

- [32] Burrowes, K. S. et al. "Pulmonary embolism: Predicting disease severity". *Philos Trans R Soc A* **369**.1954 (2011), pp. 4255–4277.
- [33] Burrowes, K. S. et al. "Anatomically based finite element models of the human pulmonary arterial and venous trees including supernumerary vessels". *J Appl Physiol* **99**.2 (2005), pp. 731–738.
- [34] Campolongo, F. et al. "An effective screening design for sensitivity analysis of large models". *Environ Model Softw* **22**.10 (2007), pp. 1509–1518.
- [35] Chambers, M. J. et al. "Structural and hemodynamic properties of murine pulmonary arterial networks under hypoxia-induced pulmonary hypertension". *P I Mech Eng H* **234**.11 (2020), pp. 1312–1329.
- [36] Chaudhary, K. R. et al. "Proliferative versus degenerative paradigms in pulmonary arterial hypertension: have we put the cart before the horse?" *Circ Res* **120**.8 (2017), pp. 1237–1239.
- [37] Chen, P. et al. "Simulation-based uncertainty quantification of human arterial network hemodynamics". *Int J Numer Method Biomed Eng* **29** (2013), pp. 698–721.
- [38] Çiçek, Ö. et al. "3D U-Net: learning dense volumetric segmentation from sparse annotation". *International conference on medical image computing and computer-assisted intervention*. Springer. 2016, pp. 424–432.
- [39] Cintrón-Arias, A. et al. "A sensitivity matrix based methodology for inverse problem formulation". *J Inverse Ill Posed Probl* **17**.6 (2009), pp. 545–564.
- [40] Clark, A. R. & Tawhai, M. H. "Temporal and spatial heterogeneity in pulmonary perfusion: a mathematical model to predict interactions between macro- and micro-vessels in health and disease". *ANZIAM J* **59**.4 (2018), pp. 562–580.
- [41] Clipp, R. B. & Steele, B. N. "Impedance boundary conditions for the pulmonary vasculature including the effects of geometry, compliance, and respiration". *IEEE Trans Biomed Eng* **56**.3 (2009), pp. 862–870.
- [42] Clipp, R. & Steele, B. "An evaluation of dynamic outlet boundary conditions in a 1D fluid dynamics model". *Math Biosci Eng* **9**.1 (2012), pp. 61–74.
- [43] Coccarelli, A. et al. "A novel porous media-based approach to outflow boundary resistances of 1D arterial blood flow models". *Biomech Model Mechanobiol* **18**.4 (2019), pp. 939–951.
- [44] Coccarelli, A. et al. "A framework for incorporating 3D hyperelastic vascular wall models in 1D blood flow simulations". *Biomech Model Mechanobiol* (2021), pp. 1–19.
- [45] Colebank, M. J. et al. "Influence of image segmentation on one-dimensional fluid dynamics predictions in the mouse pulmonary arteries". *J R Soc Interface* **16**.159 (2019), p. 20190284.
- [46] Colebank, M. J. et al. "Sensitivity analysis and uncertainty quantification of 1-D models of pulmonary hemodynamics in mice under control and hypertensive conditions". *Int J Numer Method Biomed Eng* March (2019), pp. 1–29.

- [47] Colebank, M. J. et al. "A multiscale model of vascular function in chronic thromboembolic pulmonary hypertension". *arXiv preprint arXiv:2102.06676* (2021).
- [48] Colebank, M. J. et al. "Parameter inference in a computational model of hemodynamics in pulmonary hypertension". *arXiv preprint arXiv:2101.06266* (2021).
- [49] Colunga, A. L. et al. "Deep phenotyping of cardiac function in heart transplant patients using cardiovascular system models". *J Physiol* **598**.15 (2020), pp. 3203–3222.
- [50] Come, C. E. et al. "Pulmonary Vascular Morphology as an Imaging Biomarker in Chronic Thromboembolic Pulmonary Hypertension". *Pulm. Circ.* **6**.1 (2016), pp. 0–11.
- [51] Correale, M. et al. "Endothelin-receptor antagonists in the management of pulmonary arterial hypertension: Where do we stand?" *Vasc Health Risk Manag* **14** (2018), pp. 253–264.
- [52] Cousins, W. "Boundary Conditions and Uncertainty Quantification for Hemodynamics". PhD thesis. North Carolina State University, 2013.
- [53] Cousins, W. et al. "A new physiological boundary condition for hemodynamics". *SIAM J Appl Math* **73**.3 (2013), pp. 1203–1223.
- [54] Davidoiu, V. et al. "Evaluation of noise removal algorithms for imaging and reconstruction of vascular networks using micro-CT". *Biomed Phys Eng Express* **2**.4 (2016), p. 045015.
- [55] Delcroix, M. et al. "Long-term outcome of patients with chronic thromboembolic pulmonary hypertension: results from an international prospective registry". *Circulation* **133**.9 (2016), pp. 859–871.
- [56] Dimopoulos, K. et al. "Percutaneous transluminal pulmonary angioplasty for the treatment of chronic thromboembolic pulmonary hypertension: Challenges and future directions". *Int J Cardiol* **187**.1 (2015), pp. 401–403.
- [57] Duin, R. W. van et al. "Transition from post-capillary pulmonary hypertension to combined pre- and post-capillary pulmonary hypertension in swine: a key role for endothelin". *J Physiol* **597**.4 (2019), pp. 1157–1173.
- [58] Eck, V. G. et al. "Effects of arterial wall models and measurement uncertainties on cardiovascular model predictions". *J Biomech* **50** (2017), pp. 188–194.
- [59] Eck, V. et al. "A guide to uncertainty quantification and sensitivity analysis for cardiovascular applications". *Int J Numer Method Biomed Eng* **26**.1 (2016), pp. 807–827.
- [60] Ellwein, L. M. et al. "Sensitivity analysis and model assessment: Mathematical models for arterial blood flow and blood pressure". *Cardiovasc Eng* **8**.2 (2008), pp. 94–108.
- [61] Ellwein, L. M. et al. "Image-based quantification of 3D morphology for bifurcations in the left coronary artery: Application to stent design". *Catheter Cardiovasc Interv* **87**.7 (2016), pp. 1244–1255.

- [62] Epstein, S. et al. "Reducing the number of parameters in 1D arterial blood flow modeling: less is more for patient-specific simulations". *Am J Physiol Heart Circ Physiol* **309.1** (2015), H222–H234.
- [63] Esmaily Moghadam, M. et al. "Optimization of shunt placement for the Norwood surgery using multi-domain modeling". *J Biomech Eng* **134.5** (2012).
- [64] Fedorov, A. et al. "3D Slicer as an image computing platform for the Quantitative Imaging Network". *Magn Reson Imaging* **30.9** (2012), pp. 1323–1341.
- [65] Fedullo, P. F. et al. "Chronic Thromboembolic Pulmonary Hypertension". *New Engl J Med* **345.20** (2001), pp. 1465–1472.
- [66] Feldkamp, L. A. et al. "Practical cone-beam algorithm". *J Opt Soc Am A* **1.6** (1984), pp. 612–619.
- [67] Fernandes, T. M. et al. "Treatment of Chronic Thromboembolic Pulmonary Hypertension: The Role of Medical Therapy and Balloon Pulmonary Angioplasty". *Methodist Debaquey Cardiovasc J* **12.4** (2016), pp. 205–212.
- [68] Fossan, F. E. et al. "Optimization of topological complexity for one-dimensional arterial blood flow models". *J R Soc Interface* **15.149** (2018), p. 20180546.
- [69] Frangi, A. F. et al. "Multiscale vessel enhancement filtering". *International conference on medical image computing and computer-assisted intervention*. Springer. 1998, pp. 130–137.
- [70] Fukumoto, Y. *Diagnosis and Treatment of Pulmonary Hypertension: From Bench to Bedside*. Springer, 2017.
- [71] Fung, Y & Sobin, S. "Pulmonary alveolar blood flow". *Circ Res* **30.4** (1972), pp. 470–490.
- [72] Fung, Y. C. & Sobin, S. S. "Theory of sheet flow in lung alveoli." *J Appl Physiol* **26.4** (1969), pp. 472–488.
- [73] Fung, Y. *Biomechanics: circulation*. Springer Science & Business Media, 2013.
- [74] Fung, Y. *Biomechanics: mechanical properties of living tissues*. Springer Science & Business Media, 2013.
- [75] Galié, N. et al. "The endothelin system in pulmonary arterial hypertension". *Cardiovasc Res* **61.2** (2004), pp. 227–237.
- [76] Galiè, N. et al. "2015 ESC/ERS Guidelines for the diagnosis and treatment of pulmonary hypertension". *Eur Heart J* **37.1** (2016), pp. 67–119.
- [77] Gao, Y. et al. "Endothelial and smooth muscle cell interactions in the pathobiology of pulmonary hypertension". *Am J Respir Cell Mol Biol* **54.4** (2016), pp. 451–460.
- [78] Gelman, A. et al. "Understanding predictive information criteria for Bayesian models". *Stat Comput* **24.6** (2014), pp. 997–1016.

- [79] Gerges, C. et al. "Microvascular Disease in Chronic Thromboembolic Pulmonary Hypertension: Hemodynamic Phenotyping and Histomorphometric Assessment". *Circulation* (2020), pp. 376–386.
- [80] Gerringer, J. W. et al. "Lumped-parameter models of the pulmonary vasculature during the progression of pulmonary arterial hypertension". *Physiol Rep* **6.3** (2018), pp. 1–12.
- [81] Geweke, J. "Evaluating the accuracy of sampling-based approaches to the calculation of posterior moments". *Bayesian Stat* (1992), pp. 169–193.
- [82] Ghofrani, H.-A. et al. "Riociguat for the Treatment of Pulmonary Arterial Hypertension". *New Engl J Med* **369.4** (2013), pp. 330–340.
- [83] Goldberg, P. et al. "Regression with input-dependent noise: A gaussian process treatment". *Adv Neural Inf Process Syst* **10** (1997), pp. 493–499.
- [84] Griewank, A. "On Automatic Differentiation". *Math. Program. Recent Dev. Appl.* Kluwer Academic Publishers, 1989, pp. 83–108.
- [85] Guan, D. et al. "Comparison of the Windkessel model and structured-tree model applied to prescribe outflow boundary conditions for a one-dimensional arterial tree model". *J Biomech* **49.9** (2016), pp. 1583–1592.
- [86] Guidoum, A. C. "Kernel Estimator and Bandwidth Selection for Density and its Derivatives: The kedd Package". *arXiv preprint arXiv:2012.06102* (2020).
- [87] Gul, R. et al. "Mathematical modeling and sensitivity analysis of arterial anastomosis in the arm". *Appl Math Model* **40.17-18** (2016), pp. 7724–7738.
- [88] Gunzburger, M. D. *Perspectives in flow control and optimization*. SIAM, 2002.
- [89] Haario, H. et al. "DRAM: Efficient adaptive MCMC". *Stat Comput* **16.4** (2006), pp. 339–354.
- [90] Hall, J. E. *Guyton and Hall textbook of medical physiology*. Elsevier Health Sciences, 2016.
- [91] Hasenauer, J. et al. "Parameter identification, experimental design and model falsification for biological network models using semidefinite programming". *IET Syst Biol* **4.2** (2010), pp. 119–130.
- [92] Hastie, T. et al. *The Elements of Statistical Learning*. Springer Series in Statistics. New York, NY: Springer New York, 2009.
- [93] Helmberger, M. et al. "Quantification of tortuosity and fractal dimension of the lung vessels in pulmonary hypertension patients". *PLoS One* **9.1** (2014).
- [94] Henrie, A. M. et al. "Clinical utility of tadalafil in the treatment of pulmonary arterial hypertension: An evidence-based review". *Core Evid* **10** (2015), pp. 99–108.
- [95] Hernandez-Cerdan, P. "Biopolymer networks: image analysis, reconstruction and modeling". PhD thesis. Massey University, 2018.

- [96] Hoeper, M. M. et al. "A global view of pulmonary hypertension". *Lancet Respir Med* **4.4** (2016), pp. 306–322.
- [97] Holzapfel, G. et al. "A new constitutive framework for arterial wall mechanics and a comparative study of material models". *J Elast* **61** (2000), pp. 1–48.
- [98] Horsfield, K. & Cumming, G. "Angles of branching and diameters of branches in the human bronchial tree". *Bull Math Biophys* **29.2** (1967), pp. 245–259.
- [99] Horsfield, K. "Morphometry of the Small Pulmonary Arteries in Man". *Circ Res* **42.5** (1978), pp. 593–597.
- [100] Horssen, P. van et al. "Influence of segmented vessel size due to limited imaging resolution on coronary hyperemic flow prediction from arterial crown volume". *Am J Physiol Heart Circ Physiol* **310.7** (2016), H839–H846.
- [101] Hoskins, P. R. et al. *Cardiovascular biomechanics*. Springer, 2017.
- [102] Huang, W et al. "Morphometry of the human pulmonary vasculature." *J Appl Physiol* **81.5** (1996), pp. 2123–2133.
- [103] Huberts, W. et al. "Applicability of the polynomial chaos expansion method for personalization of a cardiovascular pulse wave propagation model". *Int J Numer Method Biomed Eng* **30.12** (2014), pp. 1679–1704.
- [104] Humphrey, J. & O’rourke, S. L. *An Introduction Biomechanics*. Springer, 2016.
- [105] Humphrey, J. D. *Cardiovascular solid mechanics: cells, tissues, and organs*. Springer Science & Business Media, 2013.
- [106] Iott, J. et al. *Selecting Step Sizes in Sensitivity Analysis by Finite Differences*. Tech. rep. NASA, 1985.
- [107] Ipsen, I. C. F. et al. "Rank-Deficient Nonlinear Least Squares Problems and Subset Selection". *SIAM J Numer Anal* **49.3** (2011), pp. 1244–1266.
- [108] Ishiguro, H. et al. "Diversity of Lesion Morphology in CTEPH Analyzed by OCT, Pressure Wire, and Angiography". *JACC Cardiovasc Imaging* **9.3** (2016), pp. 324–325.
- [109] Ismail, M. et al. "Adjoint-based inverse analysis of windkessel parameters for patient-specific vascular models". *J Comput Phys* **244** (2013), pp. 113–130.
- [110] Jiang, Z. L. et al. "Diameter-defined Strahler system and connectivity matrix of the pulmonary arterial tree". *J Appl Physiol* **76.2** (1994), pp. 882–892.
- [111] Jujo, T. et al. "Evaluation of the microcirculation in chronic thromboembolic pulmonary hypertension patients: The impact of pulmonary arterial remodeling on postoperative and follow-up pulmonary arterial pressure and vascular resistance". *PLoS One* **10.8** (2015), pp. 1–18.

- [112] Kaipio, J. & Somersalo, E. *Statistical and Computational Inverse Problems*. Ed. by Antman, S. S. et al. Vol. 139. New York, NY: Springer-Verlang New York, 2005.
- [113] Kandathil, A. & ChamCarthy, M. "Pulmonary vascular anatomy & anatomical variants". *Cardiovasc Diagn Ther* **8.3** (2018), pp. 201–207.
- [114] Karau, K. L. et al. "Pulmonary arterial morphometry from microfocal X-ray computed tomography." *American journal of physiology. Heart and circulatory physiology* **281.6** (2001), H2747–56.
- [115] Kawakami, T. et al. "Novel Angiographic Classification of Each Vascular Lesion in Chronic Thromboembolic Pulmonary Hypertension Based on Selective Angiogram and Results of Balloon Pulmonary Angioplasty". *Circ Cardiovasc Interv* **9.10** (2016), pp. 1–8.
- [116] Kelley, C. T. *Iterative methods for optimization*. SIAM, 1999.
- [117] Kennedy, M. C. & O'Hagan, A. "Bayesian calibration of computer models". *J R Stat Soc Ser B* **63.3** (2001), pp. 425–464.
- [118] Khan, M. S. et al. "Meta-analysis of use of balloon pulmonary angioplasty in patients with inoperable chronic thromboembolic pulmonary hypertension". *Int J Cardiol* **291** (2019), pp. 134–139.
- [119] Kheifets, V. O. et al. "Considerations for Numerical Modeling of the Pulmonary Circulation—A Review With a Focus on Pulmonary Hypertension". *J Biomech Eng* **135.6** (2013), p. 061011.
- [120] Kheifets, V. O. et al. "Patient-specific computational modeling of blood flow in the pulmonary arterial circulation". *Comput Methods Programs Biomed* **120.2** (2015), pp. 88–101.
- [121] Kikinis, R. et al. "3D Slicer: A Platform for Subject-Specific Image Analysis, Visualization, and Clinical Support". *Intraoperative Imaging and Image-Guided Therapy*. Ed. by Jolesz, F. A. New York, NY: Springer New York, 2014, pp. 277–289.
- [122] Killick, R. et al. "Optimal detection of changepoints with a linear computational cost". *J Am Stat Assoc* **107.500** (2012), pp. 1590–1598.
- [123] Kind, T. et al. "Proportional Relations Between Systolic, Diastolic and Mean Pulmonary Artery Pressure are Explained by Vascular Properties". *Cardiovasc Eng Technol* **2.1** (2011), pp. 15–23.
- [124] Krenz, G. S. & Dawson, C. A. "Flow and pressure distributions in vascular networks consisting of distensible vessels". *Am J Physiol Heart Circ Physiol* **284.6** (2003), H2192–H2203.
- [125] Ku, D. N. "BLOOD FLOW IN ARTERIES". *Annu Rev Fluid Mech* **29.1** (1997), pp. 399–434.
- [126] Lage, J. L. & Antohe, B. V. "Darcy ' s Experiments and the Deviation to Nonlinear Flow". *J Fluids Eng* **122** (2000), pp. 619–625.
- [127] Laine, M. *MCMC toolbox for Matlab*. 2007.

- [128] Lammers, S. R. et al. "Changes in the structure-function relationship of elastin and its impact on the proximal pulmonary arterial mechanics of hypertensive calves". *Am J Physiol Heart Circ Physiol* **295.4** (2008), pp. 1451–1459.
- [129] Lan, H. et al. "A Re-Engineered Software Interface and Workflow for the Open-Source Sim-Vascular Cardiovascular Modeling Package". *J Biomech Eng* **140.2** (2018), pp. 1–11.
- [130] Lang, I. et al. "Balloon pulmonary angioplasty in chronic thromboembolic pulmonary hypertension". *Eur Respir Rev* **26.143** (2017).
- [131] Lang, I. M. et al. "Imaging in pulmonary hypertension". *JACC Cardiovasc Imaging* **3.12** (2010), pp. 1287–1295.
- [132] Lang, I. M. et al. "Risk factors and basic mechanisms of chronic thromboembolic pulmonary hypertension: a current understanding". *Eur Respir J* **41.2** (2013), pp. 462–468.
- [133] Lang, I. M. et al. "The pathobiology of chronic thromboembolic pulmonary hypertension". *Ann Am Thorac Soc* **13** (2016), S215–S221.
- [134] Lau, E. M. et al. "Assessment of ventriculo-arterial interaction in pulmonary arterial hypertension using wave intensity analysis". *Eur Respir J* **43.6** (2014), pp. 1801–1804.
- [135] Lee, P. et al. "Heterogeneous mechanics of the mouse pulmonary arterial network". *Biomechanics and Modeling in Mechanobiology* **15.5** (2016), pp. 1245–1261.
- [136] Liang, F. et al. "Multi-scale modeling of the human cardiovascular system with applications to aortic valvular and arterial stenoses". *Med Biol Eng Comput* **47.7** (2009), pp. 743–755.
- [137] Lighthill, S. J. *Mathematical biofluidynamics*. SIAM, 1975.
- [138] Madani, M. et al. "The changing landscape of chronic thromboembolic pulmonary hypertension management". *Eur Resp Rev* **26.146** (2017).
- [139] Madani, M. M. "Surgical Treatment of Chronic Thromboembolic Pulmonary Hypertension: Pulmonary Thromboendarterectomy". *Methodist Debaquey Cardiovasc J* **12.4** (2016), pp. 213–218.
- [140] Mahmud, E. et al. "Chronic Thromboembolic Pulmonary Hypertension: Evolving Therapeutic Approaches for Operable and Inoperable Disease". *J Am Coll Cardiol* **71.21** (2018), pp. 2468–2486.
- [141] Mandras, S. A. et al. "Pulmonary Hypertension: A Brief Guide for Clinicians". *Mayo Clin Proc* **95.9** (2020), pp. 1978–1988.
- [142] Marquis, A. D. et al. "Practical identifiability and uncertainty quantification of a pulsatile cardiovascular model". *Math Biosci* **304**.July (2018), pp. 9–24.
- [143] Marsden, A. L. "Optimization in Cardiovascular Modeling". *Annu Rev Fluid Mech* **46.1** (2014), pp. 519–546.

- [144] Marsden, A. L. et al. "A computational framework for derivative-free optimization of cardiovascular geometries". *Comput Method Appl Mech Eng* **197**.21-24 (2008), pp. 1890–1905.
- [145] Matthews, D. T. & Hemnes, A. R. "Current concepts in the pathogenesis of chronic thromboembolic pulmonary hypertension". *Pulm Circ* **6**.2 (2016), pp. 145–154.
- [146] McDonald, D. & Attinger, E. "The characteristics of arterial pulse wave propagation in the dog". *Inf Exchange Group* 3 (1965).
- [147] Melani, A. "Adjoint-based parameter estimation in human vascular one dimensional models". PhD. Politecnico di Milano, 2013.
- [148] Melis, A. et al. "Bayesian sensitivity analysis of a 1D vascular model with Gaussian process emulators". *Int J Numer Method Biomed Eng* **33**.12 (2017), pp. 1–11.
- [149] Memon, H. A. et al. "Chronic Thromboembolic Pulmonary Hypertension: Pearls and Pitfalls of Diagnosis". *Methodist Debaquey Cardiovasc J* **12**.4 (2016), pp. 199–204.
- [150] Miao, H. et al. "On Identifiability of Nonlinear ODE Models and Applications in Viral Dynamics". *SIAM Rev* **53**.1 (2011), pp. 3–39.
- [151] Monnet, X. & Teboul, J. L. "Transpulmonary thermodilution: Advantages and limits". *Crit Care* **21**.1 (2017), pp. 1–12.
- [152] Moore, J. A. et al. "Computational blood flow modelling". *J Biomech* **31**.2 (1997), pp. 179–184.
- [153] Morris, M. D. "Factorial sampling plans for preliminary computational experiments". *Technometrics* **33**.2 (1991), pp. 161–174.
- [154] Murphy, K. P. *Machine learning: a probabilistic perspective*. MIT press, 2012.
- [155] Murray, C. D. "The physiological principle of minimum work: I. The vascular system and the cost of blood volume". *Proc Natl Acad Sci USA* **12**.3 (1926), p. 207.
- [156] Mynard, J. et al. "Wave intensity amplification and attenuation in non-linear flow: Implications for the calculation of local reflection coefficients". *J Biomech* **41**.16 (2008), pp. 3314–3321.
- [157] Mynard, J. P. & Smolich, J. J. "One-Dimensional Haemodynamic Modeling and Wave Dynamics in the Entire Adult Circulation". *Ann Biomed Eng* **43**.6 (2015), pp. 1443–1460.
- [158] Mynard, J. P. & Valen-Sendstad, K. "A unified method for estimating pressure losses at vascular junctions". *Int J Numer Method Biomed Eng* April (2016), pp. 1–23.
- [159] Narang, N. et al. "Inaccuracy of estimated resting oxygen uptake in the clinical setting". *Circulation* **129**.2 (2014), pp. 203–210.
- [160] Neidinger, R. D. "Introduction to automatic differentiation and MATLAB object-oriented programming". *SIAM Rev* **52**.3 (2010), pp. 545–563.

- [161] Newberry, M. G. et al. “Testing Foundations of Biological Scaling Theory Using Automated Measurements of Vascular Networks”. *PLoS Comput Biol* **11.8** (2015), pp. 1–18.
- [162] Nocedal, J. & Wright, S. *Numerical optimization*. Springer Science & Business Media, 2006.
- [163] Olsen, C. H. “Modeling Heart Rate Regulation by the Baroreflex”. PhD. North Carolina State University, 2014.
- [164] Olsen, C. H. et al. *Challenges in practical computation of global sensitivities with application to a baroreceptor reflex model*. Tech. rep. North Carolina State University. Center for Research in Scientific Computation, 2013.
- [165] Olsen, C. H. et al. “Parameter subset selection techniques for problems in mathematical biology”. *Biol Cybern* (2018).
- [166] Olufsen, M. S. “Structured tree outflow condition for blood flow in larger systemic arteries”. *Am J Physiol Heart Circ Physiol* **276.1** (1999), H257–H268.
- [167] Olufsen, M. S. & Ottesen, J. T. “A practical approach to parameter estimation applied to model predicting heart rate regulation”. *J Math Biol* **67.1** (2013), pp. 39–68.
- [168] Olufsen, M. S. et al. “Numerical simulation and experimental validation of blood flow in arteries with structured-tree outflow conditions”. *Ann Biomed Eng* **28.11** (2000), pp. 1281–1299.
- [169] Olufsen, M. S. et al. “Rarefaction and blood pressure in systemic and pulmonary arteries”. *J Fluid Mech* **705** (2012), pp. 280–305.
- [170] Otto, F. “Die grundform des arteriellen pulses”. *Zeitung fur Biologie* **37** (1899), pp. 483–586.
- [171] Parker, K. H. & Jones, C. J. “Forward and backward running waves in the arteries: Analysis using the method of characteristics”. *J Biomech Eng* **112.3** (1990), pp. 322–326.
- [172] Parker, K. H. “An introduction to wave intensity analysis”. *Med Biol Eng Comput* **47.2** (2009), pp. 175–188.
- [173] Paun, L. M. & Husmeier, D. “MCMC with Gaussian Processes for fast parameter estimation and uncertainty quantification in a 1D fluid-dynamics model of the pulmonary circulation”. *Int J Numer Method Biomed Eng* November (2020), pp. 1–37.
- [174] Paun, L. M. et al. “MCMC with delayed acceptance using a surrogate model with an application to cardiovascular fluid dynamics”. *Proc. Int. Conf. Stat. Theory Appl.* (2019), pp. 1–8.
- [175] Paun, L. M. et al. “Assessing model mismatch and model selection in a Bayesian uncertainty quantification analysis of a fluid-dynamics model of pulmonary blood circulation”. *J R Soc Interface* **17.173** (2020), p. 20200886.
- [176] Payer, C. et al. “Automated integer programming based separation of arteries and veins from thoracic CT images”. *Med Image Anal* **34** (2016), pp. 109–122.

- [177] Peacock, A. J. et al. *Pulmonary Circulation : Diseases and Their Treatment, Fourth Edition*. Boca Raton, FL : Taylor and Francis, an imprint of CRC Press, 2020, 2016.
- [178] Petra, N. & Stadler, G. *Model variational inverse problems governed by partial differential equations*. Tech. rep. TEXAS UNIV AT AUSTIN INST FOR COMPUTATIONAL ENGINEERING and SCIENCES, 2011.
- [179] Philip, J. L. et al. “Pulmonary Vascular Mechanical Consequences of Ischemic Heart Failure and Implications for Right Ventricular Function”. *Am J Physiol Heart Circ Physiol* (2019).
- [180] Pironet, A. et al. “Practical identifiability analysis of a minimal cardiovascular system model”. *Comput Methods Programs Biomed* **171** (2019), pp. 53–65.
- [181] Poissy, J. et al. “Pulmonary Embolism in Patients with COVID-19: Awareness of an Increased Prevalence”. *Circulation* **142.2** (2020), pp. 184–186.
- [182] Pope, S. et al. “Estimation and identification of parameters in a lumped cerebrovascular model”. *Math Biosci Eng* **6.1** (2008), pp. 93–115.
- [183] Porenta, G. et al. “A finite-element model of blood flow in arteries including taper, branches, and obstructions”. *J Biomech Eng* **108** (1984), pp. 161–167.
- [184] Pries, A. R. et al. “Blood viscosity in tube flow: dependence on diameter and hematocrit.” *Am J Physiol Heart Circ Physiol* **263.6 Pt 2** (1992), H1770–H1778.
- [185] Pries, A. R. et al. “Resistance to blood flow in microvessels in vivo”. *Circ Res* **75.5** (1994), pp. 904–915.
- [186] Păun, L. M. et al. “MCMC methods for inference in a mathematical model of pulmonary circulation”. *Stat Neerl* **72.3** (2018), pp. 306–338.
- [187] Quadery, S. et al. “The impact of patient choice on survival in chronic thromboembolic pulmonary hypertension”. *Eur Respir J* **52** (2018), p. 1800589.
- [188] Qureshi, M. U. & Hill, N. A. “A computational study of pressure wave reflections in the pulmonary arteries”. *J Math Biol* **71.6-7** (2015), pp. 1525–1549.
- [189] Qureshi, M. U. et al. “Numerical simulation of blood flow and pressure drop in the pulmonary arterial and venous circulation”. *Biomechanics and Modeling in Mechanobiology* **13.5** (2014), pp. 1137–1154.
- [190] Qureshi, M. U. et al. “Characteristic impedance: Frequency or time domain approach?” *Physiol Meas* **39.1** (2018).
- [191] Qureshi, M. U. et al. “Hemodynamic assessment of pulmonary hypertension in mice: a model-based analysis of the disease mechanism”. *Biomech Model Mechanobiol* **18.1** (2019), pp. 219–243.
- [192] Raghu, R. et al. “Comparative study of viscoelastic arterial wall models in nonlinear one-dimensional finite element simulations of blood flow”. *J Biomed Eng* **133.8** (2011).

- [193] Ramu, B. & Thenappan, T. “Evolving Concepts of Pulmonary Hypertension Secondary to Left Heart Disease”. *Curr Heart Fail Rep* **13.2** (2016), pp. 92–102.
- [194] Randall, E. B. et al. “Global sensitivity analysis informed model reduction and selection applied to a Valsalva maneuver model”. *arXiv preprint arXiv:2005.12879* (2020).
- [195] Rasmussen, C. E. & Williams, C. K. I. *Gaussian Processes for Machine Learning*. Vol. 14. 02. Cambridge, MA: MIT Press, 2006, pp. 69–106.
- [196] Raue, A. et al. “Structural and practical identifiability analysis of partially observed dynamical models by exploiting the profile likelihood”. *Bioinformatics* **25.15** (2009), pp. 1923–1929.
- [197] Rempfler, M. et al. “Uncertainty Estimation in Vascular Networks”. *Graphs in Biomedical Image Analysis, Computational Anatomy and Imaging Genetics*. Ed. by Cardoso, M. J. et al. Cham: Springer International Publishing, 2017, pp. 42–52.
- [198] Reymond, P. et al. “Validation of a one-dimensional model of the systemic arterial tree”. *Am J Physiol Heart Circ Physiol* **297.1** (2009), H208–H222.
- [199] Riches, A. C. et al. “Blood volume determination in the mouse”. *J Physiol* **228.2** (1973), pp. 279–284.
- [200] Riihimäki, J., Vehtari, A., et al. “Laplace approximation for logistic Gaussian process density estimation and regression”. *Bayesian Anal* **9.2** (2014), pp. 425–448.
- [201] Rivolo, S. et al. “Impact of coronary bifurcation morphology on wave propagation”. *Am J Physiol Heart Circ Physiol* **311.4** (2016), H855–H870.
- [202] Rol, N. et al. “Vascular narrowing in pulmonary arterial hypertension is heterogeneous: rethinking resistance”. *Physiol Rep* **5.6** (2017), pp. 1–9.
- [203] Ronneberger, O. et al. “U-net: Convolutional networks for biomedical image segmentation”. *International Conference on Medical image computing and computer-assisted intervention*. Springer. 2015, pp. 234–241.
- [204] Safaei, S. et al. “Roadmap for cardiovascular circulation model”. *J Physiol* **594.23** (2016), pp. 6909–6928.
- [205] Saltelli, A. et al. *Global sensitivity analysis: the primer*. John Wiley & Sons, 2008.
- [206] Sankaran, S. et al. “Fast Computation of Hemodynamic Sensitivity to Lumen Segmentation Uncertainty”. *IEEE Trans Med Imaging* **34.12** (2015), pp. 2562–2571.
- [207] Sankaran, S. et al. “Physics driven real-time blood flow simulations”. *Comp Meth Appl Mech Eng* **364** (2020), p. 112963.
- [208] Sarah, M. & Zeenat, S. “Epidemiology and Pathophysiology of Chronic Thromboembolic Pulmonary Hypertension: Risk Factors and Mechanisms”. *Methodist Deakey Cardiovasc J* **12.4** (2016), pp. 195–198.

- [209] Sato, S. et al. "Scale dependence of structure-function relationship in the emphysematous mouse lung". *Front Physiol* **6**.MAY (2015), pp. 1–10.
- [210] Schäfer, M. et al. "Noninvasive wave intensity analysis predicts functional worsening in children with pulmonary arterial hypertension". *Am J Physiol Heart Circ Physiol* **315**.4 (2018), H968–H977.
- [211] Schreier, D. A. et al. "Impact of increased hematocrit on right ventricular afterload in response to chronic hypoxia". *J Appl Physiol* **117**.8 (2014), pp. 833–839.
- [212] Secomb, T. W. "Blood Flow in the Microcirculation". *Annu Rev Fluid Mech* **49**.August (2017), pp. 443–61.
- [213] Segers, P. et al. "Noninvasive pulmonary artery wave intensity analysis in pulmonary hypertension". *Am J Physiol Heart Circ Physiol* **308**.12 (2015), H1603–H1611.
- [214] Siekmann, I. et al. "MCMC can detect nonidentifiable models". *Biophys J* **103**.11 (2012), pp. 2275–2286.
- [215] Siennicka, A. et al. "Treatment of chronic thromboembolic pulmonary hypertension in a multidisciplinary team". *Ther Adv Respir Dis* **13** (2019).
- [216] Silverman, B. W. *Density estimation for statistics and data analysis*. Vol. 26. CRC press, 1986.
- [217] Simonneau, G. et al. "The pathophysiology of chronic thromboembolic pulmonary hypertension". *Eur Respir Rev* **26**.143 (2017).
- [218] Simonneau, G. et al. "Haemodynamic definitions and updated clinical classification of pulmonary hypertension". *Eur Respir J* **53**.1 (2019).
- [219] Singhal, S. et al. "Morphometry of the human pulmonary arterial tree". *Circ Res* **33**.2 (1973), pp. 190–197.
- [220] Smith, L. A. & Kennedy, J. L. "Pulmonary Hypertension and Related Disorders". *Textbook of Clinical Hemodynamics*. Second Edi. Elsevier, 2018, pp. 163–181.
- [221] Smith, R. C. *Uncertainty quantification: theory, implementation, and applications*. Vol. 12. Siam, 2013.
- [222] Spazzapan, M. et al. "The use of biophysical flow models in the surgical management of patients affected by Chronic Thromboembolic Pulmonary Hypertension". *Front Physiol* **9**.MAR (2018), pp. 1–13.
- [223] Spilker, R. L. et al. "Morphometry-based impedance boundary conditions for patient-specific modeling of blood flow in pulmonary arteries". *Ann Biomed Eng* **35**.4 (2007), pp. 546–559.
- [224] Stam, K. et al. "Pulmonary microvascular remodeling in chronic thrombo-embolic pulmonary hypertension". *Am J Physiol Lung Cell Mol Physiol* **315**.6 (2018), pp. L951–L964.
- [225] Steele, B. N. et al. "Predicting arterial flow and pressure dynamics using a 1D fluid dynamics model with a viscoelastic wall". *SIAM J Appl Math* **71**.4 (2011), pp. 1123–1143.

- [226] Stergiopoulos, N. et al. "Evaluation of methods for estimation of total arterial compliance". *Am J Physiol Heart Circ Physiol* **268**.4 (1995), H1540–H1548.
- [227] Strahler, A. N. "Part II. Quantitative geomorphology of drainage basins and channel networks". *Handbook of Applied Hydrology: McGraw-Hill, New York* (1964), pp. 4–39.
- [228] Su, J. et al. "A review of wave mechanics in the pulmonary artery with an emphasis on wave intensity analysis". *Acta Physiol.* **218**.4 (2016), pp. 239–249.
- [229] Su, J. et al. "Wave intensity analysis provides novel insights into pulmonary arterial hypertension and chronic thromboembolic pulmonary hypertension". *J Am Heart Assoc* **6**.11 (2017), pp. 1–14.
- [230] Su, J. et al. "Impact of chronic hypoxia on proximal pulmonary artery wave propagation and mechanical properties in rats". *Am J Physiol Heart Circ Physiol* **314**.6 (2018), H1264–H1278.
- [231] Sumner, T. et al. "A methodology for global-sensitivity analysis of time-dependent outputs in systems biology modelling". *J R Soc Interface* **9**.74 (2012), pp. 2156–2166.
- [232] Tabima, D. M. et al. "Persistent vascular collagen accumulation alters hemodynamic recovery from chronic hypoxia". *J Biomech* **45**.5 (2012), pp. 799–804.
- [233] Tang, B. T. et al. "Wall shear stress is decreased in the pulmonary arteries of patients with pulmonary arterial hypertension: an image-based, computational fluid dynamics study". *Pulm Circ* **2**.4 (2012), pp. 470–476.
- [234] Taniguchi, Y. et al. "The role of balloon pulmonary angioplasty and pulmonary endarterectomy: Is chronic thromboembolic pulmonary hypertension still a life-threatening disease?" *Int J Cardiol* (2020).
- [235] Tawhai, M. H. et al. "Computational Models of the Pulmonary Circulation: Insights and the Move towards Clinically Directed Studies". *Pulm Circ* **1**.2 (2011), pp. 224–238.
- [236] Taylor, C. A. et al. "Finite element modeling of blood flow in arteries". *Comput Method Appl Mech Eng* **158** (1998), pp. 155–196.
- [237] Townsley, M. I. "Structure and composition of pulmonary arteries, capillaries, and veins". *Compr Physiol* **2**.1 (2012), pp. 675–709.
- [238] Utkarsh, A. *The Paraview Guide: A Parallel Visualization Application*. Clifton Park, NY: Kitware, Inc., 2015.
- [239] Vachiéry, J. L. et al. "Pulmonary hypertension due to left heart disease". *Eur Respir J* **53**.1 (2019).
- [240] Valdez-Jasso, D. et al. "Linear and nonlinear viscoelastic modeling of aorta and carotid pressure–area dynamics under In vivo and ex vivo conditions". *Ann Biomed Eng* **39**.5 (2011), pp. 1438–1456.

- [241] Valentín, A. et al. “Complementary vasoactivity and matrix remodelling in arterial adaptations to altered flow and pressure”. *J R Soc Interface* **6**.32 (2009), pp. 293–306.
- [242] Van Rikxoort, E. M. & Van Ginneken, B. “Automated segmentation of pulmonary structures in thoracic computed tomography scans: A review”. *Phys Med Biol* **58**.17 (2013).
- [243] Van Varik, B. J. et al. “Mechanisms of arterial remodeling: Lessons from genetic diseases”. *Front Genet* **3**.DEC (2012), pp. 1–10.
- [244] Vanden Eynden, F. et al. “Proximal pressure reducing effect of wave reflection in the pulmonary circulation disappear in obstructive disease: insight from a rabbit model”. *Am J Physiol Heart Circ Physiol* **316**.5 (2019), H992–H1004.
- [245] Vanderpool, R. R. et al. “Effects of acute Rho kinase inhibition on chronic hypoxia-induced changes in proximal and distal pulmonary arterial structure and function”. *J Appl Physiol* **110**.1 (2011), pp. 188–198.
- [246] Velázquez Martín, M. et al. “Fractional Flow Reserve-guided Pulmonary Angioplasty in Chronic Thromboembolic Pulmonary Hypertension”. *Rev Esp Cardiol* **69**.9 (2016), p. 863.
- [247] Virani, S. S. et al. “Heart disease and stroke statistics—2020 update: A report from the American Heart Association”. *Circulation* (2020), E139–E596.
- [248] Vlachopoulos, C. et al. *McDonald's blood flow in arteries: theoretical, experimental and clinical principles*. CRC press, 2011.
- [249] Vosse, F. N. van de & Stergiopoulos, N. “Pulse Wave Propagation in the Arterial Tree”. *Annu Rev Fluid Mech* **43**.1 (2011), pp. 467–499.
- [250] Wagenseil, J. E. & Mecham, R. P. “Vascular extracellular matrix and arterial mechanics”. *Physiol Rev* **89**.3 (2009), pp. 957–989.
- [251] Wang, L. et al. “Hemodynamic and gas exchange effects of inhaled iloprost in patients with COPD and pulmonary hypertension”. *Int J COPD* **12** (2017), pp. 3353–3360.
- [252] Wang, Z. & Chesler, N. C. “Pulmonary Vascular Wall Stiffness: An Important Contributor to the Increased Right Ventricular Afterload with Pulmonary Hypertension”. *Pulm Circ* **1**.2 (2011), pp. 212–223.
- [253] Wang, Z. et al. “Changes in Large Pulmonary Arterial Viscoelasticity in Chronic Pulmonary Hypertension”. *PLoS One* **8**.11 (2013). Ed. by Lam, W., e78569.
- [254] Weatherald, J. et al. “Medical Management of Pulmonary Hypertension with Unclear and/or Multifactorial Mechanisms (Group 5): Is There a Role for Pulmonary Arterial Hypertension Medications?” *Curr Hypertens Rep* **19**.11 (2017).
- [255] Weibel, E. R. & Gomez, D. M. “Architecture of the human lung”. *Science* **137**.3530 (1962), pp. 577–585.
- [256] Weibel, E. R. et al. *Morphometry of the human lung*. Vol. 1. Springer, 1963.

- [257] Wells, J. M. et al. "Pulmonary artery enlargement is associated with right ventricular dysfunction and loss of blood volume in small pulmonary vessels in chronic obstructive pulmonary disease". *Circ Cardiovasc Imaging* **8.4** (2015), pp. 1–8.
- [258] Wentworth, M. T. et al. "Parameter Selection and Verification Techniques Based on Global Sensitivity Analysis Illustrated for an HIV Model". *SIAM/ASA J Uncert Quant* **4.1** (2016), pp. 266–297.
- [259] Westerhof, N. et al. "The arterial windkessel". *Med Biol Eng Compt* **47.2** (2009), pp. 131–141.
- [260] Wilkens, H. et al. "Chronic thromboembolic pulmonary hypertension (CTEPH): Updated Recommendations from the Cologne Consensus Conference 2018". *Int J Cardiol* **272** (2018), pp. 69–78.
- [261] Wilson, N. M. et al. "The Vascular Model Repository: A Public Resource of Medical Imaging Data and Blood Flow Simulation Results". *J Med Dev* **7.4** (2013). 040923.
- [262] Windberger, U. et al. "Whole Blood Viscosity, Plasma Viscosity and Erythrocyte Aggregation in Nine Mammalian Species: Reference Values and Comparison of Data". *Exp. Physiol.* **88.3** (2003), pp. 431–440.
- [263] Wright, S. P. et al. "Hemodynamic Function of the Right Ventricular-Pulmonary Vascular-Left Atrial Unit: Normal Responses to Exercise in Healthy Adults". *Am J Physiol Heart Circ Physiol* November 2020 (2020), pp. 923–941.
- [264] Wu, J. et al. "Sensitivity analysis of infectious disease models: methods, advances and their application". *J R Soc Interface* **10.86** (2013), p. 20121018.
- [265] Xiu, D. & Sherwin, S. J. "Parametric uncertainty analysis of pulse wave propagation in a model of a human arterial network". *J Comput Phys* **226.2** (2007), pp. 1385–1407.
- [266] Yang, W. et al. "Evolution of hemodynamic forces in the pulmonary tree with progressively worsening pulmonary arterial hypertension in pediatric patients". *Biomech Model Mechanobiol* **18.3** (2019), pp. 779–796.
- [267] Yang, Y. et al. "3D CFD modelling and optimization of single-phase flow in rotating packed beds". *Can J Chem Eng* **93.6** (2015), pp. 1138–1148.
- [268] Yin, M. et al. "One-dimensional modeling of fractional flow reserve in coronary artery disease: Uncertainty quantification and Bayesian optimization". *Compute Method Appl Mech Eng* **353** (2019), pp. 66–85.
- [269] Young, D. F. & Tsai, F. Y. "Flow Characteristics in Models of Arterial Stenoses - I. Steady Flow". *J Biomech* **6** (1973), pp. 395–410.
- [270] Young, D. F. & Tsai, F. Y. "Flow Characteristics in Models of Arterial Stenoses - II. Unsteady Flow". *J Biomech* **6** (1973), pp. 547–559.
- [271] Young, D. F. & Tsai, F. Y. "Flow Characteristics in Models of Arterial Stenoses - II. Unsteady Flow". *J Biomech* **6** (1973), pp. 547–559.

- [272] Yushkevich, P. A. et al. "User-guided 3D active contour segmentation of anatomical structures: Significantly improved efficiency and reliability". *Neuroimage* **31.3** (2006), pp. 1116–1128.
- [273] Yushkevich, P. A. et al. "ITK-SNAP: An interactive tool for semi-automatic segmentation of multi-modality biomedical images". *2016 38th Annual International Conference of the IEEE Engineering in Medicine and Biology Society (EMBC)*. Vol. 2016-Octob. IEEE, 2016, pp. 3342–3345.
- [274] Zhigljavsky, A. & Zilinskas, A. *Stochastic global optimization*. Vol. 9. Springer Science & Business Media, 2007.
- [275] Zhong, W. et al. "Determination of permeability and inertial coefficients of sintered metal porous media using an isothermal chamber". *Appl Sci* **8.9** (2018).

APPENDICES

APPENDIX

A

NONDIMENSIONAL ANALYSIS

The full Navier-stokes equations in cylindrical coordinates are given by

$$\left(\frac{\partial(r u_r)}{\partial r} + \frac{1}{r} \frac{\partial u_\theta}{\partial \theta} + \frac{\partial u_x}{\partial x} \right) = 0 \quad (\text{A.1})$$

$$\begin{aligned} \rho \left(\frac{\partial u_r}{\partial t} + u_r \frac{\partial u_r}{\partial r} + \frac{u_\theta}{r} \frac{\partial u_r}{\partial \theta} + u_x \frac{\partial u_r}{\partial x} + \frac{u_\theta^2}{r} \right) \\ = -\frac{\partial p}{\partial r} + \mu \left(\frac{1}{r} \frac{\partial}{\partial r} \left(r \frac{\partial u_r}{\partial r} \right) + \frac{1}{r^2} \frac{\partial^2 u_r}{\partial \theta^2} + \frac{\partial^2 u_r}{\partial x^2} - \frac{u_r}{r^2} - \frac{2}{r} \frac{\partial u_\theta}{\partial \theta} \right) \end{aligned} \quad (\text{A.2})$$

$$\begin{aligned} \rho \left(\frac{\partial u_\theta}{\partial t} + u_r \frac{\partial u_\theta}{\partial r} + \frac{u_\theta}{r} \frac{\partial u_\theta}{\partial \theta} + u_x \frac{\partial u_\theta}{\partial x} - \frac{u_r u_\theta}{r} \right) \\ = -\frac{1}{r} \frac{\partial p}{\partial \theta} + \mu \left(\frac{1}{r} \frac{\partial}{\partial r} \left(r \frac{\partial u_\theta}{\partial r} \right) + \frac{1}{r^2} \frac{\partial^2 u_\theta}{\partial \theta^2} + \frac{\partial^2 u_\theta}{\partial x^2} + \frac{2}{r} \frac{\partial u_r}{\partial \theta} - \frac{u_\theta}{r^2} \right) \end{aligned} \quad (\text{A.3})$$

$$\begin{aligned} \rho \left(\frac{\partial u_x}{\partial t} + u_r \frac{\partial u_x}{\partial r} + \frac{u_\theta}{r} \frac{\partial u_x}{\partial \theta} + u_x \frac{\partial u_x}{\partial x} \right) \\ = -\frac{\partial p}{\partial x} + \mu \left(\frac{1}{r} \frac{\partial}{\partial r} \left(r \frac{\partial u_x}{\partial r} \right) + \frac{1}{r^2} \frac{\partial^2 u_x}{\partial \theta^2} + \frac{\partial^2 u_x}{\partial x^2} \right). \end{aligned} \quad (\text{A.4})$$

Under the assumptions that the flow is irrotational with no swirl ($u_\theta = 0$) and that the flow is axisymmetric so that the velocity of the fluid is independent of the circumferential component (i.e. $\mathbf{u} = [u_r(r, x, t), 0, u_x(r, x, t)]$), the system is

$$\left(\frac{\partial(r u_r)}{\partial r} + \frac{\partial u_x}{\partial x} \right) = 0 \quad (\text{A.5})$$

$$\rho \left(\frac{\partial u_r}{\partial t} + u_r \frac{\partial u_r}{\partial r} + u_x \frac{\partial u_r}{\partial x} \right) = -\frac{\partial p}{\partial r} + \mu \left(\frac{1}{r} \frac{\partial}{\partial r} \left(r \frac{\partial u_r}{\partial r} \right) + \frac{\partial^2 u_r}{\partial x^2} - \frac{u_r}{r^2} \right) \quad (\text{A.6})$$

$$\rho \left(\frac{\partial u_x}{\partial t} + u_r \frac{\partial u_x}{\partial r} + u_x \frac{\partial u_x}{\partial x} \right) = -\frac{\partial p}{\partial x} + \mu \left(\frac{1}{r} \frac{\partial}{\partial r} \left(r \frac{\partial u_x}{\partial r} \right) + \frac{\partial^2 u_x}{\partial x^2} \right). \quad (\text{A.7})$$

A.1 Nondimensional analysis of momentum balance

To show that the transmural blood pressure changes predominately in the axial direction, consider the momentum balance in the r direction given by equation (A.6). Define the following non-dimensional quantities:

$$\begin{aligned} u_x &= U_x \tilde{u}_x, \quad u_r = U_r \tilde{u}_r, \quad x = L \tilde{x}, \\ r &= R \tilde{r}, \quad p = P \tilde{p} = (\rho U_x^2) \tilde{p} \\ t &= T \tilde{t} = \frac{R}{U_r} \tilde{t} = \frac{L}{U_x} \tilde{t}. \end{aligned} \quad (\text{A.8})$$

We require the same time scale for u_x and u_r , hence we can use equality between the two forms of T above. The momentum equation in the r direction is then

$$\frac{\partial p}{\partial r} = -\rho \left(\frac{\partial u_r}{\partial t} + u_r \frac{\partial u_r}{\partial r} + u_x \frac{\partial u_r}{\partial x} \right) + \mu \left(\frac{1}{r} \frac{\partial}{\partial r} \left(r \frac{\partial u_r}{\partial r} \right) + \frac{\partial^2 u_r}{\partial x^2} - \frac{u_r}{r^2} \right) \quad (\text{A.9})$$

$$\begin{aligned} \Rightarrow \frac{\rho U_x^2}{R} \frac{\partial \tilde{p}}{\partial \tilde{r}} &= -\rho \left(\frac{U_r}{T} \frac{\partial \tilde{u}_r}{\partial \tilde{t}} + \frac{U_r^2 \tilde{u}_r}{R} \frac{\partial \tilde{u}_r}{\partial \tilde{r}} + \frac{U_r U_x \tilde{u}_x}{L} \frac{\partial \tilde{u}_r}{\partial \tilde{x}} \right) \\ &+ \mu \left(\frac{U_r}{R^2} \frac{\partial^2 \tilde{u}_r}{\partial \tilde{r}^2} + \frac{U_r}{R^2 \tilde{r}} \frac{\partial \tilde{u}_r}{\partial \tilde{r}} - \frac{U_r \tilde{u}_r}{R^2 \tilde{r}^2} + \frac{U_r}{L^2} \frac{\partial^2 \tilde{u}_r}{\partial \tilde{x}^2} \right) \end{aligned} \quad (\text{A.10})$$

$$\begin{aligned} \Rightarrow \frac{\partial \tilde{p}}{\partial \tilde{r}} &= -\frac{R}{U_x^2} \left(\frac{U_r}{T} \frac{\partial \tilde{u}_r}{\partial \tilde{t}} + \frac{U_r^2 \tilde{u}_r}{R} \frac{\partial \tilde{u}_r}{\partial \tilde{r}} + \frac{U_r U_x \tilde{u}_x}{L} \frac{\partial \tilde{u}_r}{\partial \tilde{x}} \right) \\ &+ \frac{\mu R}{\rho U_x^2} \left(\frac{U_r}{R^2} \frac{\partial^2 \tilde{u}_r}{\partial \tilde{r}^2} + \frac{U_r}{R^2 \tilde{r}} \frac{\partial \tilde{u}_r}{\partial \tilde{r}} - \frac{U_r \tilde{u}_r}{R^2 \tilde{r}^2} + \frac{U_r}{L^2} \frac{\partial^2 \tilde{u}_r}{\partial \tilde{x}^2} \right). \end{aligned} \quad (\text{A.11})$$

Factoring out common terms on the right hand side gives

$$\begin{aligned} \Rightarrow \frac{\partial \tilde{p}}{\partial \tilde{r}} &= -\frac{R}{U_x} \frac{U_r}{U_x} \left(\frac{1}{T} \frac{\partial \tilde{u}_r}{\partial \tilde{t}} + \frac{U_r \tilde{u}_r}{R} \frac{\partial \tilde{u}_r}{\partial \tilde{r}} + \frac{U_x \tilde{u}_x}{L} \frac{\partial \tilde{u}_r}{\partial \tilde{x}} \right) \\ &+ \frac{\mu R}{\rho U_x} \frac{U_r}{U_x} \left(\frac{1}{R^2} \frac{\partial^2 \tilde{u}_r}{\partial \tilde{r}^2} + \frac{1}{R^2 \tilde{r}} \frac{\partial \tilde{u}_r}{\partial \tilde{r}} - \frac{\tilde{u}_r}{R^2 \tilde{r}^2} + \frac{1}{L^2} \frac{\partial^2 \tilde{u}_r}{\partial \tilde{x}^2} \right). \end{aligned} \quad (\text{A.12})$$

Assuming that the axial velocity is dominant, i.e. $U_r/U_x \ll 1$, we get

$$\frac{\partial \tilde{p}}{\partial \tilde{r}} \approx 0 \Rightarrow p = p(x, t). \quad (\text{A.13})$$

A similar analysis on the axial momentum equation using the same non-dimensional variables gives

$$\begin{aligned} \rho \left(\frac{\partial u_x}{\partial t} + u_r \frac{\partial u_x}{\partial r} + u_x \frac{\partial u_x}{\partial x} \right) &= -\frac{\partial p}{\partial x} + \mu \left(\frac{\partial^2 u_x}{\partial r^2} + \frac{1}{r} \frac{\partial u_x}{\partial r} + \frac{\partial^2 u_x}{\partial x^2} \right) \\ \Rightarrow \rho \left(\frac{U_x}{T} \frac{\partial \tilde{u}_x}{\partial \tilde{t}} + \frac{U_x U_r \tilde{u}_r}{R} \frac{\partial \tilde{u}_x}{\partial \tilde{r}} + \frac{U_x^2 \tilde{u}_x}{L} \frac{\partial \tilde{u}_x}{\partial \tilde{x}} \right) &= -\frac{\rho U_x^2}{L} \frac{\partial \tilde{p}}{\partial \tilde{x}} + \mu \left(\frac{U_x^2}{R^2} \frac{\partial^2 \tilde{u}_x}{\partial \tilde{r}^2} + \frac{U_x}{R^2 \tilde{r}} \frac{\partial \tilde{u}_x}{\partial \tilde{r}} + \frac{U_x}{L^2} \frac{\partial^2 \tilde{u}_x}{\partial \tilde{x}^2} \right) \end{aligned} \quad (\text{A.14})$$

Using $T = L/U_x = R/U_r$, we can write

$$\begin{aligned} \rho \left(\frac{U_x}{T} \frac{\partial \tilde{u}_x}{\partial \tilde{t}} + \frac{U_x U_r \tilde{u}_r}{R} \frac{\partial \tilde{u}_x}{\partial \tilde{r}} + \frac{U_x^2 \tilde{u}_x}{L} \frac{\partial \tilde{u}_x}{\partial \tilde{x}} \right) &= -\frac{\rho U_x^2}{L} \frac{\partial \tilde{p}}{\partial \tilde{x}} + \mu \left(\frac{U_x}{R^2} \frac{\partial^2 \tilde{u}_x}{\partial \tilde{r}^2} + \frac{U_x}{R^2 \tilde{r}} \frac{\partial \tilde{u}_x}{\partial \tilde{r}} + \frac{U_x}{L^2} \frac{\partial^2 \tilde{u}_x}{\partial \tilde{x}^2} \right) \\ \Rightarrow \rho \left(\frac{U_x^2}{L} \frac{\partial \tilde{u}_x}{\partial \tilde{t}} + \frac{U_x^2 \tilde{u}_r}{L} \frac{\partial \tilde{u}_x}{\partial \tilde{r}} + \frac{U_x^2 \tilde{u}_x}{L} \frac{\partial \tilde{u}_x}{\partial \tilde{x}} \right) &= -\frac{\rho U_x^2}{L} \frac{\partial \tilde{p}}{\partial \tilde{x}} + \mu \left(\frac{U_x}{R^2} \frac{\partial^2 \tilde{u}_x}{\partial \tilde{r}^2} + \frac{U_x}{R^2 \tilde{r}} \frac{\partial \tilde{u}_x}{\partial \tilde{r}} + \frac{U_x}{L^2} \frac{\partial^2 \tilde{u}_x}{\partial \tilde{x}^2} \right) \\ \Rightarrow \frac{\partial \tilde{u}_x}{\partial \tilde{t}} + \tilde{u}_r \frac{\partial \tilde{u}_x}{\partial \tilde{r}} + \tilde{u}_x \frac{\partial \tilde{u}_x}{\partial \tilde{x}} &= -\frac{\partial \tilde{p}}{\partial \tilde{x}} + \frac{\mu L}{\rho U_x^2} \left(\frac{U_x}{R^2} \frac{\partial^2 \tilde{u}_x}{\partial \tilde{r}^2} + \frac{U_x}{R^2 \tilde{r}} \frac{\partial \tilde{u}_x}{\partial \tilde{r}} + \frac{U_x}{L^2} \frac{\partial^2 \tilde{u}_x}{\partial \tilde{x}^2} \right). \end{aligned} \quad (\text{A.15})$$

Again utilizing $U_r/U_x = \epsilon \ll 1$, we get

$$\begin{aligned} &-\frac{\partial \tilde{p}}{\partial \tilde{x}} + \frac{\nu L}{R^2 U_x} \left(\frac{\partial^2 \tilde{u}_x}{\partial \tilde{r}^2} + \frac{1}{\tilde{r}} \frac{\partial \tilde{u}_x}{\partial \tilde{r}} \right) + \frac{\nu}{U_x L} \frac{\partial^2 \tilde{u}_x}{\partial \tilde{x}^2} \\ &= -\frac{\partial \tilde{p}}{\partial \tilde{x}} + \frac{\nu}{R U_x} \left(\frac{L}{R} \frac{\partial^2 \tilde{u}_x}{\partial \tilde{r}^2} + \frac{L}{R} \left(\frac{1}{\tilde{r}} \frac{\partial \tilde{u}_x}{\partial \tilde{r}} \right) + \frac{R}{L} \frac{\partial^2 \tilde{u}_x}{\partial \tilde{x}^2} \right) \\ &= -\frac{\partial \tilde{p}}{\partial \tilde{x}} + \frac{\nu}{R U_x} \left(\frac{1}{\epsilon} \frac{\partial^2 \tilde{u}_x}{\partial \tilde{r}^2} + \frac{1}{\epsilon} \left(\frac{1}{\tilde{r}} \frac{\partial \tilde{u}_x}{\partial \tilde{r}} \right) + \epsilon \frac{\partial^2 \tilde{u}_x}{\partial \tilde{x}^2} \right). \end{aligned} \quad (\text{A.16})$$

The above expression shows that the diffusive term $\rho \nu \epsilon r^2 u_x x^2$ can be disregarded. Our momentum equation in dimensional form is then

$$\frac{\partial u_x}{\partial t} + u_r \frac{\partial u_x}{\partial r} + u_x \frac{\partial u_x}{\partial x} = -\frac{1}{\rho} \frac{\partial p}{\partial x} + \nu \left(\frac{1}{r} \frac{\partial}{\partial r} \left(r \frac{\partial u_x}{\partial r} \right) \right). \quad (\text{A.17})$$

A.2 Nondimensional PDE solution

To numerically solve the equations, the system of PDE's is first nondimensionalized. Define the following:

$$\begin{aligned} q &= q_c \tilde{q}, \quad x = L_c \tilde{x}, \quad R = L_c \tilde{R}, \\ t &= \frac{L_c^3}{q_c} \tilde{t}, \quad \delta = L_c \tilde{\delta}, \quad p = \rho g L_c \tilde{p}, \\ A &= L_c^2 \tilde{A}, \quad A_0 = L_c^2 \tilde{A}_0, \quad h = L_c \tilde{h}, \\ E &= \rho g L_c \tilde{E}. \end{aligned} \quad (\text{A.18})$$

The non-dimensional mass balance equation is

$$\frac{q_c L_c^2}{L_c^3} \frac{\partial \tilde{A}}{\partial \tilde{t}} + \frac{q_c^2}{L_c^3} \frac{\partial \tilde{q}}{\partial \tilde{x}} = \frac{\partial \tilde{A}}{\partial \tilde{t}} + \frac{\partial \tilde{q}}{\partial \tilde{x}} = 0. \quad (\text{A.19})$$

For the momentum equation, the nondimensionalization is the same for either consistutive law. Note that the units of B are the same as $\frac{A}{\rho} \frac{\partial p}{\partial x}$, hence

$$B = (gL_c^3) \tilde{B}. \quad (\text{A.20})$$

Since B_{RHS} stems from $\frac{\partial B}{\partial x}$, the units are

$$B_{RHS} = (gL_c^2) \tilde{B}_{RHS} \quad (\text{A.21})$$

Using this to rewrite our momentum equation in nondimensional form, we have

$$\begin{aligned} \frac{\partial q}{\partial t} + \frac{\partial}{\partial x} \left(\frac{q^2}{A} + B \right) &= -\frac{2\pi\mu R}{\rho\delta} \frac{q}{A} + B_{RHS} \\ \Rightarrow \frac{q_c^2}{L_c^3} \frac{\partial \tilde{q}}{\partial \tilde{t}} + \frac{1}{L_c} \frac{\partial}{\partial \tilde{x}} \left(\frac{q_c^2}{L_c^2} \frac{\tilde{q}^2}{\tilde{A}} + (gL_c^3) \tilde{B} \right) &= \frac{\mu q_c}{\rho L_c^2} \frac{-2\pi\tilde{R}}{\tilde{\delta}} \frac{\tilde{q}}{\tilde{A}} + (gL_c^2) \tilde{B}_{RHS} \end{aligned} \quad (\text{A.22})$$

Multiplying through by q_c^2/L_c^3 gives

$$\frac{\partial \tilde{q}}{\partial \tilde{t}} + \frac{\partial}{\partial \tilde{x}} \left(\frac{\tilde{q}^2}{\tilde{A}} + \frac{gL_c^5}{q_c^2} \tilde{B} \right) = \frac{\mu L_c}{\rho q_c} \left(\frac{-2\pi\tilde{R}}{\tilde{\delta}} \right) \frac{\tilde{q}}{\tilde{A}} + \frac{gL_c^5}{q_c^2} \tilde{B}_{RHS} \quad (\text{A.23})$$

Define the Reynolds number and squared Froude's number (both non-dimensional) as

$$\mathcal{R} = \frac{q_c \rho}{L_c \mu}, \quad \text{Fr}^2 = \frac{u^2}{gL_c} = \frac{q_c^2}{gL_c^5}. \quad (\text{A.24})$$

Using the above, our final nondimensional system is

$$\frac{\partial \tilde{q}}{\partial \tilde{t}} + \frac{\partial}{\partial \tilde{x}} \left(\frac{\tilde{q}^2}{\tilde{A}} + \frac{1}{\text{Fr}^2} \tilde{B} \right) = \frac{1}{\mathcal{R}} \left(\frac{-2\pi\tilde{R}}{\tilde{\delta}} \right) \frac{\tilde{q}}{\tilde{A}} + \frac{1}{\text{Fr}^2} \tilde{B}_{RHS} \quad (\text{A.25})$$

This is the system of equations solved numerically by the Ritchmeyer two-step Lax-Wendroff method.

APPENDIX

B

ROOT FINDING AND BOUNDARY CONDITIONS

Throughout this appendix, we define $\eta = \Delta t / \Delta x$ and $\gamma = \Delta t / 2$ where Δt and Δx are the numerical step size in time and space.

B.1 Inflow

The inflow profile is assumed periodic, and can be used to determine the area A at the inlet of the network. To determine the point $q_{-1/2}^{n+1/2}$, the average flow at the half time step is

$$q_0^{n+1/2} = \frac{1}{2} (q_{-1/2}^{n+1/2} + q_{1/2}^{n+1/2}) \quad (\text{B.1})$$

$$\Rightarrow q_{-1/2}^{n+1/2} = 2q_0^{n+1/2} - q_{1/2}^{n+1/2}. \quad (\text{B.2})$$

We can then use this in the Lax-Wendroff equation

$$A_0^{n+1} = A_0^n - \eta \left((R_1)_{1/2}^{n+1/2} - (R_1)_{-1/2}^{n+1/2} \right) + \gamma \left((S_1)_{1/2}^{n+1/2} + (S_1)_{-1/2}^{n+1/2} \right) \quad (\text{B.3})$$

where $(R_1)_{-1/2}^{n+1/2} = q_{1/2}^{n+1/2}$ and $(S_1)_{-1/2}^{n+1/2} = 0$ (see Figure B.1).

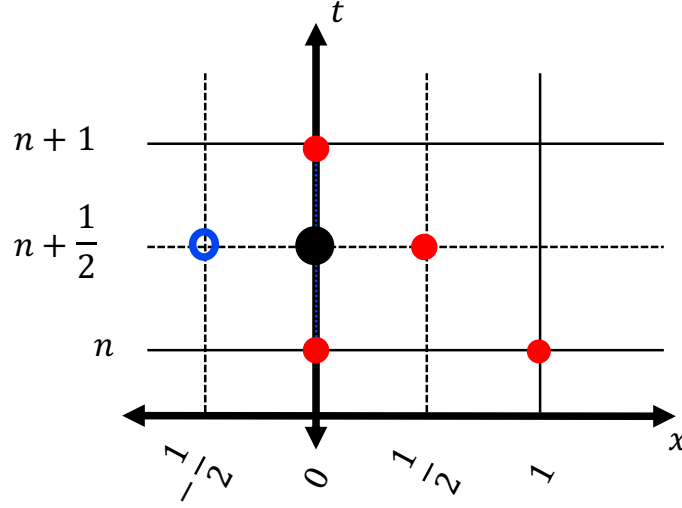


Figure B.1 Schematic of left boundary calculated using the two-step Lax-Wendroff scheme. All red points in the interior domain are known. To determine the ghost point (shown as a blue open circle), the boundary condition is applied at $x = 0$ and $t = n + 1/2$ (shown in black). Once q is determined, A is solved using the Lax-Wendroff method.

B.2 Outflow boundary condition

The discretized convolution integral is

$$q_M^n = \Delta t \left(p(A_M^n) y_M^0 + \sum_{k=1}^{N-1} p_M^{<n-k>_N} y_M^k \right). \quad (\text{B.4})$$

where $<n-k>_N$ is the modulus of the integer (mod N). Again, we require that our boundary conditions are consistent with our numerical solution via the Lax-Wendroff scheme. We can write

$$A_M^{n+1} = A_M^n - \eta \left((R_1)_{M+1/2}^{n+1/2} - (R_1)_{M-1/2}^{n+1/2} \right) \quad (\text{B.5})$$

$$q_M^{n+1} = q_M^n - \eta \left((R_2)_{M+1/2}^{n+1/2} - (R_2)_{M-1/2}^{n+1/2} \right) + \gamma \left((S_2)_{M+1/2}^{n+1/2} + (S_2)_{M-1/2}^{n+1/2} \right) \quad (\text{B.6})$$

where the components of the \mathbf{R} and \mathbf{S} are used. Since we require values at the point $M + 1/2$ (beyond the boundary, see Figure B.2) and the next time point, our unknowns from the above system are

$$A_M^{n+1}, q_M^{n+1} \quad (\text{B.7})$$

$$(R_1)_{M+1/2}^{n+1/2}, (R_2)_{M+1/2}^{n+1/2}, (S_2)_{M+1/2}^{n+1/2}. \quad (\text{B.8})$$

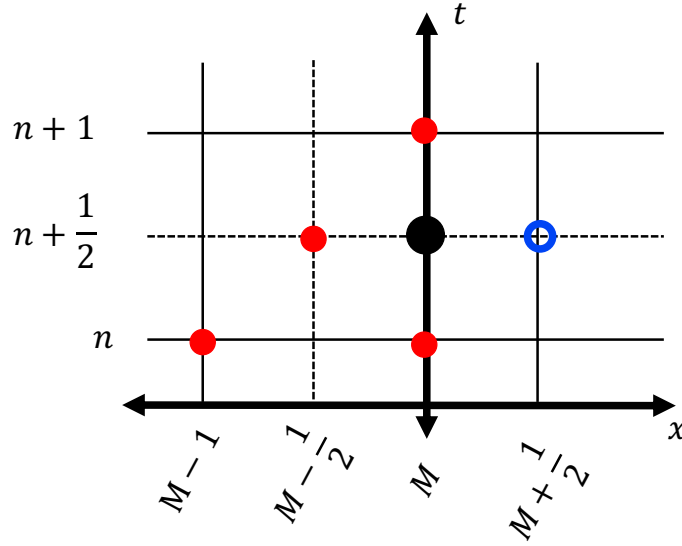


Figure B.2 Right boundary condition. All variables with a black circle are known. To determine the flow and area at $x = M$ and $t = n + 1$, a ghost point (blue circle) at $x = M + 1/2$ and $t = n + 1/2$ is introduced. The point is determined by averaging from the known values at $x = M - 1/2$ and $x = M$ (red circles).

In addition, we can compute the half spatial step in q and A using the average (as done in the inflow):

$$A_M^{n+1/2} = \frac{1}{2} (A_{M-1/2}^{n+1/2} + A_{M+1/2}^{n+1/2}) \quad (\text{B.9})$$

$$q_M^{n+1/2} = \frac{1}{2} (q_{M-1/2}^{n+1/2} + q_{M+1/2}^{n+1/2}). \quad (\text{B.10})$$

This adds two more unknowns to our system, which can be determined by the discretized convolution integral

$$q_M^{n+1/2} = \Delta t \left(p(A_M^{n+1/2}) y_M^0 + \sum_{k=1}^{N-1} p_M^{<n+1/2-k>_N} y_M^k \right) \quad (\text{B.11})$$

$$q_M^{n+1} = \Delta t \left(p(A_M^{n+1}) y_M^0 + \sum_{k=1}^{N-1} p_M^{<n+1-k>_N} y_M^k \right). \quad (\text{B.12})$$

To reduce the number of equations and unknowns, note that Eq. (B.11) can be written as

$$\frac{1}{2} (q_{M-1/2}^{n+1/2} + q_{M+1/2}^{n+1/2}) = \Delta t \left(p \left(\frac{A_{M-1/2}^{n+1/2} + A_{M+1/2}^{n+1/2}}{2} \right) y_M^0 + \sum_{k=1}^{N-1} p_M^{<n+1/2-k>_N} y_M^k \right). \quad (\text{B.13})$$

In summary, our final set of unknown variables are

$$x_1 = q_{M+1/2}^{n+1/2}, \quad x_2 = A_{M+1/2}^{n+1/2} \quad (\text{B.14})$$

$$x_3 = q_M^{n+1}, \quad x_4 = A_M^{n+1} \quad (\text{B.15})$$

with the corresponding equations to be solved

$$\begin{aligned}
A_M^{n+1} &= A_M^n - \eta \left((R_1)_{M+1/2}^{n+1/2} - (R_1)_{M-1/2}^{n+1/2} \right) \\
q_M^{n+1} &= q_M^n - \eta \left((R_2)_{M+1/2}^{n+1/2} - (R_2)_{M-1/2}^{n+1/2} \right) + \gamma \left((S_2)_{M+1/2}^{n+1/2} + (S_2)_{M-1/2}^{n+1/2} \right) \\
q_M^{n+1} &= \Delta t \left(p(A_M^{n+1}) y_M^0 + \sum_{k=1}^{N-1} p_M^{<n+1-k>_N} y_M^k \right) \\
\frac{1}{2} (q_{M-1/2}^{n+1/2} + q_{M+1/2}^{n+1/2}) &= \Delta t \left(p \left(\frac{(A_{M-1/2}^{n+1/2} + A_{M+1/2}^{n+1/2})}{2} \right) y_M^0 + \sum_{k=1}^{N-1} p_M^{<n+1/2-k>_N} y_M^k \right).
\end{aligned} \tag{B.16}$$

The residual equations are

$$(f_r)_1 = p \left(\frac{A_{M-1/2}^{n+1/2} + x_2}{2} \right) y_M^0 \Delta t + \sum_{k=1}^{N-1} p_M^{<n+1/2-k>_N} y_M^k - \frac{q_{M-1/2}^{n+1/2} + x_1}{2} \tag{B.17}$$

$$(f_r)_2 = p(x_4) y_M^0 \Delta t + \sum_{k=1}^{N-1} p_M^{<n+1-k>_N} y_M^k - x_3 \tag{B.18}$$

$$(f_r)_3 = A_M^n - \eta \left(x_1 - (R_1)_{M-1/2}^{n+1/2} \right) - x_4 \tag{B.19}$$

$$\begin{aligned}
(f_r)_4 &= -x_3 + q_M^n - \eta \left(\frac{x_1^2}{x_2} + B_{M+1/2}(x_2) - (R_2)_{M-1/2}^{n+1/2} \right) \\
&\quad + \gamma \left(F_{M+1/2}(x_1, x_2) + \frac{d}{dx_2} B_{M+1/2}(x_2) + (S_2)_{M-1/2}^{n+1/2} \right)
\end{aligned} \tag{B.20}$$

These equations are solved numerically using a Newton-Raphson routine

$$\mathbf{x}^{k+1} = \mathbf{x}^k - (\nabla \mathbf{f}(\mathbf{x}_k))^{-1} \mathbf{f}(\mathbf{x}_k) \tag{B.21}$$

where $\mathbf{f}(\mathbf{x}_k)$ is the residual of the above equations and $\nabla \mathbf{f}(\mathbf{x}_k)$ is the Jacobian matrix of the residuals. The Jacobian for this system is

$$\nabla \mathbf{f}_r = \begin{bmatrix} -1/2 & \xi_1 & 0 & 0 \\ 0 & 0 & -1 & \xi_2 \\ -\eta & 0 & 0 & -1 \\ \xi_3 & \xi_4 & -1 & 0 \end{bmatrix} \tag{B.22}$$

where

$$\xi_1 = y_M^0 \Delta t \frac{d}{dx_2} p \left(\frac{A_{M-1/2}^{n+1/2} + x_2}{2} \right) \tag{B.23}$$

$$\xi_2 = y_M^0 \Delta t \frac{d}{dx_4} p(x_4) \tag{B.24}$$

$$\xi_3 = \eta \frac{2x_1}{x_2} + \gamma \frac{d}{dx_1} F(x_1, x_2)_{M+1/2} \tag{B.25}$$

$$\xi_4 = \eta \left(\frac{x_1^2}{x_2} + \frac{d}{dx_2} B(x_2)_{M+1/2} \right) + \gamma \left(\frac{d}{dx_2} F(x_1, x_2)_{M+1/2} + \frac{d}{dx_2} B_{\text{RHS}}(x_2)_{M+1/2} \right). \tag{B.26}$$

B.3 Junction conditions

B.3.1 Bifurcation condition

To numerically solve for conservation of flow and pressure at a diverging junction, we minimize a residual based on our numerical solver and our junction conditions. The following is derived for a general bifurcation (i.e. one parent and two daughters), but can be extended to mono-, tri-, and quad-furcations.

The unknowns in at a junction are the q and A values at the $n + 1$ time steps, and the half time/half spatial values. This constitutes 18 unknown variables:

$$\begin{aligned} \mathbf{x} = & \left[(q^p)_M^{n+1} (q^p)_M^{n+1/2} (q^p)_{M+1/2}^{n+1/2} \right. \\ & (q^{d_1})_0^{n+1} (q^{d_1})_0^{n+1/2} (q^{d_1})_{-1/2}^{n+1/2} \\ & (q^{d_2})_0^{n+1} (q^{d_2})_0^{n+1/2} (q^{d_2})_{-1/2}^{n+1/2} \\ & (A^p)_M^{n+1} (A^p)_M^{n+1/2} (A^p)_{M+1/2}^{n+1/2} \\ & (A^{d_1})_0^{n+1} (A^{d_1})_0^{n+1/2} (A^{d_1})_{-1/2}^{n+1/2} \\ & \left. (A^{d_2})_0^{n+1} (A^{d_2})_0^{n+1/2} (A^{d_2})_{-1/2}^{n+1/2} \right]. \end{aligned}$$

To solve for these unknowns, we require a system of 18 equations. They are

$$\begin{aligned} (q^p)_M^{n+1} = & (q^p)_M^n - \eta \left((R_2^p)_{M+1/2}^{n+1/2} - (R_2^p)_{M-1/2}^{n+1/2} \right) \\ & + \gamma \left((S_2^p)_{M+1/2}^{n+1/2} + (S_2^p)_{M-1/2}^{n+1/2} \right) \end{aligned} \quad (\text{B.27})$$

$$\begin{aligned} (q^{d_1})_0^{n+1} = & (q^{d_1})_0^n - \eta \left((R_2^{d_1})_{1/2}^{n+1/2} - (R_2^{d_1})_{-1/2}^{n+1/2} \right) \\ & + \gamma \left((S_2^{d_1})_{1/2}^{n+1/2} + (S_2^{d_1})_{-1/2}^{n+1/2} \right) \end{aligned} \quad (\text{B.28})$$

$$\begin{aligned} (q^{d_2})_0^{n+1} = & (q^{d_2})_0^n - \eta \left((R_2^{d_2})_{1/2}^{n+1/2} - (R_2^{d_2})_{-1/2}^{n+1/2} \right) \\ & + \gamma \left((S_2^{d_2})_{1/2}^{n+1/2} + (S_2^{d_2})_{-1/2}^{n+1/2} \right) \end{aligned} \quad (\text{B.29})$$

$$(A^p)_M^{n+1} = (A^p)_M^n - \eta \left((R_1^p)_{M+1/2}^{n+1/2} - (R_1^p)_{M-1/2}^{n+1/2} \right) \quad (\text{B.30})$$

$$(A^{d_1})_0^{n+1} = (A^{d_1})_0^n - \eta \left((R_1^{d_1})_{1/2}^{n+1/2} - (R_1^{d_1})_{-1/2}^{n+1/2} \right) \quad (\text{B.31})$$

$$(A^{d_2})_0^{n+1} = (A^{d_2})_0^n - \eta \left((R_1^{d_2})_{1/2}^{n+1/2} - (R_1^{d_2})_{-1/2}^{n+1/2} \right) \quad (\text{B.32})$$

$$(q^p)_M^{n+1/2} = \frac{1}{2} \left((q^p)_{M-1/2}^{n+1/2} + (q^p)_{M+1/2}^{n+1/2} \right) \quad (\text{B.33})$$

$$(q^{d_1})_0^{n+1/2} = \frac{1}{2} \left((q^{d_1})_{-1/2}^{n+1/2} + (q^{d_1})_{1/2}^{n+1/2} \right) \quad (\text{B.34})$$

$$(q^{d_2})_0^{n+1/2} = \frac{1}{2} \left((q^{d_2})_{-1/2}^{n+1/2} + (q^{d_2})_{1/2}^{n+1/2} \right) \quad (\text{B.35})$$

$$(A^p)_M^{n+1/2} = \frac{1}{2} \left((A^p)_{M-1/2}^{n+1/2} + (A^p)_{M+1/2}^{n+1/2} \right) \quad (\text{B.36})$$

$$(A^{d_1})_0^{n+1/2} = \frac{1}{2} \left((A^{d_1})_{-1/2}^{n+1/2} + (A^{d_1})_{1/2}^{n+1/2} \right) \quad (\text{B.37})$$

$$(A^{d_2})_0^{n+1/2} = \frac{1}{2} \left((A^{d_2})_{-1/2}^{n+1/2} + (A^{d_2})_{1/2}^{n+1/2} \right) \quad (\text{B.38})$$

$$(q^p)_M^n = (q^{d_1})_0^n + (q^{d_2})_0^n \quad (\text{B.39})$$

$$(q^p)_M^{n+1/2} = (q^{d_1})_0^{n+1/2} + (q^{d_2})_0^{n+1/2} \quad (\text{B.40})$$

$$p(A_0^p, A^p, \beta)^{n+1/2} = p(A_0^{d_1}, A^{d_1}, \beta)^{n+1/2} \quad (\text{B.41})$$

$$p(A_0^p, A^p, \beta)^{n+1/2} = p(A_0^{d_2}, A^{d_2}, \beta)^{n+1/2} \quad (\text{B.42})$$

$$p(A_0^p, A^p, \beta)^{n+1} = p(A_0^{d_1}, A^{d_1}, \beta)^{n+1} \quad (\text{B.43})$$

$$p(A_0^p, A^p, \beta)^{n+1} = p(A_0^{d_2}, A^{d_2}, \beta)^{n+1} \quad (\text{B.44})$$

Note that from here, we will let $p(A) = \mathcal{F}(A)$.

The residual vectors for the above equations are as follows.

$$\begin{aligned} (f_r)_1 = & -x_1 + (q^p)_M^n - \eta \left(\frac{x_3^2}{x_{12}} + B(x_{12})_{M+1/2} - (R_2^p)_{M-1/2}^{n+1/2} \right) \\ & + \gamma \left[F(x_3, x_{12})_{M+1/2} + B_{\text{RHS}}(x_{12})_{M+1/2} + (S_2^p)_{M-1/2}^{n+1/2} \right] \end{aligned} \quad (\text{B.45})$$

$$\begin{aligned} (f_r)_2 = & -x_4 + (q^{d_1})_0^n - \eta \left((R_2^{d_1})_{1/2}^{n+1/2} - \frac{x_6^2}{x_{15}} - B(x_{15})_{-1/2} \right) \\ & + \gamma \left((S_2^{d_1})_{1/2}^{n+1/2} + F(x_6, x_{15})_{-1/2} + B_{\text{RHS}}(x_{15})_{-1/2} \right) \end{aligned} \quad (\text{B.46})$$

$$\begin{aligned} (f_r)_3 = & -x_7 + (q^{d_2})_0^n - \eta \left((R_2^{d_2})_{1/2}^{n+1/2} - \frac{x_9^2}{x_{18}} - B(x_{18})_{-1/2} \right) \\ & + \gamma \left((S_2^{d_2})_{1/2}^{n+1/2} + F(x_9, x_{18})_{-1/2} + B_{\text{RHS}}(x_{18})_{-1/2} \right) \end{aligned} \quad (\text{B.47})$$

$$(f_r)_4 = -x_{10} - \eta x_3 + (A^p)_M^n + \eta (R_1^p)_{M-1/2}^{n+1/2} \quad (\text{B.48})$$

$$(f_r)_5 = -x_{13} + \eta x_6 + (A^{d_1})_0^n - \eta (R_1^{d_1})_{1/2}^{n+1/2} \quad (\text{B.49})$$

$$(f_r)_6 = -x_{16} + \eta x_9 + (A^{d_2})_0^n - \eta (R_1^{d_2})_{1/2}^{n+1/2} \quad (\text{B.50})$$

$$(f_r)_7 = -x_2 + \frac{1}{2}x_3 + \frac{1}{2}(q^p)_{M-1/2}^{n+1/2} \quad (\text{B.51})$$

$$(f_r)_8 = -x_5 + \frac{1}{2}x_6 + \frac{1}{2}(q^{d_1})_{1/2}^{n+1/2} \quad (\text{B.52})$$

$$(f_r)_9 = -x_8 + \frac{1}{2}x_9 + \frac{1}{2}(q^{d_2})_{1/2}^{n+1/2} \quad (\text{B.53})$$

$$(f_r)_{10} = -x_{11} + \frac{1}{2}x_{12} + \frac{1}{2}(A^p)_{M-1/2}^{n+1/2} \quad (\text{B.54})$$

$$(f_r)_{11} = -x_{14} + \frac{1}{2}x_{15} + \frac{1}{2}(A^{d_1})_{1/2}^{n+1/2} \quad (\text{B.55})$$

$$(f_r)_{12} = -x_{17} + \frac{1}{2}x_{18} + \frac{1}{2}(A^{d_2})_{1/2}^{n+1/2} \quad (\text{B.56})$$

$$(f_r)_{13} = -x_2 + x_5 + x_8 \quad (\text{B.57})$$

$$(f_r)_{14} = -x_1 + x_4 + x_7 \quad (\text{B.58})$$

$$(f_r)_{15} = -\mathcal{F}(x_{11})_M^{n+1/2} + \mathcal{F}(x_{14})_0^{n+1/2} \quad (\text{B.59})$$

$$(f_r)_{16} = -\mathcal{F}(x_{11})_M^{n+1/2} + \mathcal{F}(x_{17})_0^{n+1/2} \quad (\text{B.60})$$

$$(f_r)_{17} = -\mathcal{F}(x_{10})_M^{n+1} + \mathcal{F}(x_{13})_0^{n+1} \quad (\text{B.61})$$

$$(f_r)_{18} = -\mathcal{F}(x_{10})_M^{n+1} + \mathcal{F}(x_{16})_0^{n+1} \quad (\text{B.62})$$

The Jacobian matrix, defined as the derivative in the residuals with respect to the states, can be written as

$$\nabla f_r = \begin{bmatrix} -1 & 0 & \chi_1 & 0 & 0 & 0 & 0 & 0 & 0 & 0 & 0 & 0 & \chi_2 & 0 & 0 & 0 & 0 & 0 \\ 0 & 0 & 0 & -1 & 0 & \chi_3 & 0 & 0 & 0 & 0 & 0 & 0 & 0 & 0 & 0 & \chi_4 & 0 & 0 \\ 0 & 0 & 0 & 0 & 0 & 0 & -1 & 0 & \chi_5 & 0 & 0 & 0 & 0 & 0 & 0 & 0 & 0 & \chi_6 \\ 0 & 0 & -\eta & 0 & 0 & 0 & 0 & 0 & 0 & -1 & 0 & 0 & 0 & 0 & 0 & 0 & 0 & 0 \\ 0 & 0 & 0 & 0 & 0 & \eta & 0 & 0 & 0 & 0 & 0 & 0 & -1 & 0 & 0 & 0 & 0 & 0 \\ 0 & 0 & 0 & 0 & 0 & 0 & 0 & 0 & \eta & 0 & 0 & 0 & 0 & 0 & 0 & 0 & -1 & 0 \\ 0 & -1 & \frac{1}{2} & 0 & 0 & 0 & 0 & 0 & 0 & 0 & 0 & 0 & 0 & 0 & 0 & 0 & 0 & 0 \\ 0 & 0 & 0 & 0 & -1 & \frac{1}{2} & 0 & 0 & 0 & 0 & 0 & 0 & 0 & 0 & 0 & 0 & 0 & 0 \\ 0 & 0 & 0 & 0 & 0 & 0 & 0 & -1 & \frac{1}{2} & 0 & 0 & 0 & 0 & 0 & 0 & 0 & 0 & 0 \\ 0 & 0 & 0 & 0 & 0 & 0 & 0 & 0 & 0 & -1 & \frac{1}{2} & 0 & 0 & 0 & 0 & 0 & 0 & 0 \\ 0 & 0 & 0 & 0 & 0 & 0 & 0 & 0 & 0 & 0 & 0 & -1 & \frac{1}{2} & 0 & 0 & 0 & 0 & 0 \\ 0 & 0 & 0 & 0 & 0 & 0 & 0 & 0 & 0 & 0 & 0 & 0 & 0 & 0 & 0 & 0 & -1 & \frac{1}{2} \\ 0 & -1 & 0 & 0 & 1 & 0 & 0 & 1 & 0 & 0 & 0 & 0 & 0 & 0 & 0 & 0 & 0 & 0 \\ -1 & 0 & 0 & 1 & 0 & 0 & 1 & 0 & 0 & 0 & 0 & 0 & 0 & 0 & 0 & 0 & 0 & 0 \\ 0 & 0 & 0 & 0 & 0 & 0 & 0 & 0 & 0 & 0 & \chi_7 & 0 & 0 & \chi_8 & 0 & 0 & 0 & 0 \\ 0 & 0 & 0 & 0 & 0 & 0 & 0 & 0 & 0 & 0 & \chi_7 & 0 & 0 & 0 & 0 & 0 & \chi_9 & 0 \\ 0 & 0 & 0 & 0 & 0 & 0 & 0 & 0 & 0 & \chi_{10} & 0 & 0 & \chi_{11} & 0 & 0 & 0 & 0 & 0 \\ 0 & 0 & 0 & 0 & 0 & 0 & 0 & 0 & 0 & \chi_{10} & 0 & 0 & 0 & 0 & 0 & \chi_{12} & 0 & 0 \end{bmatrix}$$

The χ terms in the Jacobian are

$$\chi_1 = -2\eta \frac{x_3}{x_{12}} + \gamma \frac{d}{dx_3} F(x_3, x_{12})_{M+1/2} \quad (\text{B.63})$$

$$\chi_2 = \eta \left(\frac{x_3^2}{x_{12}^2} - \frac{d}{dx_{12}} B(x_{12})_{M+1/2} \right) + \gamma \left(\frac{d}{dx_{12}} F(x_3, x_{12}) + \frac{d}{dx_{12}} B_{\text{RHS}}(x_{12})_{M+1/2} \right) \quad (\text{B.64})$$

$$\chi_3 = 2\eta \frac{x_6}{x_{15}} + \gamma \frac{d}{dx_6} F(x_6, x_{15})_{-1/2} \quad (\text{B.65})$$

$$\chi_4 = \eta \left(-\frac{x_6^2}{x_{15}^2} + \frac{d}{dx_{15}} B(x_{15})_{-1/2} \right) + \gamma \left(\frac{d}{dx_{15}} F(x_6, x_{15}) + \frac{d}{dx_{15}} B_{\text{RHS}}(x_{15})_{-1/2} \right) \quad (\text{B.66})$$

$$\chi_5 = 2\eta \frac{x_9}{x_{18}} + \gamma \frac{d}{dx_9} F(x_9, x_{18})_{-1/2} \quad (\text{B.67})$$

$$\chi_6 = \eta \left(-\frac{x_9^2}{x_{18}^2} + \frac{d}{dx_{18}} B(x_{18})_{-1/2} \right) + \gamma \left(\frac{d}{dx_{18}} F(x_9, x_{18}) + \frac{d}{dx_{18}} B_{\text{RHS}}(x_{18})_{-1/2} \right) \quad (\text{B.68})$$

$$\chi_7 = -\frac{d}{dx_{11}} \mathcal{F}(x_{11}) \quad (\text{B.69})$$

$$\chi_8 = \frac{d}{dx_{14}} \mathcal{F}(x_{14}) \quad (\text{B.70})$$

$$\chi_9 = \frac{d}{dx_{17}} \mathcal{F}(x_{17}) \quad (\text{B.71})$$

$$\chi_{10} = -\frac{d}{dx_{10}} \mathcal{F}(x_{10}) \quad (\text{B.72})$$

$$\chi_{11} = \frac{d}{dx_{13}} \mathcal{F}(x_{13}) \quad (\text{B.73})$$

$$\chi_{12} = \frac{d}{dx_{16}} \mathcal{F}(x_{16}) \quad (\text{B.74})$$

$$(\text{B.75})$$

B.3.2 Trifurcation condition

For the trifurcation conditions, additional equations are added to the bifurcation conditions. For any additional daughter branch d_i , the new states include

$$x_i = \left[(q^{d_i})_0^{n+1} (q^{d_i})_0^{n+1/2} (q^{d_i})_{-1/2}^{n+1/2} (A^{d_i})_0^{n+1} (A^{d_i})_0^{n+1/2} (A^{d_i})_{-1/2}^{n+1/2} \right] \quad (\text{B.76})$$

for each branch. Additional residual equations correspond to the Lax-Wendroff solution and half time steps (one for q and one for A in each), and pressure-continuity at the daughter branch at the $n + 1/2$ and n time steps; hence, each daughter branch adds 6 additional equations and unknowns. For a trifurcation,

$$\begin{aligned}
\mathbf{x} = & \left[(q^p)_M^{n+1} (q^p)_M^{n+1/2} (q^p)_{M+1/2}^{n+1/2} \right. \\
& (q^{d_1})_0^{n+1} (q^{d_1})_0^{n+1/2} (q^{d_1})_{-1/2}^{n+1/2} \\
& (q^{d_2})_0^{n+1} (q^{d_2})_0^{n+1/2} (q^{d_2})_{-1/2}^{n+1/2} \\
& (q^{d_3})_0^{n+1} (q^{d_3})_0^{n+1/2} (q^{d_3})_{-1/2}^{n+1/2} \\
& (A^p)_M^{n+1} (A^p)_M^{n+1/2} (A^p)_{M+1/2}^{n+1/2} \\
& (A^{d_1})_0^{n+1} (A^{d_1})_0^{n+1/2} (A^{d_1})_{-1/2}^{n+1/2} \\
& (A^{d_2})_0^{n+1} (A^{d_2})_0^{n+1/2} (A^{d_2})_{-1/2}^{n+1/2} \\
& \left. (A^{d_3})_0^{n+1} (A^{d_3})_0^{n+1/2} (A^{d_3})_{-1/2}^{n+1/2} \right].
\end{aligned}$$

The Jacobian for the trifurcation is then given in Eq. (B.77)

[illegible]

The χ terms in the Jacobian are

$$\chi_1 = -2\eta \frac{x_3}{x_{15}} + \gamma \frac{d}{dx_3} F(x_3, x_{15})_{M+1/2} \quad (\text{B.78})$$

$$\chi_2 = \eta \left(\frac{x_3^2}{x_{15}^2} - \frac{d}{dx_{15}} B(x_{15})_{M+1/2} \right) + \gamma \left(\frac{d}{dx_{15}} F(x_3, x_{15}) + \frac{d}{dx_{15}} B_{\text{RHS}}(x_{15})_{M+1/2} \right) \quad (\text{B.79})$$

$$\chi_3 = 2\eta \frac{x_6}{x_{18}} + \gamma \frac{d}{dx_6} F(x_6, x_{18})_{-1/2} \quad (\text{B.80})$$

$$\chi_4 = \eta \left(-\frac{x_6^2}{x_{18}^2} + \frac{d}{dx_{18}} B(x_{18})_{-1/2} \right) + \gamma \left(\frac{d}{dx_{18}} F(x_6, x_{18}) + \frac{d}{dx_{18}} B_{\text{RHS}}(x_{18})_{-1/2} \right) \quad (\text{B.81})$$

$$\chi_5 = 2\eta \frac{x_9}{x_{21}} + \gamma \frac{d}{dx_9} F(x_9, x_{21})_{-1/2} \quad (\text{B.82})$$

$$\chi_6 = \eta \left(-\frac{x_9^2}{x_{21}^2} + \frac{d}{dx_{21}} B(x_{21})_{-1/2} \right) + \gamma \left(\frac{d}{dx_{21}} F(x_9, x_{21}) + \frac{d}{dx_{21}} B_{\text{RHS}}(x_{21})_{-1/2} \right) \quad (\text{B.83})$$

$$\chi_7 = 2\eta \frac{x_{12}}{x_{24}} + \gamma \frac{d}{dx_{12}} F(x_{12}, x_{24})_{-1/2} \quad (\text{B.84})$$

$$\chi_8 = \eta \left(-\frac{x_{12}^2}{x_{24}^2} + \frac{d}{dx_{24}} B(x_{24})_{-1/2} \right) + \gamma \left(\frac{d}{dx_{24}} F(x_{12}, x_{24}) + \frac{d}{dx_{24}} B_{\text{RHS}}(x_{24})_{-1/2} \right) \quad (\text{B.85})$$

$$\chi_9 = -\frac{d}{dx_{14}} \mathcal{F}(x_{14}) \quad (\text{B.86})$$

$$\chi_{10} = \frac{d}{dx_{17}} \mathcal{F}(x_{17}) \quad (\text{B.87})$$

$$\chi_{11} = \frac{d}{dx_{20}} \mathcal{F}(x_{20}) \quad (\text{B.88})$$

$$\chi_{12} = \frac{d}{dx_{23}} \mathcal{F}(x_{23}) \quad (\text{B.89})$$

$$\chi_{13} = -\frac{d}{dx_{13}} \mathcal{F}(x_{13}) \quad (\text{B.90})$$

$$\chi_{14} = \frac{d}{dx_{16}} \mathcal{F}(x_{16}) \quad (\text{B.91})$$

$$\chi_{15} = \frac{d}{dx_{19}} \mathcal{F}(x_{19}) \quad (\text{B.92})$$

$$\chi_{16} = \frac{d}{dx_{22}} \mathcal{F}(x_{22}) \quad (\text{B.93})$$

B.4 Ring like lesions

Physiologically, it is more common to have a ring-like stenosis at a bifurcation, meaning that the pressure loss term will influence our typical bi- and tri-furcation conditions. The pressure loss term should be applied in conjunction with the typical pressure bifurcation conditions. Recall that the loss at a stenosis can be written as

$$\begin{aligned}
p_p(L, t) &= p_d(0, t) + \frac{\mu K_v}{2\pi(r^p)^3} q + \frac{\rho K_t}{2(A^p)^2} \left(\frac{A^p}{A_s} - 1 \right)^2 |q|q + \frac{\rho K_u L_s}{A^p} \frac{\partial q}{\partial t} \\
&= p_d(0, t) + \frac{8\mu L_s \pi}{(A^p)^2 \mathcal{C}} q + \frac{\rho K_t}{2(A^p)^2} \left(\frac{1}{\mathcal{C}} - 1 \right)^2 |q|q + \frac{\rho K_u L_s}{A^p} \frac{\partial q}{\partial t}
\end{aligned}$$

where \mathcal{C} is the stenosis severity, A_s/A_p . The time derivative of the flow is approximated as

$$\frac{\partial q}{\partial t} = \frac{q^{n+1} - q^n}{\Delta t} = \frac{q^{n+1} - q^n}{2\gamma}. \quad (\text{B.94})$$

Then the states we need to solve for are

$$\begin{aligned}
\mathbf{x} = & \left[(q^p)_M^{n+1} (q^p)_M^{n+1/2} (q^p)_{M+1/2}^{n+1/2} \right. \\
& (q^{d_1})_0^{n+1} (q^{d_1})_0^{n+1/2} (q^{d_1})_{1/2}^{n+1/2} \\
& (q^{d_2})_0^{n+1} (q^{d_2})_0^{n+1/2} (q^{d_2})_{1/2}^{n+1/2} \\
& (A^p)_M^{n+1} (A^p)_M^{n+1/2} (A^p)_{M+1/2}^{n+1/2} \\
& (A^{d_1})_0^{n+1} (A^{d_1})_0^{n+1/2} (A^{d_1})_{M+1/2}^{1/2} \\
& \left. (A^{d_2})_0^{n+1} (A^{d_2})_0^{n+1/2} (A^{d_2})_{M+1/2}^{1/2} \right].
\end{aligned}$$

The equations that need to be solved for a bifurcation are

$$\begin{aligned}
(q^p)_M^{n+1} &= (q^p)_M^n - \eta \left((R_2^p)_{M+1/2}^{n+1/2} - (R_2^p)_{M-1/2}^{n+1/2} \right) \\
&+ \gamma \left((S_2^p)_{K+1/2}^{n+1/2} + (S_2^p)_{K-1/2}^{n+1/2} \right)
\end{aligned} \quad (\text{B.95})$$

$$\begin{aligned}
(q^{d_1})_0^{n+1} &= (q^{d_1})_0^n - \eta \left((R_2^{d_1})_{1/2}^{n+1/2} - (R_2^{d_1})_{-1/2}^{n+1/2} \right) \\
&+ \gamma \left((S_2^{d_1})_{1/2}^{n+1/2} + (S_2^{d_1})_{-1/2}^{n+1/2} \right)
\end{aligned} \quad (\text{B.96})$$

$$\begin{aligned}
(q^{d_2})_0^{n+1} &= (q^{d_2})_0^n - \eta \left((R_2^{d_2})_{1/2}^{n+1/2} - (R_2^{d_2})_{-1/2}^{n+1/2} \right) \\
&+ \gamma \left((S_2^{d_2})_{1/2}^{n+1/2} + (S_2^{d_2})_{-1/2}^{n+1/2} \right)
\end{aligned} \quad (\text{B.97})$$

$$(A^p)_M^{n+1} = (A^p)_M^n - \eta \left((R_1^p)_{M+1/2}^{n+1/2} - (R_1^p)_{M-1/2}^{n+1/2} \right) \quad (\text{B.98})$$

$$(A^{d_1})_0^{n+1} = (A^{d_1})_0^n - \eta \left((R_1^{d_1})_{1/2}^{n+1/2} - (R_1^{d_1})_{-1/2}^{n+1/2} \right) \quad (\text{B.99})$$

$$(A^{d_2})_0^{n+1} = (A^{d_2})_0^n - \eta \left((R_1^{d_2})_{1/2}^{n+1/2} - (R_1^{d_2})_{-1/2}^{n+1/2} \right) \quad (\text{B.100})$$

$$(q^p)_M^{n+1/2} = \frac{1}{2} \left((q^p)_{M-1/2}^{n+1/2} + (q^p)_{M+1/2}^{n+1/2} \right) \quad (\text{B.101})$$

$$(q^{d_1})_0^{n+1/2} = \frac{1}{2} \left((q^{d_1})_{-1/2}^{n+1/2} + (q^{d_1})_{1/2}^{n+1/2} \right) \quad (\text{B.102})$$

$$(q^{d_2})_0^{n+1/2} = \frac{1}{2} \left((q^{d_2})_{-1/2}^{n+1/2} + (q^{d_2})_{1/2}^{n+1/2} \right) \quad (\text{B.103})$$

$$(A^p)_M^{n+1/2} = \frac{1}{2} \left((A^p)_{M-1/2}^{n+1/2} + (A^p)_{M+1/2}^{n+1/2} \right) \quad (\text{B.104})$$

$$(A^{d_1})_0^{n+1/2} = \frac{1}{2} \left((A^{d_1})_{-1/2}^{n+1/2} + (A^{d_1})_{1/2}^{n+1/2} \right) \quad (\text{B.105})$$

$$(A^{d_2})_0^{n+1/2} = \frac{1}{2} \left((A^{d_2})_{-1/2}^{n+1/2} + (A^{d_2})_{1/2}^{n+1/2} \right) \quad (\text{B.106})$$

$$(q^p)_M^n = (q^{d_1})_0^n + (q^{d_2})_0^n \quad (\text{B.107})$$

$$(q^p)_M^{n+1/2} = (q^{d_1})_0^{n+1/2} + (q^{d_2})_0^{n+1/2} \quad (\text{B.108})$$

$$\begin{aligned} p(A_0^p, A^p, \beta)^{n+1/2} &= p(A_0^{d_1}, A^{d_1}, \beta)^{n+1/2} + \zeta_1 \frac{(q^p)_0^{n+1/2}}{((A^p)_0^{n+1/2})^2} \\ &+ \zeta_2 \left((A^p)_0^{n+1/2} \right)^{-2} \left(\frac{(A^p)_0^{n+1/2}}{A_s} - 1 \right)^2 \|(q^p)_0^{n+1/2}\| (q^p)_0^{n+1/2} \\ &+ \zeta_3 \frac{1}{(A^p)_0^{n+1/2}} \left(\frac{(q^p)_0^{n+1/2} - (q^p)_0^n}{2\gamma} \right) \end{aligned} \quad (\text{B.109})$$

$$\begin{aligned} p(A_0^p, A^p, \beta)^{n+1/2} &= p(A_0^{d_2}, A^{d_2}, \beta)^{n+1/2} + \zeta_1 \frac{(q^p)_0^{n+1/2}}{((A^p)_0^{n+1/2})^2} \\ &+ \zeta_2 \left((A^p)_0^{n+1/2} \right)^{-2} \left(\frac{(A^p)_0^{n+1/2}}{A_s} - 1 \right)^2 \|(q^p)_0^{n+1/2}\| (q^p)_0^{n+1/2} \\ &+ \zeta_3 \frac{1}{(A^p)_0^{n+1/2}} \left(\frac{(q^p)_0^{n+1/2} - (q^p)_0^n}{2\gamma} \right) \end{aligned} \quad (\text{B.110})$$

$$\begin{aligned}
p(A_0^p, A^p, \beta)^{n+1} &= p(A_0^{d_1}, A^{d_1}, \beta)^{n+1} + \zeta_1 \frac{(q^p)_0^{n+1}}{((A^p)_0^{n+1})^2} \\
&+ \zeta_2 ((A^p)_0^{n+1})^{-2} \left(\frac{(A^p)_0^{n+1}}{A_s} - 1 \right)^2 |(q^p)_0^{n+1}| (q^p)_0^{n+1} \\
&+ \zeta_3 \frac{1}{(A^p)_0^{n+1}} \left(\frac{(q^p)_0^{n+1} - (q^p)_0^n}{2\gamma} \right)
\end{aligned} \tag{B.111}$$

$$\begin{aligned}
p(A_0^p, A^p, \beta)^{n+1} &= p(A_0^{d_2}, A^{d_2}, \beta)^{n+1} + \zeta_1 \frac{(q^p)_0^{n+1}}{((A^p)_0^{n+1})^2} \\
&+ \zeta_2 ((A^p)_0^{n+1})^{-2} \left(\frac{(A^p)_0^{n+1}}{A_s} - 1 \right)^2 |(q^p)_0^{n+1}| (q^p)_0^{n+1/2} \\
&+ \zeta_3 \frac{1}{(A^p)_0^{n+1}} \left(\frac{(q^p)_0^{n+1} - (q^p)_0^n}{2\gamma} \right)
\end{aligned} \tag{B.112}$$

We define $p(A) = \mathcal{F}(A)$ as the tube law, and $G(q, A)$ as the pressure loss due to ring-like lesions. Also define the following constants for the pressure loss term:

$$\zeta_1 = \frac{8\pi\mu L_s}{\mathcal{C}} \tag{B.113}$$

$$\zeta_2 = \frac{\rho K_t}{2} \left(\frac{1}{\mathcal{C}} - 1 \right)^2 \tag{B.114}$$

$$\zeta_3 = \rho K_u L_s. \tag{B.115}$$

Note that we treat \mathcal{C} as a constant, i.e., even though the area of the parent vessel does change, we assume that the stenosis expands by a proportional amount. The residual vectors for the above equations are as follows.

$$\begin{aligned}
(f_r)_1 &= -x_1 + (q^p)_M^n - \eta \left(\frac{x_3^2}{x_{12}} + B(x_{12})_{M+1/2} - (R_2^p)_{M-1/2}^{n+1/2} \right) \\
&+ \gamma \left[F(x_3, x_{12})_{M+1/2} + B_{\text{RHS}}(x_{12})_{M+1/2} + (S_2^p)_{M-1/2}^{n+1/2} \right]
\end{aligned} \tag{B.116}$$

$$\begin{aligned}
(f_r)_2 &= -x_4 + (q^{d_1})_0^n - \eta \left((R_2^{d_1})_{1/2}^{n+1/2} - \frac{x_6^2}{x_{15}} - B(x_{15})_{-1/2} \right) \\
&+ \gamma \left((S_2^{d_1})_{1/2}^{n+1/2} + F(x_6, x_{15})_{-1/2} + B_{\text{RHS}}(x_{15})_{-1/2} \right)
\end{aligned} \tag{B.117}$$

$$\begin{aligned}
(f_r)_3 &= -x_7 + (q^{d_2})_0^n - \eta \left((R_2^{d_2})_{1/2}^{n+1/2} - \frac{x_9^2}{x_{18}} - B(x_{18})_{-1/2} \right) \\
&+ \gamma \left((S_2^{d_2})_{1/2}^{n+1/2} + F(x_9, x_{18})_{-1/2} + B_{\text{RHS}}(x_{18})_{-1/2} \right)
\end{aligned} \tag{B.118}$$

$$(f_r)_4 = -x_{10} - \eta x_3 + (A^p)_M^n + \eta(R_1^p)_{M-1/2}^{n+1/2} \quad (\text{B.119})$$

$$(f_r)_5 = -x_{13} + \eta x_6 + (A^{d_1})_0^n - \eta(R_1^{d_1})_{1/2}^{n+1/2} \quad (\text{B.120})$$

$$(f_r)_6 = -x_{16} + \eta x_9 + (A^{d_2})_0^n - \eta(R_1^{d_2})_{1/2}^{n+1/2} \quad (\text{B.121})$$

$$(f_r)_7 = -x_2 + \frac{1}{2}x_3 + \frac{1}{2}(q^p)_{M-1/2}^{n+1/2} \quad (\text{B.122})$$

$$(f_r)_8 = -x_5 + \frac{1}{2}x_6 + \frac{1}{2}(q^{d_1})_{1/2}^{n+1/2} \quad (\text{B.123})$$

$$(f_r)_9 = -x_8 + \frac{1}{2}x_9 + \frac{1}{2}(q^{d_2})_{1/2}^{n+1/2} \quad (\text{B.124})$$

$$(f_r)_{10} = -x_{11} + \frac{1}{2}x_{12} + \frac{1}{2}(A^p)_{M-1/2}^{n+1/2} \quad (\text{B.125})$$

$$(f_r)_{11} = -x_{14} + \frac{1}{2}x_{15} + \frac{1}{2}(A^{d_1})_{1/2}^{n+1/2} \quad (\text{B.126})$$

$$(f_r)_{12} = -x_{17} + \frac{1}{2}x_{18} + \frac{1}{2}(A^{d_2})_{1/2}^{n+1/2} \quad (\text{B.127})$$

$$(f_r)_{13} = -x_2 + x_5 + x_8 \quad (\text{B.128})$$

$$(f_r)_{14} = -x_1 + x_4 + x_7 \quad (\text{B.129})$$

$$(f_r)_{15} = -\mathcal{F}(x_{11})_M^{n+1/2} + \mathcal{F}(x_{14})_0^{n+1/2} + G(x_2, x_{11}) \quad (\text{B.130})$$

$$(f_r)_{16} = -\mathcal{F}(x_{11})_M^{n+1/2} + \mathcal{F}(x_{17})_0^{n+1/2} + G(x_2, x_{11}) \quad (\text{B.131})$$

$$(f_r)_{17} = -\mathcal{F}(x_{10})_M^{n+1} + \mathcal{F}(x_{13})_0^{n+1} + G(x_1, x_{10}) \quad (\text{B.132})$$

$$(f_r)_{18} = -\mathcal{F}(x_{10})_M^{n+1} + \mathcal{F}(x_{16})_0^{n+1} + G(x_1, x_{10}) \quad (\text{B.133})$$

The Jacobian for the system of equations is

$$\nabla f_r = \begin{bmatrix} -1 & 0 & \chi_1 & 0 & 0 & 0 & 0 & 0 & 0 & 0 & 0 & \chi_2 & 0 & 0 & 0 & 0 & 0 & 0 \\ 0 & 0 & 0 & -1 & 0 & \chi_3 & 0 & 0 & 0 & 0 & 0 & 0 & 0 & 0 & \chi_4 & 0 & 0 & 0 \\ 0 & 0 & 0 & 0 & 0 & 0 & -1 & 0 & \chi_5 & 0 & 0 & 0 & 0 & 0 & 0 & 0 & 0 & \chi_6 \\ 0 & 0 & -\eta & 0 & 0 & 0 & 0 & 0 & 0 & -1 & 0 & 0 & 0 & 0 & 0 & 0 & 0 & 0 \\ 0 & 0 & 0 & 0 & 0 & \eta & 0 & 0 & 0 & 0 & 0 & 0 & -1 & 0 & 0 & 0 & 0 & 0 \\ 0 & 0 & 0 & 0 & 0 & 0 & 0 & 0 & \eta & 0 & 0 & 0 & 0 & 0 & 0 & 0 & -1 & 0 \\ 0 & -1 & \frac{1}{2} & 0 & 0 & 0 & 0 & 0 & 0 & 0 & 0 & 0 & 0 & 0 & 0 & 0 & 0 & 0 \\ 0 & 0 & 0 & 0 & -1 & \frac{1}{2} & 0 & 0 & 0 & 0 & 0 & 0 & 0 & 0 & 0 & 0 & 0 & 0 \\ 0 & 0 & 0 & 0 & 0 & 0 & 0 & -1 & \frac{1}{2} & 0 & 0 & 0 & 0 & 0 & 0 & 0 & 0 & 0 \\ 0 & 0 & 0 & 0 & 0 & 0 & 0 & 0 & 0 & 0 & -1 & \frac{1}{2} & 0 & 0 & 0 & 0 & 0 & 0 \\ 0 & 0 & 0 & 0 & 0 & 0 & 0 & 0 & 0 & 0 & 0 & 0 & -1 & \frac{1}{2} & 0 & 0 & 0 & 0 \\ 0 & -1 & 0 & 0 & 1 & 0 & 0 & 1 & 0 & 0 & 0 & 0 & 0 & 0 & 0 & 0 & 0 & 0 \\ -1 & 0 & 0 & 1 & 0 & 0 & 1 & 0 & 0 & 0 & 0 & 0 & 0 & 0 & 0 & 0 & 0 & 0 \\ 0 & \chi_7 & 0 & 0 & 0 & 0 & 0 & 0 & 0 & 0 & \chi_8 & 0 & 0 & \chi_9 & 0 & 0 & 0 & 0 \\ 0 & \chi_7 & 0 & 0 & 0 & 0 & 0 & 0 & 0 & 0 & \chi_8 & 0 & 0 & 0 & 0 & 0 & \chi_{10} & 0 \\ \chi_{11} & 0 & 0 & 0 & 0 & 0 & 0 & 0 & 0 & 0 & \chi_{12} & 0 & 0 & \chi_{13} & 0 & 0 & 0 & 0 \\ \chi_{11} & 0 & 0 & 0 & 0 & 0 & 0 & 0 & 0 & 0 & \chi_{12} & 0 & 0 & 0 & 0 & 0 & \chi_{14} & 0 \end{bmatrix}$$

The χ terms in the Jacobian are

$$\chi_1 = -2\eta \frac{x_3}{x_{12}} + \gamma \frac{d}{dx_3} F(x_3, x_{12})_{M+1/2} \quad (\text{B.134})$$

$$\chi_2 = \eta \left(\frac{x_3^2}{x_{12}^2} - \frac{d}{dx_{12}} B(x_{12})_{M+1/2} \right) + \gamma \left(\frac{d}{dx_{12}} F(x_3, x_{12}) + \frac{d}{dx_{12}} B_{\text{RHS}}(x_{12})_{M+1/2} \right) \quad (\text{B.135})$$

$$\chi_3 = 2\eta \frac{x_6}{x_{15}} + \gamma \frac{d}{dx_6} F(x_6, x_{15})_{-1/2} \quad (\text{B.136})$$

$$\chi_4 = \eta \left(-\frac{x_6^2}{x_{15}^2} + \frac{d}{dx_{15}} B(x_{15})_{-1/2} \right) + \gamma \left(\frac{d}{dx_{15}} F(x_6, x_{15}) + \frac{d}{dx_{15}} B_{\text{RHS}}(x_{15})_{-1/2} \right) \quad (\text{B.137})$$

$$\chi_5 = 2\eta \frac{x_9}{x_{18}} + \gamma \frac{d}{dx_9} F(x_9, x_{18})_{-1/2} \quad (\text{B.138})$$

$$\chi_6 = \eta \left(-\frac{x_9^2}{x_{18}^2} - \frac{d}{dx_{18}} B(x_{18})_{-1/2} \right) + \gamma \left(\frac{d}{dx_{18}} F(x_9, x_{18}) + \frac{d}{dx_{18}} B_{\text{RHS}}(x_{18})_{-1/2} \right) \quad (\text{B.139})$$

$$\chi_7 = \zeta_1 \frac{1}{x_{11}^2} + \zeta_2 \frac{1}{x_{11}^2} \frac{2x_2}{|x_2|} + \zeta_3 \frac{1}{2\gamma} \frac{1}{x_{11}} \quad (\text{B.140})$$

$$\chi_8 = -\frac{d}{dx_{11}} \mathcal{F}(x_{11}) - 2\zeta_1 \frac{1}{x_{11}^3} x_2 - 2\zeta_2 \frac{1}{x_{11}^3} |x_2| x_2 - \zeta_3 \frac{1}{x_{11}^2} \frac{x_2 - (q^p)_M^n}{2\gamma} \quad (\text{B.141})$$

$$\chi_9 = \frac{d}{dx_{14}} \mathcal{F}(x_{14}) \quad (\text{B.142})$$

$$\chi_{10} = \frac{d}{dx_{17}} \mathcal{F}(x_{17}) \quad (\text{B.143})$$

$$\chi_{11} = \zeta_1 \frac{1}{x_{10}^2} + \zeta_2 \frac{1}{x_{10}^2} \frac{2x_1}{|x_1|} + \zeta_3 \frac{1}{2\gamma} \frac{1}{x_{10}} \quad (\text{B.144})$$

$$\chi_{12} = -\frac{d}{dx_{10}} \mathcal{F}(x_{10}) - 2\zeta_1 \frac{1}{x_{10}^3} x_1 - 2\zeta_2 \frac{1}{x_{10}^3} |x_1| x_1 - \zeta_3 \frac{1}{x_{10}^2} \frac{x_1 - (q^p)_M^n}{2\gamma} \quad (\text{B.145})$$

$$\chi_{13} = \frac{d}{dx_{13}} \mathcal{F}(x_{13}) \quad (\text{B.146})$$

$$\chi_{14} = \frac{d}{dx_{16}} \mathcal{F}(x_{16}) \quad (\text{B.147})$$

B.5 Web-like lesions

Web-like lesions are placed at the center of vessel segments and are modeled as monofurcations, i.e. a vessel with one daughter branch. The pressure loss at the web is

$$Y \equiv \Delta p_{\text{web}} = L_w \left(\frac{\mu}{K_{\text{perm}}} \frac{q}{A} + \frac{\rho G_w}{K_{\text{perm}}^{1/2}} \left(\frac{q}{A} \right)^2 \right). \quad (\text{B.148})$$

The states are The residual vectors for the states are

$$\begin{aligned} (f_r)_1 = & -x_1 + (q^p)_M^n - \eta \left(\frac{x_3^2}{x_9} + B(x_9)_{M+1/2} - (R_2^p)_{M-1/2}^{n+1/2} \right) \\ & + \gamma \left[F(x_3, x_9)_{M+1/2} + B_{\text{RHS}}(x_9)_{M+1/2} + (S_2^p)_{M-1/2}^{n+1/2} \right] \end{aligned} \quad (\text{B.149})$$

$$\begin{aligned}
(f_r)_2 = & -x_4 + (q^d)_0^n - \eta \left((R_2^d)_{1/2}^{n+1/2} - \frac{x_6^2}{x_{12}} - B(x_{12})_{-1/2} \right) \\
& + \gamma \left((S_2^d)_{1/2}^{n+1/2} + F(x_6, x_{12})_{-1/2} + B_{\text{RHS}}(x_{12})_{-1/2} \right)
\end{aligned} \tag{B.150}$$

$$(f_r)_3 = -x_7 - \eta x_3 + (A^p)_M^n + \eta (R_1^p)_{M-1/2}^{n+1/2} \tag{B.151}$$

$$(f_r)_4 = -x_{10} + \eta x_6 + (A^d)_0^n - \eta (R_1^d)_{1/2}^{n+1/2} \tag{B.152}$$

$$(f_r)_5 = -x_2 + \frac{1}{2}x_3 + \frac{1}{2}(q^p)_{M-1/2}^{n+1/2} \tag{B.153}$$

$$(f_r)_6 = -x_5 + \frac{1}{2}x_6 + \frac{1}{2}(q^d)_{1/2}^{n+1/2} \tag{B.154}$$

$$(f_r)_7 = -x_8 + \frac{1}{2}x_9 + \frac{1}{2}(A^p)_{M-1/2}^{n+1/2} \tag{B.155}$$

$$(f_r)_8 = -x_{11} + \frac{1}{2}x_{12} + \frac{1}{2}(A^d)_{1/2}^{n+1/2} \tag{B.156}$$

$$(f_r)_9 = -x_2 + x_5 \tag{B.157}$$

$$(f_r)_{10} = -x_1 + x_4 \tag{B.158}$$

$$(f_r)_{11} = -\mathcal{F}(x_8)_M^{n+1/2} + \mathcal{F}(x_{11})_0^{n+1/2} + Y(x_2, x_8) \tag{B.159}$$

$$(f_r)_{12} = -\mathcal{F}(x_7)_M^{n+1} + \mathcal{F}(x_{10})_0^{n+1} + Y(x_1, x_7) \tag{B.160}$$

The Jacobian for the system of equations can then be written as

$$\nabla f_r = \begin{bmatrix} -1 & 0 & \chi_1 & 0 & 0 & 0 & 0 & 0 & \chi_2 & 0 & 0 & 0 \\ 0 & 0 & 0 & -1 & 0 & \chi_3 & 0 & 0 & 0 & 0 & 0 & \chi_4 \\ 0 & 0 & -\eta & 0 & 0 & 0 & -1 & 0 & 0 & 0 & 0 & 0 \\ 0 & 0 & 0 & 0 & 0 & \eta & 0 & 0 & 0 & -1 & 0 & 0 \\ 0 & -1 & \frac{1}{2} & 0 & 0 & 0 & 0 & 0 & 0 & 0 & 0 & 0 \\ 0 & 0 & 0 & 0 & -1 & \frac{1}{2} & 0 & 0 & 0 & 0 & 0 & 0 \\ 0 & 0 & 0 & 0 & 0 & 0 & 0 & -1 & \frac{1}{2} & 0 & 0 & 0 \\ 0 & 0 & 0 & 0 & 0 & 0 & 0 & 0 & 0 & 0 & -1 & \frac{1}{2} \\ 0 & -1 & 0 & 0 & 1 & 0 & 0 & 0 & 0 & 0 & 0 & 0 \\ -1 & 0 & 0 & 1 & 0 & 0 & 0 & 0 & 0 & 0 & 0 & 0 \\ 0 & \chi_5 & 0 & 0 & 0 & 0 & 0 & \chi_6 & 0 & 0 & \chi_7 & 0 \\ \chi_8 & 0 & 0 & 0 & 0 & 0 & \chi_9 & 0 & 0 & \chi_{10} & 0 & 0 \end{bmatrix}$$

The χ terms in the Jacobian are

$$\chi_1 = -2\eta \frac{x_3}{x_9} + \gamma \frac{d}{dx_3} F(x_3, x_9)_{M+1/2} \quad (\text{B.161})$$

$$\chi_2 = \eta \left(\frac{x_3^2}{x_9^2} - \frac{d}{dx_9} B(x_9)_{M+1/2} \right) + \gamma \left(\frac{d}{dx_9} F(x_3, x_9) + \frac{d}{dx_9} B_{\text{RHS}}(x_9)_{M+1/2} \right) \quad (\text{B.162})$$

$$\chi_3 = 2\eta \frac{x_6}{x_{12}} + \gamma \frac{d}{dx_6} F(x_6, x_{12})_{-1/2} \quad (\text{B.163})$$

$$\chi_4 = \eta \left(-\frac{x_6^2}{x_{12}^2} + \frac{d}{dx_{12}} B(x_{12})_{-1/2} \right) + \gamma \left(\frac{d}{dx_{12}} F(x_6, x_{12}) + \frac{d}{dx_{12}} B_{\text{RHS}}(x_{12})_{-1/2} \right) \quad (\text{B.164})$$

$$\chi_5 = L_w \left(\frac{\mu}{x_8 K_{\text{perm}}} + \frac{2\rho G_w}{K_{\text{perm}}^{1/2}} \frac{x_2}{x_8^2} \right) \quad (\text{B.165})$$

$$\chi_6 = -\frac{d}{dx_8} \mathcal{F}(x_8) - L_w \left(\frac{\mu}{K_{\text{perm}}} \frac{x_2}{x_8^2} + \frac{2\rho G_w}{K_{\text{perm}}^{1/2}} \frac{x_2^2}{x_8^3} \right) \quad (\text{B.166})$$

$$\chi_7 = \frac{d}{dx_{11}} \mathcal{F}(x_{11}) \quad (\text{B.167})$$

$$\chi_8 = L_w \left(\frac{\mu}{x_7 K_{\text{perm}}} + \frac{2\rho G_w}{K_{\text{perm}}^{1/2}} \frac{x_1}{x_7^2} \right) \quad (\text{B.168})$$

$$\chi_9 = -\frac{d}{dx_7} \mathcal{F}(x_7) - L_w \left(\frac{\mu}{K_{\text{perm}}} \frac{x_1}{x_7^2} + \frac{2\rho G_w}{K_{\text{perm}}^{1/2}} \frac{x_1^2}{x_7^3} \right) \quad (\text{B.169})$$

$$\chi_{10} = \frac{d}{dx_{10}} \mathcal{F}(x_{10}) \quad (\text{B.170})$$

$$(\text{B.171})$$

APPENDIX

C

DRAM ALGORITHM

The delayed rejection adaptive Metropolis (DRAM) algorithm is outlined in Algorithm 4. This Markov chain Monte Carlo (MCMC) technique combines the traditional Metropolis algorithm with (1) a second proposal point (the *delayed rejection* component), and (2) an updating step where the covariance of the parameter distribution is updated (the *adaptive* component). As noted by Paun et al. [186], DRAM is superior in convergence to Metropolis-Hastings or adaptive Metropolis when inferring parameters for the 1D hemodynamics model, increasing convergence rates by utilizing both the rejection and adaptation steps.

Algorithm 4: Delayed rejection adaptive Metropolis (DRAM) algorithm

1. Define the DRAM design parameters: the number of observations encoded in the prior $n_s (= 1)$; the mean squared error of the observations σ_s^2 ; the length of the adaptation interval before updating the covariance $k_0 (= 100 \text{ steps})$; the number of chain iterations before terminating M
 2. Compute $\theta_0 = \arg \min_{\theta} J(\theta)$, where $J = \mathbf{r}^T \mathbf{r}$ is the sum of squared residuals.
 3. Set $SS_0 = J(\theta_0)$ and initial variance estimate as $s_0^2 = \frac{SS_0}{N-P}$
 4. Determine initial covariance estimate $C = s_0^2 [S^T(\theta_0)S(\theta_0)]^{-1}$ and the Cholesky factorization $R = \text{Chol}(C)$
 5. **for** $i = 1, 2, \dots, M$
 - (a) Draw a sample $\xi_k \sim \mathcal{N}(0, 1)$ and compute candidate parameter $\theta_{\text{cand}} = \theta_{k-1} + R\xi_k$
 - (b) Draw a uniform random sample $u_\alpha \sim U(0, 1)$
 - (c) Set $SS_{\text{cand}} = J(\theta_{\text{cand}})\mathbf{r}(\theta_{\text{cand}})$
 - (d) Calculate the acceptance probability $\alpha(\theta_{\text{cand}}|\theta_{k-1}) = \min(1, e^{-(SS_{\text{cand}} - SS_{k-1})/2s_{k-1}^2})$
 - (e) **if** $u_\alpha < \alpha$
 - i. Set $\theta_k = \theta_{\text{cand}}$ and $SS_k = SS_{\text{cand}}$
 - else (Delayed Rejection)**
 - i. Set $\gamma_2 = \frac{1}{5}$ and sample $\xi_k \sim \mathcal{N}(0, 1)$
 - ii. Construct second-state candidate $\theta_{\text{DR}} = \theta_{k-1} + \gamma_2 R\xi_k$ and draw the sample $u_{\text{DR}} \sim U(0, 1)$
 - iii. Compute $SS_{\text{DR}} = J(\theta_{\text{DR}})$ and acceptance probability $\alpha_{\text{DR}}(\theta_{\text{DR}}|\theta_{\text{cand}}, \theta_{k-1})$ defined in equation (5.38)
 - iv. **if** $u_{\text{DR}} < \alpha_{\text{DR}}$
 - Set $\theta_k = \theta_{\text{DR}}$ and $SS_k = SS_{\text{DR}}$
 - v. **else**
 - Set $\theta_k = \theta_{k-1}$ and $SS_k = SS_{k-1}$
 - end if**
 - (f) Update the error variance s_k^2 according to an inverse-gamma distribution, i.e. $s_k^2 \sim \text{Inv-Gamma}(a, b)$ where $a = \frac{1}{2}(n_s + N)$ and $b = \frac{1}{2}(n_s \sigma_s^2 + SS_k)$
 - (g) **if** $\text{mod}(k, k_0) = 1$ (**Adaptive Metropolis**)
 - Update the covariance $C_k = s_P \text{Cov}(\theta_0, \theta_1, \dots, \theta_{k-1}) + \epsilon I_{\mathcal{P}}$
 - (h) **else**
 - $C_k = C_{k-1}$
 - (i) **end if**
 - (j) Compute $R = \text{Chol}(C_k)$
 - end for**
-